Contribution to experimental study of mechanical and thermal damage in crystalline hard rocks

Mohammad Keshavarz Bakhshaiesh

UNIVERSITÉ JOSEPH FOURIER – GRENOBLE I

TERRE, UNIVERS & ENVIRONNEMENT

THÈSE

Pour obtenir le grade de

DOCTEUR DE L'UNIVERSITÉ JOSEPH FOURIER

Spécialité : Terre Solide

Présentée par :

Mohammad KESHAVARZ BAKHSHAIESH

Contribution to experimental study of mechanical and thermal damage in crystalline hard rocks

Composition du Jury :

A. M. BOULLIER	Directrice de recherche CNRS - Grenoble	Présidente
D. FABRE	Professeur CNAM - Paris	Rapporteur
J. ZHAO	Professeur EPF - Lausanne	Rapporteur
K. AMINI HOSSEINI	Professeur assistant IIEES - Téhéran	Examinateur
S. HALL	Chargé de recherche CNRS - Grenoble	Examinateur
K. SU	Ingénieur TOTAL - Pau	Examinateur
F. PELLET	Maître de conférences HDR UJF - Grenoble	Directeur de thèse
B. LORET	Professeur INP - Grenoble	Co-directeur de thèse

Thèse préparée au sein du Laboratoire 3S-R, « Sols, Solides, Structures et Risques »

Juin, 2009

Acknowledgements

I would first like to deeply thank my thesis supervisor associate professor Frederic Pellet and my co-advisor professor Benjamin Loret. Without their care and consideration, this work would likely not have matured.

Moreover, I would like to thanks Professor Denis Fabre, Professor Jian Zhao, Professor Anne-Marie Boullier, Dr. Steve Hall, Dr. Kambod Amini Hosseini and Dr. Kun Su the referees of my thesis for reviewing the thesis and their valuable comments.

My involvement to this work began four years ago when I was working as an engineering geologist in International Institute of Earthquake Engineering and Seismology (IIEES) in Iran. I want to thank Professor Mohammad Kazem Jafari for his valuable scientific support and his encouragement during the long period of my work in IIEES and during working on my thesis. I also benefited a great encouragement from Professor Mohsen Ghafori Ashtiany, previous director of IIEES, for which I am especially thankful. These two were earlier supporters and provided me with useful contacts during the process.

I also want to thank the French scientific counsel in Iran for providing the fellowship that allowed me to live in France at the beginning of my studies.

I would like also to give special thanks to Dr. Kambod Amini Hosseini. He was not only a member of my thesis jury but also I have benefited from his valuable comments during preparation of my manuscript.

I thank the support and the encouragement of Professor Pierre Foray, head of the team GEO in laboratory 3S-R. I would like to thank all the people who helped me during preparation of specimens and conducting laboratory tests, including Christophe Rousseau, Yves Orengo, Steve Hall, Roger Sabbia and Thomas Gabet. I also want to express my appreciation for all my friends in 3S-R laboratory specially miss Rachel Gelet for her precious notes for preparing my presentation.

Finally, my special thanks also to my family and to the family of my wife. Most important, to my wife Tahereh, and to my sons Ehsan and Babak, who put up with a string of trips abroad, lost week ends, and deal with odd working hours.

Mohammad Keshavarz

June, 2009

Abstract

The main objective of this work is to investigate crack propagation and damage evolution using acoustic emission (AE) to predict failure of rock during loading. In this research we recorded AE parameters in granite and gabbro rocks under stress, to establish a pattern of AE variation before failure that can be used in earthquake prediction. In order to investigate the effect of thermal and stress induced damages on AE parameters, a few tests were also conducted using pre-damaged specimens. AE monitoring, mechanical tests, elastic wave velocity measurements and microscopic investigations were used for these purposes. In order to compare the AE records in pure uniaxial compression (UC) and indirect tensile tests, a few Brazilian tests were carried out using AE monitoring. Plotting of the accumulated hits and the accumulated energy AE parameters versus time shows that the AE energy parameter is a more effective way to monitor crack propagation and to predict the failure of specimens than the conventional AE hits. According to AE records from granite and gabbro under UC test, three sharp steps of dramatic AE activity were distinguishable. The first one occurred at about 25 % and the second one at 60% of stress. The last step occurred when the stress level reached 90 to 95% of the ultimate strength of the rock. These steps are comparable to crack initiation (σ_{ci}), crack damage (σ_{cd}) thresholds and uniaxial compression strength (σ_{ucs}) in the stress-strain diagram presented by Martin (1993). The same steps were detectable during the Brazilian tests.

Comparing the acoustic emissions data for intact and thermally treated samples showed a considerable difference in the number and steps of acceleration of AE activity. It appears that microcrack evolution due to thermal damage plays a key role in the reduction of the number of AE hits during uniaxial tests on pre-heated specimens. The AE records of intact and thermally treated specimens of gabbro below 600°C are comparable. However, there is a significant difference between the records of specimens heated to more than 600°C and unheated gabbro. A drastic decrease in the uniaxial strength and elastic wave velocity was also evident in specimens that had been heated to above 600°C. Based on all the investigated parameters, we found that 600°C is a critical temperature that causes physical and mechanical (strength and elasticity modulus) degradation to the gabbro rock subjected to thermal treatment. On the other hand, it was observed that the damage due to ultra high stresses was less than that due to thermal effects, especially in the mechanical parameters. However, AE parameters were more affected by stress damage than thermal heating.

Keywords: *Uniaxial loading, crystalline rocks, acoustic emission, infrared radiation, damage evolution, thermal treating*

Contribution à l'étude expérimentale de l'endommagement mécanique et thermique de roches cristallines.

Résumé

Le principal objectif de ce travail est l'étude de l'endommagement et de la propagation de la fissuration dans des roches pour prédire leur rupture en utilisant les paramètres d'émission acoustique (EA). Nous avons étudié l'endommagement mécanique et thermique sur des roches de type gabbro et granite, soumises à des contraintes uniaxiales, afin d'identifier un modèle de variation de l'EA avant rupture qui pourrait être corrélé aux mesures faites avant un tremblement de terre. Afin de comparer l'effet de la température et l'effet d'un chargement mécanique sur les paramètres de l'EA, des essais de compression simple ont été réalisés sur des échantillons endommagés thermiquement et des échantillons endommagés mécaniquement sous fort confinement. Nous avons effectué lors de ces essais des mesures d'EA, des mesures de vitesse des ondes élastiques et une étude microscopique post mortem sur les éprouvettes. Par ailleurs, afin de comparer les paramètres de l'EA sous chargement de compression uniaxiale et sous chargement de traction indirecte, quelques essais brésiliens ont été effectués. L'analyse du nombre d'évènements acoustiques et de l'accumulation d'énergie en fonction du temps, montre que le paramètre d'énergie est plus efficace pour caractériser la propagation des fissures et pour prédire la rupture. Sur la base du paramètre d'énergie, au moins trois étapes de forte activité acoustique sont distinguées : la première se situe à environ 25% de la contrainte maximum admissible et la seconde apparaît à 60 %. La dernière étape apparaît vers 95% de la contrainte maximum. Les étapes observées sont analogues aux seuils de contrainte-déformation présentés par Martin (1993) à savoir: l'initiation de la fissuration (σ_{ci}), la propagation d'endommagement (σ_{cd}) et la contrainte maximum dans la roche (σ_{ucs}). Durant un essai Brésilien trois étapes sont aussi clairement enregistrées.

La comparaison des données sur les émissions acoustiques entre des échantillons intacts et des échantillons endommagés en température, montre une différence considérable du nombre des événements acoustiques. Les résultats d'EA des échantillons intacts et traités thermiquement en dessous de 600°C sont comparables. Par contre, il existe

une différence significative entre les mesures de l'EA faites sur les échantillons chauffés à plus de 600°C et celles faites sur un échantillon non chauffé. Sur la base de tous les paramètres que nous avons étudiés, nous avons constaté que 600°C est une température critique qui engendre des dégradations physiques et mécaniques (résistance et module d'élasticité), dues au chargement thermique, sur ce type de gabbro. Enfin, nous avons observé que l'endommagement dû à un chargement triaxial sous fortes contraintes de confinement (650 MPa) avait moins d'effet que l'endommagement induit par un chargement thermique.

Mots clés: *Chargement uniaxial, roches cristallines, émission acoustique, rayon infra rouge, évolution d'endommagement, traitement thermique.*

Table of contents

Chapter 5: Acoustic emission monitoring and infrared measurements under stress during laboratory tests

Chapter 6: AE monitoring, physical measurements and mechanical tests on thermally and mechanically damaged gabbro

List of Symbols

AE	acoustic emission
IR	infrared radiation
MS	micro-seismic activity
SWAT	stress wave analysis technique
NDE	non destructive evaluation
ΣN	the total number of events observed during a specific period of time.
ΣE	the sum of the energy emitted during a specific period of time.
Q	amplification facture
ζ	damping ratio
SNR	Signal + Noise-to-Noise Ratio
Ap-p	Peak-to-Peak Amplitude
NR	The number of events (ΔN) observed per unit time (ΔT)
tD	Event Duration
FFT	Fast Fourier Transform
SNR	Signal + Noise-to-Noise Ratio
Δt	Time-between-Event
AE/MS	acoustic emission/micro-seismic
EDZ	excavation damage/disturbed zone around tunnels
LST	anomalous land surface temperature
RS	remote sensing technology
IRTI	infrared radiation temperature imaging technique
ΔP	infrared radiant flux
ΔT_{max}.	maximum infrared temperature
ΔT_{avr}	average infrared temperature
Vp	primary elastic wave velocity
Vs	secondary elastic wave velocity
UCS	uniaxial or unconfined compressive strength
LVDT	Linear Variable Differential Transformers
ε_v	volume deformation
ε_{axial}	axial deformation
ε_{radial}	radial or lateral deformation

σ_{t-h}	tensile strength along horizontal diameter
σ_1	major principal stress
σ_3	minor principal stress
σ_t	tensile strength of the rock
σ_c	compressive strength of the rock
E	elasticity modulus
ν	Poisson's ratio
φ	friction angle
σ_{cc}	crack closure stress
σ_{ci}	crack initiation stress
σ_{cd}	crack development stress
σ_{ucs}	uniaxial compression strength
PDT	peak definition time
HDT	hit definition time
HLT	hit lockout time
J	the black-body irradiance or energy flux density
T_f	the final temperature that specimen was heated
α_v	thermal expansion coefficient
∂T	temperature difference
∂v	volumetric change due to temperate difference
MD	mechanically damaged specimen
TD	thermally damaged specimen

Chapter 1

Introduction

1.1 General introduction

In recent years, the process of rock failure has become especially urgent with reference to predicting earthquakes and to various dynamic rock pressure manifestations in rock masses (Pellet et al, 2007). In rock mechanics, fracturing of rock has long been studied to help understand the behavior of a particular rock mass when under stress. In general, loading of rock samples will cause some changes in the mechanical and physical behavior that can be measured in the laboratory. In most cases, before a rock mass failure, some measurable changes in the rock parameters have been reported, including acoustic emissions, elastic wave velocity, temperature and infrared radiation, as well as low frequency electromagnetic emissions (Friedemann, 2003; Ouzounov et al., 2004). These parameters could be used for long-term evaluation of the stability of underground excavations or fault rupture and, as a result, could be used for earthquake prediction. In particular, this might help to understand how microcracks in a rock sample, under an applied stress, combine to ultimately produce macroscopic failure. Such understanding is also of an engineering interest, particularly how cracks are formed under in situ stress around an underground excavation such as a tunnel or borehole. The use of ultrasonic techniques has provided the ability to remotely, and nondestructively, examine the interior of rock masses. Previous studies, (e.g. Falls, 1993), using ultrasonic propagation techniques, have examined existing microcracks, and have used acoustic emissions to locate the fracturing whilst it occurs. Such investigations have shown these techniques to be extremely effective.

In this thesis, acoustic emissions (AE) monitoring, infrared radiation (IR) and elastic wave velocity changes during loading of rock have been used to study damage evolution

and prediction of rock failure. This work is part of a project submitted to the International Institute of Earthquake Engineering and Seismology (IIEES) to study the feasibility of earthquake prediction by monitoring precursors from stress-induced rock. The aim of this thesis is to show the advantages of using AE in combination with other techniques to study rock damage evolution. This thesis takes AE studies a step further by investigating intact and pre-stressed damaged and heat-treated brittle rock specimens, following the crack evolution and failure predictions on a laboratory scale. Since the higher frequency AE events are more similar to earthquake motion, this research also investigates the feasibility of earthquake prediction by measurement of precursors in stressed rocks.

1.2 Research motivations and objectives

The main motivation of this study is to use acoustic emissions to monitor the crack propagation and to predict catastrophic failure of rock under stress. In this research we recorded AE parameters in two types of brittle rocks under stress to establish a pattern of AE variation before failure that could be used in earthquake prediction. Crystalline granite and gabbro rocks were used for this purpose. Simple uniaxial compression tests were carried out on intact, stress pre-damaged and thermally treated specimens. By monitoring the AE events and measuring the micro-deformation simultaneously in a few tests, the efficiency of this technique was compared with conventional AE monitoring methods. In order to compare the AE records in pure uniaxial compression and indirect tensile tests, a few Brazilian tests were carried out using AE monitoring.

Since damage cracks are known the main source of AE events, the survey of a pre-damaged specimen could give a good insight into understanding the physical relationship between damage and AE events during loading of rocks. Therefore, some additional tests were performed on thermal- and stress pre-damaged gabbro rock using AE monitoring techniques and by measuring the mechanical and physical changes that take place due to these damages. For the first time, to the author's knowledge, fresh gabbro has been used for thermal and mechanical damage experiments to investigate two types of damage by AE monitoring and to compare the results with the intact rock. The probable mechanisms of alterations in the samples and interpretation of the results will be discussed in this thesis. The following main tasks were performed to achieve the proposed research objectives:

1. Monitoring the variation of acoustic emission of intact Lavasan granite and North African gabbro under uniaxial compression tests;
2. Comparing the effectiveness of AE's energy and hit rate parameters to predict rock failure;
3. Studying crack propagation and failure mechanisms of gabbro rock under Brazilian tests using AE monitoring and comparing the results with uniaxial compression tests;
4. Studying ultra high triaxial stress pre-damaged and thermally treated gabbro specimens by AE monitoring to investigate the effects of the induced damage on physical and mechanical characteristics of hard rock as well as the effects on the AE parameters;
5. Calibrating the Hoek and Brown criteria and the Mohr Coulomb fit of African gabbro under ultra high compression triaxial tests;
6. Investigating the mineralogical effect of thermal treatment and stress damage of gabbro rock at the microscopic scale;
7. Investigating the feasibility of using a combined method of AE and infrared radiation study to use in earthquake prediction in the field based on the laboratory results and a literature survey.

1.3 Thesis outline

In chapter 2 we will present the basic concepts of the AE, IR and elastic wave methods in rock engineering studies, as well as the advantages and disadvantages of these methods. Investigations over the last four decades and new approaches to the above mentioned fields are discussed in chapter 3. Laboratory experiments on selected granite and gabbro rocks are outlined in chapter 4, and conventional AE monitoring of intact specimens under simple unixial compression and indirect tensile tests are discussed in chapter 5. The laboratory test procedures and AE monitoring techniques are also described in these two chapters. In chapter 6, special investigations using AE monitoring of pre-damaged specimens are presented. The effects of stress and thermal damage on AE records and the physical and mechanical parameters of hard rock are also discussed in this chapter. Chapter 7 draws the main conclusions together and describes the contributions of this thesis to understanding the role of AEs in failure prediction of intact and damaged rock.

Chapter 2

General concepts of acoustic emission and Infrared techniques

2. 1. Introduction

In this chapter, basic concepts, terminology and common equipment setup associated with the acoustic emission, as it applies to both laboratory and field studies in geotechnical area, are described. Consideration is also given to the recent applications of this technique. Since the earthquake prediction feasibility is one of the main aims of this research, infrared technique has also been discussed in this chapter as one of the new developed method in rock engineering and earthquake prediction science.

It is generally accepted that most solids, when stressed, emit sub-audible noises or low-level seismic signals (Hardy, 2003). There are a variety of terms to describe the phenomenon, including acoustic emission (AE), micro-seismic (MS) activity, seismo-acoustic activity, rock noise, stress wave analysis technique (SWAT), elastic shocks, and elastic radiation. However, in this thesis, this phenomenon will be referred as acoustic emission. In rock like materials, the origin of acoustic emission is not very clearly understood, but it appears to be related to the process of deformation and failure which are accompanied by a sudden release of strain energy (Hardy, 1981). In geologic materials, which are mainly polycrystalline in nature, AE may originate at the micro-level as a result of dislocations or at the macro-level by twinning, grain boundary movement, or initiation and propagation of fractures through and between mineral grains (Hardy, 2003). It is assumed that the sudden release of stored elastic strain energy accompanying these processes generates an elastic stress wave, which travels from the point of origin within the material, to a boundary where it is observed as AE.

In recent years, the application of AE techniques in geotechnical engineering has rapidly increased. This technique has been used for stability monitoring in mines, petroleum and natural gas caverns, radioactive waste repositories, and geothermal reservoirs. AE techniques are increasingly being used in laboratory-scale studies of both, basic and applied nature. Hardy (2003) has provided a detailed review of a wide range of geotechnical AE applications, AE concept, monitoring techniques, and the Kaiser effect. We have used it to prepare the next sections.

2. 2. Acoustic Emission (AE)

Acoustic emissions (AEs) are the stress waves produced by the sudden internal stress redistribution of the materials caused by the changes in the internal structure. Possible causes of the internal-structure changes are crack initiation and crack growth, crack opening and crack closure, dislocation movement, twinning, and phase transformation in monolithic materials and fiber breakage and fiber-matrix debonding in composites (Huang et al., 1998). Most of the sources of AEs are damage-related; thus, the detection and monitoring of these emissions are commonly used to predict material failure. Monitoring of acoustic emissions produced in the failure process of rocks has been shown to be very useful in assessing the stages of failure, the locations of active deformation and characterization of modes of rupture.

Based on source of pulses, there are two types of acoustic methods. A schematic drawing of the two different acoustic measurement methods is presented in figure 2. 1. The first is the sonic technique it utilizes two transducers; one a transmitter, generates a mechanical signal within the material, the other is a receiver, monitors the transmitted signals and any modifications resulting from stress changes. In contrast the AE technique utilizes only a receiving transducer (one or several) which monitors self-generated (passive) acoustic signals occurring within the material (Hardy, 2003).

By using three or more transducers it is possible to localize the source of events. Mostly the numbers of events per time unit or the number of counts per time unit are recorded. Each event is formed by a number of counts, which are the peaks above the background noise threshold of the recorded event. Other parameters of the signal (e.g. the frequency content, the energy, the duration of each signal) are sometimes also obtained and analyzed.

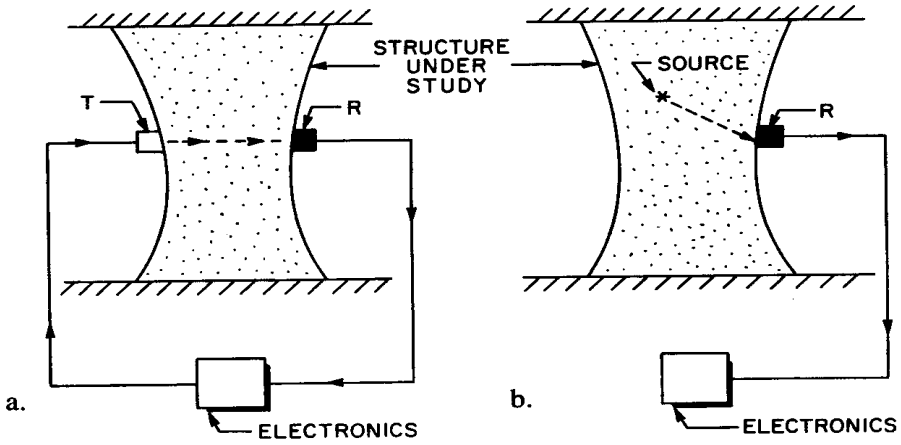

Figure 2.1: Two acoustic techniques utilized to evaluate the behaviour of geologic structures. a. sonic technique and b. AE/MS technique (Hardy, 2003).

One limitation of the method is that performing a test is rather complicated procedure with relatively sophisticated instruments (Hardy, 2003). The basic equipment for AE monitoring is relatively simple; a transducer which often is an accelerometer, an amplification system and a recording equipment. A filter system is also included to take away the background noise.

The fundamental frequency character of an observed AE signal depends on the characteristics of the sources and the distance between the source and the monitoring transducers. Frequencies below 1 Hz have been observed at large scale field sites, whereas in laboratory studies AE/MS signals have often been observed to contain frequencies greater than 500 kHz (Fig. 2.2).

The method has been successfully applied both in laboratory tests and for in-situ monitoring. Besides the applications of AE in research endeavors, AE has been widely used in industries, including for the detection of faults or leakage in pressure vessels, tanks, and piping systems. AE is also used to monitor the welding and corrosion progress.

The difference between the AE technique and other non destructive evaluation (NDE) methods is that AE detects the activities inside the materials, while other NDE methods attempt to examine the internal structures of the materials (Hardy, 1992). Furthermore, AE only needs the input of one or more relatively small sensors on the surface of the structure or specimen being examined so that the structure or specimen can be subjected to the in-service or laboratory operation while the AE system continuously monitors the progressive damage. Other NDE methods, such as ultrasound and x-ray, have to access the whole

structure or specimen, and therefore, the structure or specimen often needs to be disassembled and taken to the laboratory to be examined.

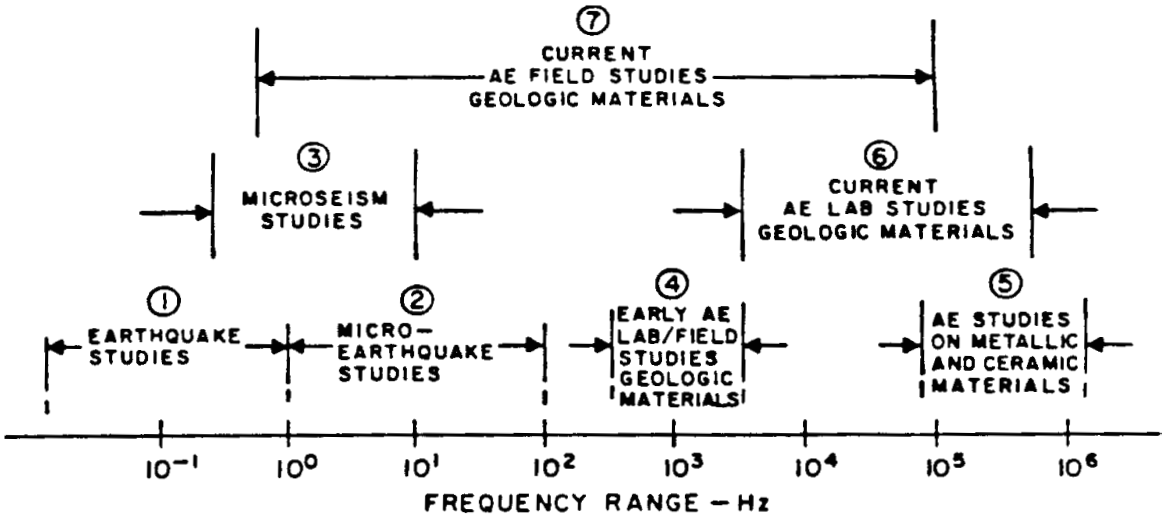

Figure 2.2: Frequency ranges over which AE and other associated studies have been conducted (Hardy, 2003).

2. 2. 1. AE parameters

An AE "event" generates a mechanical wave pulse. From a single AE "event" various signal wave trains ("hits") may result in the detection system, due to propagation phenomena, such as reflections, and sensor characteristics. In order to discriminate the first "hit" of an AE "event" from spurious signals and thus reduce uncertainty in the location of an AE source, the detection system used incorporates time parameters to be adjusted by the system operator. Figure 2.3 shows the main characteristics of an AE "hit". One should be aware that, by the term "energy", used in the detection system, is meant the area under the envelope of the rectified time signal wave train.

A variety of parameters are used to describe AE signals observed during laboratory and field AE studies. In most of the laboratory AE studies, the AE signals themselves are not recorded, rather, these signals are processed on-line using analog or digital techniques to provide various parameters like, event rate or energy rate. Figure 2.4 illustrates a typical section of AE data and an expanded AE event.

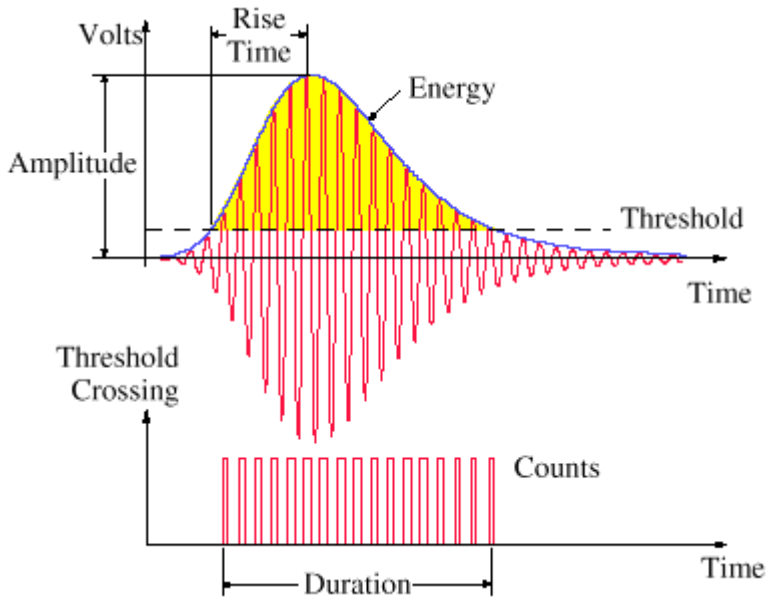

Figure 2.3: Main parameters of an acoustic emission hit (Huang et al, 1998)

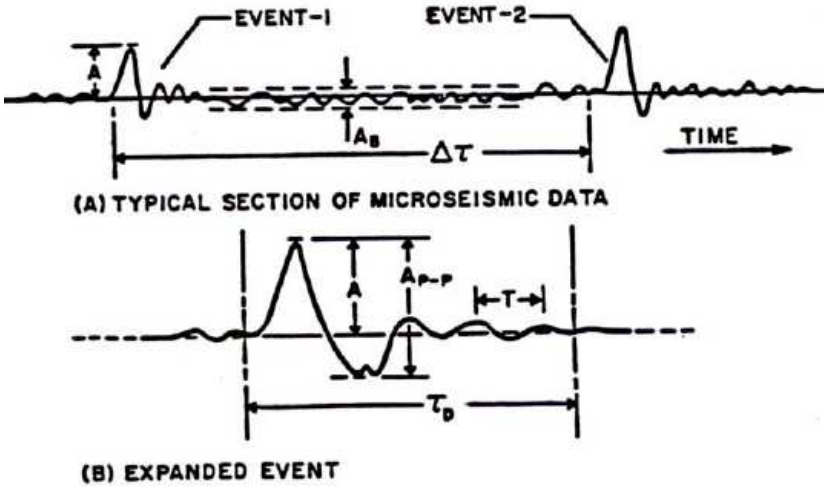

Figure 2.4: Typical sections of AE Data and an Expanded AE Event (Hardy, 1992).

According to Hardy (1994 and 2003) in the time domain such data is commonly described in terms of the following parameters:

- **Accumulated activity (N):** The total number of events observed during a specific period of time.
- **Accumulated Energy (ΣE):** The sum of the energy emitted by all events observed during a specific period of time.

- **Amplification Factor (Q):** The amount of mechanical gain of a structure when excited at a resonant frequency. The ratio of the amplitude of the steady state solution (amplitude at resonance) to the static deflection for the same force F. The amplification factor is a function of the system damping. For a damping ratio $\zeta=0$ (no damping) the amplification factor is infinite, for $\zeta=1$ (critically damped) there is no amplification.
- **Amplitude (A):** The instantaneous magnitude of an oscillating quantity such as sound pressure. The peak amplitude is the maximum value. Acoustic amplitude is measured and expressed in three ways: displacement, velocity and acceleration. Amplitude is also the y-axis of the vibration time waveform and spectrum; it helps define the severity of the vibration.
- **Background Amplitude:** The signal level presents in the absence of well-defined events. **Background noise:** Noise from all sources unrelated to a particular sound that is the object of interest. Background noise may include airborne, structure borne, and instrument noise.
- **Signal + Noise-to-Noise Ratio (SNR):** The ratio of the event plus background amplitude to the background amplitude.
- **Bandpass filter:** A filter that attenuates signals both below and above the desired passband.
- **Dynamic range:** The range between the loudest and the softest sounds that are in a piece of music, or that can be reproduced by a piece of audio equipment without distortion (a ratio expressed in decibels). In speech, the range rarely exceeds 40 dB; in music, is greatest in orchestral works, where the range may be as much as 75 dB.
- **Peak-to-Peak Amplitude ($A_{p\text{-}p}$)** is the amplitude measured between the maximum positive and negative peaks of the event.
- **Event Rate (NR):** The number of events (ΔN) observed per unit time (ΔT).
- **Energy (E):** The square of the event amplitude.
- **Energy Rate(ER):** The sum of the energy emitted by all events observed per unit time (ΔT).
- **Event Duration (t_D):** The total time of occurrence for an individual event.
- **Fast Fourier Transform (FFT):** The FFT is an algorithm, or digital calculation routine, that efficiently calculates the discrete Fourier transform from the sampled

time waveform. In other words it converts, or "transforms" a signal from the time domain into the frequency domain.

- **Free field:** An environment in which a sound wave may propagate in all directions without obstructions or reflections. Anechoic rooms can produce such an environment under controlled conditions.
- **Frequency:** The measure of the rapidity of alterations of a periodic signal, expressed in cycles per second or Hz. Average Fundamental Frequency (f) is the reciprocal of the average period computed over n cycles of the event.
- **Frequency response:** The changes in the sensitivity of a circuit, device, or room with frequency.
- **Peak:** The maximum positive or negative dynamic excursion from zero (for an AC coupled signal) or from the offset level (for a DC coupled) of any time waveform. Sometimes referred to as "true peak" or "waveform peak"
- **Peak-to-peak:** The amplitude difference between the most positive and most negative value in the time waveform.
- **Signal + Noise-to-Noise Ratio (SNR):** The ratio of the event plus background amplitude to the background amplitude.
- **Period:** A signal that repeats the same pattern over time is called periodic, and the period is defined as the length of time encompassed by one cycle, or repetition. The period of a periodic waveform is the inverse of its fundamental frequency.
- **Phase:** Phase is the measure of progression of a periodic wave. Phase identifies the position at any instant which a periodic wave occupies in its cycle. It can also be described as the time relationship between two signals.
- **Signal-to-noise (SN) Ratio:** The range or distance between the noise floor (the noise level of the equipment itself) and the music signal.
- **Time-between-Event (Δt):** The time between successive events, i.e., the time between the beginning of one event and the beginning of the next.
- **Wavelength:** The distance that sound wave travels to complete one cycle. The distance between one peak or crest of a sine wave and the next corresponding peak or crest. The wavelength of any frequency may be found by dividing the speed of sound by the frequency.

2.2.2. What information can AE studies provide?

Acoustic monitoring can tell us a lot of about the behavior of a volume of rock or concrete over time. In particular, these methods are ideal for the delineation and for the characterization of damage. Such damage may occur as the result of stress field changes or material degradation. In many early investigations, AE studies were used in laboratory rock mechanical experiments, and the number of AE 'events' was used as a simple measure of damage within the sample. More recently these techniques have become more sophisticated and considerable information can now be obtained in both laboratory and in situ studies. Acoustic methods can be used to:

- Indicate where damage is taking place: Using the arrival times of the seismic phases, the AE/MS events can be located within the rock with great accuracy.
- Assess the extent of the damage: The location of events and the event rate can be used to assess the areas within a material where most damage is occurring. The velocity of seismic waves within the material (derived from passive seismic tomography) can also be used to assess areas of damage as in general, regions of high damage will show lower velocities when compared to those from intact material.
- Determine information on the damage mechanism: The shape of the waveforms recorded at each sensor is a function of the source mechanism and the path effects experienced by the acoustic energy as it travels from the source to the receiver. From these data it is therefore possible to derive information about the orientation and mechanism (e.g. shear, isotropic) of the failure.
- Derive information relating to the stress field: Studies have indicated a relationship between zones with high velocity anomalies and regions of higher stress and, therefore, increased damage potential. These may be identified by passive tomographic imaging and used in conjunction with stress models derived from numerical modeling and/or in situ measurements. In addition, the orientation of the principal stresses acting at the source of the acoustic activity can be interpreted from waveform processing of the AE/MS activity.
- Determine material properties of the volume: As energy travels through rock, concrete or other materials the frequency and amplitude are affected by the

material properties. Measurements of seismic velocity, anisotropy and attenuation are therefore sensitive to changes in these material properties.

- Assess the time-dependent behavior of the material in response to engineering activities.
- The response of the material may vary with time in response to excavation or other engineering activities: The ability of acoustic methods to monitor in a continuous and passive manner is one of their greatest assets.

2.2.3. AE applications

The AE technique has been widely used in industries, including for the detection of cracks or leakage in pressure vessels, tanks, and piping systems. AE is also used to monitor the welding and corrosion progress.

The difference between the AE technique and other non-destructive evaluation (NDE) methods is that AE only needs the input of one or more relatively small sensors on the surface of the structure or specimen being examined (Huang et al., 1998). Therefore, the structure or specimen can be subjected to the in-service or laboratory operation while the AE system continuously monitors the progressive damage. Other NDE methods, such as ultrasound and x-ray, have to access the whole structure or specimen, and therefore, the structure or specimen often needs to be disassembled and taken to the laboratory to be examined. The research on AE can be generally divided into two categories:

2.2.3.1. Traditional acoustic emission

The traditional AE method only captures certain parameters (sometimes called AE features), including AE counts, peak levels, and energies. Then, the AE features are correlated with the defect formation and failures. These AE characteristics are only related to the captured signals and do not account for the source of the signal and wave propagation.

When the AE transducer senses a signal over a certain level (i.e., the threshold), an AE event is captured. The amplitude of the event is defined at the peak of the signal. The number of times the signal rises and crosses the threshold is the count of the AE event. The time period between the rising edge of the first count and the falling edge of the last count is the duration of the AE event. The time period between the rising edge of the first count

and the peak of the AE event is called the rise time. The area under the envelope of the AE event is the energy.

Figure 2.5 presents a typical AE system setup. The AE transducers are generally very sensitive piezoelectric sensors. Because the traditional AE technique only uses AE features, the actual waveforms are not critical to this method (Huang et al., 1998). The AE sensors (transducers) used are usually resonance sensors, which are only very sensitive to a certain frequency. Since the AE signals are very weak, a preamplifier is connected right after the AE transducer to minimize the noise interference and prevent the signal loss. Sometimes, the transducer and the preamplifier are built as a unit. Then, the signals pass through a filter to remove the noise. The signals are amplified by the main amplifier before being sent to the signal conditioner. Next, the AE features are subtracted and stored in a computer for further analysis. During investigations, other parameters, such as load, deformation, pressure, and temperature, can also be recorded as parametric inputs.

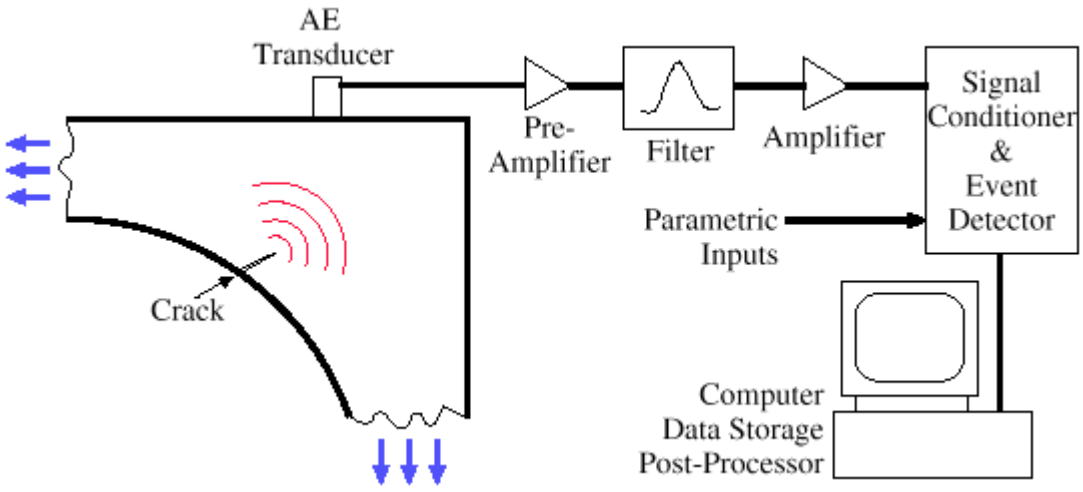

Figure 2.5: A typical AE system and definition of AE events (Huang et al., 1998)

2.2.3.2. Source-function and waveform analysis

The reason that traditional AE only uses some of the features of AE signals is because of the limitations of sensors as well as data-capturing and analysis capabilities. In recent years, due to the improvement of transducer technology, wide-band, and high-sensitivity sensors have been developed to capture the whole waveform. The rapid advancement of computer technology has made quick data acquisition and analysis of AE waveforms

feasible. It is now possible to characterize the nature of AE sources from the waveform captured by the new AE systems.

Research has been conducted on the techniques used to characterize the source of AE by examining the AE signals and using wave propagation for source-function and waveform analyses. The location-filtering technique discriminates the AE from noise signals by using the speed of wave propagation. Figure 2.6 shows an example of a location-filtering method that employs four AE sensors to identify the sources of the signals in a smooth cylindrical-bar fatigue sample of a nickel-based super alloy (Huang et al., 1998). The source of the AE signal is located in the gauge-length section only when the two inner sensors pick up the signal earlier than the two outer sensors, as exhibited in figure 2.6. If one of the outer sensors picks up a signal first, the signal has likely originated from the hydraulic system, load train, or other noise sources.

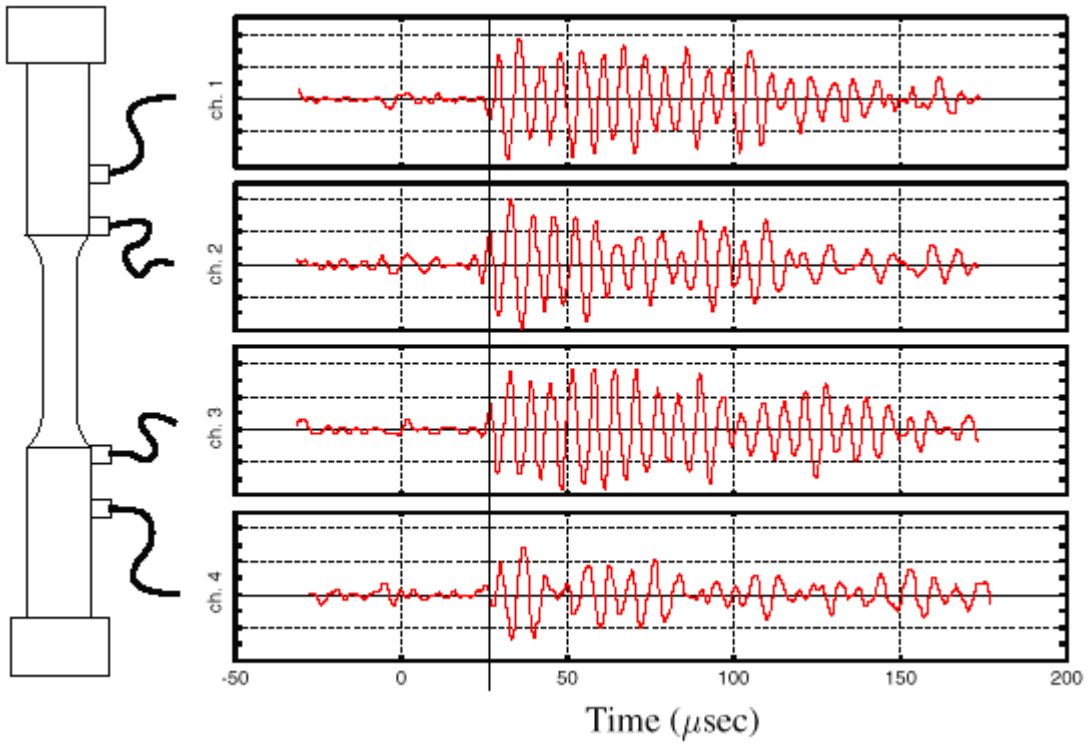

Figure 2.6: Investigation of the source location of AE signals by the arrival times of several AE sensors in a cylindrical bar (Huang et al., 1998).

Ideally, it is possible to solve inverse wave-propagation problems to identify the source of the AE signals detected using one or more sensors by analyzing the whole waveforms. But it is extremely complex and difficult to solve the inverse problem without any information of the source. Alternately, many researchers have been analytically studying the responses of some known AE sources, such as the elastic wave emitted from a finite mode I through-crack, from which the characteristics of AE sources can be identified.

2.2.3.3. Kaiser effect and Felicity ratio

Josef Kaiser a German researcher was the first person to observe the phenomenon that now bears his name (Hardy, 2003). The discovery was made during a study of the AE response of metals in the early 50s. Kaiser indicated that metals retain a memory of the previously applied stress field. The effect can be seen as a jump in cumulative hit rate versus stress dependency (Figure 2.7). A number of researchers have studied the Kaiser effect in geomaterials since the 1970's, and have discussed the factors that influence stress memory recollection of rocks under uniaxial and triaxial conditions. This technique has been developed and tried by various researchers in the past with the aim of providing a practical technique for retrieving the Kaiser effect (Hardy, 2003).

The Felicity ratio is the presence of acoustic emission, detectable at a fixed predetermined sensitivity level [threshold] at stress levels below those previously applied (ASTM E, 1316). Studies have shown that the Felicity Effect starts to appear when crack widths are greater than 0.15 to 0.20 mm (Tinkey et al., 2000). An evaluation criterion, the Felicity ratio, has been proposed to quantify the degree of deterioration. This ratio is defined as the stress at the onset of AE divided by the maximum prior stress; a Felicity ratio less than unity indicates damage.

Kaiser effect is a manifestation of the fundamental ability of heterogeneous solids to accumulate, to hold and to reproduce information about stress experienced in the past (Lavrov, 2001). The technique is a functionally workable technology, and it is anticipated that the rapid and economical determination of the in-situ stress in the rock is possible. It seems, however, that no satisfactory results have been obtained to date. The conclusions obtained are still contradictory, especially that regarding how long the stress memory can be retained (Lavrov et al., 2002).

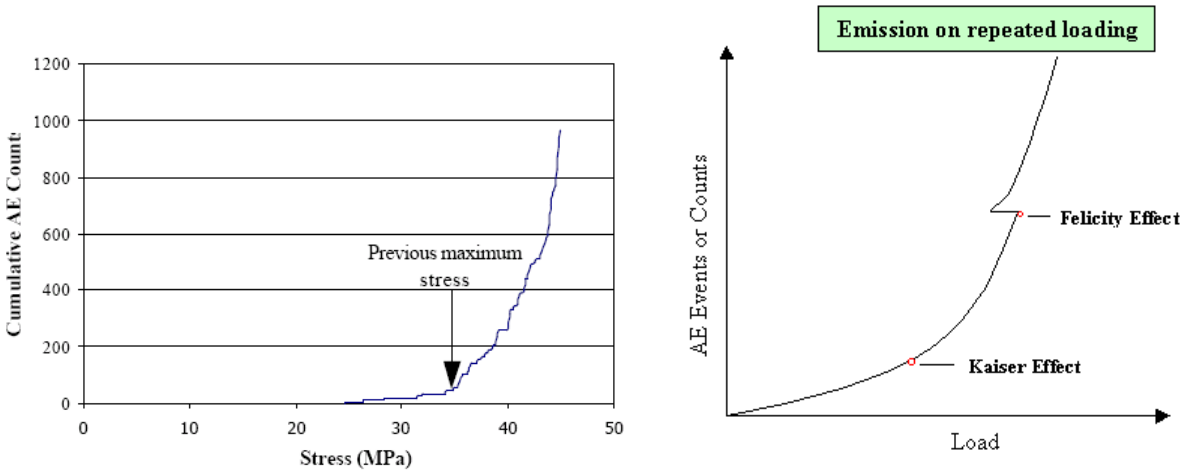

Figure 2.7: (a) Typical Kaiser effect (Villaescusa et al, 2002) and (b) Felicity ratio (Lavrov, 2001)

2.2.4. Laboratory Monitoring Systems

In laboratory, AEs monitor in a rock mass by installing an array of sensors around the volume and recording signals using a sophisticated electronic system (Hardy, 2003). The sensors use normally are ultrasonic (>30 kHz) piezoelectric transducers. When an elastic strain wave passes into the transducer through the front face there is a displacement across the piezoelectric element affixed behind. This generates a voltage output that can then be captured by an appropriate recording system.

AE laboratory studies involve the detection and processing of events occurring in a finite body (specimen or model). This is very much in contrast to the field AE studies where infinite or semi-infinite bodies are often involved. The major differences between AE laboratory and field studies are the smaller source dimensions, the finite nature of the structure under study and shorter source-to-transducer distances (Hardy, 2003). Hence, the data detected during laboratory AE studies generally exhibits the following characteristics:

- High dominant signal frequencies,
- Low signal amplitudes,
- High event rates, and
- Signal complexities due to stress wave reflection from specimen or model boundaries.

The finite nature of the specimen in laboratory AE studies has advantages as well as disadvantages. Since the specimen generally consists of a single type of material, the wave propagation complexities due to reflection and refraction within the specimen itself is eliminated. However, it may give rise to problems due to reflections at free boundaries and at specimen-test fixture interfaces. Care must also be taken with respect to the resonant frequencies of the structure and the associated test fixtures, and also the effect of the transducer on these frequencies. A number of studies have indicated that the frequency spectra of AE events detected in laboratory structures do reflect these intrinsic resonant frequencies, at least to a limited degree.

2.2.4.1 Laboratory Transducers

Most AE laboratory studies in the geotechnical area involve the detection of events with dominant frequencies in the range 50 kHz - 500 kHz. However, the common range based on the availability of commercial transducers, which include accelerometers, AE-transducers and piezoelectric elements, is 100 kHz - 600 kHz. In the current study, AE-transducers were utilized and only this type will be discussed here.

AE-transducers have become commercially available in the last 25 years. Such transducers consist of a single piezoelectric disc mounted on a flat sole or wear-plate and contained within a suitable protective housing (Figure 2.8). In use the transducer is attached to the structure under study. An AE wave striking the wear plate induces a stress within the piezoelectric disc that generates an equivalent output voltage. Most of the AE transducers are used in the resonant mode to achieve higher sensitivity. However, a number of transducers with a flat frequency response, over a somewhat extended frequency range are also available.

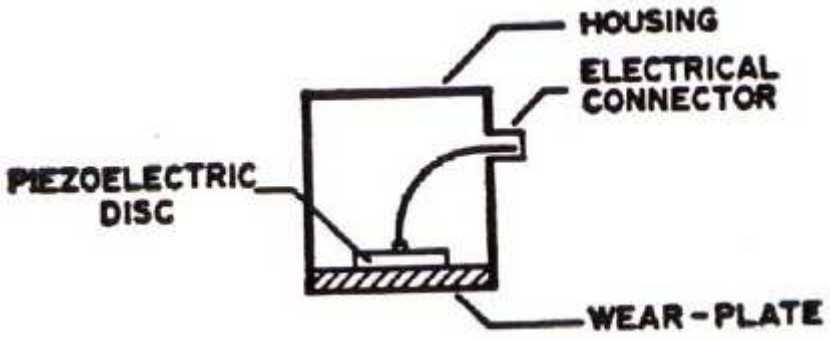

Figure 2.8: Basic Construction of a Simple AE-Transducer (Hardy, 1992)

AE-transducers are supplied by manufacturers in two forms, namely the single-ended and differential form. The differential form of AE-transducer, due to its more complex piezoelectric element configuration, can be utilized with a suitable differentiable pre-amplifier to cancel out electrical noises. This increases the effective signal-to-noise ratio (SNR) of the overall monitoring system.

2.2.4.2 Monitoring Facilities

The simplest AE monitoring system is the single-channel parametric type. Figure 2.8 shows a block diagram of one such system. The major disadvantage of a parametric system is that the detailed character of the AE signals is lost, however, such a system is capable of conveniently processing the large number of high frequency signals normally encountered in laboratory studies in geologic materials.

The parameter development section of the monitoring facility consists of a number of elements combined to provide the desired AE parameters, like threshold detector, digital counter, count rate module, accumulated counts module, etc. which are described below:

1. Threshold Detector: The Purpose of the threshold detector is to convert analogue AE signals to a pulse format. Figure 2.9 illustrates an incoming analogue signal and the equivalent pulse output based on a threshold level of ΔV. The threshold detector usually is a form of Schmidt trigger circuit, which produces a square pulse of fixed amplitude and duration each time the incoming signal exceeds a specific voltage level, denoted as the threshold level.

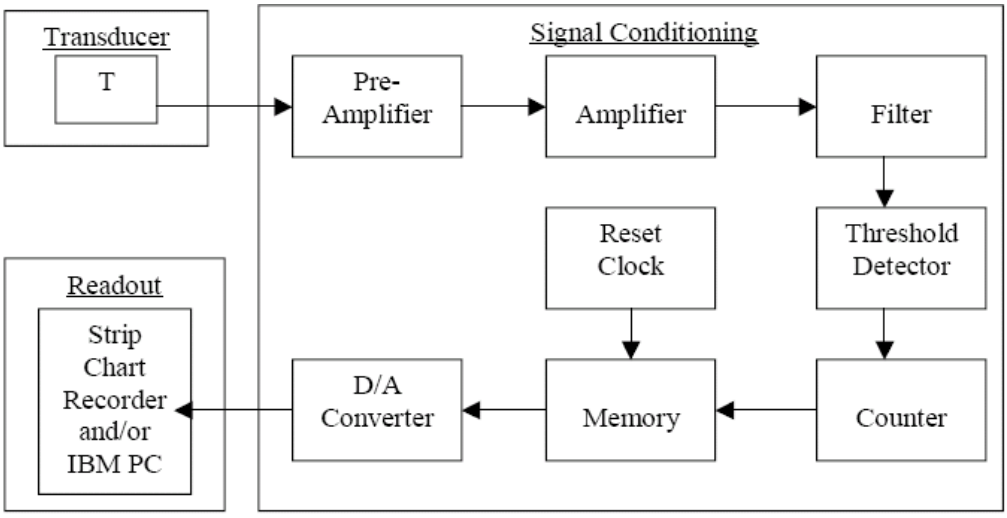

Figure 2.9: Single-Channel AE Monitoring Facility (Hardy, 1992)

As depicted in figure 2.10 the incoming signal exceeds the threshold level (ΔV) three times (points 1, 3 and 5) during the duration of the event (ΔT). At each of these times, a pulse is generated at the output of the threshold detector. These are known as ring-down pulses. It should also be noted that figure 2.5 depicts a case of a single AE event generating three ring-down pulses. In general, AE activity may therefore be defined in terms of event counts (NE) or the number of ring-down counts (NRD). This presents a certain degree of ambiguity since the relationships between NRD and NE will depend on the amplitude of the incoming event and the selected threshold level.

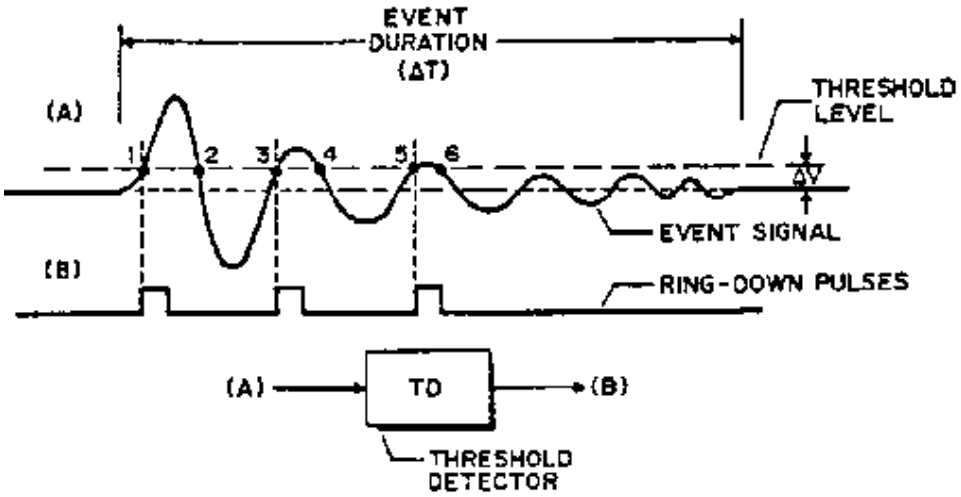

Figure 2.10: Pulse Output from a Threshold Detector in Response to an Incoming AE Event, (A): Incoming AE Event, (B): Pulse Output (after Hardy, 1985).

2. Digital Counter: The function of a digital counter is to accept the incoming pulses from the threshold detector, count, totalize and store these, and provide a suitable output. As illustrated in figure 2.11, stored data may be displayed visually using accessory elements, and such counters are usually equipped with circuits to provide start, stop and reset (storage dump) functions.

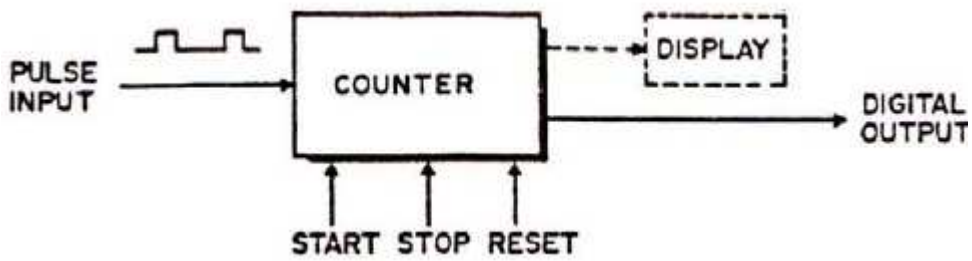

Figure 2.11: Format of a Typical Digital Counter (Hardy, 1985).

3. Total (Accumulated) Counts Module: The parameter development module for generating total count data is depicted in figure 2.11. Here pulses generated by the threshold detector, in response to the AE analogue input signal, are fed into a counter. The output of the counter is a digital signal equivalent to the total number of counts accumulated.

4. Count Rate Module: The total counts module is slightly modified with an addition of a reset clock to generate the count rate data (figure 2.12). The function of the reset clock is to provide a reset pulse to the counter at selected intervals of time. In operation, pulses generated by the threshold detector, in response to the incoming signals, are fed into the counter and accumulate until the clock generates a reset pulse. This dumps the counter, dropping the digital output to zero, and initiating a new count sequence. The equivalent count rate of such a system is equal to the total number of counts accumulated between reset pulses divided by the time between such pulses.

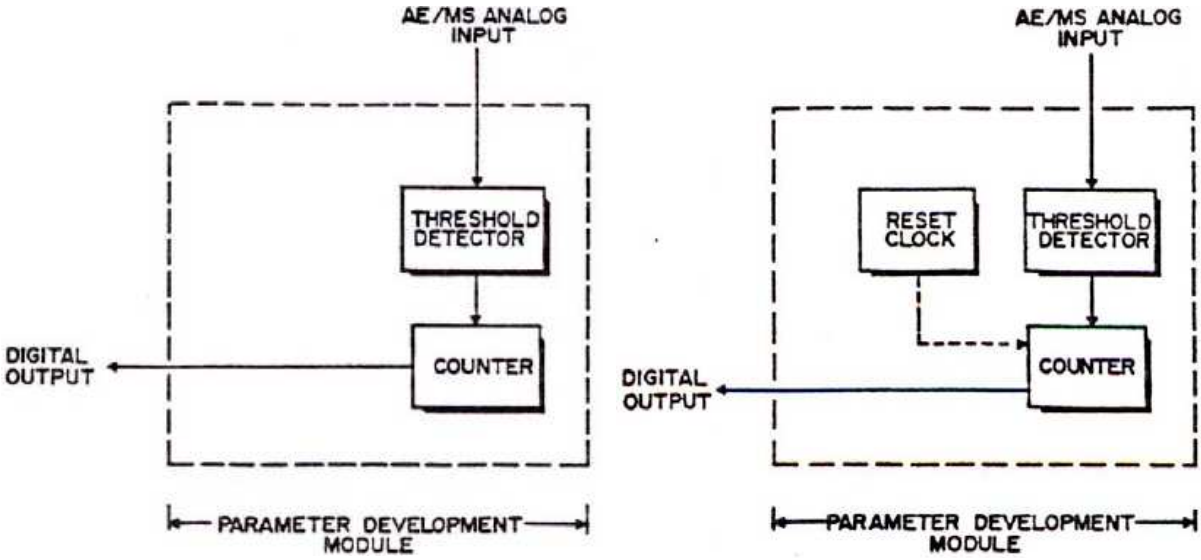

Figure 2.12: Block diagram of a parameter development module for generating accumulated hit (left) and hit rate (right) data (Hardy, 1985).

2.2.5. Advantages of Acoustic Emission data

- **Data quantity.** AEs are abundant during rock physics experiments, especially when microcracking proliferates under high stresses. Hence, a large amount of data exists during an experiment that could be available for material test studies.

- **Data quality.** Due to the use of modern multi-channel digital monitoring systems and arrays of sensors, high quality data is often obtained. This has high data sampling and high amplitude resolution.
- **Array coverage.** The use of an array for AE monitoring, often with as many as 16 sensors, and the ability to distribute this in an optimal manner around the rock volume, gives the opportunity for very good focal coverage. This is a major problem encountered in other fields of seismology where the positioning of an array is restricted by access or logistics.
- **Rock mass behavior.** Because AE monitoring is often in a very confined rock mass, such as a laboratory sample or small region of a tunnel wall, then the rock is likely to have a reasonably isotropic, homogeneous behavior over the source-receiver path. Although, at ultrasonic wavelengths (millimeters) propagation becomes complicated due to microcrack or crystal fabric, bedding alignment and open fractures. In other fields of seismology the source-receiver path is often much more complicated with the seismic wave traveling through very complex, layered and variable materials.
- **Constrained rock mass properties.** AE monitoring is often performed during an experiment as one of many scientific measurements conducted on the same rock mass. These may include other ultrasonic measurements such as velocity or attenuation studies, or may include more diverse measurements such as permeability or strain. This means that the small rock volume over which AE monitoring takes place often has very well studied and hence constrained properties.
- **Sensor Logistics.** For this thesis, the sensors used are commercially available piezoelectric transducers. These are usually used for non-destructive testing of materials, and for engineering applications. Transducer designs are extremely variable depending upon the manufacturer, the application and the frequency response required. Because piezoelectric transducers are commercially available, they are easy to obtain at reasonable cost, and are generally made to high specifications and sensitivity limits. They are also easy to handle and can be adapted quite efficiently to most experimental regimes.

2.2.6. Disadvantages of Acoustic Emission Data

Piezoelectric transducers are not designed specifically for ultrasonic amplitude studies. It is the response of the sensors to incident elastic waves that produces the main problems in ultrasonic amplitude studies.

- **Sensor response.** It is unknown whether piezoelectric transducers respond to particle displacement, velocity or acceleration, or some frequency-dependent mixture of the three (Hardy, 2003). Furthermore, it is highly likely that sensors of different models and/or manufacturers respond differently piezoelectric transducers also have complicated frequency response functions. Some appear to have a broadband response whereas others are very resonant.
- **Uniaxial monitoring.** All commercial piezoelectric transducers are uniaxial in design. No rotation of S-wave energy can hence be performed as triaxial sensors are required.
- **Sensor azimuthally dependency.** Ultrasonic wavelengths are of the same dimensions as the piezoelectric transducers used to record them. This gives an azimuthally dependency at these high frequencies.
- **Sensor coupling.** Amplitudes from piezoelectric transducers are highly dependent upon how well the transducer is coupled to the transmission medium.
- **Qualitative data.** The commercial AE systems can only estimate qualitatively how much damage is in the material and approximately how long the components will last. So, other NDE methods are still needed to do more thorough examinations and provide quantitative results.
- **Noise problem.** Service environments are generally very noisy, and the AE signals are usually very weak. Thus, signal discrimination and noise reduction are very difficult, yet extremely important for successful AE applications.

2.3. Infrared radiation technique (IR)

One type of light is infrared, which can be used to measure the heat radiated by an object. Infrared waves have wavelengths that are longer than visible light and shorter than microwaves. The heat detected in infrared rays is a product of the motion of atoms and molecules. The hotter it is the more molecule motion occurs. Everything above 0°K

(Kelvin) radiates infrared, even cold objects such as ice cubes. These light rays can be detected with a special thermal infrared camera which allows to visually seeing the infrared energy emitted by any object. The camera converts the thermal signal into a temperature; these temperatures are what are seen in the picture and are colour coded.

Thermal infrared radiation refers to electromagnetic waves with a wavelength of between 3.5 and 20 micrometers (figures 2.13 and 2.14). Most remote sensing applications make use of the 8 to 13 micrometer range. The main difference between thermal infrared and the infrared discussed above is that thermal infrared is emitted energy, whereas the near infrared (photographic infrared) is reflected energy (Luong, 1993).

Infrared heating is the transfer of thermal energy in the form of electromagnetic waves. IR is just one part of the electromagnetic spectrum that includes visible light and other forms of electromagnetic energy: gamma rays, X-rays, ultraviolet rays, visible light, infrared rays, microwave and radio waves.

There are several physical laws that explain the properties of infrared radiation. The first and probably most important of these laws states that there is a positive relationship between radiant efficiency and the temperature of an infrared source. Radiant efficiency is the percentage of radiant output from a heat source. The proportion of the energy transmitted from a heat source by each of the three heat source methods is dependent on the physical and ambient characteristics surrounding the heat source, and, in particular, the source's temperature. The Stefan-Boltzman law of radiation states that as the temperature of a heat source is increased, the radiant output increases to the fourth power of its temperature. The conduction and convection components increase only in direct proportion with the temperature change. In other words, as the temperature of a heat source is increased, a much greater percentage of the total energy output is converted into radiant energy.

2.3.1. Thermomechanical theory and heat radiation of stressed rocks

If we neglect work against gravity, almost all mechanical work done during deformation must be converted into heat. Because faults are sites of concentrated tectonic work, they are favorable places to look for evidence of mechanically generated heat.

The heat radiation, considering the time derivative of equation 2.1.

Identify isolated area of thermal infra-red increase. The temperature may typically increase by 2 to 4 degrees C or higher than the sounding area.

$$\tau V > q \qquad (2.1)$$

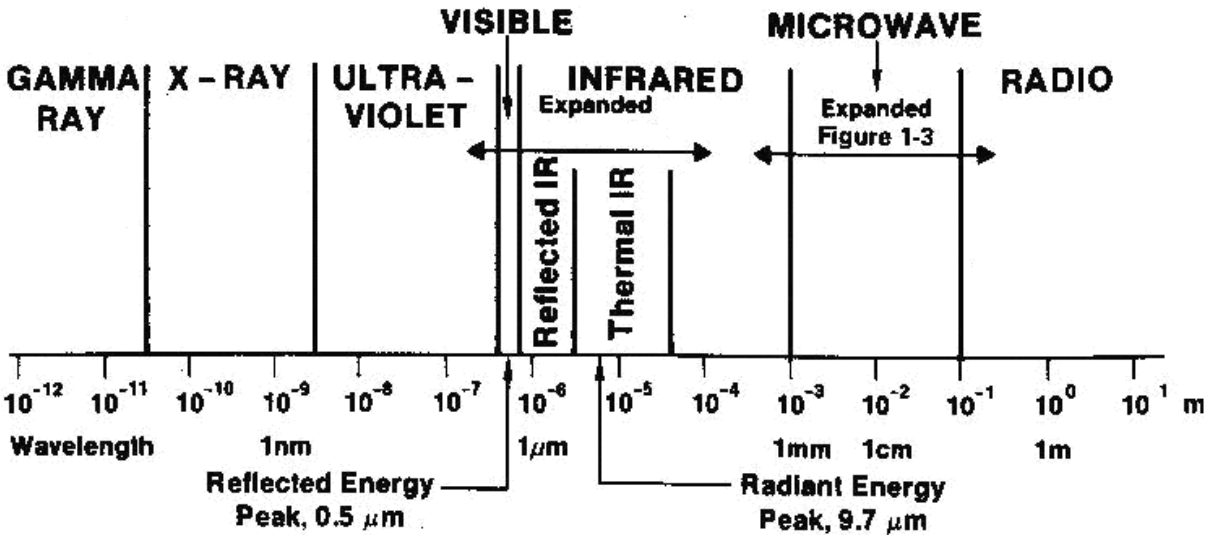

Figure 2-13: Electromagnetic spectrum.

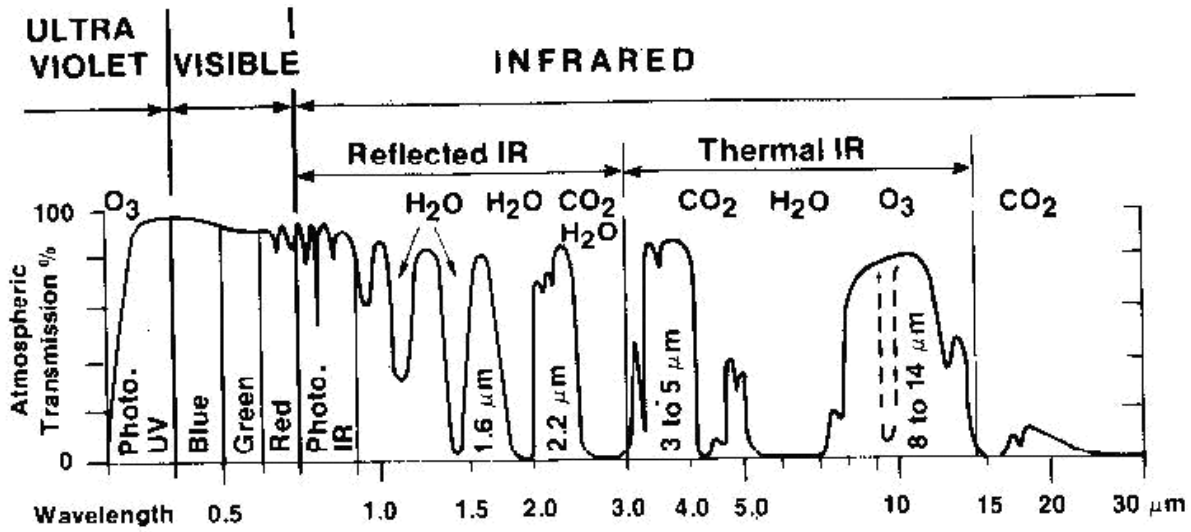

Figure 2-14: Expanded version of the visible, infrared and microwave regions of electro magnetic spectrum (Finkenthal, 1996)

In this inequality, "τ" is the mean shear stress acting on a fault sliding at velocity *v* and *q* is the heat flow generated by the fault.

There are two classes of thermomechanical effects in faulting. There will be a steady-state thermal signature resulting from the work of faulting averaged over geological time. The other is a transient heat pulse that may also occur from the coseismic slip during earthquakes in that case the value of V to be used in equation 2.1 is a particle velocity appropriate for dynamic slip, 10-100 m/s.

Such fracture and failure problems are notoriously intractable. The heterogeneous state of the Earth and the inaccessibility of the fault zone to direct measurement impose further difficulties.

2.3.2. Infrared thermography measurements

Infrared thermography is a technique for producing heat pictures from the invisible radiant energy emitted from stationary or moving objects at any distance and without surface contact, or in way influencing the actual surface temperature of the objects under consideration (Luong, 1993). As it is mentioned previously, if the work against gravity would ignored, almost all mechanical work done during deformation must be converted into heat. Geological faults are sites of concentrated tectonic work and are therefore the obvious place to look for evidence of mechanically generated heat.

In the two last decades infrared thermography has been used in different field investigations as well as in laboratory studies, with applications in aerial thermal land mapping, geological survey, geotechnical instrumentation, leakage insulation and construction practices for rock-like and rock engineering. The experimental studies have indicated that the structure of the rock material changes as loading and associated physical and chemical phenomena take place internally, including fracturing, ionization, electron excitation, energy accumulation, consumption, and conversion, etc. (Wu et al., 2000). The detectable IR radiation temperature reflects the variation of the thermal radiation energy, and could also reflect the physical and chemical mechanisms, providing some precursor warning signals of rock failure, collapse and disasters. Wu et al. (2000) addressed two types of infrared imaging systems: Aerial imagery and ground – based imagery. The first system uses aerial recorded data for interpreting heat abnormality, while the second type detects and interprets heat changes in laboratory and field studies. Table 2.1 shows this

classification. In chapter 3 the results of a few prefer studies in both laboratory and field are presented.

Table 2.1: The application of infrared radiation and remote sensing technology (Wu et al., 2000)

Air-based satellite, aircraft	Ground-based -desktop, tripod, human-hands
Military movement monitoring	Military object monitoring
Military placement detection	Machine manufacture monitoring
Missile trajectory	Electrical equipment testing
Weapon IR image-guidance	Heat equipment monitoring
Earth resource investigation	Sub-surface defect detection
Mineral exploration	Friction-welding measurement
Geothermal surveying	Animal behaviour analysis
Plant cover investigation	Medical diagnosis
Forest disaster diagnosis	Buildings diagnosis
Regional wetland mapping	Piping corrosion inspection
Global change monitoring	Crystal growth observation
Regional pollution monitoring	Stress-related damage
Urbanization monitoring	Tire friction measurement
Biological environment monitoring	Material fatigue test
Earthquake forecast	Slope diagnosis
	Rock failure and collapse disaster detection

Chapter 3

Overview of previous studies on Acoustic emission, infrared radiation and elastic wave velocity changes due to stress

3.1. Introduction

From the early 1970s to now, AE monitoring has been mostly used to evaluate the stress memory by Kaiser Effect, seismicity and b-value studies, crack propagation, heterogeneity in geomechanics. The results of some of the most important investigations (laboratory and in-situ testing) have been presented in this chapter. Recent studies of infrared radiation and elastic wave velocity changes of stress induced rock have also been discussed. In chapter 2 the different concepts of acoustic emission and infrared investigation techniques are presented. In this chapter we review the previous studies on acoustic emission, infrared radiation and elastic wave velocity changes during loading, in rock mechanics studies and their applications in studies of failure mechanisms and earthquake prediction. For these purposes the results of some of the most important investigations are briefly presented. Since this work is part of a project that has been presented in IIEES to study feasibility of earthquake prediction by monitoring of precursors, some general applications of AE and IR studies in rock mechanics have also been discussed. The two main branches of IR research, laboratory and remote sensing studies, have been considered in this review. In addition, the studies of elastic wave velocity changes during stress variations in field and in laboratory investigations have been considered.

3.2. Acoustic Emission

Since the early 1970s there has been an increasing interest in the use of acoustic emission/microseismic (AE/MS) techniques for the laboratory and field investigation of geological materials and structures (Hardy, 2003). AE laboratory studies involve the detection and processing of events occurring in a finite body (specimen or model), in contrast to field studies where infinite or semi-infinite bodies are generally involved.

Acoustic emission (AE) has been widely used to evaluate cracking processes in laboratory specimens and engineering structures because of its high sensitivity to crack initiation and crack growth. The AE technique, at its most basic level, considers the hit-rate of events recorded using transducers in 4 contact areas within the test sample or apparatus to provide insight into the timing of fracture processes and, in particular, the onset of failure. Such analysis can be extended to consider amplitude, energy and time-based attributes to further characterize the recorded events and to attempt to classify different types of events and thus monitor changes in the failure mode. Furthermore, the so-called b-value (originally used to analyze historical earthquake records) has been used to assess AE variations over time. Such analysis can help in understanding the mechanisms involved in rock failure.

As Hardy (2003) has noticed, there is little doubt that the initial development of the AE/MS techniques was associated with studies in the geotechnical field. In this regard the pioneering work of Obert and Duvall in the late 1930s appears to represent the true beginning of the subject. Although in subsequent years, AE/MS studies in mining and other geotechnical areas continued to develop, many of the major developments, however, occurred within the disciplines of geophysics and material science. Table 3.1 outlines a number of the major developments associated with the field-oriented applications of the AE techniques during the last 70 years.

3.2.1. Kaiser effect

There have many attempts by various researchers to utilize the Kaiser effect to determine in-situ stress in rocks. Utagawa et al. (1997) have reported, on the basis of laboratory experiments using tuff, sandstone and granite in dry condition, that the stress memory can be retained for a long time (more than one year). They have also shown that it is possible to estimate the previous stress by using the AE signature in the second and/or

third reloading, even when the Kaiser effect is not clear in the first reloading due to noise associated with crack closure or compaction.

Table 3.1: Some of the early and recent investigations of AE technique (Hardy, 2003).

Date	Investigators	Study Area
Early Studies		
1939	Obert and Duvall (USA)	Hard rock mines
1940	USA/Canada/USSR	Various field applications
1953	Buchheim (Germany)	Coal and salt mine studies
1955	Crandel (USA)	Tunnel safety
1959	Vinogradov (USSR)	Mine studies
1962	Beard (USA)	Tunnel safety
Transitional Studies		
1963	Cook (South Africa)	Rock bursts
1964	Susuki et al. (Japan)	Mine studies
1965	Neyman et al. (Poland)	Coal mine safety
1967	Goodman and Black (USA)	Slope stability
1969	Duvall, Blake and Leighton (USA)	Rock bursts
1970	Baule et al. (Germany)	Rock bursts
Recent Studies		
1971	Hardy (USA)	Coal mine safety
1972	Koerner et al. (USA)	Soil studies
1975	Leighton (USA)	Coal mine safety
1976	Hayashi (Japan)	In-situ stress evaluation
1978	Will (Germany)	Coal mine safety
1978	McKavanagh and Enever (Australia)	Coal outbursts
1978	Van Zyl Brink (South Africa)	Rock bursts
Recent Studies (continued)		
1981	Albright and Pearson (USA)	Salt cavern stability
1981	Frantti (USA)	Mine subsidence
1982	Ohtsu (Japan)	Concrete
1982	Niitsuma (Japan)	Hydraulic fracturing of Geothermal reservoirs
1983	Holcomb (USA)	Kaiser Effect
1984	Hardy (USA)	Sinkhole monitoring and rock slope stability
1984	Young (Canada)	Rock bursts
1985	Wood and Harris (Australia)	Massive structures
1985	Carabelli (Italy)	Gravity dam stability
1985	Armstrong (USA)	Earthquake prediction
1985	Ge and Hardy (USA)	Transducer array geometry
1990	Ge (Canada)	Source location optimization And matrix analyses
1990	Niitsuma et al. (Japan)	Crack waves
1993	Niitsuma et al. (Japan)	Triaxial doublet analyses
1995	Itakura et al. (Japan)	Fractural analysis

Based on acoustic emission, a technique for the estimation of the full stress tensor was developed and tested by Villaescusa et al. (2002) at the Western Australia School of Mines. They concluded that the experimental results on oriented core samples are comparable with the hollow inclusion over-coring method.

These proposed stress measurement techniques, based on the Kaiser effect, exhibit considerable advantages in comparison with other conventional stress measurement methods. However, even at the earliest stages of studies on the Kaiser effect in rocks, it was recognized that a number of fundamental questions have to be answered before it can be used in practice for stress measurement. The most important question relates to the Kaiser effect manifestation in rocks previously loaded in triaxial compression. Another important question is the Kaiser effect manifestation during cyclic loading, where the loading or displacement rates are different from cycle to cycle (Lavrov, 2001). The effect of load rating on stress memory in brittle rock, investigated by Lavrov (2001) and Lavrov et al, (2002) used two loading modes for uniaxial compression and Brazilian tests and concluded that damage resulting from a slow loading rate can be revealed by using fast reloading.

3.2.2. Hydraulic fracturing

Byerlee and Lockner (1977) located AEs during the injection of water into a sandstone sample. At failure, the AEs clustered around the point at which injection was being performed and then delineate the advancement of the fracture front through the sample. Ishida (2001) published the results of experimental work on the efficiency of hydraulic fracturing with water injection using AE monitoring. He has used four granites with different grain sizes. By using fault plane solutions of acoustic emission he has concluded that shear fracturing is dominant in the specimens with larger grains whereas the tensile fracturing is dominant in smaller grains. The AE count rates increased with closing and reopening hydraulically induced cracks. Finally he concluded that AE monitoring could improve the reliability and the accuracy of hydraulic fracturing stress measurements.

3.2.3. Seismicity and b-value

During the deformation of rock in laboratory experiments, small cracking events, or microfractures, occur, which radiate elastic waves in a manner similar to earthquakes. These radiations were detected during uniaxial and triaxial compression tests and their

frequency-magnitude relation studied. In recent years a few studies have employed the Gutenberg and Richter relationship to study AE events (Young and Collins, 2001; Lavrov et al., 2001):

$$logN = a + bM \tag{3.1}$$

Where N is the number of events that occurred with magnitude M, and ***a*** and ***b*** are constants. The dependence of the parameter b on rock type, stress, and confining pressure was studied and the basis of similarity between rock deformation experiments in the laboratory and deformation of the crust was demonstrated.

The source technique that characterizes each AE event by representing the discontinuities within the material in terms of equivalent sets is another approach used in rock engineering. This is an analytical technique that employs the travel-time-difference method to localize the source of events (Hardy, 2003). During the last two decades a few valuable investigations have been carried out in this field using the AE monitoring technique. The effect of stress anisotropy on the brittle failure of granite is investigated under uniaxial compression by using AE monitoring (Zang et al., 1998). Non-standard asymmetric compression tests were performed on cores of granite, in which 20 percent of the core top surface remains unloaded (figure 3.1). Compared to standard uniaxial tests with symmetric loading, in the asymmetric test both a greater quantity and more localized distributions of emission event hypocentres were reported. Focal amplitudes were determined at a 10 mm source distance and maximum amplitudes measured at eight piezoceramic sensors lead to b-values that drop before rock failure (figure 3.3).

The diagrams in figure 3.2 show the cumulative detected number of AE events and stress (for symmetric tests) or force (for asymmetric tests) versus time of loading for the four granite samples.

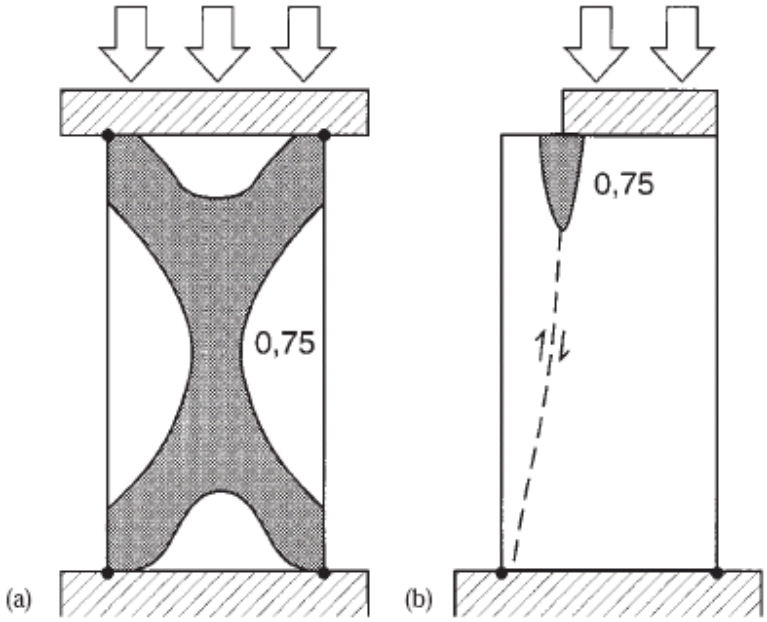

Figure 3.1: Contour plot of stress concentration factor 0.75 (shaded area) during (a) symmetric and (b) asymmetric compressive loading. Line 0.75 defines the rock volume in which the minimum principal stress exceeds 75 per cent of the corresponding extreme value [S3=−126 MPa in (a) and S3=−562 MPa in (b)]. Hatched areas indicate compression plates. Dashed line in (b) indicates expected shear rupture path (Zang et al., 1998).

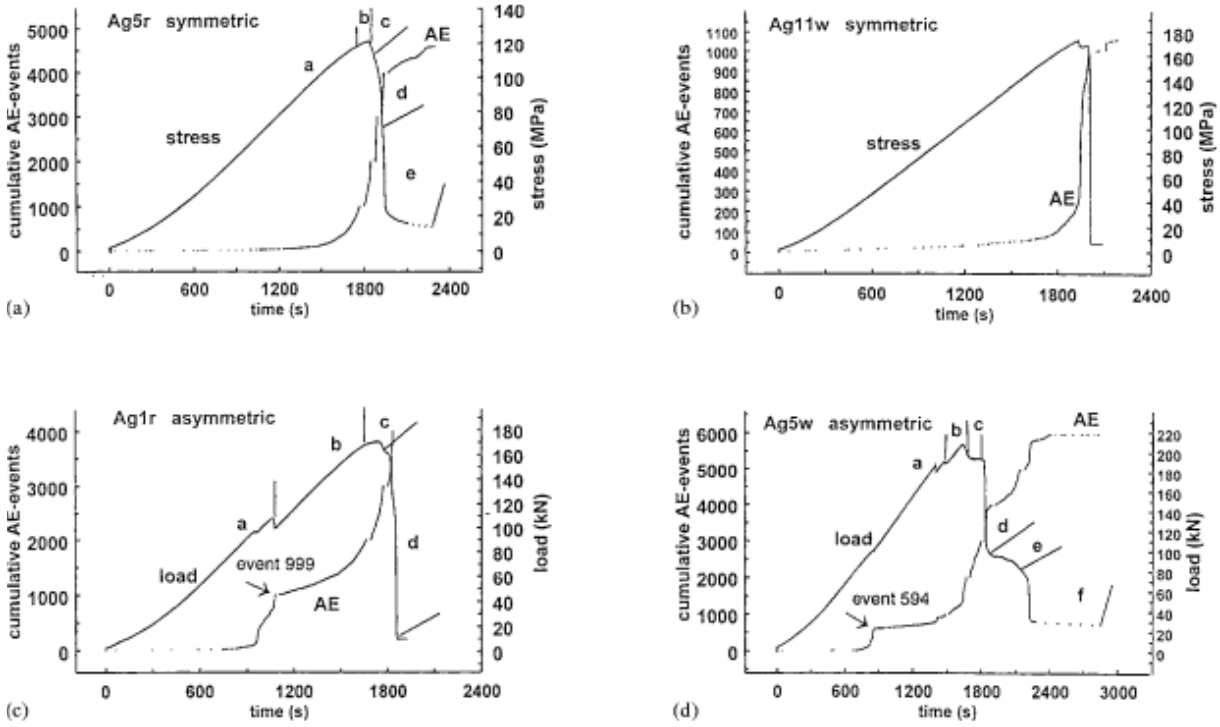

Figure 3.2: Cumulative number of detected events and stress for symmetric or force for asymmetric loaded cores as a function of time for different specimens (Zang et al., 1998).

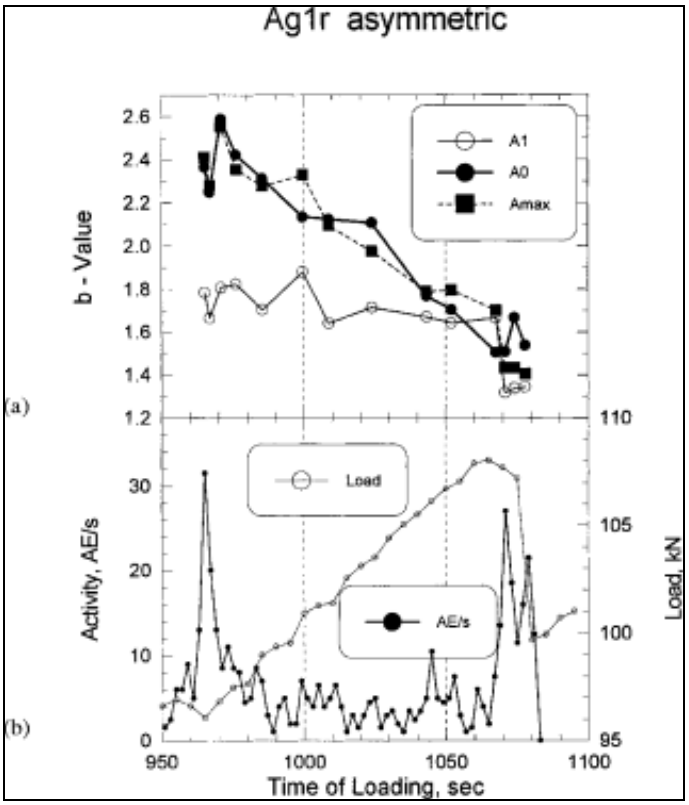

Figure 3.3: (a) The b-value calculated from the first pulse (A1), the maximum (Amax) and the focal amplitude (Ao) of acoustic emission event wavelets of the asymmetric test on core Ag1r. (b) The event rate and force versus time data are shown for reference (Zang et al., 1998).

Lei et al. (2000c) monitored the spatio-temporal distribution of acoustic emission (AE) during fault nucleation under conditions of constant-rate loading. In order to examine the effect of asperities on faulting, they conducted a series of experiments on mudstone with quartz veins. They concluded that: (1) AE activity was initiated close to the peak stress, and almost all AE hypocenters appeared at the intersections of the veins and the fault planes, suggesting that the vein asperities control faulting; (2) the b-value changed with time and shows multiple large and short-term fluctuations; (3) the change of the b-value correlated closely with the spatio-temporal hierarchy of the fracture process; and (4) fault segments along the bedding plane show behavior of slip having large compressive deformation before the peak stress, while the vein asperities show large precursor prior to dynamic rupture.

A biaxial compression test on a sandstone specimen was performed with monitoring of AE by Fernanda et al. (2002). The AE events were modeled as displacement discontinuities. The sources of the post-peak events were characterized as being caused predominantly by slip in the direction of the global failure plane, although components of

displacement associated with closing were identified. They suggested that the use of an amplitude sensitivity parameter for quantitative acoustic emission characterization may be appropriate if a suitable relationship between the amplitude sensitivities and the normalized frequency of the recorded signals can be established. Based on AE results they concluded that the failure plane was mainly associated with shear mechanisms.

In 2004 Young et al. published the results of five years of study on AE. They noticed that there is a number of seismic processing and analysis methods that are not routinely performed, and these can provide significant added value to an interpretation of rock mass structure and competence. They addressed these methods as:

- **Source parameter analysis:** Analysis of spatial and temporal trends in the seismic activity over periods of weeks to years, including the difference in seismic response versus lithology, and the effect of confinement on rock mass stability, as well as magnitude frequency (b-value) trends to identify spatial and temporal differences in rock mass response.
- **Source mechanism studies:** Analysis of the failure mechanics of seismic events as functions of the pressure and tension forces (moment tensor) acting at the source, and the orientation of failure, giving information about movement on existing geological structures, and new cracks and damage zone creation.
- **Source location refinement:** The use of methods such as relative location where events can be more accurately located relative to a master event and clustering/collapsing techniques to aid in the interpretation of seismic data through the analysis of the source location error.

The source locations of acoustic emission and microseismicity of the seismic events induced by excavation were used to map out the extent of the excavation damage/disturbed zone (EDZ) around tunnels (Young et al., 2004). Results from these studies are shown to assist in understanding the effect of confining pressures on AE activity around tunnels, and the mechanics of rock failure in the EDZ. In addition, examples of the use of seismic sources to produce repeat measurements of seismic velocity along ray-paths in 3D orientations through a rock mass are given. The authors concluded that this method is highly sensitive for quantifying changes in rock properties such as Young's modulus (Figure 3.4), as well as for modelling the change in crack density and saturation occurring in a rock mass over time. An overall decrease in Young's modulus of 4% was calculated, with the majority of change occurring within the first 2 years of measurements.

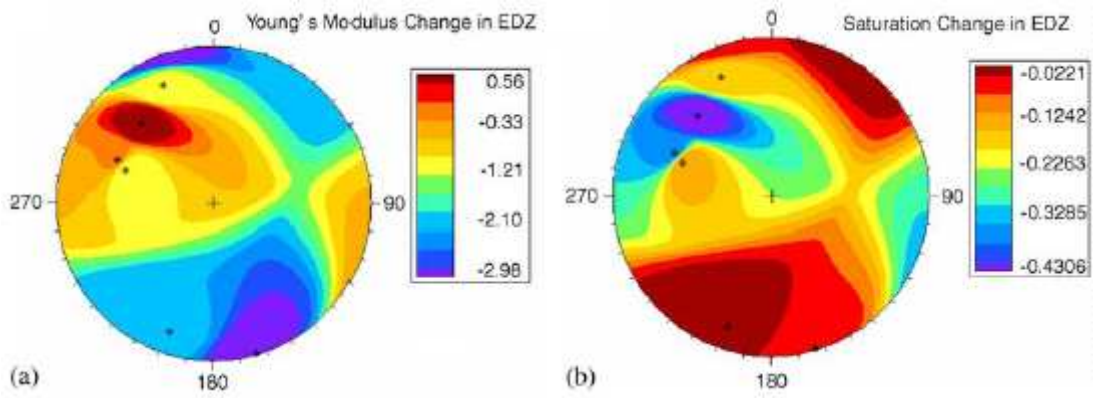

Figure3.4: 3D variation of the change in (a) Young's modulus (in GPa), and (b) crack saturation, for ray paths through the EDZ of the main TSX tunnel (Young et al., 2004).

3.2.4. Crack propagation studies

Acoustic Emission is a physical process that is one of many reflections of material failure, and for this reason AE has been used for developing of a wide class of non-destructive testing (NDT) techniques for practical applications. The brittle fracture of rocks and the associated physical phenomena are of concern to the mechanisms of earthquakes and their precursors. Many studies have been done in this field in the last four decades, most of them focusing on the deformation and failure process of rocks or analogue materials and their implications in earthquake processes and precursors by using acoustic emission, strain measurement and other techniques.

Scholz (1968) located AEs during the compression of granite to macroscopic failure. The author noted that above 92% of the peak stress microcracks coalesced in some manner along the eventual fracture plane. The nucleation and growth of macroscopic fault planes in granite and sandstone samples by locating acoustic emission (AE) sources have been studied by Lockner et al. (1991). In this research axial stress was controlled to maintain a constant AE rate rather than the more conventional loading conditions such as constant strain rate or constant stress, and the failure process in triaxial experiments was successfully retarded. The authors showed that, the post-failure stress curve was followed quasistatically, extending to minutes or hours the fault growth process that normally would occur violently in a fraction of a second. In addition, three-dimensional locations of AE events were determined by analyzing the relative arrival times of AE pulses recorded on a network of transducers attached to the sample. AE locations showed that the fault

propagated as a fracture front (process zone) with in-plane dimension of 10-50 mm (Figure 3.5). Finally they concluded that the brittle fracture process, under triaxial conditions, involved three stages: (1) Distributed damage during loading of the sample to peak stress, (2) fault nucleation and (3) fault propagation.

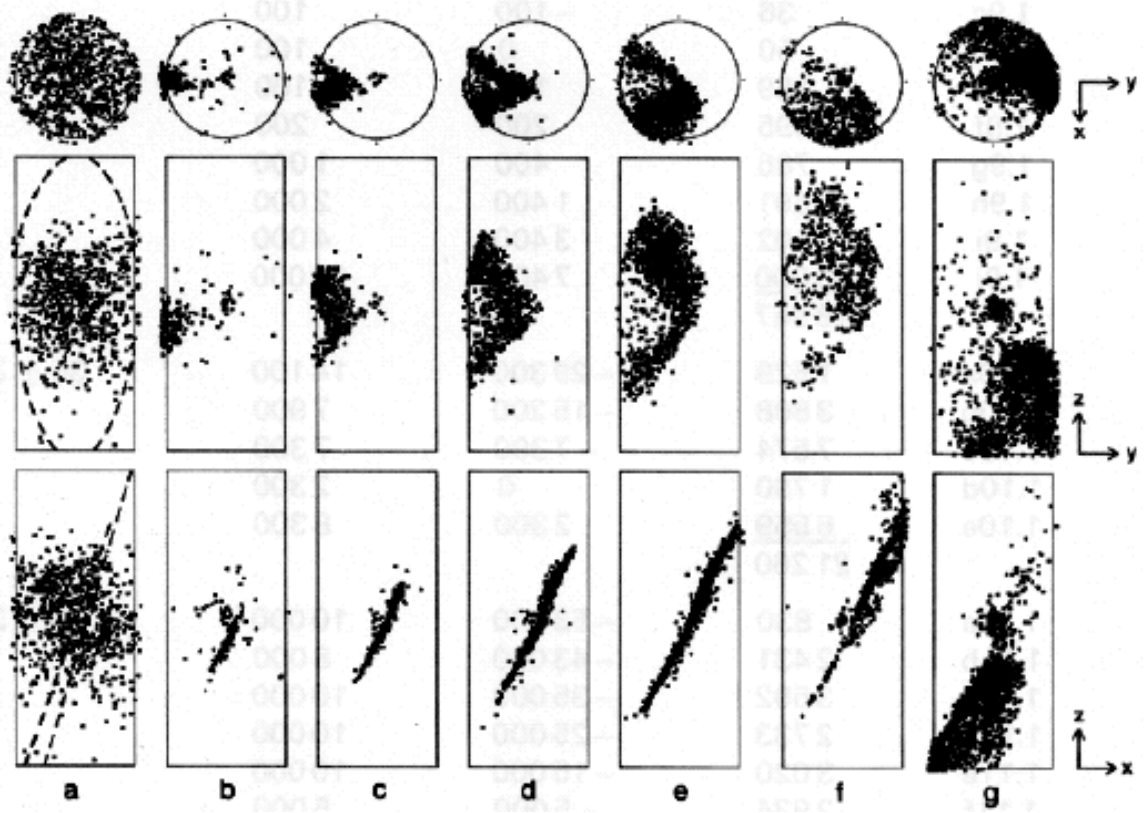

Figure 3.5: Plots of AE locations for granite sample G1. Bottom plot of each set is view looking along-strike of eventual fracture plane. Middle plot is face-on view of fault in which sample has been rotated counter clockwise 90°. Top plot is view looking down on sample. Projections of surface trace of eventual fault plane are shown in (a) for reference. Fault nucleation occurs in plot (b). Lockner et al. (1991).

Laboratory testing by Eberhardt et al. (1998) investigated the effects of brittle fracture on the progressive degradation of rock mass strength. The crack initiation and propagation thresholds, two key components in the brittle-fracture process, were investigated using AE monitoring. They used energy and amplitude for recognizing the type of cracks. Calculations of the acoustic event energy, based on the peak amplitude and duration of the event wave, indicated that the acoustic events generated through crack closure are much smaller than those generated through stress-induced tensile cracking. Plots of the elastic

impulse energy and its stress- dependent rate change (figure 3.6) show that the size of the events in terms of energy dramatically increased shortly after crack initiation began.

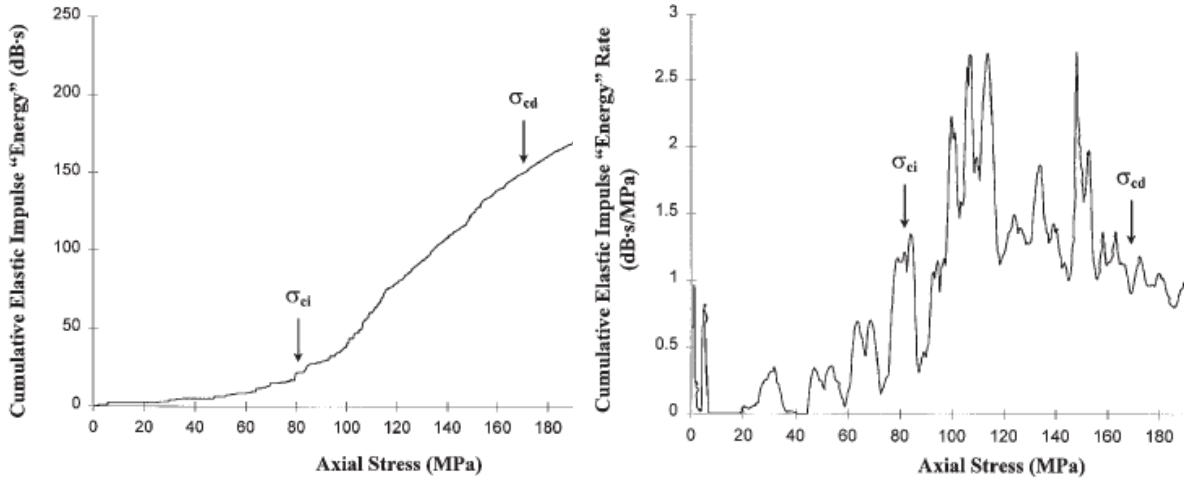

Figure 3.6: Plot of cumulative elastic impulse energy vs. axial stress and the stress-dependent energy rate vs. axial stress for a 130 Level pink granite (Eberhardt et al., 1998).

Based on uniaxial testing on granite they concluded:

- Crack closure involved both axial and lateral strain components.
- Near-linear elastic behavior was seen only in axial strain measurements. Lateral strain followed a nonlinear trend throughout the entire test, as depicted through continuously decreasing values of lateral stiffness.
- The combined use of moving point regression analysis (performed on the axial, lateral, and volumetric stress-strain curves) and acoustic emission response (including the event properties and energy calculations) provided the most accurate and reliable means of identifying crack initiation (σ_{ci}).
- Analysis of both the axial and lateral stiffness curves indicates that a significant rate change in strain occurs prior to the crack damage threshold, possibly marking the small-scale coalescence of cracks.

A model for failure prediction utilizing acoustic emission data has been developed (Dunegan, 1988) for man- made materials and structures. It has been observed that materials or structures containing cracks that are loaded to failure, such that failure occurs below general yield, exhibit a power law increase in activity prior to failure. A failure prediction model is presented based on detecting high frequency events from boreholes evenly spaced on a 10km grid. Data from several types of crack propagation in man-made materials are presented and show that the failure model can accurately predict failure from

crack growth in these materials. Finally he proposed that three long-term microcracking phases, primary, secondary and nucleation, can be identified based on the changes in these parameters. In the primary phase, the AE rate increases gradually with stress, corresponding to early microcracking (mainly tensile mode) during the loading period. In the secondary and nucleation phases, the event rate and b-value also exhibit large simultaneous short-term fluctuations.

The results of laboratory investigation into the identification and quantification of stress-induced brittle fracture damage in rock are given by Eberhardt et al. (1999). Results derived from monocyclic loading tests demonstrate that damage, and the subsequent deformation characteristics of the damaged rock, can be easily quantified by normalizing the stresses and strains observed in the progression from one stage of crack development to another. They presented two levels of crack development, crack initiation, and crack damage, and concluded that for pink Lac du Bonnet granite they were occurring at 0.39 and 0.75 of the ultimate uniaxial compression strength. Acoustic emissions were found to provide a direct measure of the rapid release of energy associated with damage-related mechanisms. Their results indicated that approximately 55% of the damage-causing mechanisms leading up to unstable crack propagation occur prior to crack coalescence and 45% occur afterwards.

Lei et al. (2000b) studied the localization of deformation acceleration in the period prior to dynamic failure in schist rock under triaxial compression using AE monitoring. They reported two different processes operating during the quasistatic nucleation of a shear fault, namely, a process zone in front of the fault tip and a “wake” of damage zone following the process zone. From the mutual changes of b value and self-exciting strength observed in their experiments, they concluded that, under a realistic approximation of the dynamic conditions of the Earth, these observations are meaningful for predicting earthquakes as well as rock bursts.

The phenomenon of compaction localization, mechanical deformation and microstructural observations were conducted on the 3 types of sandstones with porosities ranging from 13 to 24% are studied by Baud et al. (2004). In that research the constitutive behaviour, failure mode, acoustic emission (AE) activity and spatial distribution of damage were investigated. A hybrid localization mode involving high-angle shear bands and diffuse compaction bands has been observed in sandstones with intermediate porosities. Also they reported the development of high-angle shear bands has been characterized by the continuous accumulation of AE.

The fracture and damage mechanisms of rock, induced by the accumulation of microcracks, were investigated by moment tensor analysis and the moving point regression technique using acoustic emission (AE) monitoring (Chang and Lee, 2004). The tests were performed under triaxial compression conditions and strain rate data obtained from the tests. Two types of rock, granite and marble, were used in this research. Crack types for AE sources obtained under uniaxial compression were analyzed. For both granite and marble, approximately 60% of the total AE sources obtained before the peak strength were classified as shear cracks, whereas tensile and shear cracks comprised 25% and 15% of the total cracks, respectively. They concluded that the propagation and coalescence of microcracks are dominated by shear cracks. In addition, shear failure became more dominant as the confining pressure increased. Two granite and marble rocks were used in this research. Crack types for AE sources obtained under uniaxial compression were analyzed as shown in figure 3.7. For both Granite and Marble, approximately 60% among the total AE sources obtained before the peak strength was classified as shear cracks; whereas tensile and shear cracks comprised 25% and 15% of the total cracks, respectively. The results showed that the propagation and the coalescence of microcracks are dominated by shear cracks.

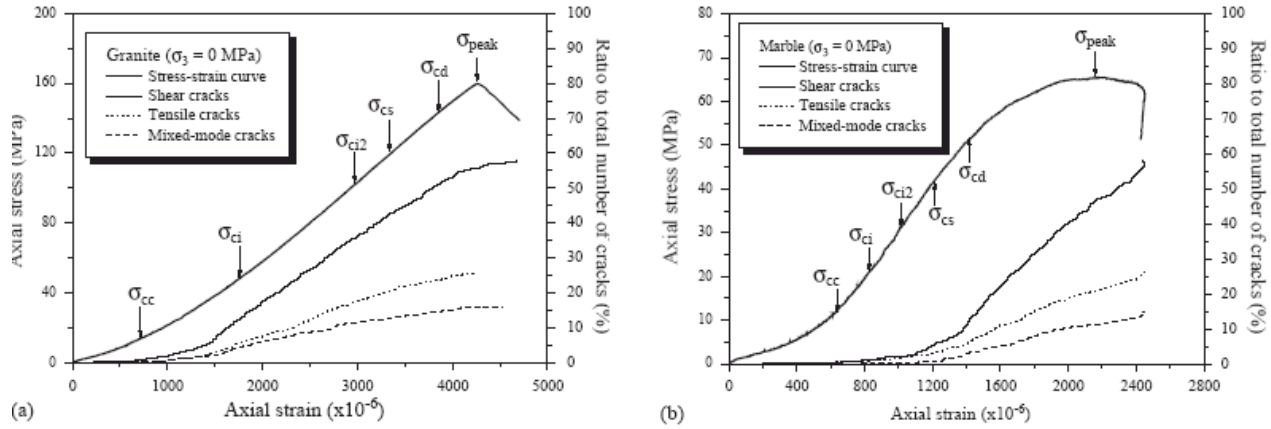

Figure 3.7: Ratio of number of cracks in different types to the total number of cracks under uniaxial compression: (a) Hwangdeung granite; and (b) Yeosan marble (Chang and Lee, 2004).

The results showed also that damage thresholds, except the crack closure stress, increased linearly with confining pressure. The results of the moment tensor analysis showed that shear failure was a major microscopic failure mechanism of rock under triaxial compression. In addition, shear failure became more dominant as the confining pressure increased.

A valuable experimental work has been done for the localization of deformation acceleration in the period prior to dynamic failure in hornblende schist rock under triaxial compression using acoustic emission (AE) monitoring by Lei et al. (2000b). They have developed a multichannel data collection system for studying the dynamics of fault nucleation under condition of constant stress (creep) loading. Based on the AE localization they concluded that the fault initiated at one end of the core and then propagated into the unfaulted rock with a process zone (fault front) of intense cracking. Also they found that there were two different processes operating during the quasi-static nucleation of a shear fault, namely, a process zone in front of the fault tip and a "wake" of damage zone following the process zone.

3.2.5. AE study on pre-existing cracks and heterogeneity

The heterogeneities in a rock, including pre-existing cracks, grain boundaries and local strength distribution associated with rock-forming minerals, have been studied using AE monitoring. There are a considerable number of studies in rock mechanics because of fault nucleation. In order to understand the role of heterogeneities at different scales, a few investigations have been done in recent years. Lei et al. (2000c) reported the results of experimental studies on two coarse-grained granite rocks, one with pre-existing cracks and the other crack-free. They showed significantly different behaviors in AE activities: In granite with pre-existing cracks they observed that, before the fault nucleation, AE activity was low and showed increasing b-values with increasing stress. However, in the other specimen a large number of AEs were observed and showed short-term b-value anomalies - mutual fluctuations on a decreasing background were reported. Finally they concluded that 1) pre-existing cracks are the most dominant factor of all heterogeneities that govern the fault nucleation process in laboratory rock samples, and 2) failure predictability is dependent on the pre-existing crack density.

A numerical parameter-sensitivity analysis was presented by Tang et al. (2000) to evaluate the effect of heterogeneity under uniaxial compression loadings using AE monitoring. In this research they concluded that prediction of the macro fracture location is difficult in a homogeneous rock type since the failure of the specimen is completely brittle. It was found that tension fractures are the dominant failure mechanism in both splitting and faulting processes. Finally, based on the numerical simulation, they concluded that faulting is mainly a process of tensile fractures, often en echelon fractures, developed in a highly stressed shear band.

The faulting process and mechanical asperities in a granitic porphyry sample was investigated using acoustic emission (AE) waveform recording (Lei et al., 2003). The experimental result showed that quasistatic nucleation of the heterogeneous fault is associated with the failure of asperities on the fault plane. They also used b-values to identify the failure process in granite specimens. Based on these investigations the fracturing of an asperity is characterized by a dense spatial clustering of AE events and a change in b-value, which is manifest in three typical stages of failure: (1) foreshocks exhibiting a decrease in b-values, (2) a period of main shocks corresponding to a minimum in b-value, and (3) aftershocks of increasing b-value. The progressive fracture of several coupled asperities results in short-term precursory fluctuations in both b-values and AE rate. They also reported that the microcracking activity during faulting shows three distinctive phases: primary, secondary, and nucleation phases as shown in figure 3.8.

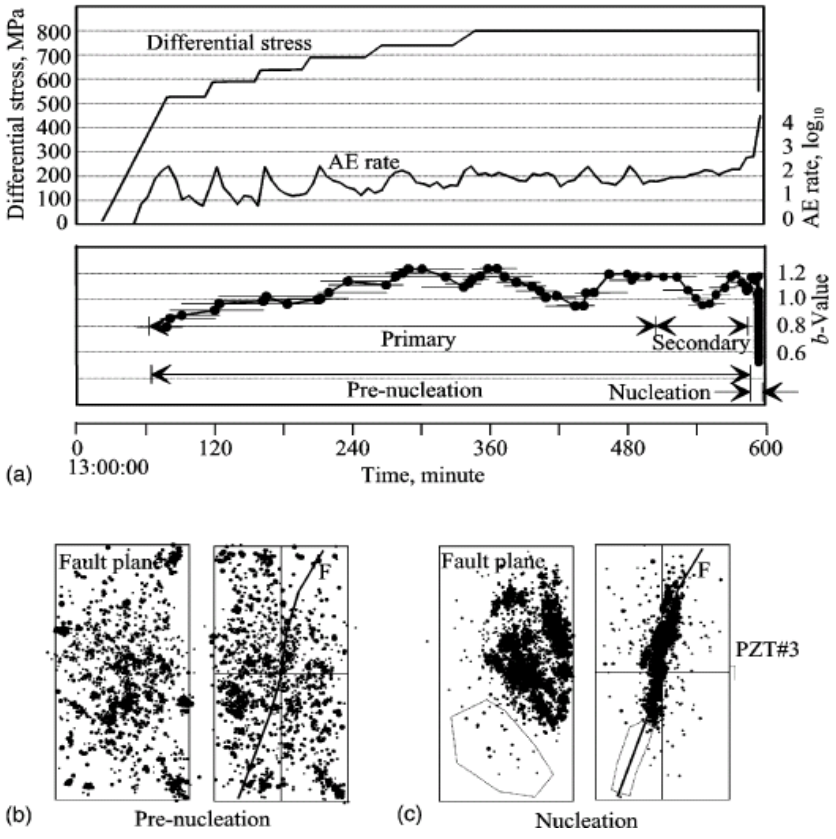

Figure 3.8: (a) Differential stress, rate of AE occurrence, and b-value vs. time. (b and c) Hypocenters in the pre-nucleation/nucleation phases projected onto two orthogonal planes parallel and perpendicular to the fault plane. F indicates the actual ruptured fault. AE hypocenter data for the events that occurred in the area enclosed by the dashed lines were not recorded since the 32-channel waveform recording system saturated before the dynamic rupture (Lei et al., 2003).

Prikry et al. (2003) carried out laboratory experiments on rock samples to understand the relationship between the acoustic emission (AE) parameters and the rock fabric. AE activity was recorded during uniaxial compression with constant stress rate on several granite rocks with variable microfabric (e.g. grain size, shape and crystallographic preferred orientation) and macrofabric (e.g. magmatic isorientation, metamorphic banding). It was shown that the energy-frequency distribution of AE events strongly reflects the fabric of the samples. They concluded that AE parameters like acoustic rate or cumulative energy are highly sensitive to fabric arrangement in rocks with pronounced structure such as foliation, lineation etc. They concluded also that AE parameters like acoustic rate or cumulative energy are highly sensitive to fabric arrangement in rocks with pronounced fabric such as foliation, lineation etc. AE monitoring and direct microscopic observations also were confirmed that tensile crack growth is dominant fracture mechanism of uniaxially stressed rock.

Lei et al. (2004) carried out laboratory tests on four types of rock samples with pre-existing joints or potential fracture planes using AE monitoring. The main data used in this study included (1) event rates calculated from the maximum amplitude data, (2) seismic b-values for the magnitude–frequency relationship as calculated from the maximum amplitude data, (3) hypocenters determined using the first arrival times at the 32 receivers, (4) the fractal dimension of the hypocenter distribution, and (5) the self-excitation strength for AE occurrence. Based on the experimental results they suggested that precursory anomalies related to earthquakes and other events associated with rock failure are strongly dependent on the heterogeneity of the fault or rock mass. A homogeneous fault or rock mass appears to fracture unpredictably without a consistent trend in precursory statistics, while inhomogeneous faults fracture with clear precursors related to the nature of the heterogeneity.

Hall et al. (2006) are presented results of experiments carried out on natural, dry specimens of Neapolitan fine-grained tuff to investigate the failure evolution. Based on AE monitoring and high resolution photography data they segmented failure evolution of the rock as: (1) crack closure; (2) linear stress-strain response and crack initiation with stable crack growth; (3) crack damage and unstable crack growth leading to failure. They have resulted that monitoring of rock-sample failure with a combination of high resolution photographs and AE, even with just standard AE attributes (such as energy and hits), can

provide improved insight into failure processes, fracture mechanisms and coalescence in rock bridges.

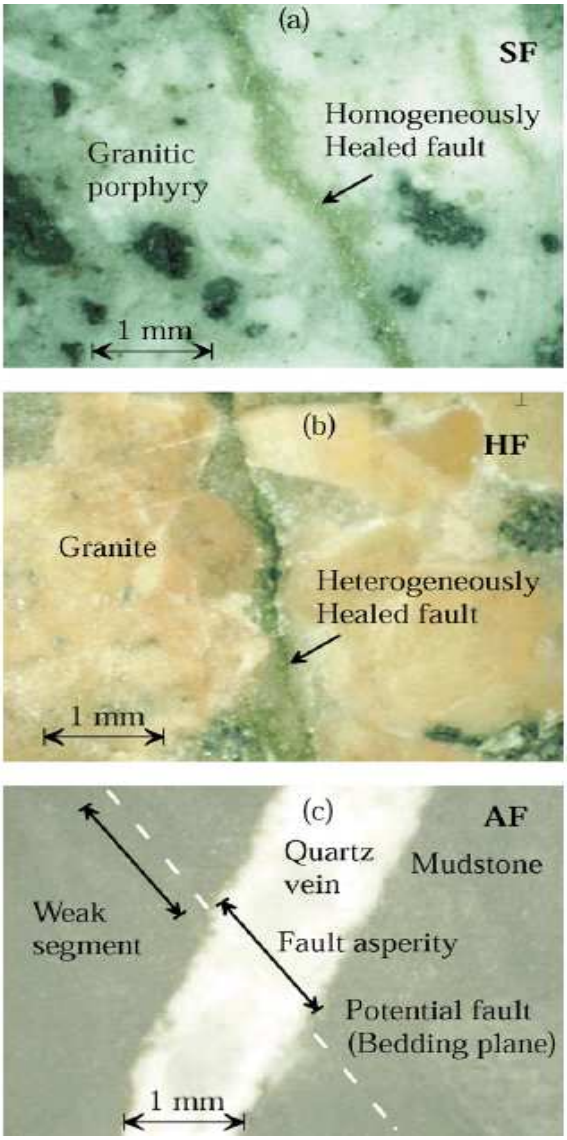

Figure 3.9: Photomicrographs showing pre-existing or potential faults in the tested samples (Lei et al., 2004).

3.2.6. AE monitoring of thermal treated specimens

Stress affected rock investigations by AE monitoring is started in the 50s but application of AE monitoring to evaluation of thermal affected materials is a new and challenging task for non-destructive testing in civil engineering. The effect of temperature on rock properties has been widely studied on laboratory-scale specimens, however, in literature review we have found a lesser research of using AEs records from thermal treated rock like materials.

In general, heating of rocks has two main components; the effect of temperature on macroscopic properties and secondly studies on grain-scale effects, like microcracking. Based on experimental studies, Menendez et al. (1999) concluded that thermal cracking in rock is due to the thermal expansion between adjacent minerals and produced inter granular cracking. Jansen et al. (1993) used ultrasonic tomography and AEs to map fracturing induced under thermal loading in a 15cm Lac du Bonnet granite cube. Macroscopic failure initiated along the surface and then extended into the cube towards the heat source. The authors related the observed failure to the stress pattern developed by strong thermal gradients in the sample. Similar results were obtained for thermally induced fracturing in a granite cylinder by Carlson et al. (1993). Wanne and Young (2006) numerically modelled the results of laboratory rock cylinder was subjected to cyclic thermal loading where the temperature was gradually increased in every cycle. They resulted that the failure temperature depends on the value of thermal expansion and on the material strength.

The influence of thermal damage on physical parameter of granite has been investigated by Chaki et al. (2007). They showed that the heat treatment increases the void space inside the material. Between 500 and 600°C, the granite samples are strongly damaged because of the anisotropic expansion linked to the quartz transition α/β which occurs at 573°C and room pressure (figure 3.10). They concluded other physical properties of heat treated granite, such as ultra sonic attenuation, elastic wave velocity and permeability are completely depending on void space generated by microcracking and quartz phase transition.

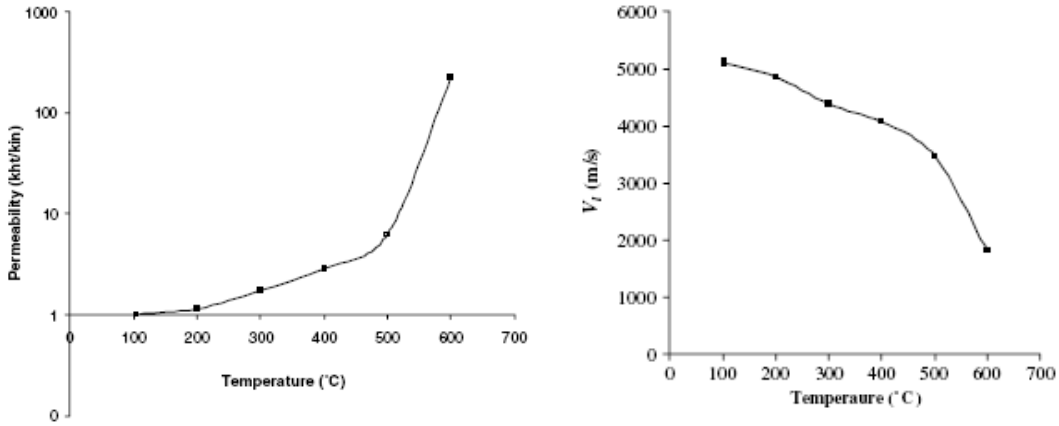

Figure 3.10: Evolution of gas permeability (left) and longitudinal wave velocity (right) versus heat treatment (Chaki et al., 2007)

3.2.7. AE monitoring in-situ

In spite of extensive laboratory studies with AE monitoring, the use of AE in field investigations is limited. Some research of this type has been done specifically to determine excavation damage zones (EDZ) in tunneling operations (Young and Collins, 2001).

Falls and Young (1998) investigated the damage zone in a tunnel 420 m below ground. They measured elastic wave (Vp) and monitored AE in their research and suggested:

- AE monitoring in the floor of the tunnel showed that small amounts of AEs continued to occur in the notch region of the tunnel floor over two years after excavation was completed. Ultrasonic-velocity studies both in the floor and the wall of the tunnel showed that the velocity increased into the rock from the tunnel surface; in the floor, this effect was seen up to 2 m from the tunnel surface. Most of the change occurred within the first 0.5 m from the tunnel perimeter.
- AE and microseismic events show a strong clustering in the roof and floor of the tunnel where the maximum tangential stresses are concentrated. Low-level AE activity continues to occur in these regions months or even years after the completion of the excavation (figure 3.11).
- There was a distinct velocity decrease below background levels approaching the tunnel wall. The effect was greatest within the first 0.5 m of the tunnel in the sidewall. The low-velocity zone was more extensive in the tunnel floor, extended to about 2 m from the floor of the tunnel. Secondly, very clear velocity anisotropy existed with P-waves propagating more slowly in a direction perpendicular to the tunnel perimeter,
- Finally the results indicated that the stress conditions can play a greater role in determining the extent of excavation disturbance than the excavation method. While the smooth-blasting excavation technique resulted in more AE activity than the tunnel-boring machine, the velocity results indicate that, in both cases, the disturbance was minimal compared to the damage at the high-stress Mine-by tunnel.

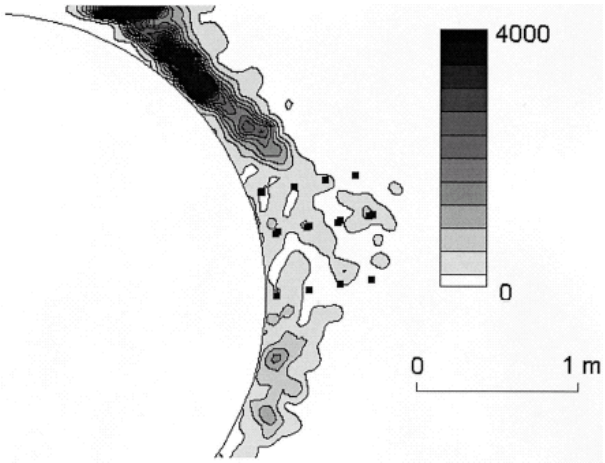

Figure 3.11: Event density of AE activity recorded in the sidewall of the Mine-by tunnel during excavation. The sensor locations are shown as black square (Falls and Young, 1998).

Shiotani et al. (2001) used Acoustic Emission to predict eventual rock failure. They installed AE sensors into a rock slope and evaluated AE signals in the laboratory. Based on the experimental results, criteria for classifying fracture states were proposed. Then, applying the criteria to the field data, estimated fracture states were compared with internal slope behavior evaluated from the displacement, borehole-strain, temperature, etc. From their results they recommend the use of AE to evaluate rock slope stability.

Young and Collins (2001) used micro-seismic (MS) and acoustic emission (AE) recording for delineating the extent of the excavation damage zone EDZ in tunneling operations. They concluded that using this method is not only a valuable tool for delineating the extent of the EDZ but also an effective approach for quantifying the change in material properties such as crack density that occur during the development of the EDZ.

Acoustic emission measurements have been used in field studies for microcrack identification by Spies and Einsenblatter (2001), using the location and the frequency distributions of magnitudes and spacing of acoustic emission events. By using geological observations they concluded that a cluster of microcracks marked the boundary of the exposed fracture plane with a diameter of 8 m.

A study to quantify of the degree of damage, in terms of crack density calculated from the crack length, and the extent, from microseismic event monitoring data was carried out by Cai and Kaiser (2005). They developed a method to characterize the dynamic properties in the EDZ using microseismic monitoring data. Their approach found that a realistic crack size corresponding to a microseismic event can be established by applying a tensile cracking model instead of the traditional shear model, commonly used in earthquake data

analysis. They reported that brittle rock failure is the result of tensile crack initiation, propagation, accumulation, and interaction.

3.3. Infrared thermography measurement

Infrared thermography is a technique for producing heat picture from the invisible radiant energy emitted from stationary or moving objects at any distance and without surface contact, or in way influencing the actual surface temperature of the objects view (Luong, 1993). In fact if we neglect work against gravity, almost all mechanical work done during deformation must be converted into heat. Because faults are sites of concentrated tectonic work, they are favorable places to look for evidence of mechanically generated heat.

In the two last decades this technique has been used in different field investigations as well as in laboratory studies. The application of infrared thermographic technology to aerial thermal land mapping, geological survey, geotechnical instrumentation, leakage insulation and construction practices for rock-like and rock engineering has been extended in recent years. The experimental studies have indicated that the structure of the rock material changes on loading and associated physical and chemical phenomena take place internally, including fracturing, ionization, electron excitation, energy accumulation, consumption, and conversion etc(Wu, 2000). The detectable IR radiation temperature will reflect the variation of the thermal radiation energy, and could also reflect the physical and chemical mechanisms and provide some precursor warning signals of rock failure, collapse and disasters. Some scientists have classified infrared and remote sensing (RS) technology and its applications as: air-based and ground-based (Wu et al., 2000 and Luong, 1993). Different applications of each category are presented previously, in chapter 2 (table 2.1).

3.3.1. Remote sensing investigations

The main research in remote sensing has focused on earthquake prediction using satellite image processing, after Zuji and Xudeng (1990) reported abnormal increases in surface radiation temperatures in infrared thermal images from NOVA climate satellites several days before and after many strong earthquakes. The cause of earthquakes is related to changes in the stress field of the earth's crust that produces an increase in electromagnetic radiation, including the infrared radiation that has a thermal effect. Wu

and Wang (1988) postulated that the earth's crust under pressure might present some infrared thermal forewarning prior to an earthquake, and perhaps this message could be detected by a remote sensor The remote sensing technique has also been used in mining engineering where it has been used successfully to predict rock burst disasters. For example, in 1985, Yu reported that the temperature rose up to 60° C in the coal burst of a mine in Britain. Anomalous land surface temperature (LST) increases of 3–4 C° were observed, for example, prior to the Bhuj, Gujarat (India) M = 7.7 earthquake (after Ouzounov and Freund, 2004) .

Chen et al. (2006) reported a thermal anomaly before than Chi-Chi earthquake in Taiwan (21 September 1999). A satellite TIR image indicated anomalous hot fluid flow in porous aquifers in the South China Sea offshore from Hainan Island. This thermal anomaly consisted of a 200km-wide region of sea water, with a depth of 50 to 90m, in which the water temperature exceeded 25°C, compared to the background range of 14 to 25°C. The image was collected 72 min before the earthquake; satellite images recorded at other times showed no such anomaly in the South China Sea. The authors concluded that a pre-earthquake thermal anomaly is normal, and in some cases can develop weeks in advance (figure 3.12).

The relationship between thermal anomalies and seismic activity was established for Middle Asia on the basis of a 7-year series of thermal images. Indeed, satellite thermal images have been used for earthquake prediction in China and Japan (Andrew et al., 2002). Based on this research, a thermal anomaly was located near Beijing, at the interface between the mountains and plain. This anomaly was about 700 km in length and 50 km in width and appeared about 6–24 days before and continued for about a week after an earthquake. Such thermal anomalies, with amplitudes of about 3°C, appear to be sensitive to crustal earthquakes with a magnitude more than 4.7 and for distances of up to 1000 km. Andrew et al. (2002) also reported the analysis of digital images for Japan that show that an anomaly appears 7–10 days before the main shock; however the tectonic position of these anomalies is not clear.

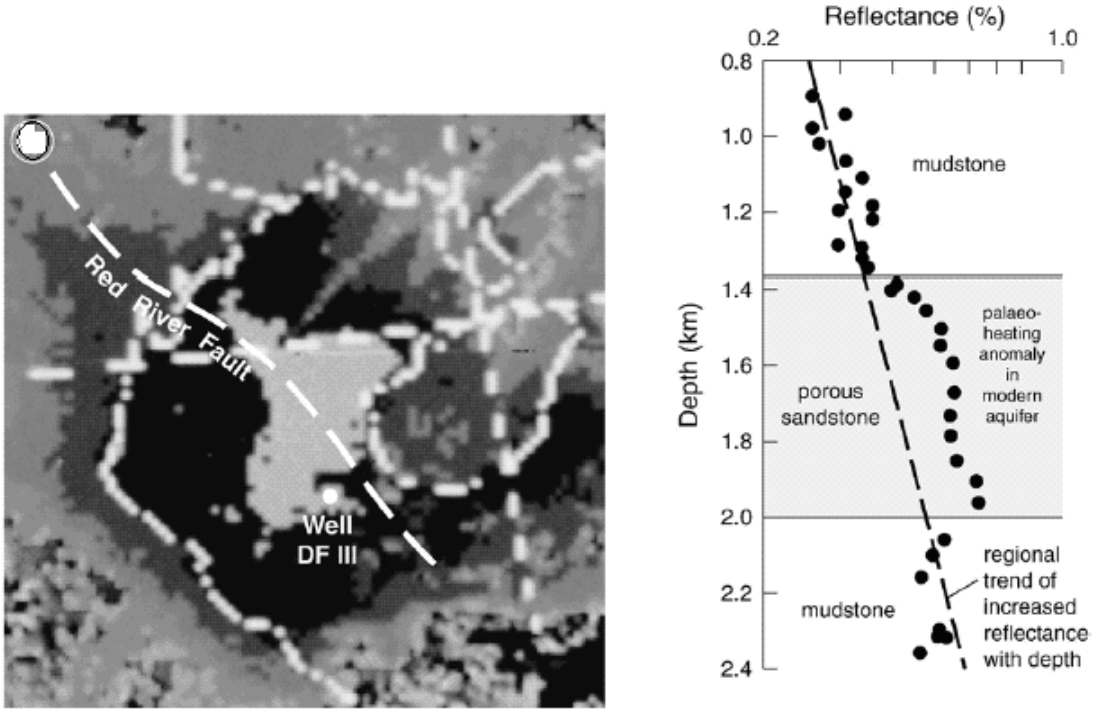

Figure 3.12: Satellite TIR image (10.5 to 12.5μm wavelength), showing 200km-wide thermal anomaly (light image west of Hainan Island, representing temperature above 25℃, compared to a background range of 14 to 25℃). Image collect ed 00:35 local time, 21 September 1999, 72min before Chi-Chi earthquake at 01:47. Images taken at other times do not exhibit the anomaly. Soil profile from anomaly region (left), showing anomalous paleo-heating in sandstone aquifer, recognised by increased reflectance compared with regional trend (after Chen et al., 2006).

3.3.2. Laboratory studies

Although remote sensing research using the IR technique in the field is limited, laboratory studies using thermography are extensive. Cyclic loading in uniaxial and triaxial compression tests, studies on impact effects at different velocities, and shear loading tests are common investigations that have used IR technology. Such investigations are carried out on rock or rock-like samples; Luong, in 1987, first used this technique to study concrete during loading and fracturing (Lixin et al., 2006a, b). Wu and Wang (1998) using infrared radiation imaging (IRI) on uniaxially loaded coal and sandstone specimens, identified three kinds of abnormal features in the IR thermal image and IRT temperature; as precursors of rock failure, a stress level of around 0.79 ultimate strength could be taken as a ‘precaution index’ for the stability monitoring of coal and rock. Later, a large amount of IR imaging experiments on rock fracturing was conducted in China (Wu et al., 2006).

The laboratory research of Ouzounov and Freund (2004) should be mentioned; their experiments were carried out using a 1500 tone press at the Geophysical Laboratory,

Carnegie Institution of Washington, and the pressure was increased at a constant rate until failure. IR emission from the rock surface was monitored during the test. These laboratory experiments provide evidence for mid-IR emission from the surface of a block of granite when the center undergoes high levels of stress. They proposed that mid-IR emissions arise (i) from the activation of p-holes in the portion of the rock undergoing deformation, (ii) from the migration of these charge carriers to the surface, and (iii) from the energy released during positive-hole recombination at the rock surface. Positive-hole in this research in essence, an O^- in a matrix of O^{2-} represents a defect electron or "hole" that resides in the oxygen with two proton dominated valence as a positive hole or p-hole for short.

New research on infrared thermography using cyclic loading in reinforced concrete was reported by Luong and Dang Van (2005). Experimental results are summarized in figure 3.13 and illustrate how the fatigue limits are determined using a graphical procedure. The threshold of critical thermal dissipation is roughly the same for different chosen numbers of load cycles.

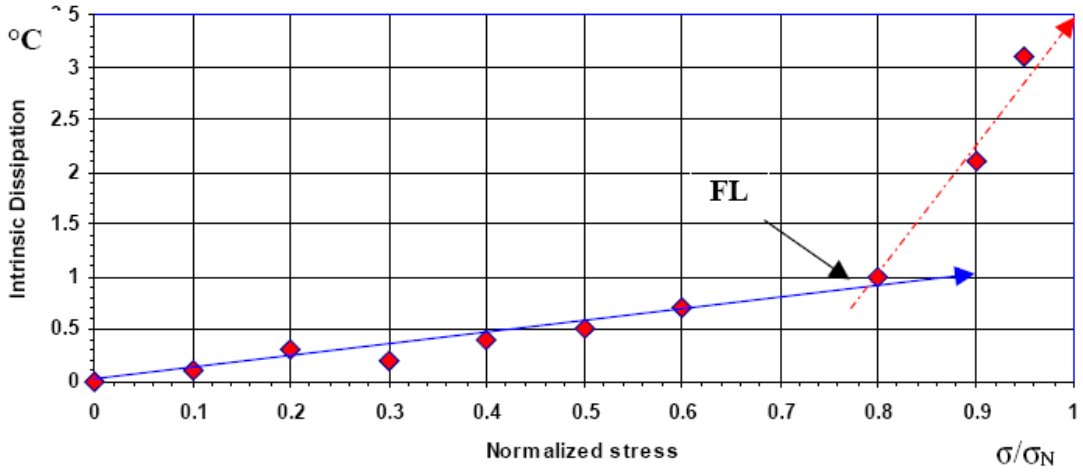

Figure 3.13: Graphical determination of the fatigue limit FL of a plain concrete. Ddissipation is given in degrees Celsius proportional to energy (Luong and Dang Van, 2005).

These experiments show that the infrared thermographic technique can provide the fatigue limit of concrete within a few hours instead of several months when using for instance, the traditional standard staircase method. They also reported that the stress limit could be understood as a threshold of acceptable damage for plain concrete under compressive loading. Their results highlight the advantages of differential infrared thermography: first, to observe the physical manifestation of damage and the mechanism

of failure of concrete, second, to detect the occurrence of intrinsic dissipation localization, and third, to evaluate the fatigue strength in a very short time, compared to traditional testing techniques.

Wu et al. (2000) developed a new inter-disciplinary topic, remote sensing rock mechanics (RSRM), which takes remote sensing, rock mechanics, rock physics and informatics as its scientific and technical disciplines and serves the geosciences, rock mechanics and rock engineering fields. The experimental methods, instruments, and some typical results concerning the relations between the IR radiation and rock stress are introduced.

They concluded that: (1) the IR radiation energy, including IR radiation temperature and IR spectral radiation intensity, increases with loading, (2) the IR radiation temperature increases with depth inside the rock specimen surface, (3) the IR radiation temperature increases with rock strength, and (4) the IR thermal image can anticipate the stress transfer process and rock fracturing location. Based on the experimental results they concluded that the rock's IR radiation temperature increases with loading. In general, the incremental increase of IR temperature is 0.2 – 2.1°C. Figure 3.14 is an example of the relationship between stress and temperature increments during a uniaxial compression test on fine diorite. Based on some experimental works, (Wu et al., 2000) suggested that:

1) There are three kinds of IR radiation temperature features and three kinds of IR thermal features during the loading and failure process of coal and sandstone.

2) The precursor indication through IR detection is comparable to that of acoustic emission detection and electrical resistance detection. A stress component of the 0.79 ultimate compression strength should be taken as the `stress-caution-zone' for ground stress.

Some research has been conducted to find a relationship between rock characteristics and IR radiation. According to a study by Liu et al. (2006), the higher the rock strength, the higher the IR radiation temperature increment. Figure 3.15 shows the curve between the maximum IR radiation temperature increment and the samples' strength. It is probable that more mechanical energy will accumulate inside the sample if the strength is higher; thus, more electromagnetic energy will be radiated, and more heat energy will be obtained from the mechanical energy.

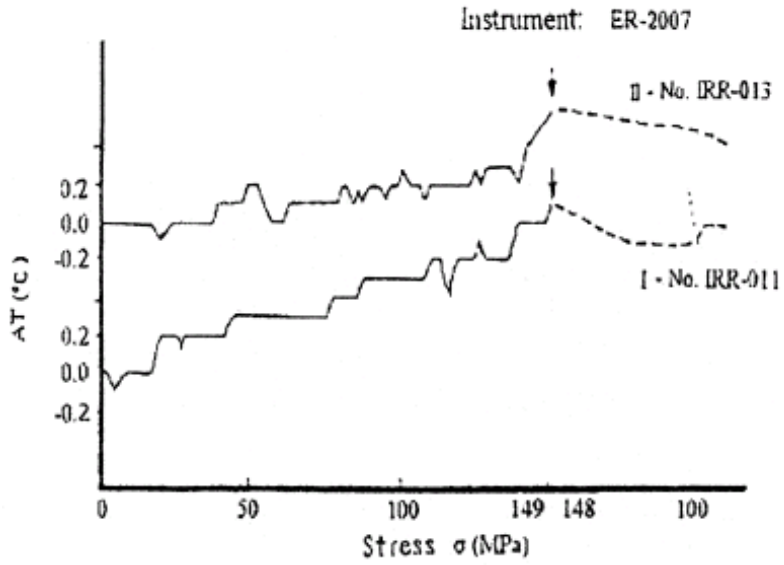

Figure 3.14: The variation of the IR radiation temperature of water-saturated fine diorite (Wu et al., 2000)

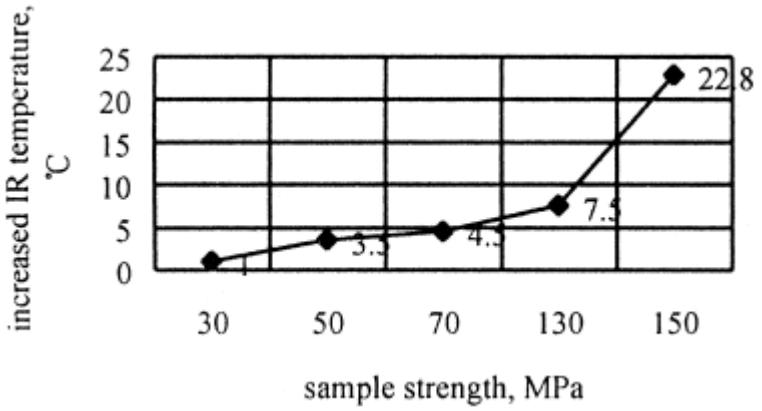

Figure 3.15: The relation between maximum IR radiation temperature increment and the sample's strengths (Liu, 2006).

Liu et al. (2006) studied different kinds of rock in order to detect the IR features of rocks at failure. The loading conditions include uniaxial compression, compressively induced shearing, three-point bending impact and bullet impact. The experimental results showed that the IR features are very different at different failure modes induced by the various loading conditions. The results in table 3.2 indicate that the greater the shearing strength, the higher the IRTI (IR temperature increment), with the correlation between IRTI and shearing strength being a positive correlation.

The experiments in this study included quasi-static and dynamic rock loading. The quasistatic loading experiments included uniaxial compression and compressively induced

shearing, and the dynamic loading experiments included bullet impact and three-point bending impact. The developed apparatus for shear loading has been shown in figure 3.16.

The relationship between IRTI and shearing tilt angle was also studied in this research. The mean IRT of three samples is shown in table 3.3. The IRT of the same type of rock differs when the shearing tilt angle changes. The IRTI at shearing tilt angles 60° and 70° is higher than that at 45°, although the relationship between 60° and 70° is uncertain.

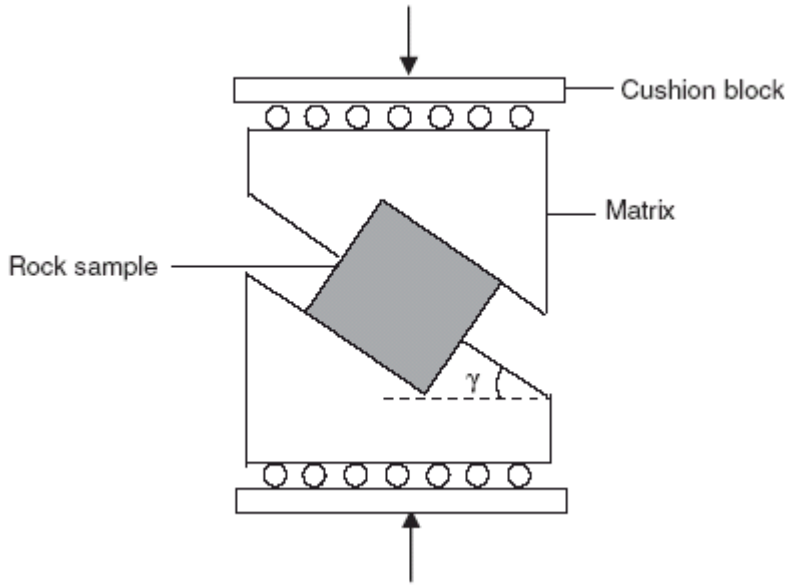

Figure 3.16: Diagrammatic sketch of the compressively induced shearing experiment (Liu et al., 2006).

Table 3.2: Shearing strength and IRTI of rocks when the shearing tilt angle is 60° (Liu et al., 2006).

Rock type	Shearing strength (MPa)	IRTI (°C)
Marble	31.5	3.7
Lime rock	44.0	10.8
Granodiorite	47.5	31.7
Gabbro	72.9	85.4

Table 3.3: Measuring results of the IRTI values at different shearing tilt angles (Liu et al., 2006).

Rock type	IRTI (°C)		
	$\gamma = 45°$	$\gamma = 60°$	$\gamma = 70°$
Marble	0.56	3.68	7.4
Lime rock	0.21	10.8	>43.0[a]
Granodiorite	8.3	32	>36.6[a]
Gabbro	11.25	85.38	17.34

[a]Indicates that the actual value exceeds the limit set by the thermal imager.

Based on the above experimental results:

(1) The IR features of rock at failure are different under different loading configurations due to the different fracture types generated. In the quasistatic case, the IRTI of a compressively-induced shearing fracture is greater than that of a uniaxial compression fracture, while the IRTI of an impact fracture is the highest. For a tension fracture, either in quasistatic or dynamic conditions, the IRTI is almost invariant. The main factor influencing the IR during the failure of rock is the frictional heat effect.

(2) The IR remote sensing technique is an important and effective means to detect rock failure. It can detect both the temperature distribution on the rock surface at failure, and can also detect the nature and some properties of the fracture.

Wu et al. (2004) measured TIR (transient infrared) by using low velocity impacts in the laboratory and compared these results using back analysis of impact energy. Figure 3.17 shows typical IR images at different impacting velocities, including the verification velocity of 8.5 m/s. Based on these images they concluded that:

- If the velocity is no higher than 15 m/s, which could be considered as the first critical impacting velocity for marble, the abnormal IR pattern of the impacting region is approximately a circle; within the first critical velocity, the higher the impacting velocity, the brighter the IR image.
- If the impacting velocity is higher than the first critical velocity, the IR images lose their central symmetrical characteristics and become complicated because of the damage in the target area.

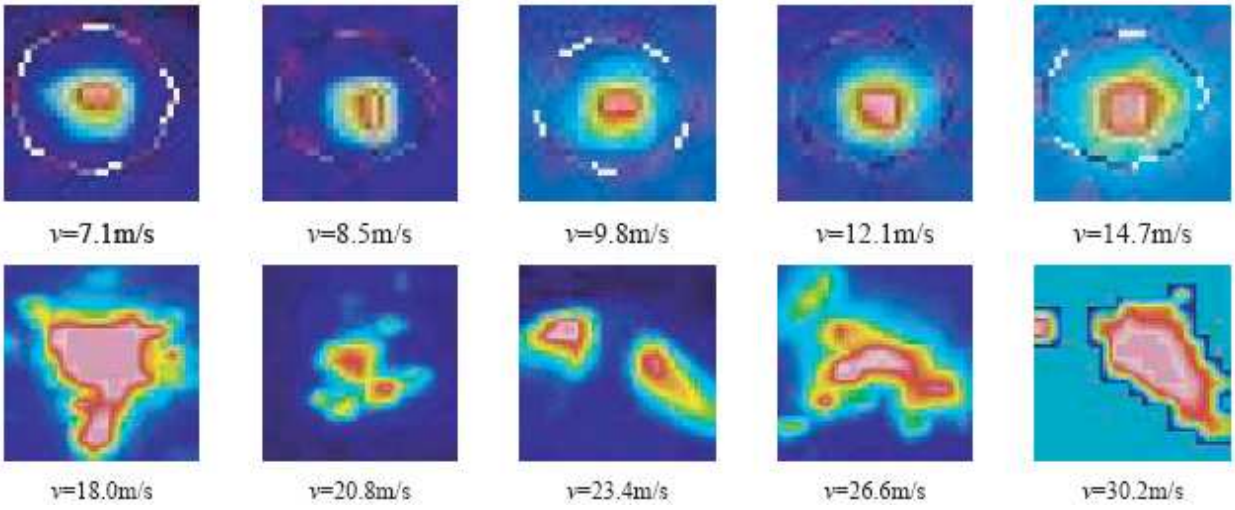

Figure 3.17: Transient IR thermal images at different impacting velocities (Wu et al., 2004).

Shi et al. (2007) successfully monitored the transient process of rock using a thermal infrared (TIR) imager. The geometric features and the radiant characteristics of the infrared thermography in the target region were extracted and regressively analyzed. They concluded that: (1) there is a critical velocity at which target thermography is regular and centrally symmetrical; (2) within the critical velocity, the impacting velocity is linearly correlated to the perimeter of target thermography and is quadratically correlated to the TIR temperature increment (figure 3.18). In this research, two IR images were selected for the quantitative analysis: one is the last frame of thermographies before the impact, and the other is the first frame after impaction. A circle covering the target region with variations in TIR radiation, whose centre is the impaction centre, is defined as target thermography.

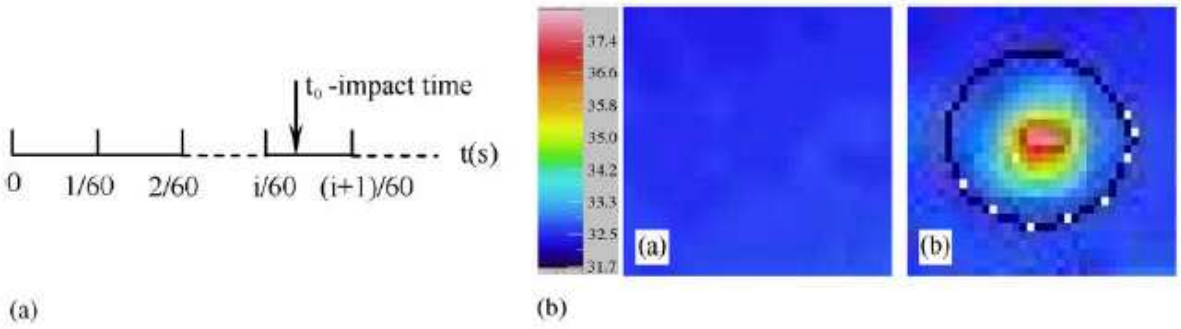

Figure 3.18: The process of extracting the geometric parameters from target thermography: initial thermography, (b) segmentation with a threshold and (c) boundary extract (Shi et al., 2007).

Also the data from the experiment on impacting velocity (v) and the increment of the maximum TIR radiation temperature (Δmax) are shown in figure 3.19.

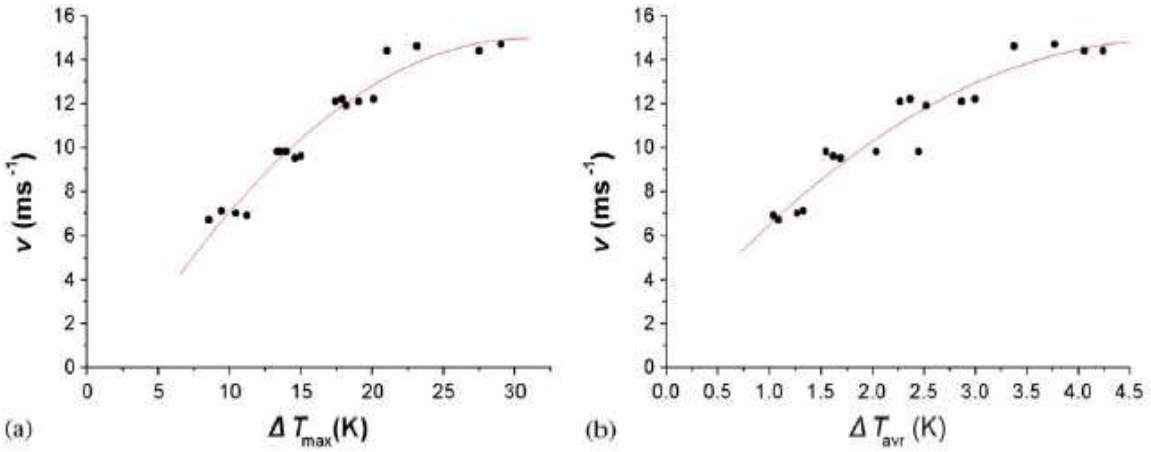

Figure 3.19: The correlation between impacting velocity and the TIR temperature increment: (a) v vs. Δmax and (b) v vs. ΔTavr (Shi et al., 2006)

According to infrared remote sensing experiments Shi et al. (2007) concluded that:

1. There is a critical velocity for impacting normally on rock; for marble, this velocity is 14–15 m/s. Within this critical velocity, the target thermography is regular or centrally symmetrical. The critical velocity is dependent on the properties of the rock, and also the head size and shape of the projectile. The critical velocity is a potential index for detecting the rock properties of the target via TIR remote sensing detection.
2. Within the critical velocity, the impacting parameters are well correlated with the geometric parameters of the target thermography: When the rock is impacted normally, the impacting velocity (v) is linearly correlated to the perimeter (Pe) of the target thermography, while the projectile kinetic energy (W) is linearly correlated to the area (A) of the target thermography.
3. Within the critical velocity, the impacting parameters are also well correlated with the radiant parameters of the target thermography. In conditions where the rock impacts normally, the projectile kinetic energy (W) is linearly correlated to the increment of the TIR radiant flux (ΔP), while the impacting velocity (v) is quadratically correlated to the increment of the TIR temperature (ΔT_{max}. and ΔT_{avr}.).
4. TIR imaging detection is an effective and practical method for monitoring and back analysis of rock impaction. As rock is a complex material with mineral compositions that exhibit significant local variation, the discrete transient TIR radiation from the target is inevitable.

A theoretical model for temperature enhancement of the ground surface layer in the vicinity of fault systems in the Earth's crust was developed by Surkov et al (2006). According to this model, fluid filters upwards from a lower depth to the Earth's surface to provide an increase in the ground temperature. Their conclusion is that the tectonic stress in the fault zone results in the gradual squeezing-out of water from lower depths towards the ground surface.

Wu et al. (2002) presented a series of laboratory experimental results on granite and marble that monitored the TIR radiation changes with rock deformation. They concluded that (1) the overall surface IR radiation temperature of loaded rock increases with rock deformation, while the TIR anomaly occurs with rock fracturing after its elastic deformation stage, (2) the average TIR temperature of the rock surface and the TIR radiation energy from the rock surface is proportional to rock stress and is cubic curvilinear to the mechanical work input before failure, (3) the TIR-anomaly characteristics of the rock surface reflect the features of rock deformation or rock failure, i.e., the TIR anomaly will be positive if the deformation (failure) is compressive or shearing, while it will be negative if tensile, and finally (4) the TIR-anomaly stresses for the marble failure and granite failure are, respectively, 0.97 and 0.82 maximum uniaxial strength.

3.4. Elastic wave velocity variations under stress

As discussed above seismic-wave velocity and amplitude are very sensitive to changes in rock properties. A number of investigations have been done using AE and elastic wave changes measurements. Ayling et al. (1995) published the results of triaxial compression tests on porous rocks, monitoring AE and elastic-wave propagation measurements simultaneously. Vs and Vp were measured in the direction of the maximum principal compressive loading axis (figure 3.20).

Meglis et al. (1995) published the results of investigations on the effect of stress path on the formation of damage around holes. They tested 3 granite blocks (52×52×22 cm) with a central hole under various load conditions and monitored the AE and elastic wave velocity changes during the tests. Both uniaxial and biaxial loading were used in this research. They concluded that the AE activity was associated both with fracturing close to the hole and with the boundary conditions of the applied load. Velocities measured parallel to the hole axis decreased following each load cycle. This decrease correlated primarily with the formation of large crack planes oriented parallel to the unconfined face.

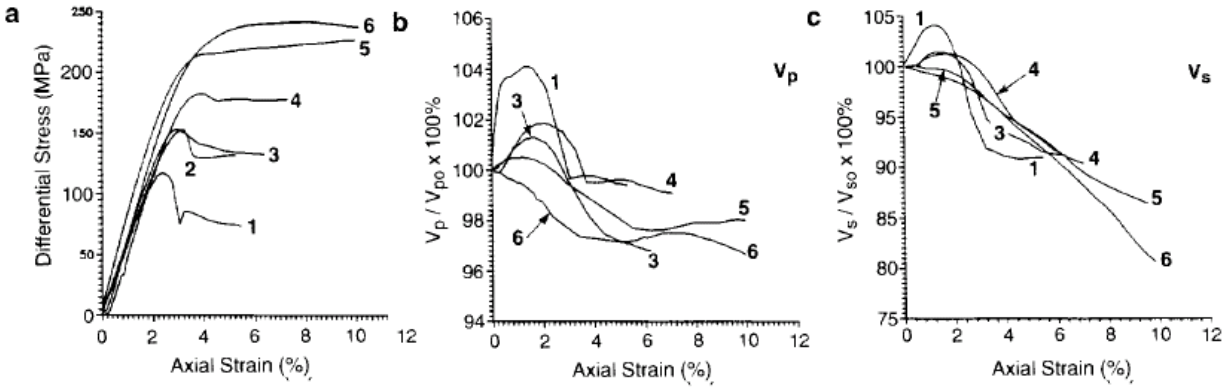

Figure 3.20: A series of curves showing (a) stress, (b) changes in compressional wave velocity, and (c) change in shear wave velocity against strain for sandstone samples at confining pressures of 15, 25, 30, 50, 100 and 200 MPa, shown by curves 1, 2, 3, 4 and 5 respectively (Ayling et al., 1995).

Young et al. (2004) used a method based on acoustic emission and elastic wave changes for monitoring microcracking at the Underground Research Laboratory in Pinawa, Manitoba, Canada. By using the source locations of the seismic events induced by the excavation, they mapped the extent of the excavation damage/disturbed zone (EDZ) around tunnels. The change in P- and S-wave velocity over a 4/5-year period is presented in figure 3.21 for a source–receiver pair in similar positions. They reported very small changes in P- and S-wave velocity can be detected depending upon the ray path length and sampling rate. They suggested that this study has highlighted the advantages of using advanced seismic-processing and analysis methods, as well as the complementary method of velocity interferometry, to increase the understanding of rock-mass response to excavation and thermally-induced stresses.

In laboratory experiments, Stanchits et al. (2003 and 2006) measured changes in P-wave velocity and attenuation during the injection of water into a granite sample as it was loaded to failure. Anisotropic P-wave velocity and attenuation fields were determined during the experiment using an array of 13 piezoelectric transducers. They observed considerable changes in P-wave velocity and peak-to-peak amplitudes of P- and S-waves at 86 and 95 percent of peak stress. Transient increases in attenuation of up to 483 dB/meter were also reported and were associated with diffusion of water into the sample. Finally they concluded that the velocity and attenuation of P-waves are sensitive to the process of opening of microcracks and the subsequent re-saturation of these cracks as water diffuses in from the surrounding region.

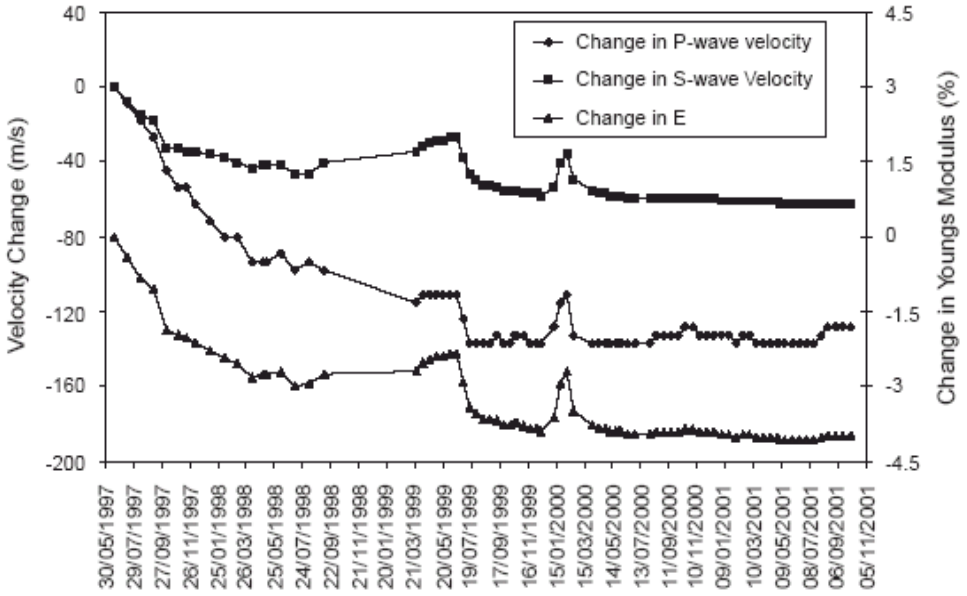

Figure 3.21: Change in P- and S-wave velocity for a source–receiver pair, a 4% decrease in Young's modulus is estimated to have occurred in the damage zone around the tunnel over the 4/5 year monitoring period (Young et al., 2004).

The result of acoustic emissions (AE), compressional (P), shear (S) wave velocities, and volumetric strain of Etna basalt under triaxial compression tests has been published by Trovato et al (2006). They concluded that:

- With increasing axial load, P-wave velocities only show a small increase.
- With increasing differential stress AE activity in basalt increased with a significant contribution of tensile events.
- Close to failure the relative contribution of tensile events and P-wave velocities decreased significantly.
-Crack orientation, defined as the average orientation over its entire length with respect to the long axis of the sample has been estimated.

Pellet et al. (2007) and Pellet and Fabre (2006) experimentally studied the variation of shear wave velocity and acoustic emission simultaneously under uniaxial loading. They observed an increase in Vs by loading up to 85 percent of the ultimate uniaxial strength of the specimens. They proposed that the use of AE techniques with simultaneous measurements of the elastic wave changes could be a useful approach for predicting rock failure and thus also for earthquake prediction.

The results of acoustic emissions (AE), compressional (P) and shear (S) wave velocities, and volumetric strain in Etna basalt under triaxial compression tests was published by Trovato et al. (2006). They concluded that:

- With increasing axial load, P-wave velocities only show a small increase.

- With increasing differential stress, AE activity in basalt increased with a significant contribution of tensile events.

- Near failure, the relative contribution of tensile events and P-wave velocities decreased significantly.

3.5. Discussion and Conclusions

In earthquake prediction, predictive precursors assume a causal relationship with the main shock and provide information about a possible earthquake hazard better than that achieved by assuming a random distribution of earthquakes (Knopoff et al., 1996). Because these are precursors, it implies that there is a defined time prior to the main shock.

This work is a part of project that has been presented in IIEES to study feasibility of earthquake prediction using precursors. The main objective of this chapter was to summarize the recent activities and success in rock failure prediction as a small-scale earthquakes using three well known precursors; acoustic emission, infrared radiation and elastic wave changes during loading of rock and rock-like materials. The main results can be summarized as follows:

- Acoustic emission (AE) has been widely used to evaluate cracking processes in laboratory specimens and engineering structures because of its high sensitivity to crack initiation and growth. Since crack propagation is considered to be the primary reason for initiating acoustic emission during the loading of a rock specimen, the theory of crack propagation has received considerable attention. Many experimental results and numerical simulations are now available on this subject that is useful for understanding failure mechanisms and precursors. Some useful new results on crack propagation and nucleation were also included, which is helpful in understanding the complexity of earthquake dynamics.
- Some investigations have been done on seismology and b-value studies using AE records. The magnitude and number of events, as well as the energy and amplitude of events, are considered in rock failure processes. Also several studies have been done using moment tensor analysis for fracture study. The results of experiments and numerical simulations of the brittle fracturing process with heterogeneity in material

and structure, provide useful data for a thorough understanding of earthquake mechanisms and the related precursors.

- The evaluation of stress memory in rock samples using AE is a new method in rock engineering. Some research uses this method for stress measurement in rock engineering projects as well as in earth crust stress measurements. A few results on frictional behavior of non-homogeneous faults and earthquake nucleation have been obtained, which helps in comprehending the complexity of earthquake dynamics.

Evaluation of hydraulic fracturing in rock engineering projects using AE is another emerging field. New research shows that AE monitoring can improve the reliability and the accuracy of hydraulic fracturing stress measurements. Some limited in-situ studies (especially in tunnels) have used AE monitoring as a key element of failure evaluation. In these studies the excavation damage zone (EDZ) in tunneling operations are determined.

It is obvious that the use of AE will become more prevalent because it can provide unique insights into damage processes. The problems encountered in AE - including noise reduction, reliability, and difficulty in solving the inverse problems of wave propagation in source-function and waveform analyses - represent areas of future endeavor in AE science and technology. There is also a great need to develop AE theories for new applications. For example AE monitoring of thermally treated specimens is a new field of application of this method in geomechanical sciences. Even though there is limited research available in this field, it seems it could be useful to use the unique ability of AE records for assessing the pre- heated rock like materials.

Although AE has been used in materials-related studies for about four decades, there are still many problems. The most important difficulty is associated with the reliability of AE results. Many researchers simply use AE equipment to collect a large amount of data and use the results to explain the material failures qualitatively, without paying too much attention to the sensor calibration and attachment. Sometimes, no distinctions are made between noises and real AE signals. Therefore, it is very difficult to compare results from different papers. This also causes confusion in investigating the reliability of various AE systems.

When comparing AE results in various materials, one finds that there are more publications regarding composites, rocks, and ceramics than metals. The reason for this trend is that the AE signals are stronger and vary more significantly in composites, rocks, and ceramics than in metals. On the other hand, because of the homogeneity and simplicity

of metals, the wave propagation in metals should not be as complex as in composites and rocks, since there are less reflections, diffractions, and scattering in metals. Therefore, metals represent a good subject for studying source-function and waveform analyses.

The infrared investigations have increased over the last two decades. Reviewing the literature shows that there are two main branches where infrared measurements are used: Remote sensing studies using satellite image processing, and thermography in laboratory scale experiments. Earthquake predictions using thermal anomalies have been considered, especially in recent years. Also studies of rock and concrete failure in the laboratory using infrared techniques are other applications of this method.

Seismic-wave velocity is very sensitive to alterations in rock properties. A number of investigations have been done by AE and elastic wave change measurements. Recent studies show that using of this method in conjunction with other precursors, such as acoustic emission, could be more effective in recognizing the damage and failure that occurs in rock.

Finally it should be noted that no experiment can completely duplicate the natural conditions; the main role of the laboratory study is to establish physical models and to validate theories. Even so, the force driving the development of laboratory studies comes from field observations and studies. The recent studies indicate that the heterogeneity in material and structure of rock and the complexity of time processes is still one of the key problems in the study of seismology and consequently earthquake prediction.

Chapter 4

Mechanical tests on two intact igneous hard rocks, including ultra high pressure triaxial tests

4.1 Introduction

Evaluation of mechanical and physical properties of rocks is important for all types of rock research. Uniaxial compressive strength, elastic modulus, tensile strength and elastic wave velocities are the most common and interesting parameters and their evaluation is vital for various engineering and research projects (Hoek and Brown, 1997).

In this chapter the laboratory test procedures are presented and the results discussed. Two main igneous rocks were selected for these studies: Lavasan granite from North of Tehran and North African gabbro. The reasons for selecting these rocks are discussed in the following sections.

After preparation of the samples, a few conventional tests were carried out to evaluate the geophysical and geomechanical parameters. Uniaxial, triaxial and Brazilian tests were performed and elastic wave velocity and other physical parameters were measured for this purpose. We also used ultra high pressure triaxial tests to study the behaviour of strong gabbro and to calibrate related criteria. In the first section, the geological setting, mineralogy and petrology of granite and gabbro are discussed. Thin sections were prepared for microscopic studies. The procedure for sample preparation and laboratory investigation are presented and, finally, the investigated parameters of rocks will be commented upon.

4.2 General characteristics of selected rocks

The reasons for selecting Lavasan granite and North African gabbro are as follows:

- Approximate isotropy in geomechanical parameters,
- Distinctive AE characteristics in laboratory tests,
- Vicinity of Lavasan granite to the Mosha Fault, north of Tehran. Since the feasibility of using in-situ studies to predict earthquakes is the objective of this research, an active fault, the Mosha Fault near Tehran, could be used for pilot field investigations and possible future earthquake monitoring.
- The low porosity ratio of the rocks, about 1.0 percent for granite and less than 0.5 percent for gabbro, decreases the effect of pore closure during loading. In general, the formation process of granite and gabbro under high pressure and high temperature allows very little open pore space. Consequently the selected specimens have a fracture system rather than a pore system.

4.2.1. Petrology and mineralogy of Lavasan granite

Granite samples were taken from the exposed geological record in the vicinity adjacent to the Mosha main thrust fault. The Mosha Fault is one of the major active faults in Central Alborz as shown by its strong historical seismicity and its clear morphological signature. Situated north of Tehran city, this fault is about 150 km long with N100°E inclination. It represents an important potential seismic source that threatens the Iranian metropolis (Jackson et al., 2002). A few intrusion rocks have been formed around this thrust. Although some of the trap rock here differs somewhat in appearance, its structure and composition are very similar. According to macro petrology, most of these intrusion rocks are granite, consisting of crystallized plagioclases, feldspars, mica, hornblende and quartz. The Lavasan intrusion mass is one of the largest plutonic rock masses in this area. Figure 4.1 shows the location of Lavasan granite and the position of the Mosha Fault.

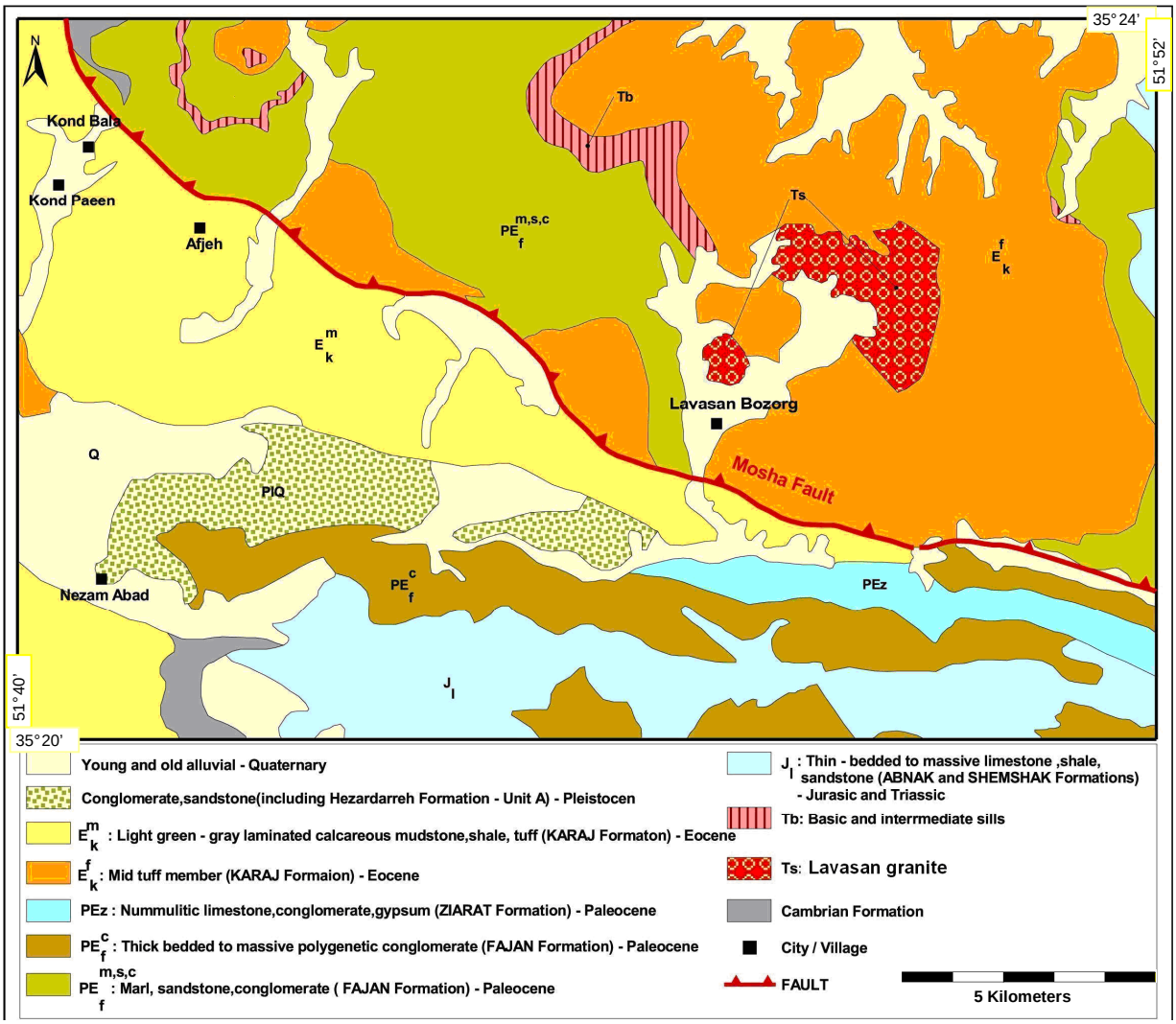

Figure 4.1: Location of Mosha Fault and geological setting of Lavasan granite (GSI, 2008).

The rock mineralogy is almost homogeneous. To study its mineralogy in detail, we prepared a few thin sections for viewing under a polarized light microscope. Figure 4.2 shows a thin section from this rock. The polarized light microscope was able to show the textural relationships as well as quantitative compositions of minerals in the specimen. In general, the rock has a silicate composition and mineralogy and possesses a subhedral granular texture, with the boundaries between crystals not clearly defined due to alterations and the development of secondary minerals. Only the shapes of plagioclases are clear while the

remaining crystals have no definitive shape in thin section. It should be noted that, depending on the general shape of the crystals, three textures can be distinguished; (1) euhedral granular, (2) subhedral granular and (3) anhedral. Based on this classification, Lavasan granite is subhedral granite.

The rock is gray to pale green. A siliceous matrix cements the medium- to coarse-grained feldspars, quartz and K^+, Na^+ and Ca^{++}-enriched plagioclases. Ferro magnesium oxides, such as pyroxene, are the other key minerals in this rock. Alteration of the pyroxenes to amphibole and chlorite gives a pale green coloration to the intrusion mass. Chlorite, muscovite and carbonate minerals are the secondary types of minerals that were formed initially or secondarily by alteration or replacement of original minerals.

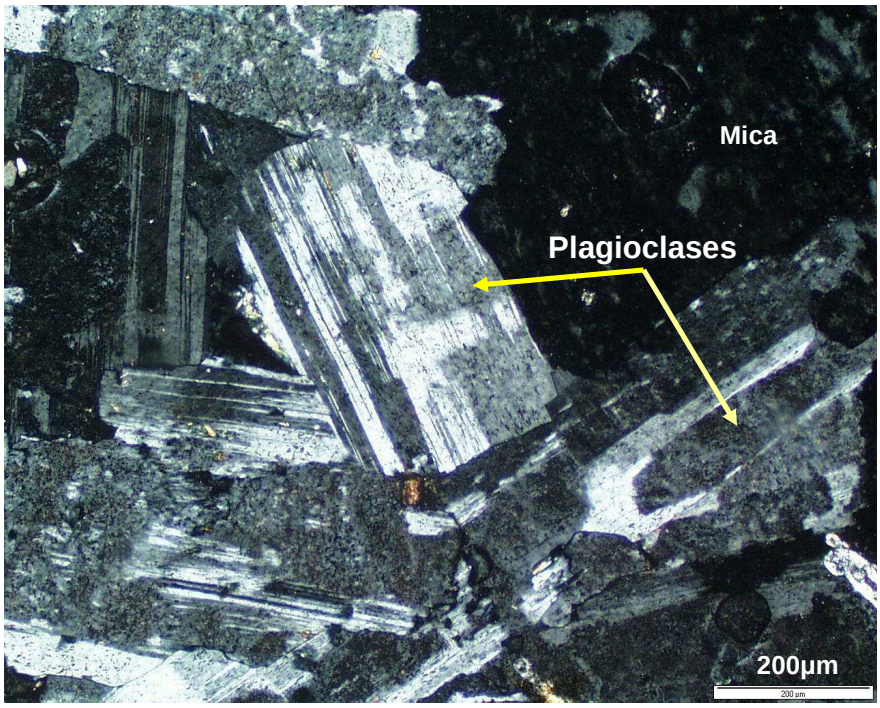

Figure 4.2: A thin section of Lavasan granite view through polarized light microscope. Dark area in top right of the picture is mica and secondary serizite

4.2.2. Petrology and mineralogy of North African Gabbro

Cubes of the gabbro used were exported from Algeria to France for construction purposes. Homogeneous and sound specimens were required in this study, so all specimens were cored from a single small cubical sample. Gabbro is generally formed when the heavy pyroxene and olivine crystals settle to the bottom of the diabase magma chamber while the rock is still molten (Mackenzie et al., 1982). In appearance, North African gabbro has a dark green color with uneven fracture surfaces. The mineral grain aggregates have almost identical sizes and are small, so this gabbro is called equigranular (all crystals are of approximately the same size). Thin section studies by normal and polarized light under a microscope showed that the rock was composed essentially of plagioclase and pyroxene minerals. Almost 60 percent of the minerals are various types of plagioclase minerals while pyroxene minerals are the second most abundant minerals (almost 40 percent). Two types of pyroxenes, namely ortho-pyroxene ($MgSiO_3$) and clino-pyroxene ($FeSiO_3$) minerals were visible in the thin sections; this gabbro is a two pyroxene gabbro. In figure 4.3, a photo of a thin section is presented. Some of the orthopyroxene crystals contain narrow lamellae of augite (Fig. 4.3). Ilmenite ($FeTiO_3$) and magnetite (Fe_3O_4) minerals were distinguished as minor crystals with less than 1 percent.

From a petrologic point of view, a symplectite texture could also be seen in the thin sections. Symplectite is a term applied to fine-grained intergrowths resulting from the combined growth of two or more minerals as they replace another mineral (Winter, 2001). Replacement may be partial or complete but are common in intrusion rocks. For this particular gabbro rock, the texture is defined as Myrmekite, an intergrowth of dentritic quartz in a single crystal of plagioclase. If there is a lack of quartz, Myrmekite also occurs preferentially where plagioclase is in contact with K-feldspar (Mackenzie et al., 1982). The lamellar intergrowth between two pyroxenes is also common in this gabbro; from the thin section studies we found that ortho-pyroxene crystals host clino-pyroxenes (figure 4.4).

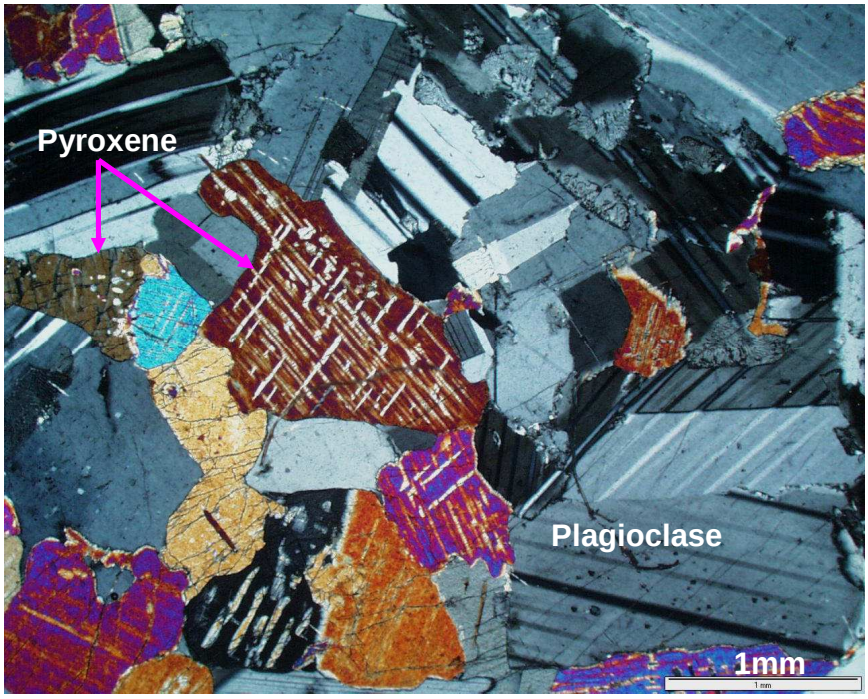

Figure 4.3: Microscopic view of minerals in a thin section of gabbro rock. Well mineralized pyroxenes are the main minerals with plagioclase in the matrix.

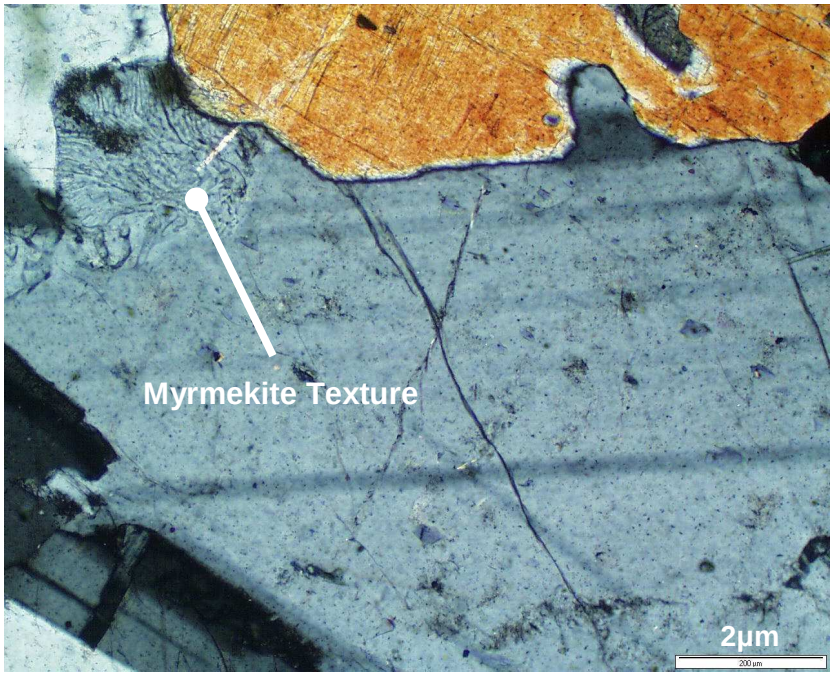

Figure 4. 4: Myrmekite texture in North African gabbro. Myrmekite has formed in the plagioclase at the boundary with K-feldspar.

4.3. Sample preparation

Forty core specimens, 45 mm in diameter and 100 mm in length, were prepared from Lavasan granite. Twenty-five core specimens were drilled from the gabbro cube in two different sizes; 12 cylindrical specimens with a 70 mm diameter and 140 mm length were prepared and 13 were cored with a 40 mm diameter and 90 mm length. The samples were prepared based on existing standards (ISRM, 1972) with smooth and exactly parallel planes to make sure that the load is equally distributed over the loaded surfaces of the samples. The grinding machine of Laboratoire Géophysique Interne et Tectonophysique (LGIT) in Grenoble was used for this purpose. The smoothness and the parallelism (with an end parallelism of 0.01 mm) of each sample were tested using a V-block and displacement dial gauge (figure 4.5).

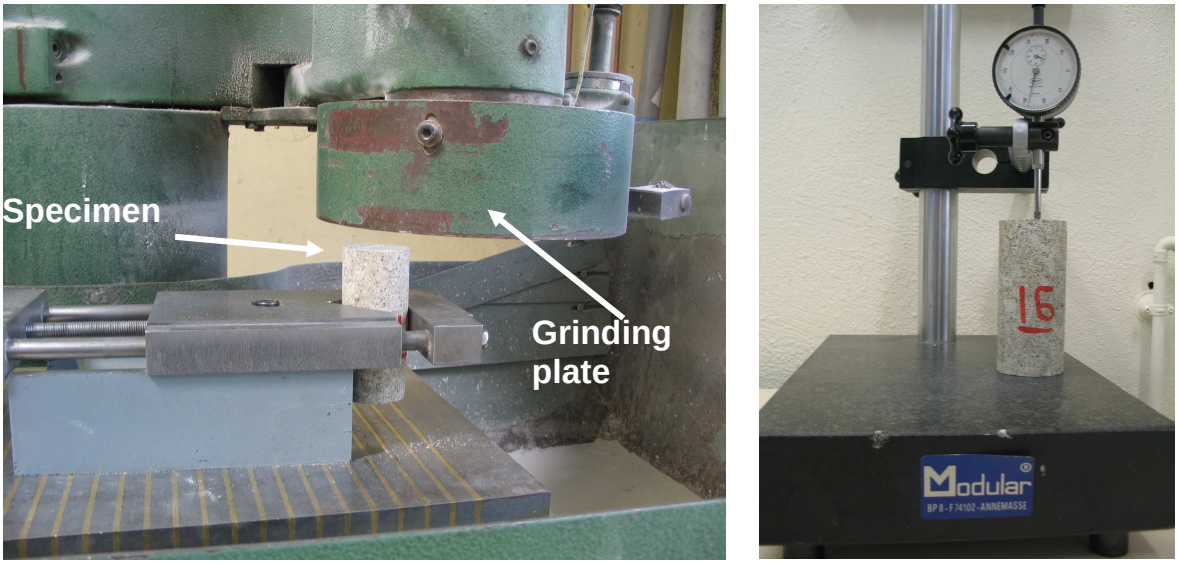

Figure 4.5: Grinding machine at LGIT for smoothing the ends of a specimen (left) and displacement dial gauge (right)

4.4. Measurement of elastic wave velocity Vp and Vs

Young's modulus and Poisson's coefficient of the prepared specimens were evaluated by measuring the primary and the secondary elastic wave velocity. These parameters are also necessary to locate the source of the events in AE studies. The equations 4.1 and 4.2 show the dynamic elasticity value and Poisson's ratio estimation using elastic wave velocity.

$$\upsilon_d = \frac{\left(V_p^{\,2} - 2V_s^{\,2}\right)}{2\left(V_p^{\,2} - V_s^{\,2}\right)} \tag{4.1}$$

and:

$$E_d = \frac{(1-2\upsilon)(1+\upsilon)}{(1-\upsilon)} \times V_p^2 \tag{4.2}$$

For both of the rocks studied, the velocities of the stress waves in the prepared samples were measured in the LGIT. Figure 4.6 shows the experimental set-up for these measurements and the components that were used, including a laboratory pulse velocity meter, piezoelectric crystals, etc. A special viscous coupling agent was used between the transducers and the sample giving a thin bond. High-frequency electrical pulses transmitted to one crystal create a stress wave that could be received by the second crystal and reconverted to an electrical signal. A delay line allows the received waveform to be aligned with the sending waveform on an oscilloscope and the required delay to achieve these measures shows the travel time of the pulse through the specimen.

The velocities at which elastic waves are transmitted through the rock depend on the elastic properties of the specimen. Crack porosity, composition, density, alteration and mineral orientation are the most important factors responsible for variations in seismic velocities. For this study, the compression wave velocity (Vp) and shear wave velocity (Vs) were measured using the SOFRANEL Model 5052 G located in LGIT (figure 4.7). This equipment provides a direct measurement of the velocity of sound waves in a core specimen. In this apparatus, shear and longitudinal waves are produced by a ceramic element located at one end of a columnar sample and detected by a second element at the opposite end. Determination of propagation velocity is then a straightforward matter of dividing the distance between the elements by the time-of-flight.

The velocities of primary and secondary waves were measured for all 40 specimens of granite and 25 specimens of gabbro. A record of P wave form is shown in figure 4.8 as an example. The average measured Vp and Vs for granite and gabbro specimens are presented in the table 4.2. The measured values for all samples are presented in detail in appendix I. It should be noticed that it was not possible to detect a wave in the receiver for some of the granite specimens due to internal damage or other reasons that should be investigated in the future.

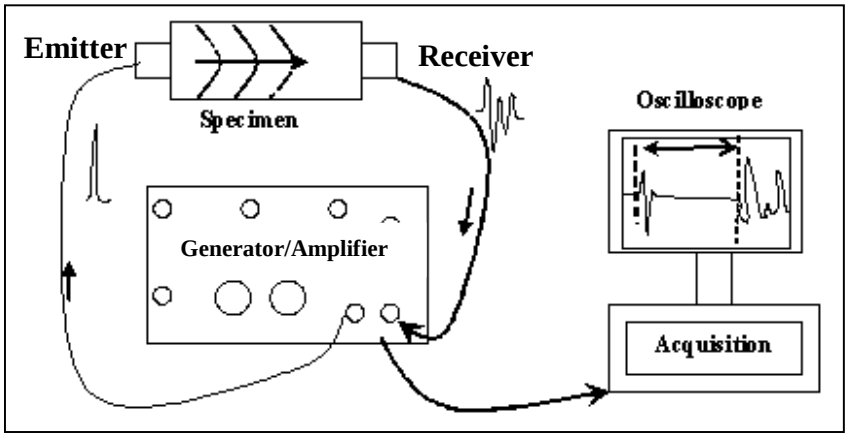

Figure 4.6: Schematic diagram of the Vp and Vs measurement apparatus (Orengo, 2003 with modifications)

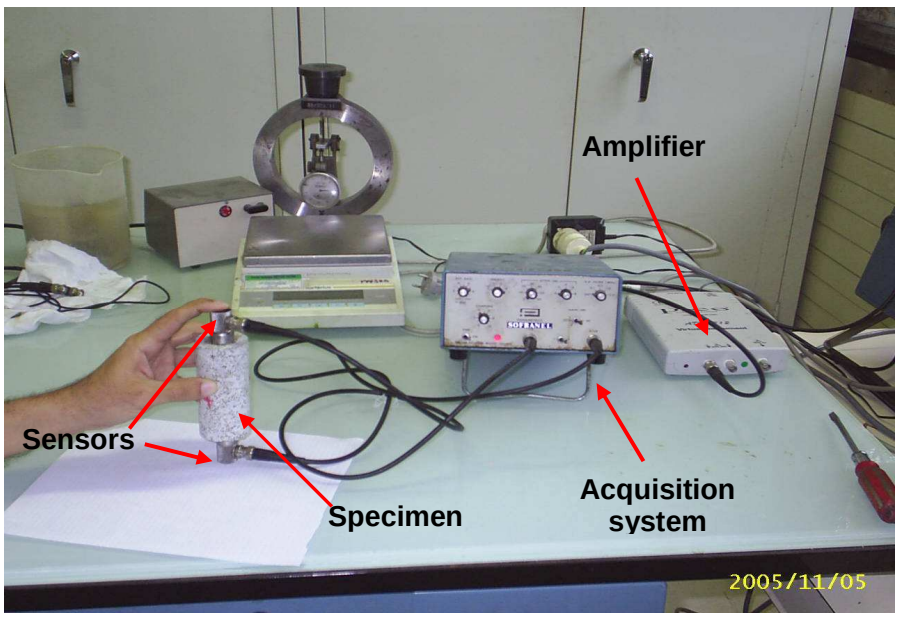

Figure 4.7: A view of the Vs and Vp measurement system

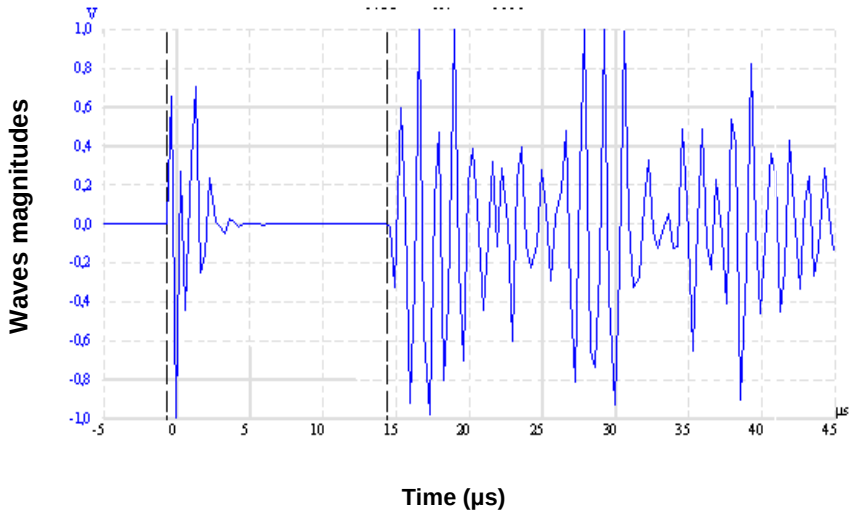

Figure 4.8: Example of longitudinal wave record

4.5. Evaluation of mechanical properties

The general characteristics and mechanical properties of granite and gabbro were assessed by laboratory tests. A series of conventional tests were carried out: Bulk specific gravity, porosity and elastic wave velocity were measured based on ASTM guidelines (2001). In addition, Brazilian tests, standard uniaxial and triaxial tests were performed. The type and the number of tests performed are presented in table 4.1 and the average values of the test results are summarized in table 4.2.

Table 4.1: Type and number of tests on granite and gabbro specimens

Lavasan Granite			
Type of test	**Number of tests**	**Geometry of specimens L×D (mm)**	**No. of specimens**
Simple uniaxial compression	10	100 × 45	Gr1, Gr3, Gr5, Gr6, Gr7, Gr10 Gr12, Gr15, Gr16, Gr17
Porosity and bulk specific gravity	3	Unshaped pieces	Gr11, Gr22, Gr33
Measuring of Vp and Vs	40	100 × 45	Gr1 to Gr40
AE monitoring in uniaxial test	9	100 × 45	Gr1, Gr3, Gr6, Gr7, Gr10, Gr12, Gr15, Gr16, Gr17
North African Gabbro			
Simple uniaxial compression	4	140 × 70	Ga1(650), Ga3, Ga4 and Ga10
Porosity and bulk specific gravity	3	Unshaped pieces	Ga11, Ga22, Ga33
Measuring of Vp and Vs	10	140 × 70	Ga1 to Ga10
High pressure Triaxial	2	140 × 70	Ga1(650) and Ga2(200)
Brazilian	6	20 ×40	Gab1 to Gab6
Brazilian	5	35 ×70	Gab7 to Gab11
AE monitoring in uniaxial test	4	140 × 70	Ga1(650)*, Ga3, Ga4 and Ga10

* Before the uniaxial test, the specimen was damaged during ultra high triaxial loading by a Giga press.

Table 4.2: Physical properties of tested specimens

Properties	Lavasan Granite	North African Gabbro	ASTM No.
Bulk specific gravity (g/cm3)	2.65± 0.07	2.90 ± 0.05	D 6473
Porosity (%)	1.0	<0.5	D 3148
P-wave velocity (m/s)	4051± 239	6560 ± 99	D 2845
S-wave velocity (m/s)	2537 ± 170	4078 ± 76	D 4623
Poisson's ratio	0.27 ± 0.05	0.21 ± 0.03	D 4623
Young's modulus [GPa]	30 ± 3.5	88 ± 2.5	D 4015
Tensile strength [MPa]	-	11.5 ± 0.9	D 3967–95a
Uniaxial compressive strength [MPa]	131 ± 20	226 ± 11	D 5520

4.5.1. Uniaxial compression test

The uniaxial or unconfined compressive strength (UCS) test is by far the most common laboratory test undertaken for rock mechanics studies, that is assuming one accepts the point load index test as a field test (after Pells J. N. in Hudson, 1993). The UCS test is the basic test in numerous design methods. Applications include:

- Estimation of the onset of compression or shear failure around underground openings,
- Estimation of rock pillars in underground mining,
- Estimation of triaxial strength via empirical failure criteria,
- Estimating rock elasticity modulus for calculation of displacements and settlements,
- Assessing allowable end bearing and side shear values for rock socketed pile foundations,
- Assessing excavation characteristics whether by ripping, by drag picks or road headers, by disc cutters on TBMs or by percussion drills, and
- Assessing blasting requirements.

Details of the protocols to perform UCS tests are described in ISRM (1972) and ASTM D 3148-72.

4.5.1.1. Test procedures

Three uniaxial compression tests are carried out on each of the two types of rock to evaluate the geomechanical parameters using the protocol ASTM (2001). The loading system consisted of a testing machine, load cell, sensors, and controller. The Schenck press system was used to supply load to the specimens (figure 4.9). Using this servo–controlled machine it is possible to control the velocity of loading from 0.1 μm/s to 20mm/s. The maximum load of the machine is 1000 kN with a precision of about 0.02 % (Gatelier, 2001; Gatelier et al., 2002). Three Linear Variable Differential Transformers (LVDT) arranged in a triangular position around the loading plate, were used to measure the vertical displacement and to make sure that the force acts vertically on the specimen during the tests.

The strain measurement device used both electrical resistance strain gauges and the LVDT to measure lateral and axial deformations. The gauges were mounted in the central part of the cylindrically shaped samples using X 60 superglue.

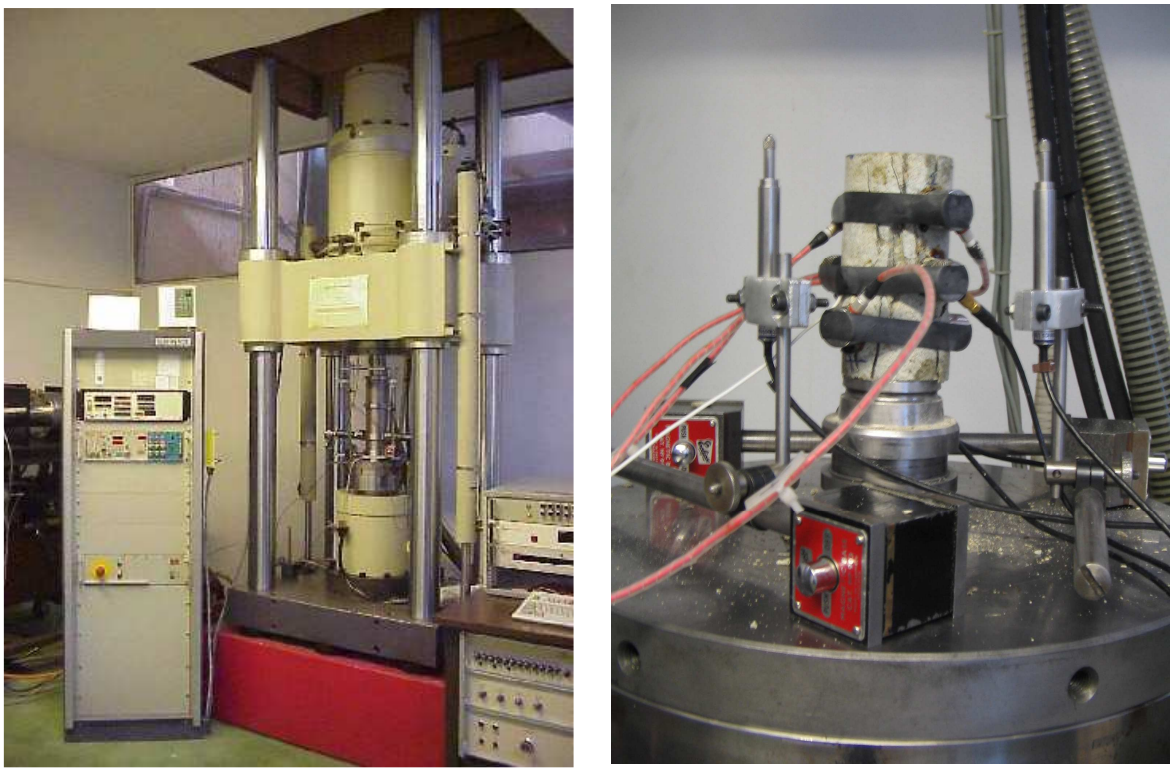

(a) **(b)**

Figure 4.9: Schenck Press (a) General view (b) Detail of the cell and sensors AE and LVDT

Normal and lateral strains on the samples were measured using surface-bonded electric resistance strain gauges. Two axial gauges were mounted on the specimens to measure the longitudinal strain and two other strain gauges fixed for measuring lateral strain (figure 4.10). All specimens were assumed to be homogeneous and isotropic.

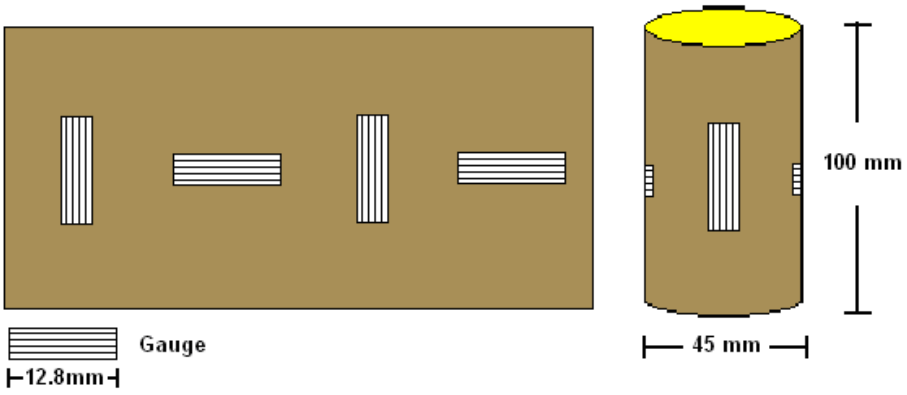

Figure 4.10: Set up of axial and lateral strain gauges glued to the specimen (extended scheme)

Table 4.3: Summary of geomechanical parameters of specimens

Sample No.	Size (mm) L×D	No. of axial gauges	No. of lateral gauges	$\sigma_{c\ max.}$ (MPa)	E (GPa)	ɣ	Vs(m/s)	Vp(m/s)
Lavasan Granite								
Gr1	95×45	2	2	142	35	0.31	2527	4105
Gr3	101×45	2	2	121	25	0.30	2441	3820
Gr5	101×45	1	-	138	27	-	-	-
Gr6	99×45	2	2	147	31	0.26	2782	4282
Gr7	100×45	2	2	125	29	0.25	2276	3695
Gr10	101×45	1	-	123	31	-	2606	4252
Gr12	101×45	-	-	138	-	-	2595	4152
Gr15	100×45	-	-	135	-	-	2747	4278
Gr16	100×45	-	-	122	-	-	2447	3764
Gr17	100×45	-	-	136	-	-	2750	4274
North African Gabbro								
Ga1(650)*	142×70	2	2	160	61	0.25	3364	5650
Ga3	141×70	2	2	216	85	0.23	3997	6468
Ga4	141×70	2	2	238	88	0.23	4088	6546
Ga10	143×70	2	2	225	85	0.20	4150	6666

***** Ga1 was previously damaged under ultra high triaxial loading. The results of the uniaxial test and elastic wave measurements are presented in the next chapter

4.5.1.2. Interpretation and comparison of the uniaxial test results

Uniaxial tests were carried out under constant strain rate conditions (3 to 4 $\times 10^{-3}$ mm/s) on samples with a length/diameter ratio of approximately 2:1. The axial and lateral strains were monitored continuously by strain gauges and LVDTs. All samples were loaded to macroscopic failure.

The results of the tests on four granite specimens are shown in figures 4.11 to 4.14 as an example. Other uniaxial test results on granite are presented in appendix I. The results of uniaxial compression tests for three gabbro specimens are presented in figures 4.15 to 4.17. The volumetric behaviors of the specimens during testing were calculated: The volume deformation ($\varepsilon_v = \varepsilon_1 + 2\varepsilon_3$) explains the dispersion of volume in response to loading.

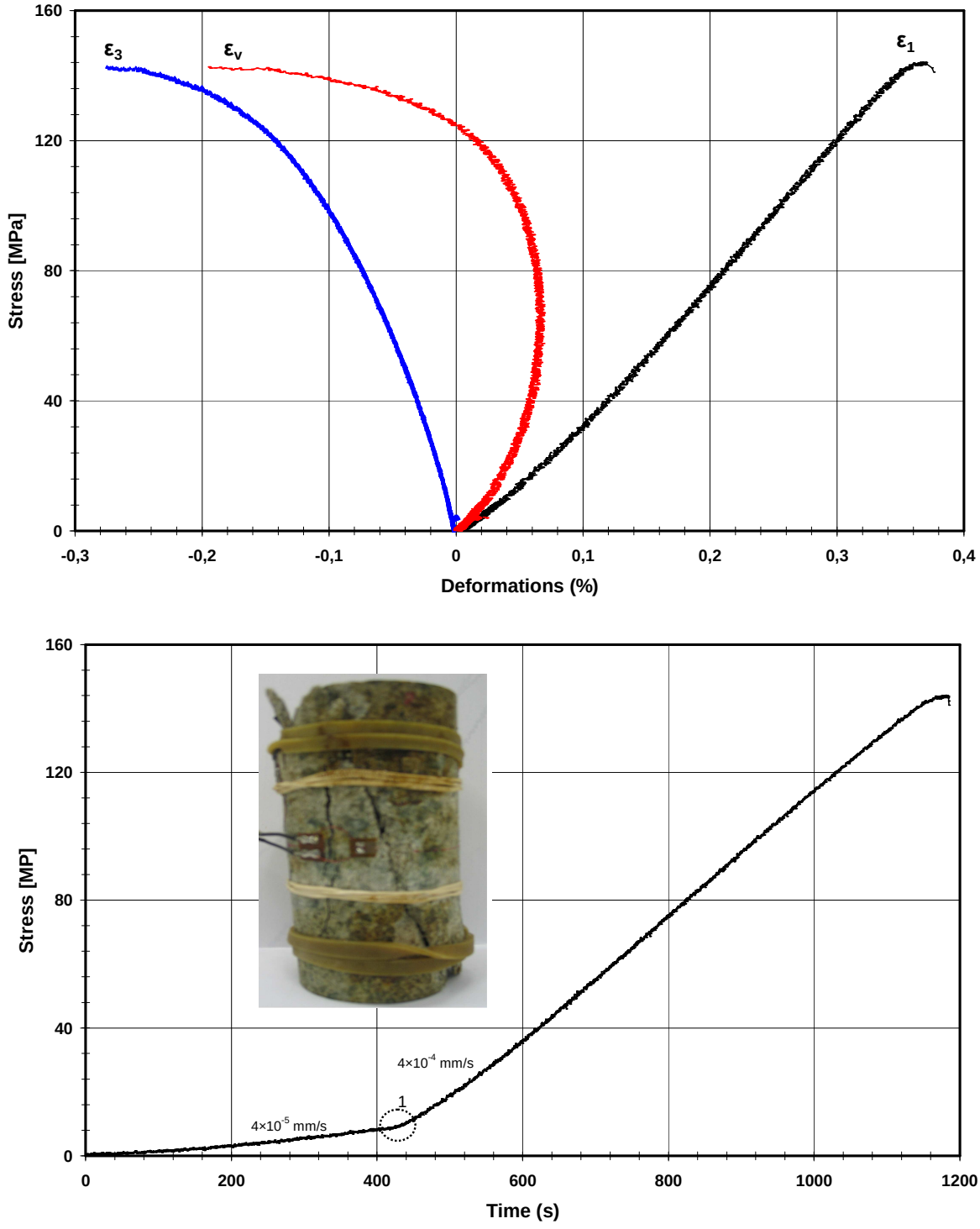

4.11: Stress versus deformations (above) and stress versus time (below) curves of granite specimen Gr1 during uniaxial compression test. At the point 1 the rate of loading was increased to 4×10^{-4} mm/s in order to reach failure at an appropriate time. ε_1, ε_3 and ε_v are axial, lateral and volumetric deformations, respectively.

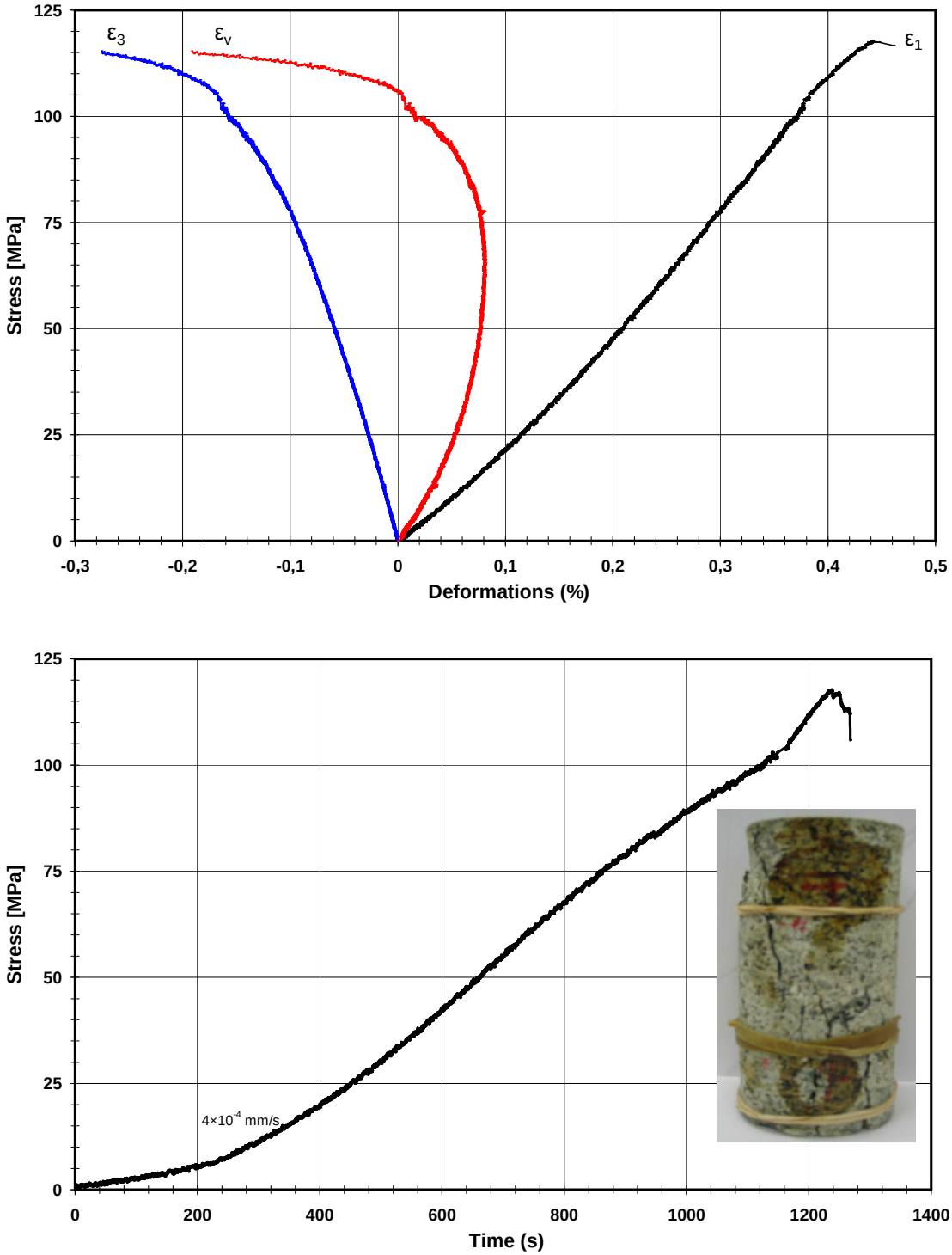

4.12: Stress versus deformations (above) and stress versus time (below) curves of granite specimen Gr3 during uniaxial compression test

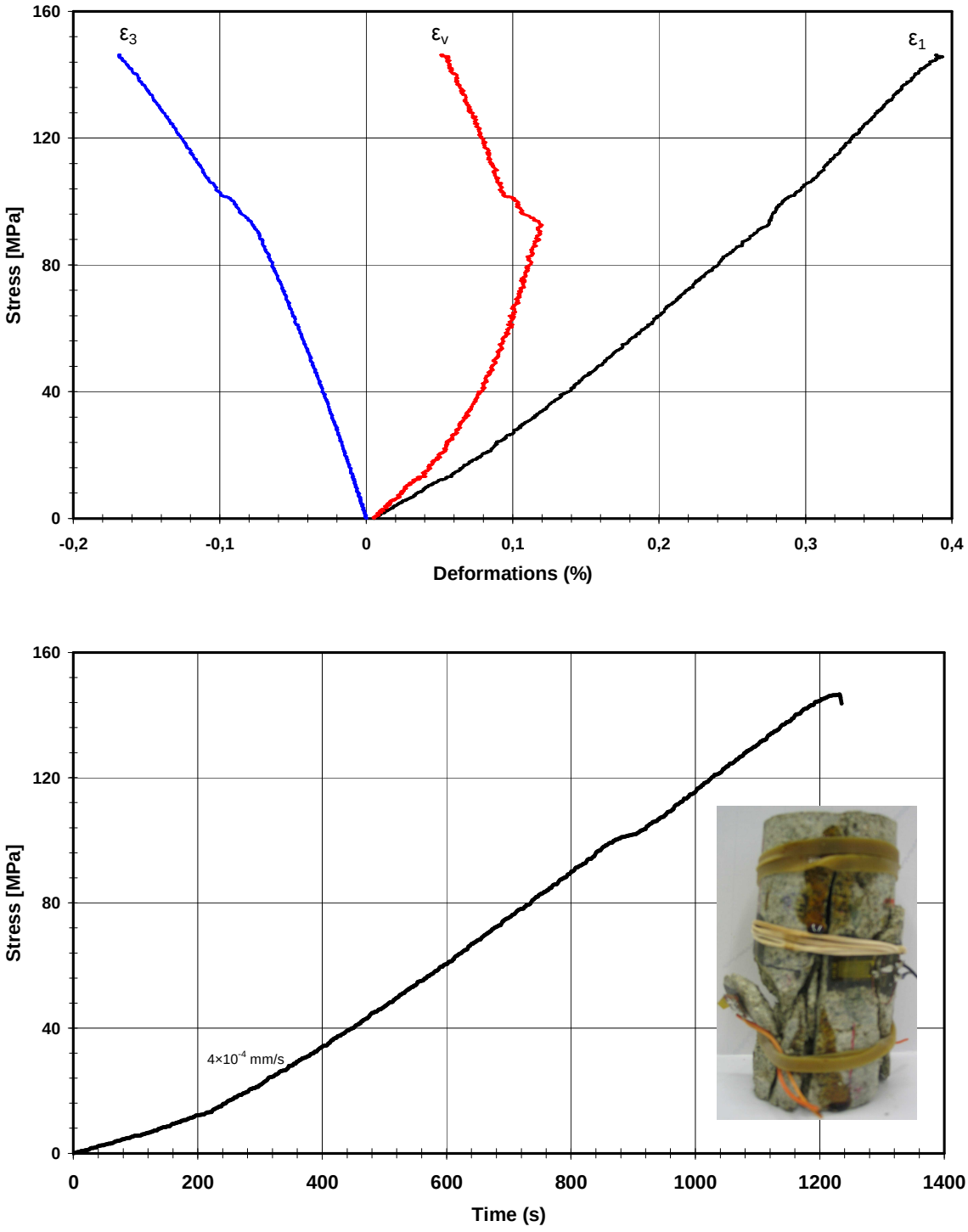

4.13: Stress versus deformations (above) and stress versus time (below) curves of granite specimen Gr6 during uniaxial compression test

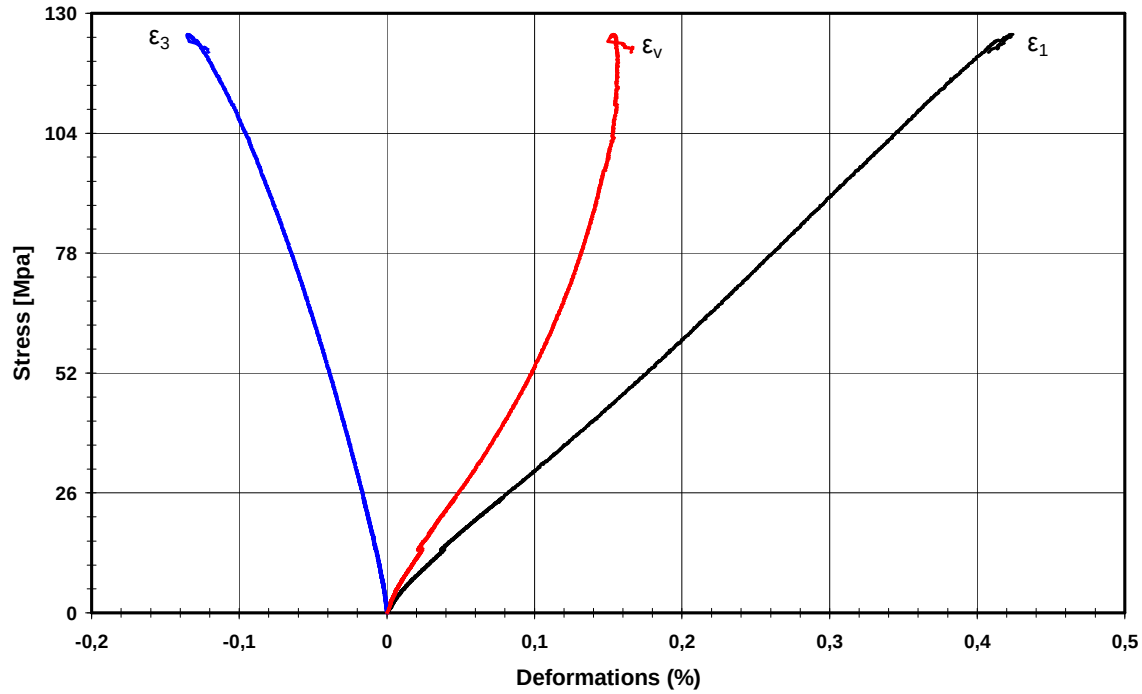

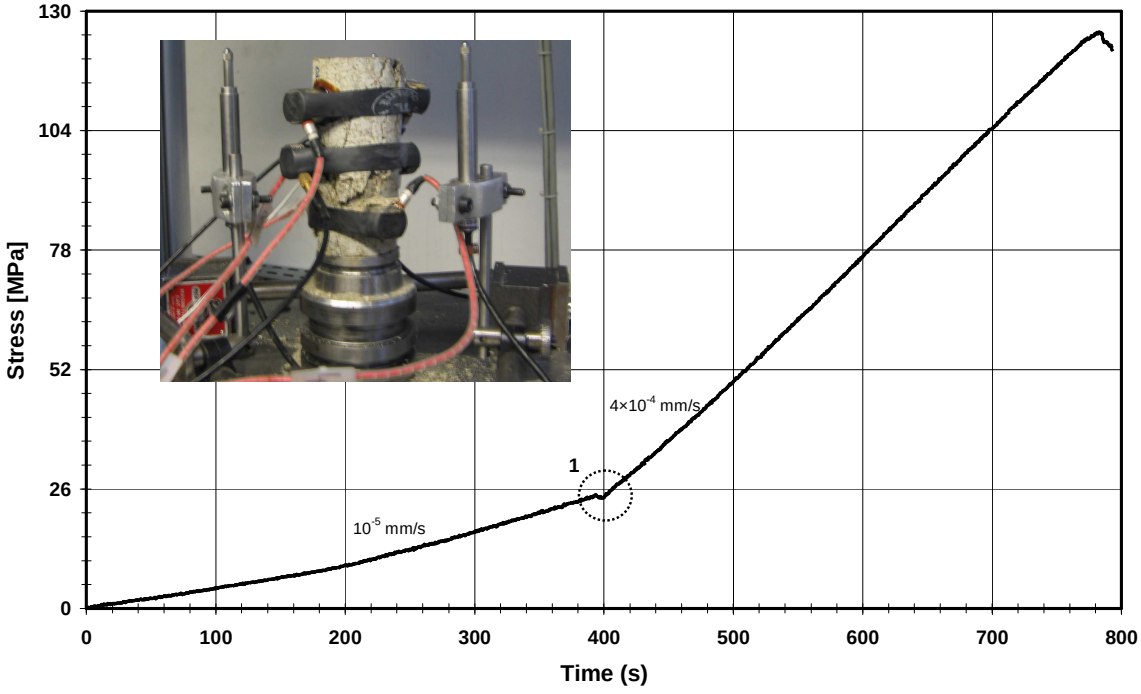

4.14: Stress versus deformations (above) and stress versus time (below) curves of granite specimen Gr7 during uniaxial compression test. At the point 1 the rate of loading was increased.

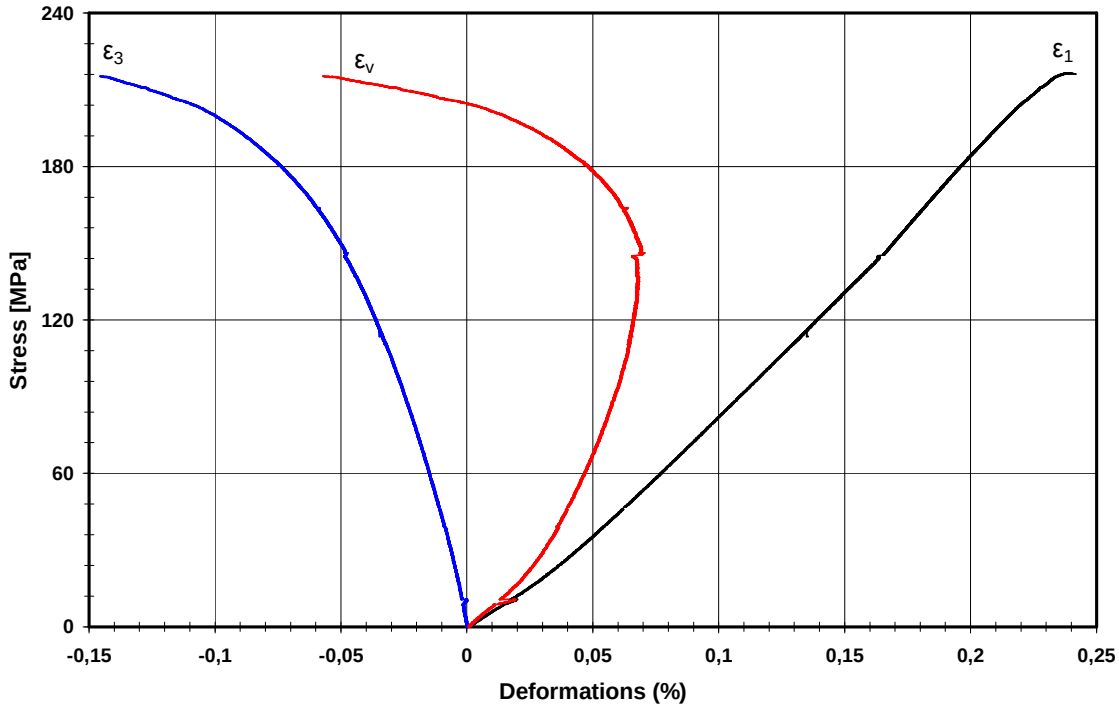

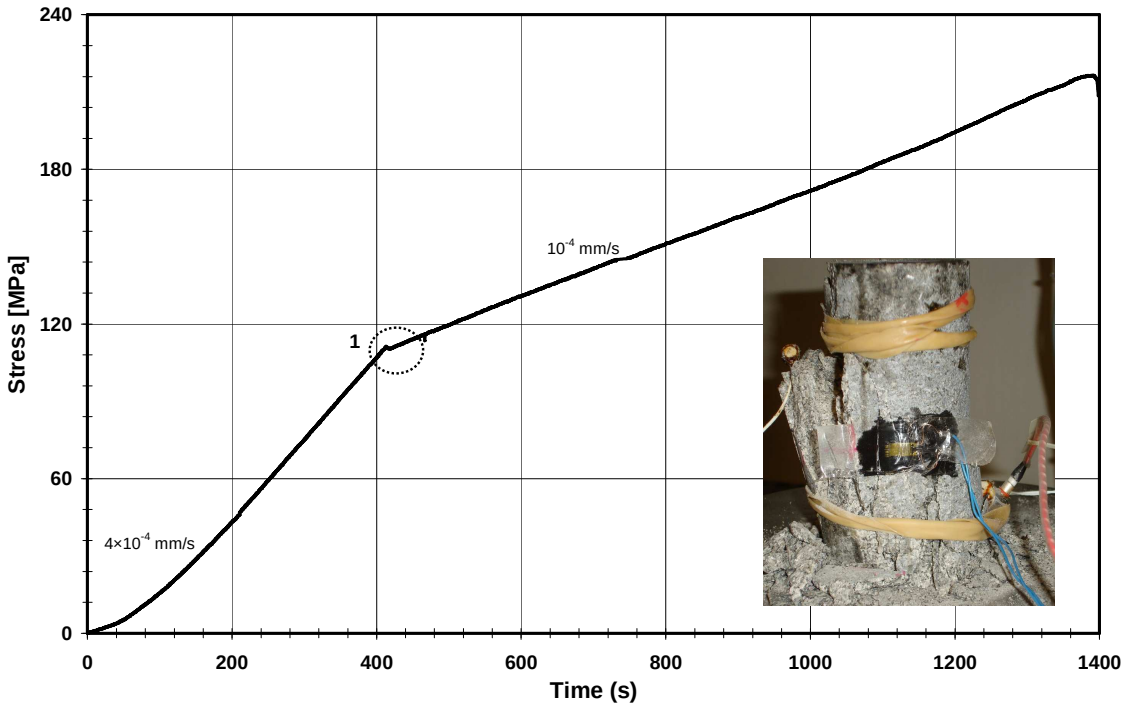

4.15: Stress versus deformations (above) and stress versus time (below) curves of gabbro specimen Ga3 duringuniaxial compression test. At the point 1 the rate of loading was divided in two to avoid damage to the press machine.

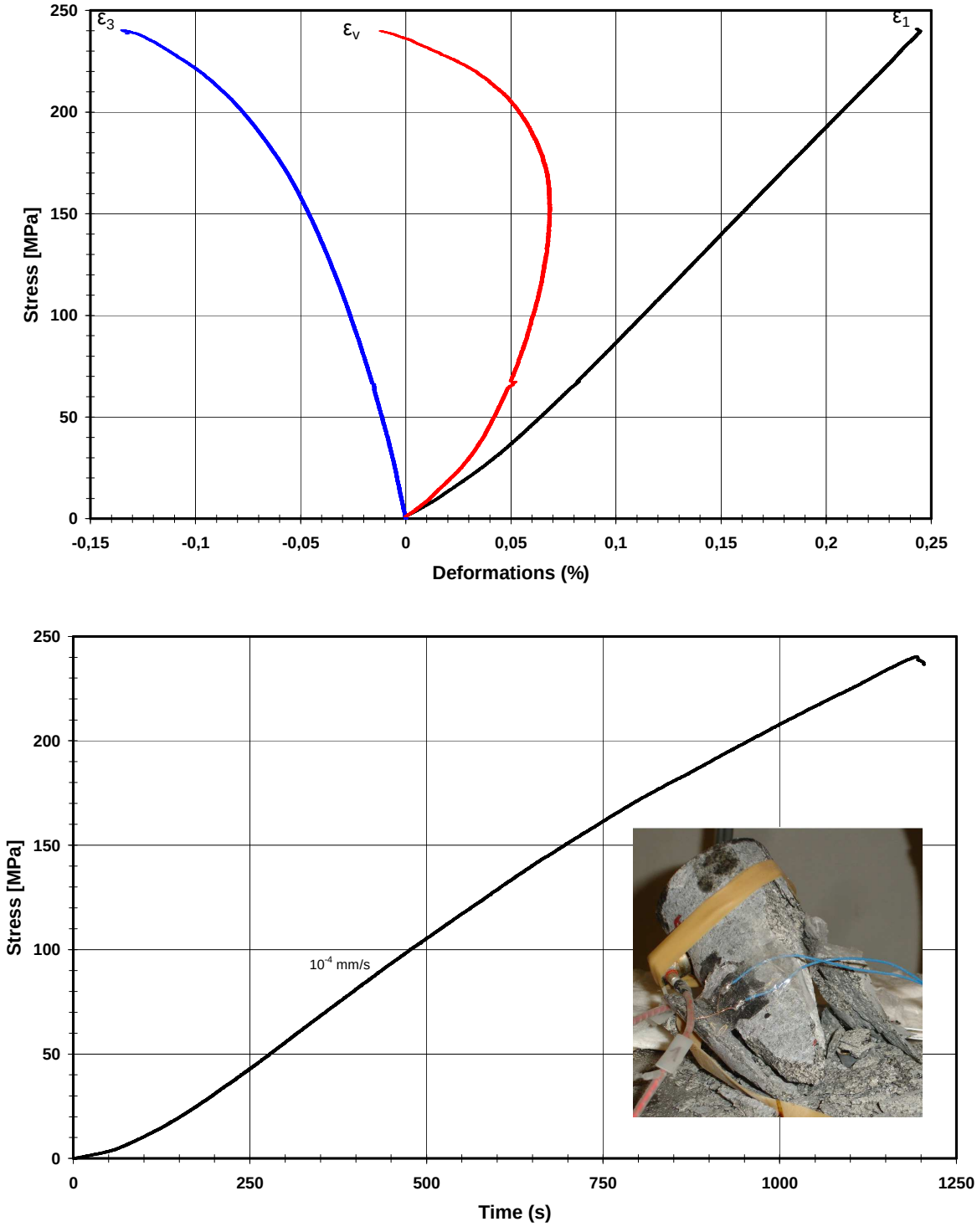

4.16: Stress versus deformations (above) and stress versus time (below) curves of gabbro specimen Ga4 during uniaxial compression test.

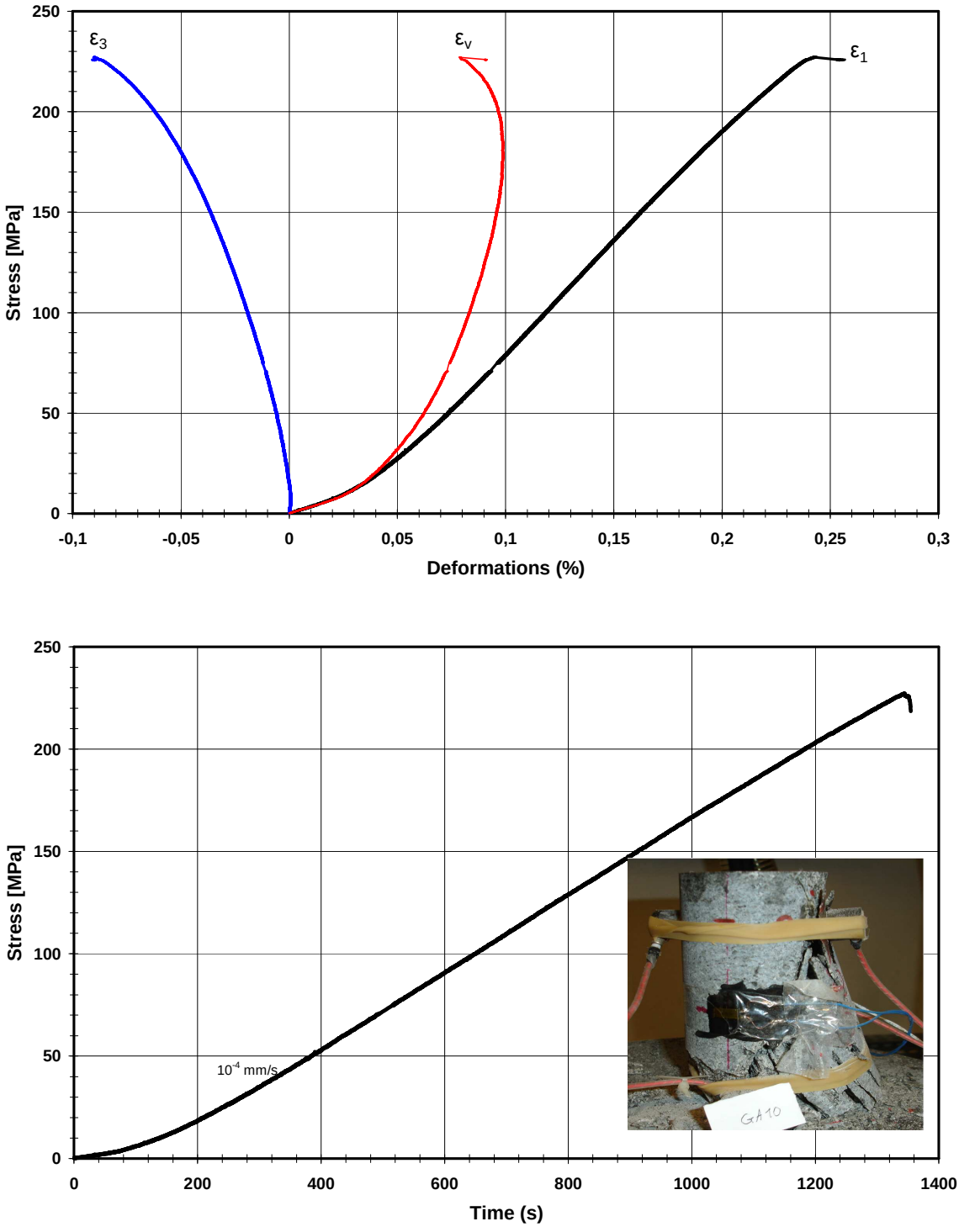

4.17: Stress versus deformations (above) and stress versus time (below) curves of gabbro specimen Ga10 during uniaxial compression test.

4.5.2. Brazilian Test

The indirect tension test, also called the Brazilian test, is a common method of assessing tensile strength. The Brazilian tension test, also known as the splitting test, is widely used to evaluate the tensile strength of rocks since it is easy to prepare and test specimens. Tensile strength data are sometimes useful, and very occasionally are justified for an engineering project. The compression-induced extensional fracturing generated in this test is also more representative of the in situ loading and failure of rocks.

In the Brazilian tension test, a circular disk of rock is placed between two platens and loaded in compression producing a nearly uniform tensile stress distribution normal to the loaded (vertical) diametric plane, leading to the failure of the disk by splitting (Rocco et al., 1999). Figure 4.18 shows a schematic diagram of the test and failure pattern.

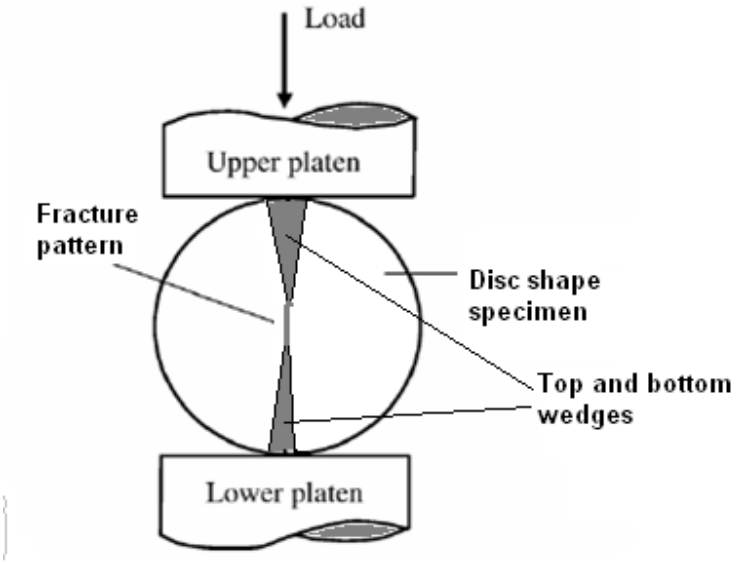

Figure 4.18: Schematic diagram of the indirect tension test assembly and failure pattern

This tensile stress σ_{t-v} is estimated from the elastic theory (Frocht, 1948):

$$\sigma_{t-v} = \frac{2P}{\pi LD} \tag{4.3}$$

where P is the load, and L and D are the length and diameter of the disk. Along the horizontal diametral plane, tensile stress (and equivalent strain) values rapidly decrease from a peak level (Eq. 4.3) as a function of distance x from the centre of the disk:

$$\sigma_{t-h} = \frac{2P}{\pi LD}\left[\frac{D^2 - 4x^2}{D^2 + 4x^2}\right]^2 \tag{4.4}$$

Equation 4.2 implies that measurement of the near maximum value of the tensile strain along the horizontal diameter is possible with large diameter specimens and/or short strain gages (Aydin and Basu, 2006).

Cylindrical specimens with a diameter (D) approximately equal to 40 and 70 mm and thickness (L) approximately equal to the radius were prepared. The cylindrical surfaces were cleared of obvious tool marks and any irregularities across the thickness. The end faces were flattened to within 0.25 mm and parallel to within 0.25°. Loading was applied continuously at a constant rate so that failure occurred within 150-180 seconds.

This investigation involved testing 11 gabbro disc-shaped specimens of two different diameter sizes (40 and 70 mm). The specimens were cored from the same block that the specimens for uniaxial and triaxial tests were prepared from previously. The diameters and the length-diameter ratios (L/D) of the specimens were within ISRM (1978) and ASTM D3967–95a specifications.

The Schenck press was used to apply the load. An internal gauge and LVDT were used to measure the vertical displacement. For all tests, the strain rate was maintained at 10^{-5}/s for 200 seconds.

The results of the Brazilian tests are presented in table 4.4. Figure 4.19 also shows the stress– deformation and stress-time graphs for the tested specimens. It should be noted that the diameters of specimens Gab1 to Gab7 and Gab8 to Gab11 were 70 and 40mm, respectively.

Table 4.4: Brazilian test results

No. Specimen	Length (mm)	Length/Diameter*	Tensile strength [MPa]
Gab1	**35**	**0.50**	**10.3**
Gab2	**32**	**0.46**	**11.3**
Gab3	**31**	**0.44**	**11.6**
Gab4	**33**	**0.47**	**12.1**
Gab5	**34**	**0.49**	**11.6**
Gab6	**36**	**0.51**	**10.9**
Gab7	**22**	**0.55**	**12.1**
Gab8	**20**	**0.50**	**10.6**
Gab9	**21**	**0.52**	**10.2**
Gab10	**19**	**0.48**	**13.5**
Gab11	**22**	**0.55**	**12.1**
Mean/Standard deviation			**11.5/0.95**

* The diameters of specimens of Gab1 to Gab6 were 70 mm and Gab7 to Gab11 had 40 mm diameters.

Review of the fracture patterns showed two visible wedges at the top and bottom of the disc-shaped specimens (figure 4.20). The wedges were more visible in the specimens with the larger diameter (70 mm); it seems that the larger contact surface area plays a key role in this phenomenon. In other words, when the contact area between the specimen and the loading plate is too small, the contact areas are almost a liner; the fracture shape is planar in the mid part of the disc. With a large contact surface, however, the contact area makes a pseudo uniaxial loading system at the top and bottom of the specimen and the disc fails by the formation of two wedges at the two opposite sides of the disc.

The AE events were recorded continuously for all the Brazilian tests and the results will be discussed in the next chapter, with a consideration of the AE parameters and an interpretation of the failure mechanism.

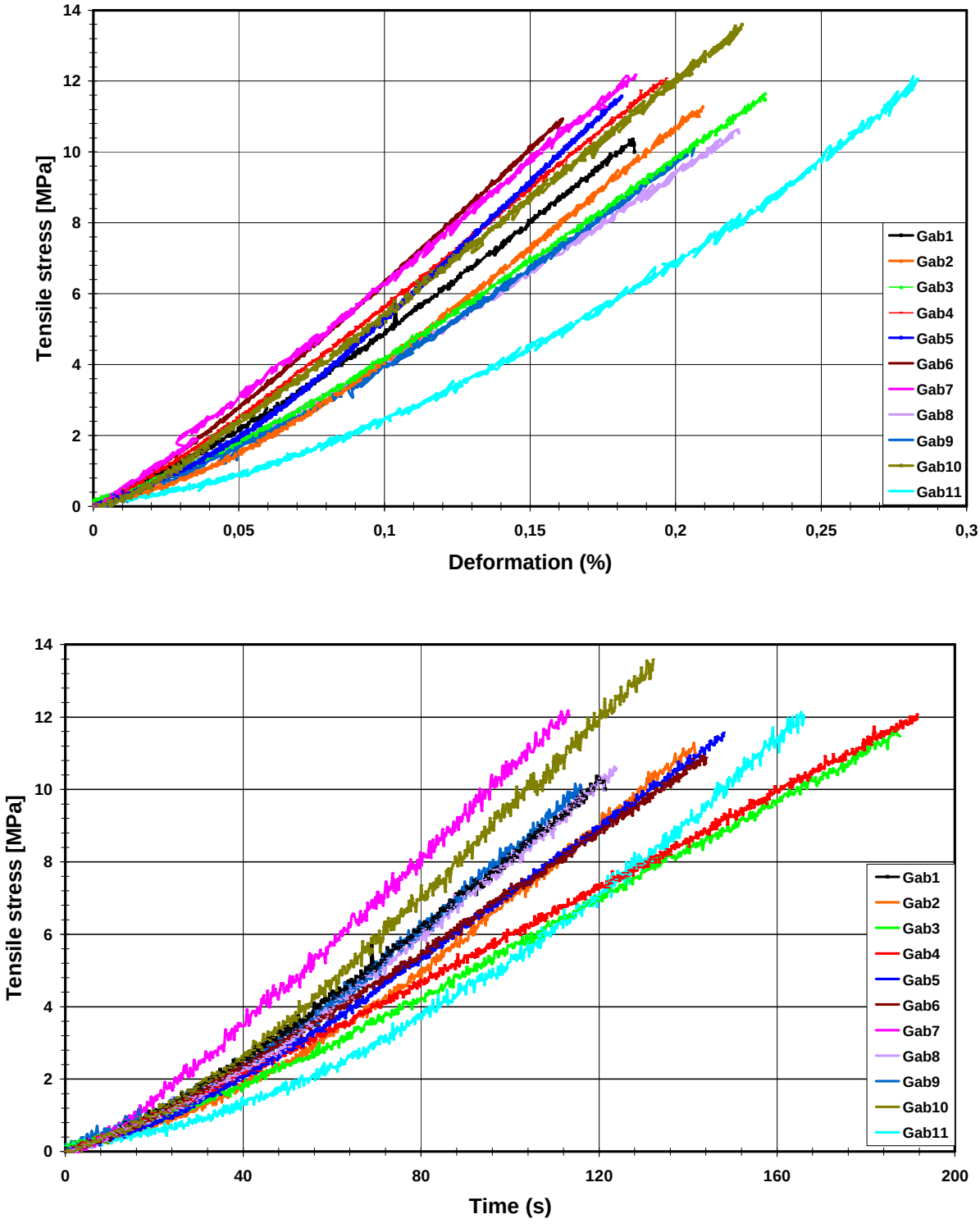

4.19: Stress versus deformation (above) and stress versus time (down) curves of specimens Gab1 to Gab11 under Brazilian test. The diameters of specimens Gab1 to Gab6 and Gab7 to Gab11 were 70 and 40mm respectively.

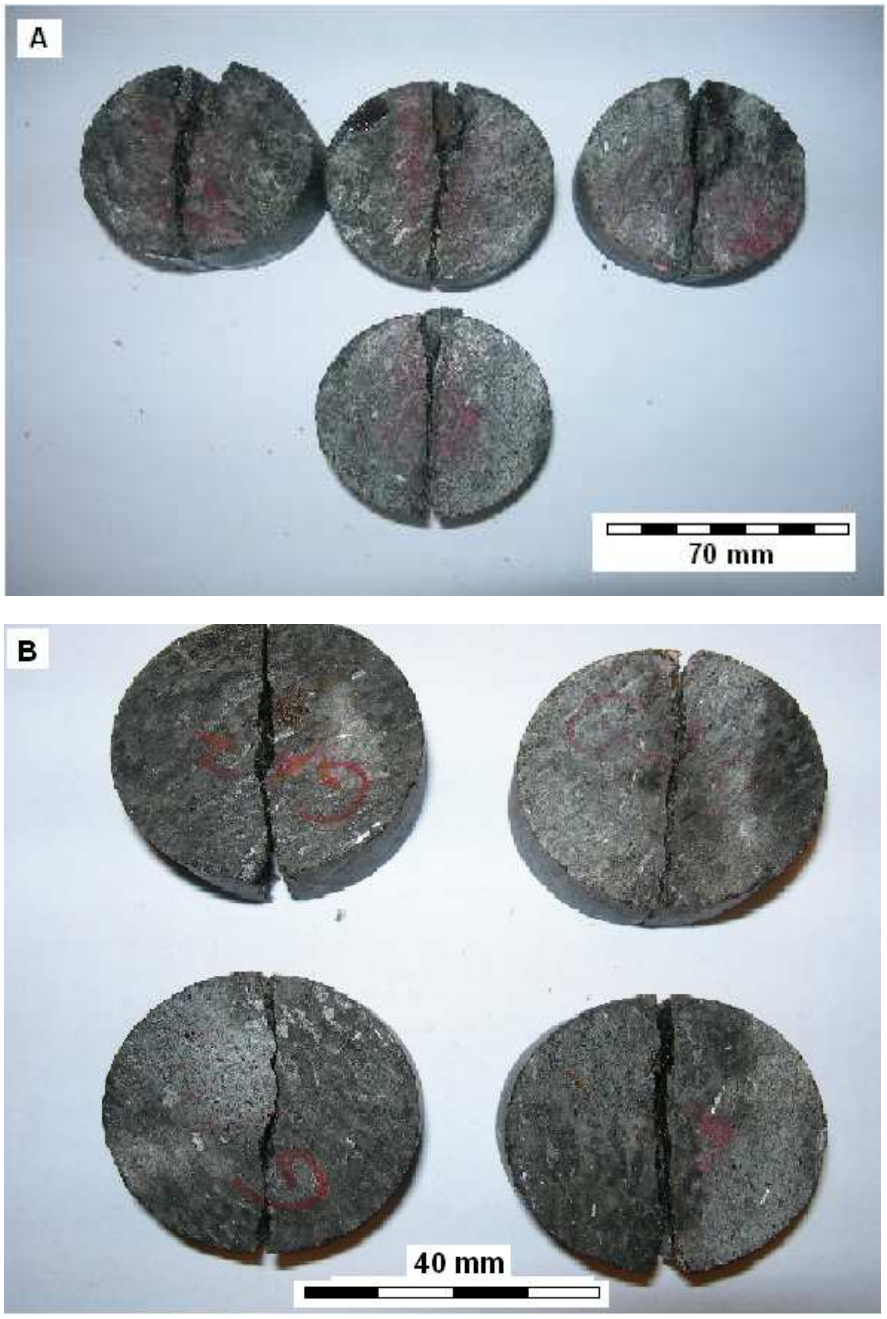

Figure 4.20: Failure shapes of two sizes of gabbro specimens after Brazilian test. While wedges developed in the large size samples at the top and the bottom of plates (A), linear patterns were observed in the smaller size samples (B).

4.5.3. Ultra high pressure triaxial tests

Triaxial tests have been used for many years by researchers and practitioners alike, to gain an understanding of rock behaviour under a three-dimensional state of stress and to verify, and even validate, mathematical expressions that have been derived to represent rock behaviour in analytical and numerical models (after Elliot, G. M. in Hudson, 1993). Recently, increased attention has been drawn to using the triaxial test to investigate creep behaviour, the influence of heat on rock strength, and the strength and deformation behaviour of rock around deep drill holes as well as the earth's fault zones. These studies have further increased our understanding of the physical mechanisms that control rock strength, and have improved our understanding of the constitutive behaviour of rock. In addition, these studies have required variations from the conventional test configuration and procedures, and have consequently presented special practical problems. The guidelines for carrying out triaxial tests and interpreting the results are discussed in ISRM (1978).

In order to evaluate the mechanical parameters as well as studying the resulting damage, a few triaxial tests were carried out in this research. The aim of these tests was to characterize the behaviour of gabbro under ultra high triaxial loads. Since the study of damage evolution using acoustic emission monitoring was one of the aims of this research, a Giga press with high capacity of loading was used to apply the axial and confinement loads. The Hoek-Brown criterion and the Mohr-Coulomb envelope were evaluated. These tests also make it possible to highlight the irreversible nature of the damage due to high confining pressures and the stress path of the gabbro.

4.5.3.1. Presentation of Giga press

High confining pressure tests were carried out using the Giga press. Figure 4.18 shows a general view of the press and a cross-section of the confinement cell in which the specimen is placed. This press was designed by the THIOT-ENGINEERING Company to test concretes under ultra high pressures. The machine can perform tests up to 0.85GPa confining stress and about 2.4 GPa axial stress on cylindrical specimens with 140 mm height and 70 mm diameter.

The specimens of rock are placed inside the confining cell as shown in figure 4.21. The fluid used to apply the confining pressure, di-2-ethylhexyl azelate (DOZ), is injected into the cell through the upper plug. The fluid is pressurized, up to a maximum of 850 MPa, by means of a multiplying jack from an initial pressure of 25 MPa. The axial force is generated by a jack of 13 MN capacity, which is located under the cell, and is transmitted to the specimen by a piston that passes through the lower plug of the cell. The details of the pressure and deformation system, as well as the data acquisition machine, are presented by Gabet (2006).

4.5.3.2. Preparation of specimens and measurement of deformations

Like uniaxial tests, the circular cylindrical specimens with a height to diameter ratio of 2 were prepared by cutting and grinding. Two tests were performed to assess the triaxial behaviour of gabbro rock and to obtain a stress-damaged specimen for AE studies. For these purposes, cylindrical specimens were prepared with a 70 mm diameter and 140 mm length (a ratio of L/D = 2). The specimen, surrounded by a membrane impermeable to the confinement fluid, was positioned between 2 loading heads made of tungsten carbide. It was placed inside the cell by a mobile device that allowed the specimen to be centered and to fix the axial displacement sensor (LVDT). The pressure sensor was situated in the entry port of cell. The specimen was also instrumented with axial and lateral strain gauges. These strain gauges allow the measurement of local strains. The positions of the gauges and LVDT on the sample are shown in figure 4.22. Other sensors, such as the pressure sensor, were situated at the exit of the multiplier jack.

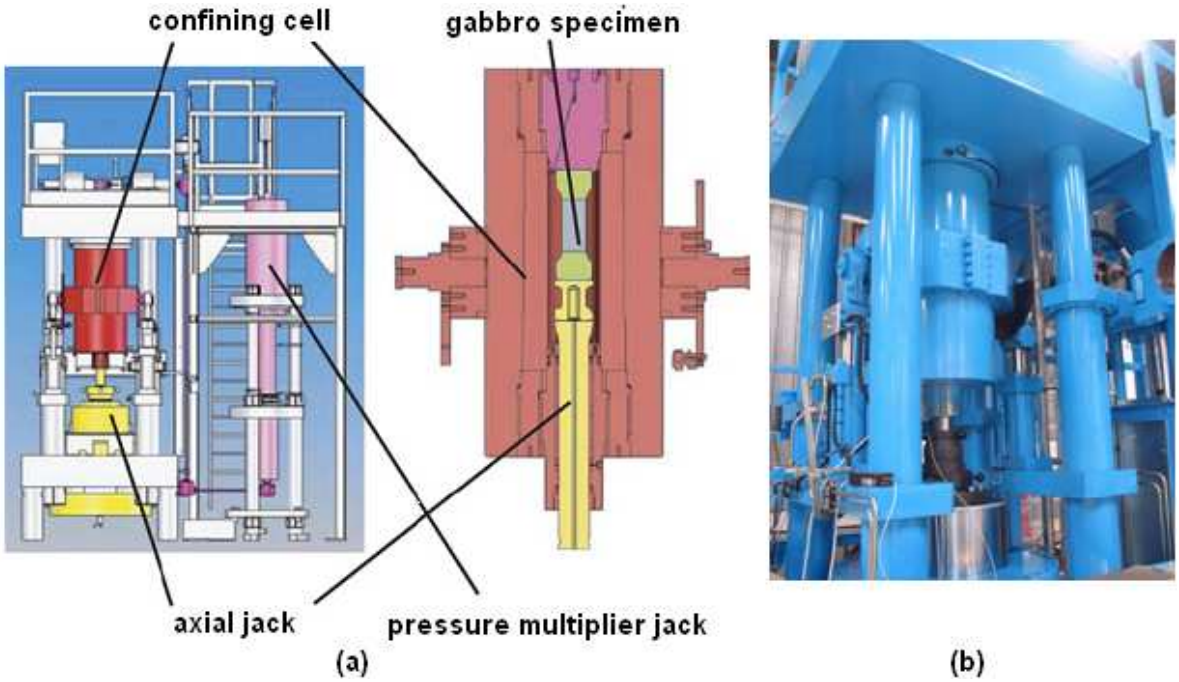

Figure 4.21: Schematic sketch of main components of the Giga press and confinement cell (a) and a photo of the cell of the press (b) (Gabet et al, 2006 with modification)

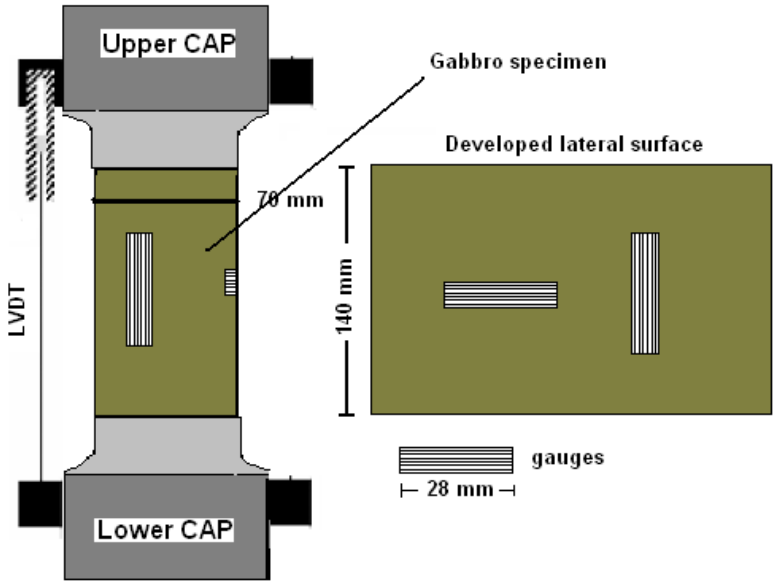

Figure 4.22: Scheme of strain measurement devices; gauges and LVDT

Since gabbro is a hard rock and the tests performed involved ultra high pressure, a special setup was needed to protect the gauges and wires from probable damage. In brief, the following steps were carried in preparing the specimens for triaxial tests in the Giga press:

- Prepare a smooth surface by grinding with medium-coarse emery cloth,
- Draw the lines of collage on the surface of specimens,
- Apply the gauges using super glue,
- Weld the wires to the gauge sides,
- Cover the gauges by hard plastic shields to protection them from damage,
- welding a small plaque to wires,
- Wrap the sample in impermeable membranes and pass the electrical wires through the membranes.

Figure 4.23 shows a prepared specimen with membranes and gauges wires.

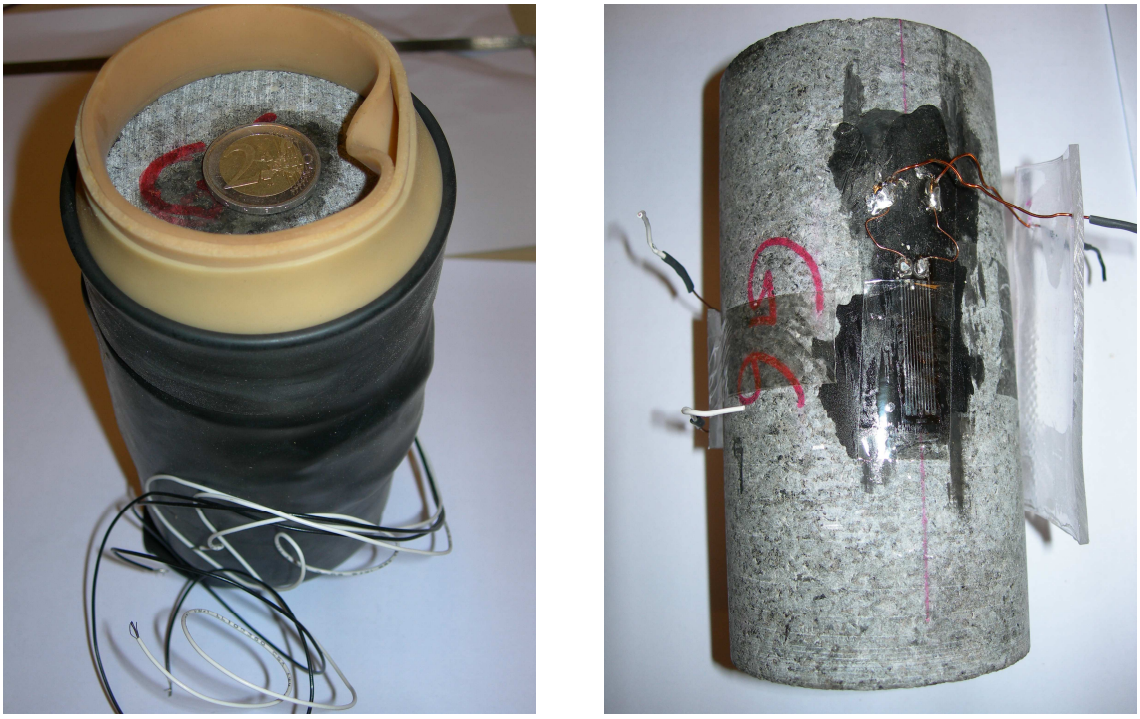

Figure 4.23: The prepared specimen with 4 different membranes (left) and electrical resistance gauges and the protections (right)

4.5.3.3. Triaxial behaviour of gabbro

Two triaxial tests were conducted at confining pressures of 200 and 650 MPa. The prepared specimen was placed in a triaxial cell (figure 4.21) and a desired confining stress was applied and maintained by a hydraulic pump. The specimen was then further compressed under a stiff compression machine with a spherical seating. The phase discharge was symmetrical about the phase of charge. The axial stress was applied with a constant stress rate and the load was measured by a load transducer. Triaxial compressive strength, Young's modulus (at 50% of failure stress) and Poisson's ratio (at 50% of failure stress) was calculated from the axial failure load and stress and strain relationship.

Triaxial compressive strength, σ_1, was calculated as the axial failure load divided by the initial cross sectional area of the specimen. Axial tangential Young's modulus at 50% of triaxial compressive strength, Et50%, was calculated as the slope of the tangent line of the axial stress - axial strain curve at a stress level equal to 50% of the ultimate uniaxial strength. Poisson's ratio, at 50% of triaxial compressive strength, was calculated using the same method as for the uniaxial test.

➢ Triaxial test with 650 MPa confining stress

To evaluate gabbro behaviour under ultra high stresses, a triaxial test was performed on specimen Ga1 (650) using the maximum capacity of the Giga press. For this purpose, the confining pressure was applied at a rate of 100 MPa per minute. The confining stress increased up to 650 MPa and then axial loading was applied up to the maximum capacity of the Giga press (2350 MPa). Figure 4.24 shows the confining, axial, mean and deviatoric stresses versus time. Figure 4.25 shows also the axial stress versus corresponding axial (ε_x), lateral deformations (ε_θ) and volumetric changes during loading and unloading paths. Volumetric change was calculated by the $\varepsilon_v = \varepsilon_1 + 2\varepsilon_3$ formula.

In spite of using almost the maximum capacity of the Giga press, at the end of test there was no apparent damage to the specimen. However, a small amount of residual strain (0.07%) could be seen in the stress–strain curve. To evaluate the possible damage, elastic wave velocities of the specimen were measured before and after the triaxial test. The results of these measurements, as well as the results of mechanical tests and AE monitoring on this specimen, will be presented in chapter 6.

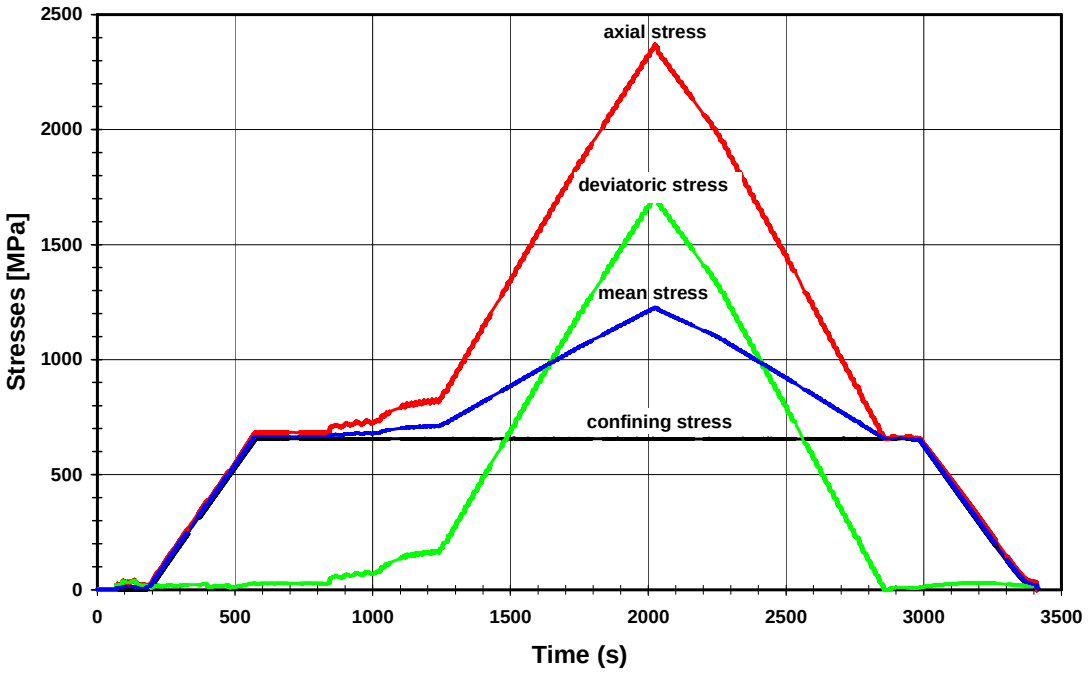

Figure 4.24: Stresses versus time of specimen Ga1 (650) during ultra high triaxial test

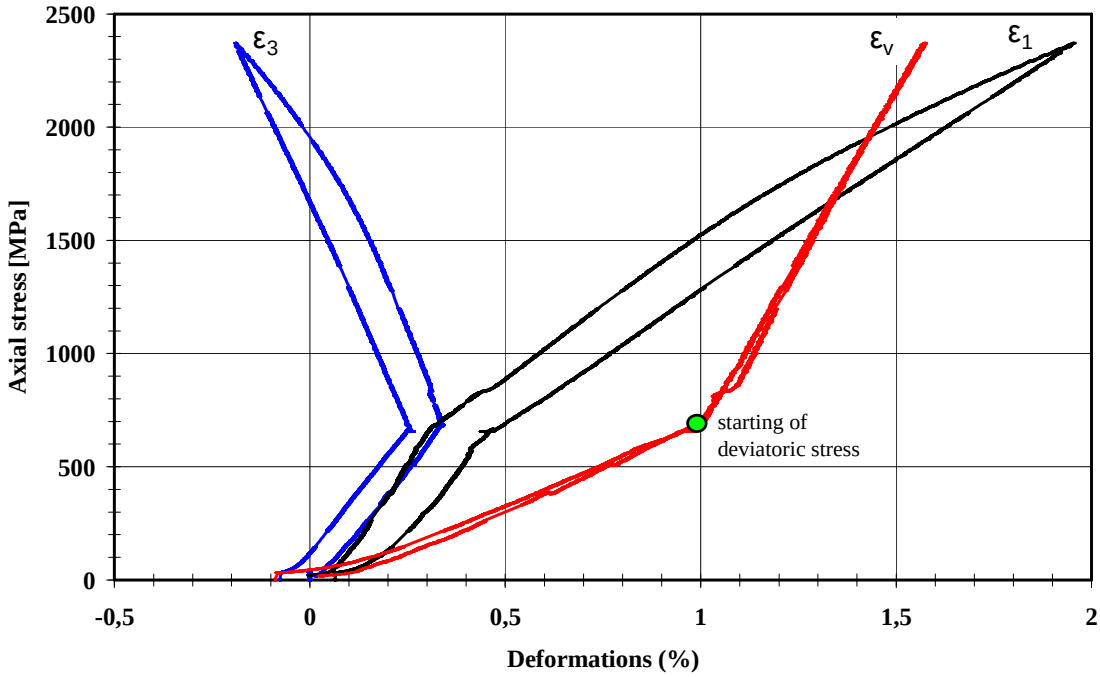

Figure 4.25: Axial stress versus axial, lateral and volumetric deformations of specimen Ga1 (650) during ultra high triaxial test

➢ Triaxial test with 200 MPa confining stress

Since the gabbro specimen did not fail under 650 MPa confining stress, we carried out another test with 200 MPa confining stress. The preparation of the specimen was the same as presented in section 4.5.3.2. Confining stress was applied at 100MPa per minute then axial loading was carried out at the same loading rate up to failure. Axial and lateral deformations were continuously measured by resistance electrical gauges and the LVDT. In this case the specimen failed at a maximum axial loading of approximately 1480 MPa. The failed specimen shows a planar surface of failure with 65° of horizon (figure 4.26). Due to the high applied stresses, considerable fine cataclastic breccias could be seen between the two parts of the specimen. Figure 4.26 shows the stresses vs time curves of the specimen Ga2 (200). Figure 4.27 also shows the curve of axial stress vs deformations. The results of these two tests have been used to calibrate the Hoek-Brown and Mohr-Coulomb criteria.

Figure 4.26: Specimen Ga2 (200) after ultra high triaxial test. The sharp, planar failure surface is obvious in this photo.

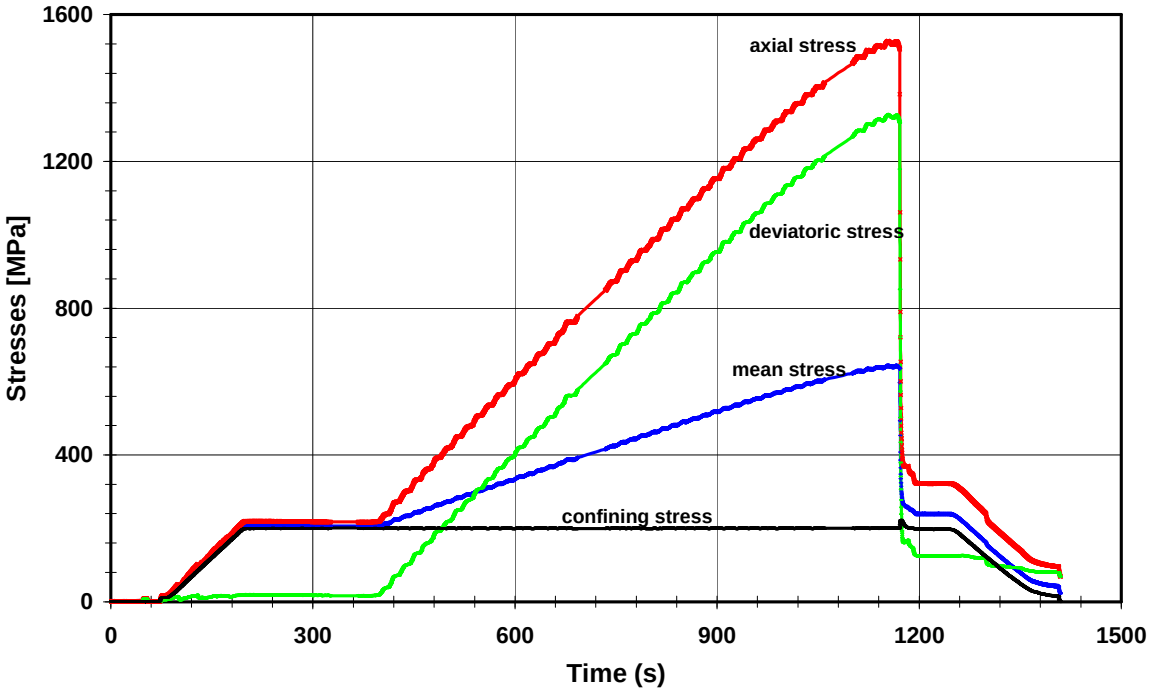

Figure 4.27: Stresses versus time of gabbro specimen Ga2 (200) under triaxial test

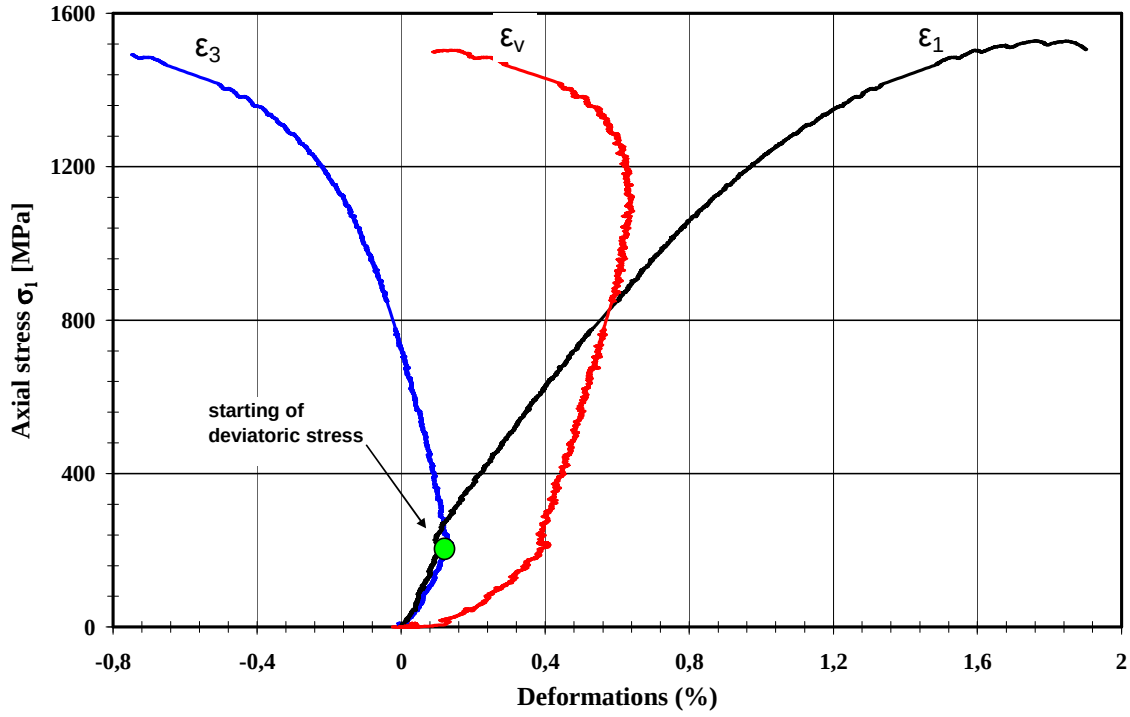

Figure 4.28: Axial, lateral and volumetric deformations versus axial stress, specimen Ga2 (200)

4.5.3.4 Comparison of the two triaxial tests

The figures 4.24 to 4.28 show the results of stress-deformation curves and volumetric changes of specimens Ga1 (650) and Ga2 (200). The figures also show the hydrostatic loading and deviator stress stages. The maximum capacity of the Giga machine was used to evaluate gabbro under ultra high stresses. Specimen Ga1 (650) was loaded to 650MPa confining pressure and then loaded axially up to 2300MPa. Unloading followed the same scheme. We found that the ultimate strength of this rock was higher than the maximum capacity of the machine under 650MPa confining pressure. Therefore, to estimate the needed parameters, another test was conducted with a confining stress of 200MPa.

The stress-deformation curves that were recorded by LVDT and electrical gauges showed good agreement for both Ga1 (650) and Ga2 (200) specimens. The volumetric behaviors of the two specimens were comparable in the hydrostatic phase. In spite of more than 1.4 percent volume decrease of specimen Ga1 (650) in loading, the residual strain after unloading was less than 0.2 percent. It seems that the specimen was still in the elastic phase and was not significantly damaged. The result of a uniaxial compression test, elastic wave velocity measurements and thin section studies on this mechanically-damaged specimen will be presented in the next chapter.

For specimen Ga2 (200), we used a confining stress of 200 MPa. The specimen failed abruptly at an axial stress of 1430 MPa. Based on axial gauge data, up to 1000 MPa of axial loading, both the axial and lateral records are linear. Changes were observed for larger loads. The maximum axial and lateral deformations at the failure point, according to electric resistance gauge signals, were about 1.7 and 0.75 percent, respectively. The volume of the specimen decreases as long as the mean stress is lower than 500 MP, and then the contraction phase is followed by dilatation.

4.5.3.5 Calibration of failure criteria parameters

Hoek and Brown (1980a and 1980b) introduced a failure criterion in an attempt to provide input data for the analyses required to design underground excavations in hard rock. The criterion was derived from the results of research at brittle failure of intact rock by Hoek (1968) and on model studies of jointed rock mass behaviour by Brown (1970). The criterion

started from the properties of the intact rock and then introduced factors to reduce these properties on the basis of the characteristics of joints in a rock mass. The original Hoek-Brown criterion is defined by the equation:

$$\sigma_1 = \sigma_3 + \sigma_{ci}\left(m\frac{\sigma_1}{\sigma_{ci}} + s\right)^{0.5} \quad (4.5)$$

- where σ_1 and σ_3 are the major and minor effective principal stresses at failure,
- σ_{ci} is the uniaxial compressive strength of the intact rock material and;
- *m* and s are material constants, where s = 1 for intact rock.

To plot the Mohr's stress circle, one need to perform a group of triaxial compression tests at different confining stress levels. Since this type of study is not the main concern of our research, RocLab software was used to obtain the Mohr's stress circle. RocLab is a software program for determining rock mass strength parameters, based on the generalized Hoek-Brown failure criterion. The software is a product of Rocscience Inc. and it gives relatively appropriate results. Failure envelopes (Mohr-Coulomb or Hoek and Brown) and parameters of specified failure criterion were determined using this software.

Each of the parameters used as input for the Hoek-Brown criterion – σ_{ci} and *m* - can be estimated using convenient charts and tables presented in this software. These charts and tables are accessed by selecting the "Pick" button located beside each of the input parameter edit boxes in the sidebar. The steps of evaluation of Hoek-Brown criteria and drawing of Mohr-Coulomb circle by this software are presented below:

The dialog box for estimation of *m* and other parameters are shown below in figure 4.29 and figure 4.30. After all required parameters are input, the Hoek-Brown parameters are calculated by the software and a graph is drawn. The results are presented in figure 4.31. The graph is drawn based on the parameters that were obtained through the Brazilian and simple uniaxial tests (table 4.5).

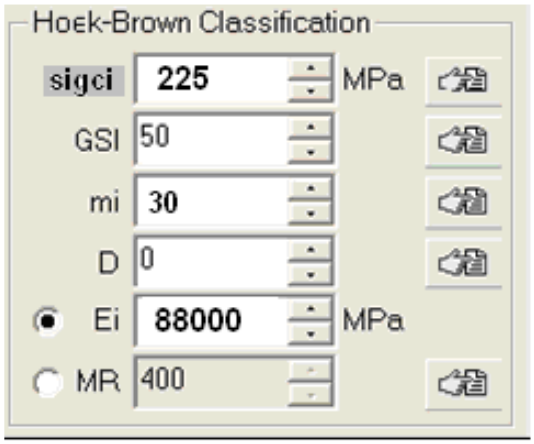

Figure 4.29: A table for choosing input parameters for plotting Hoek-Brown criteria using RocLab software

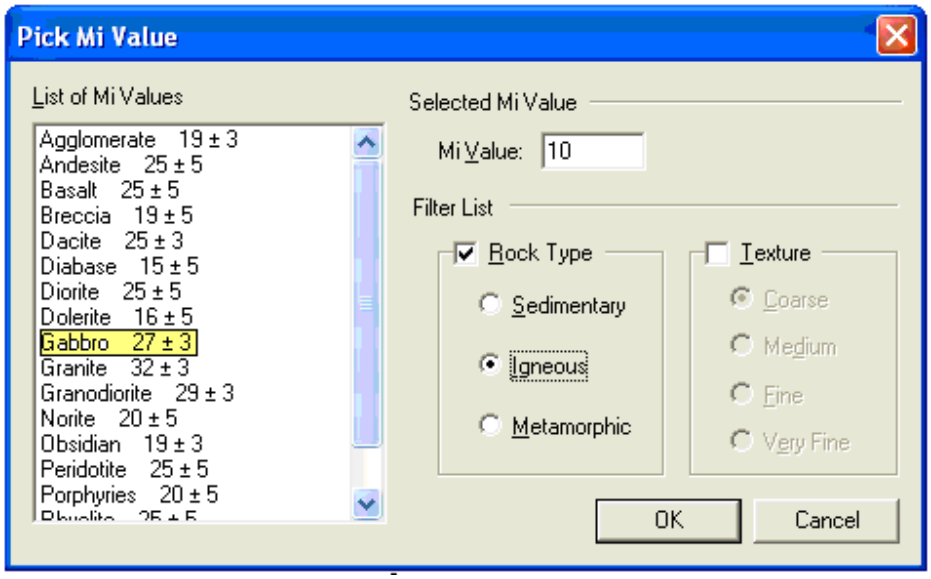

Figure 4.30: Different rock mi values based on Hoek-Brown characterization

Based on the uniaxial test, we also calculated the Young's modulus, the maximum strength and the Poisson's ratio at about 88 GPa, 225 MPa and 0.2 respectively.

Table 4.5: Mechanical parameters of gabbro rock obtained by simple uniaxial compression tests

Elasticity Modulus [MPa]	Max. Uniaxial Strength [MPa]	Max. Tensile Strength [MPa]
100	230	12

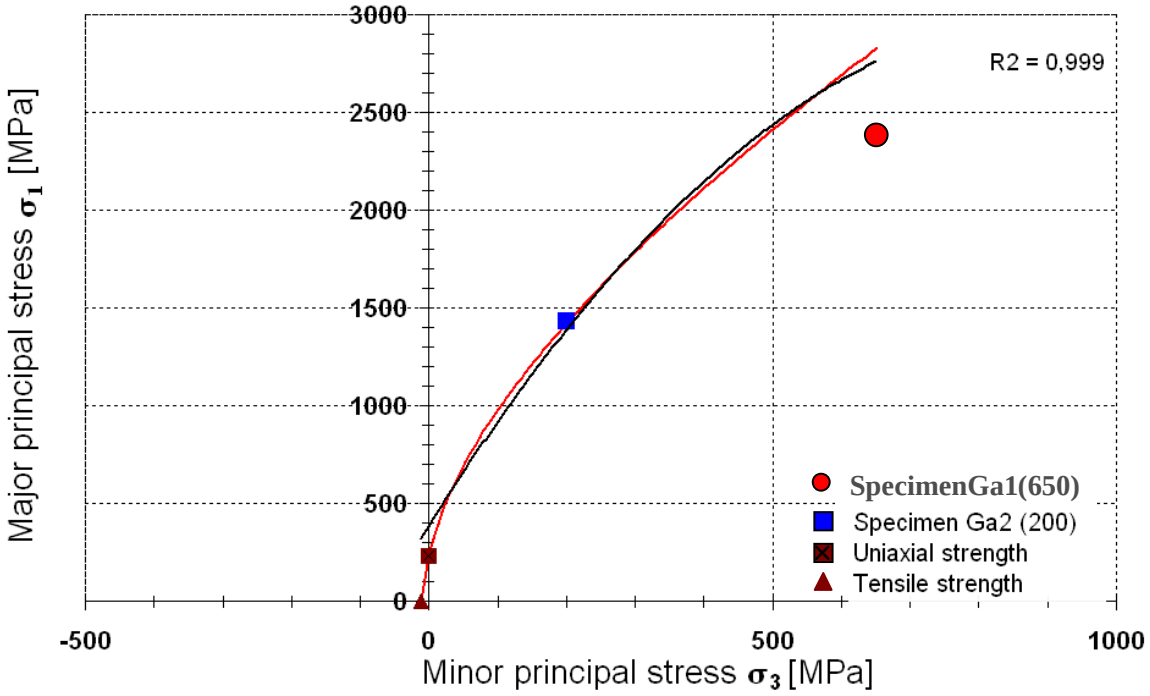

Figure 4.31: Principal stress and Hoek and Brown failure criterion for African Gabbro based on triaxial tests. The results of two triaxial tests -Ga1 (650) and Ga2 (200) - are shown on the graph.

Equivalent Mohr-Coulomb Parameters

In addition to the Hoek-Brown failure criterion parameters, RocLab calculates the equivalent Mohr-Coulomb parameters (cohesion and angle of friction). Since most rock engineering software is still written in terms of the Mohr-Coulomb failure criterion, the calculation of equivalent Mohr-Coulomb parameters from the Hoek-Brown failure criterion is an important feature of this program.

Failure Envelope Range

It is important to note that the Failure Envelope Range option has a direct effect on the calculated Mohr-Coulomb parameters. For details about the Mohr-Coulomb fitting procedure, and the significance of the Failure Envelope Range option, see Hoek and Brow (1980a). For drawing the failure envelope range using of this program, a few points are worth mentioning:

1. When the Failure Envelope Range option = General, note that $\sigma_{3max} = \sigma_{ci}$: This is based on the empirical observation that the stress range associated with brittle failure occurs when σ_3 is less than about one-quarter of σ_{ci}.

2. When the Failure Envelope Range option = Custom, any value of sigma3max can be entered. The Failure Envelope Range has no effect on the calculated Hoek-Brown parameters.

The corresponding Mohr-Coulomb envelope can be viewed by selecting the Mohr-Coulomb Envelope option from the toolbar or the Analysis menu. Figure 4.32 shows the Mohr-Coulomb envelope for gabbro based on a triaxial test and evaluated parameters. The stress path for this rock is also presented in figure 4.33 and the calculated c and φ parameters are shown in figure 4.34.

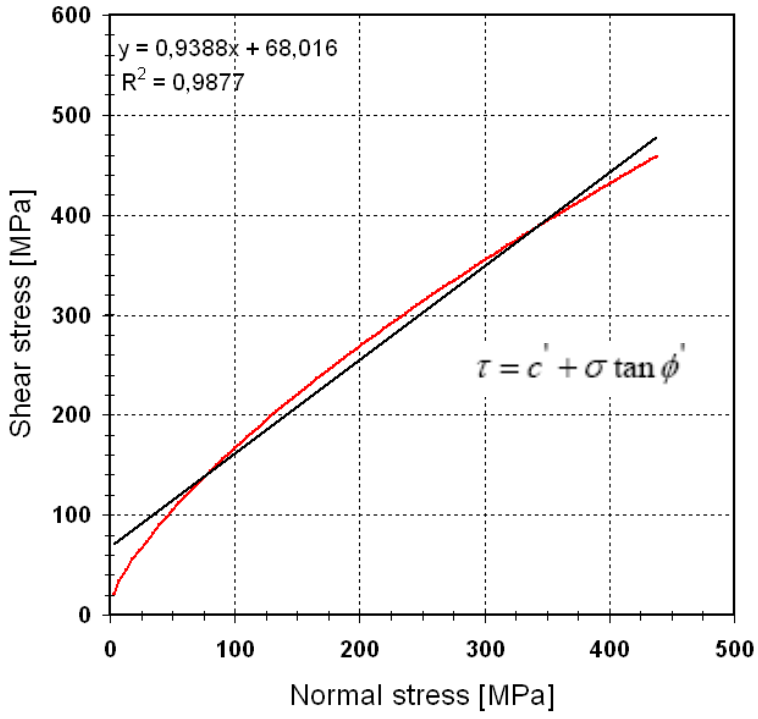

Figure 4.32: Mohr-Coulomb envelope based on the Ga2 (200) triaxial test result using RocLab

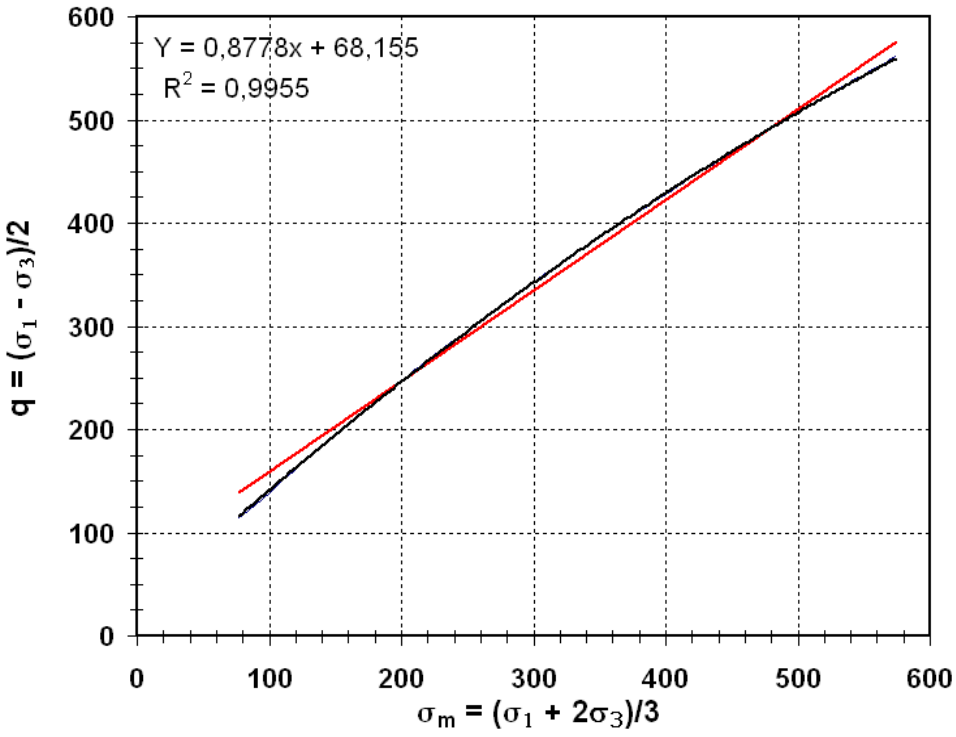

Figure 4.33: Proportional tests: loading paths in the stress space for Ga2 (200).

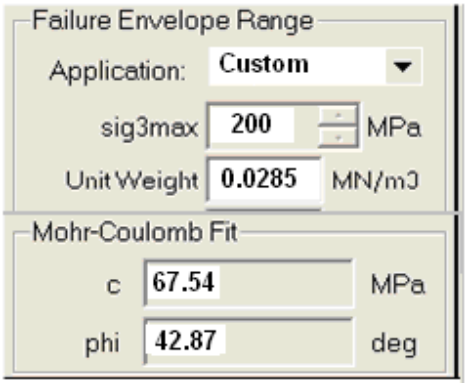

Figure 4.34: The results of failure envelope in RocLab based on Ga2 (200) specimen test

4.6 Concluding remarks

This chapter focused on presenting the results of laboratory tests that were performed on selected granite and gabbro to evaluate their physical and mechanical properties. The geological characteristics of rocks, elastic wave measurements, uniaxial and triaxial compression and Brazilian tests results, as well as the test procedures, were discussed briefly. Results of the two triaxial tests carried out using the Giga press under ultra high confining pressure were also presented in this chapter. Below are some key findings:

1. Based on microscopic study, Lavasan granite is a medium size intrusion rock with alkali rich plagioclase, quartz and mica minerals. Some of Fe- and Mg-rich minerals are slightly altered to secondary minerals like amphibole, which give a pale green colour to the rock mass. North African gabbro is a well crystallized two pyroxene (ortho and clino pyroxenes) gabbro with Ca^{2+} rich plagioclases. No evidences of alterations have been seen in microscopic investigation.

2. The primary (Vp) and the secondary (Vs) elastic wave velocities are respectively 4050 and 2537 m/s for granite rock and 6560 and 4080 m/s for gabbro rock.

3. The average uniaxial compression strengths for granite and gabbro are about 130 and 225 MPa respectively. The average elasticity modulus for granite is 30 GPa and the average Poisson's ratio is about 0.27. For gabbro, the elasticity modulus is about 90 GPa with a Poisson's ratio about 0.2. Eleven Brazilian tests were performed on two different sizes of gabbro specimens; these showed an unconfined tensile strength of about 12 MPa. The size of the specimens does not play a major role in the tensile strength.

4. Two triaxial tests were also performed under ultra high stresses using the Giga press. RocLab software was used to calculate the Hoek-Brown failure criterion and to plot the Mohr-Coulomb and stress path envelopes. The maximum axial stress of gabbro rock is about 1480 MPa under 200 MPa confining pressure. The cohesion of gabbro in this condition is 68 MPa and internal friction is about 43°.

Chapter 5

Acoustic emission monitoring and infrared radiation measurements under stress during laboratory tests

5.1 Introduction

Loading of rock samples will cause changes in the mechanical and physical behaviour that can be measured in the laboratory. Before the rock mass fractures, some measurable changes in the rock parameters, such as acoustic emissions (AE), temperature radiations and low frequency electromagnetic emissions have been reported (Ouzounov et al., 2004; Friedemann, 2002, 2003; Hardy, 2003; Wu et al., 2002; Lockner, 1991). In chapter 4 the results of conventional laboratory investigations on Lavasan granite and North African gabbro presented. In this chapter we try to discover a relationship between AE activities and the evolution of failure during the loading of a hard rock in order to establish a general approach for monitoring and predicting catastrophic failure in rock masses.

The results of acoustic emission monitoring, shear wave velocity changes and infrared measurements during loading on Lavasan granite and North African gabbro are discussed in this chapter. Firstly, the procedure to calibrate and to set-up the AE system will be presented. Then the results of the uniaxial tests on granite and on gabbro specimens using appropriate AE set-ups will be discussed, including the results of a few Brazilian tests that were conducted on gabbro specimens. For all of the tests, AE events were recorded continuously until the failure of the specimens. Four transducers were used to monitor the AE in uniaxial tests and two transducers monitored events in the Brazilian tests. Before

discussing the experimental analysis, a brief explanation of crack initiation and crack propagation of stressed rocks in laboratory studies is presented based on the available literature.

In the final part of this chapter, results of infrared radiation measurements under cyclic uniaxial loading are presented. Since the prediction of failure of stressed rocks using precursors is the main objective of the thesis and considering the importance of infrared radiation measurement in this regard, a few tests were performed using the facilities at Laboratoire Mécanique du Solide (LMS) in Palaiseau. We also compared the AE evolution with deformation data and we will discuss the advantages and the disadvantages of each method.

5.2 Determination of damage evolution in uniaxial tests

A number of techniques have been developed to detect and study crack growth in brittle materials. The most common of these involves the use of electric resistance strain gauges to measure slight changes in sample deformation that can be related to the closing and opening of cracks (Bieniawski, 1967). To a lesser extent, acoustic emission monitoring has been used to correlate the number of acoustic events to various strain gauge responses (Ohnaka and Mogi, 1982; Thiercelin, 1980; Khair 1984; Eberhadt et al., 1998). Other techniques to detect crack growth have involved the use of photoelasticity, optical diffraction patterns, scanning electron microscopes, laser speckle interferometry, ultrasonic probing, infrared and electrical resistivity.

In this research, the AE technique was used to determine crack growth and failure events during uniaxial loading. Micro deformation data was also recorded for examination and comparison of the results. The results of the uniaxials test were presented previously in chapter 4.

5.2.1 Stress–strain curve

Strain gauge measurements have provided insight into delineating the stages of crack development in rock. The general underlying idea behind these studies is that the failure process can be broken down into a number of stages based largely upon the stress-strain characteristics displayed through axial and lateral deformation measurements recorded during uniaxial and triaxial laboratory tests (Eberhardt et al., 1998). Based on the stress-

strain behaviour of a loaded material (figure 5.1), Martin (1993) defined these stages as being (1) crack closure, (2) linear elastic deformation, (3) crack initiation and stable crack growth, (4) critical energy release and unstable crack growth, and (5) failure and postpeak behaviour. Crack closure occurs during the initial stages of loading ($\sigma < \sigma_{cc}$ in Fig. 5.1, where σ is the total axial stress and σ_{cc} is the stress at crack closure) when pre-existing cracks orientated at an angle to the applied load close. During crack closure, the stress-strain response is nonlinear, exhibiting an increase in axial stiffness (i.e., deformation modulus). The extent of this nonlinear region is dependent on the initial crack density and geometrical characteristics of the crack population. Once the majority of pre-existing cracks are closed, linear elastic deformation takes place. The elastic constants (Young's modulus and Poisson's ratio) of the rock are calculated from this linear portion of the stress-strain curve. Crack initiation (σ_{ci}) represents the stress level where micro fracturing begins and is marked as the point where the lateral and volumetric strain curves depart from linearity. Crack propagation can be considered as being either stable or unstable.

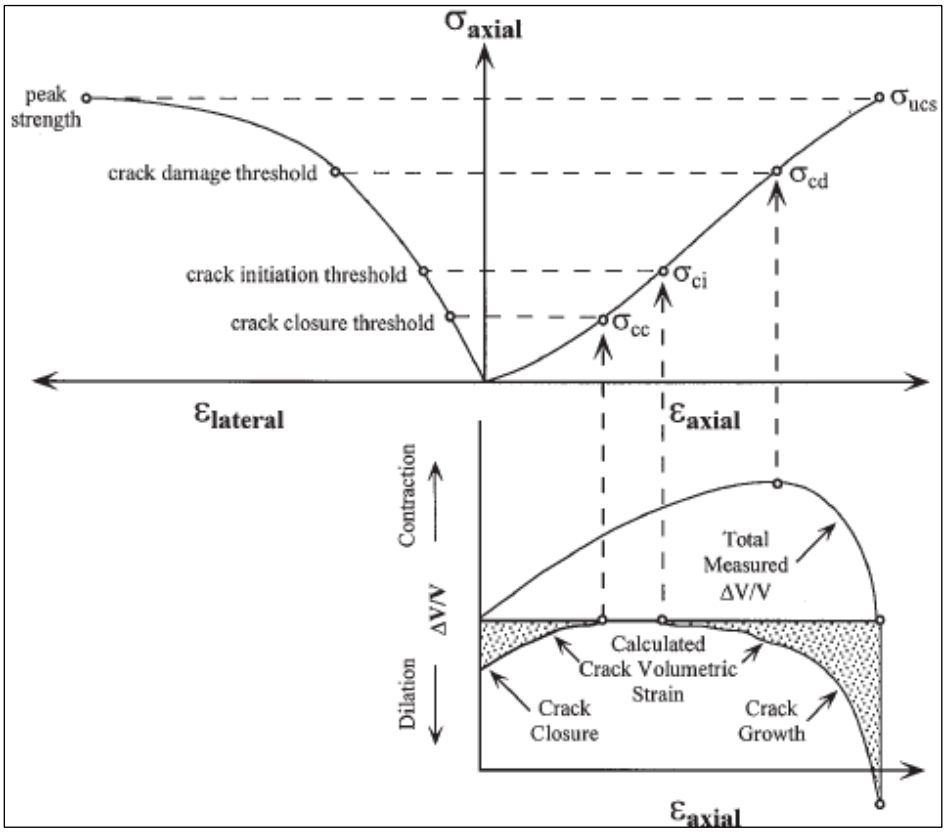

Figure 5.1: Stress-strain diagram showing the elements of crack development (Martin, 1993). Note that only the axial (ε_{axial}) and lateral ($\varepsilon_{lateral}$) strains are measured; the volumetric strain and crack volume are calculated. σ_{axial}, axial stress; σ_{ucs}, peak strength; ΔV, change in volume and V is the initial volume.

Under stable conditions, crack growth can be stopped by controlling the applied load. Unstable crack growth occurs at the point of reversal in the volumetric strain curve and is also known as the point of critical energy release or crack damage stress threshold σ_{cd} (Martin, 1993). Bieniawski (1967) defines unstable crack propagation as the condition that occurs when the relationship between the applied stress and the crack length ceases to exist and other parameters, such as the crack growth velocity, take control of the propagation process. Under such conditions, crack growth would continue even if the applied load were kept constant.

5.2.2 Acoustic emission and failure evolution

As explained in chapter two, acoustic emissions are due to the stress waves produced by the sudden internal stress redistribution of the materials caused by changes in the internal structure. There are several different sources for acoustic emission but crack initiation and crack growth are the most common causes of this phenomenon (Hardy, 2003; Thiercelin, 1980). Since most sources of AEs are damage-related, the detection and monitoring of these emissions are commonly used to predict material failure. This is an important issue in civil engineering and can provide early warnings of severe, sudden failures; AE can detect the accumulation of micro damage inside components, especially under service conditions. The monitoring of acoustic emissions produced in the failure process of rocks has been shown to be very useful in assessing the stages of failure, the locations of active deformation and the characterization of modes of rupture. This method has been successfully applied both in laboratory tests and for in-situ monitoring.

Recording the number of AE events is the most conventional method for evaluation of damage procedure in rock. In addition to recording the number of events and correlating this number to the measured deformation response in the rock, it is also possible to record certain properties of the AE waveforms (Salah, 1982). The signal waveform of an acoustic event is affected by the characteristics of the source, the path taken from the source to the sensor, the sensor characteristics, and the recording system. Generally, these waveforms are complex and using them to characterize the source can be difficult. Due to these complexities, AE waveform analysis can range from simple parameter measurements to more complex pattern recognition (Eberhardt, 1998). The characteristics of an acoustic event may also be used to approximate the release of kinetic energy through the AE event.

The true energy is directly proportional to the area under the acoustic emission waveform which in turn can be measured by digitizing and integrating the waveform signal. However, this can be both difficult and time consuming. As noted in chapter 2, the energy of an event can be approximated as the square of the peak amplitude (Lockner et al., 1991) or the square of the peak amplitude multiplied by the event duration (Hardy, 2003). The resulting values are actually more representative of the event power (the units are given in dB), but are commonly referred to as energy calculations in the literature due to their approximately linear relationship with energy. This type of energy analysis helps in highlighting AE events with abnormally large amplitudes or durations.

In this research, acoustic emissions were monitored during loading using four acoustic transducers in uniaxial compression (UC) tests and two transducers for Brazilian tests, which were attached directly to the specimens. We have used the AE event numbers and AE event energy parameters to evaluate the failure procedure in two types of igneous rocks. The AE results are compared at different stages of rock deformation that are recorded by electrical strain gauges during loading. In the following sections, details of AE monitoring in UC and Brazilian tests are discussed.

5.3 Acoustic emission monitoring

5.3.1 Apparatus and procedures for the test

The minimum AE measuring system consists of three elements: a sensor, pre-amplifier, and AE signal processor. In this study a MISTRA 2001model IPC610BP-260F-PIII866MHz system was used for data acquisition. The AE set-up also used standard pre-amplifiers, Physical Acoustic Corporation 1220A, and four transducers (Physical Acoustic Corporation, R15, diameter = 17 mm). These transducers have a poor frequency response in that they are not broad-band (main operating frequency range is between 100-600 kHz) and have significant resonance.

Acoustic emissions generated during rock deformation were detected using transducers that were mounted on the sides of the specimens. Three pilot tests were carried out for optimizing the set-up, based on rock characteristics, ambient noise and parameters of the equipment used. In this set-up, signals from the AE transducers were pre-amplified by 40dB gain passed through a frequency filter (100-1000 kHz) and a post-amplifier of 45 dB gain inside the recording system. In each case, full waveform data were recorded for events with

a sampling rate of 4 MHz and 1024 points. The system settings were kept constant for all the tests except the trigger threshold, which was adjusted within the range 35-45 dB to achieve the best monitoring depending on the specific situations (noise etc). The variations in coupling between the transducers and the specimen were also determined before each test using the standard "pencil-break" test. Other settings were: Peak Definition Time = 50 μs; Hit Definition Time = 200 μs; Hit Lockout Time = 300 μs (see Physical Acoustics Corporation, 2001, for details).

Table 5.1 summarizes the number of AE monitoring tests during simple compression and Brazilian tests performed on Lavasan granite and North African gabrro.

Table 5.1: Number of AE monitoring during uniaxial and Brazilian tests

Lavasan Granite			
Type of test	**Number of tests**	**Geometry of specimens L×D (mm)**	**No. of specimens**
Simple uniaxial compression test	**10**	**100 × 45**	**Gr1, Gr3, Gr6, Gr7, Gr10 Gr12, Gr13, Gr15, Gr16, Gr17**
North African Gabbro			
Simple uniaxial compression test	**4**	**140 × 70**	**Ga1(650)*, Ga3, Ga4, Ga10**
Brazilian	**6**	**20 ×40**	**Gab1 to Gab6**
Brazilian	**5**	**35 ×70**	**Gab7 to Gab11**

* This specimen was previously damaged in triaxial test by ultra high confining and axial stresses.

5.3.2. AE monitoring during unconfined compressive tests

Uniaxial compression test was performed on 14 samples of Lavasan granite and North African gabbro. Results of the tests were presented previously in chapter 4. Based on the Society for Testing and Materials Standards (designation ASTM D4543-85), the length to diameter ratios were approximately 2 to 2.5. Considerable care was taken to minimize the influence of end effects on strain gauge and AE transducer readings. This entailed the use of a specially constructed frame that allowed for the sample ends to be highly polished. Measurements of end surface flatness and perpendicularity are lower than those recommended by ASTM standards. Each sample was instrumented with four Micro-Measurement electric resistance precision strain gauges (two axial and two lateral at 90° intervals, 12.7 mm in length, with a 5% strain limit) to record sample deformation and four AE transducers to record acoustic emissions. Strain gauges were mounted directly on the

cleaned sample surface. Three LVDTs were also used during tests to ensure that the load direction did not change during tests. Prior to uniaxial testing, P- and S-wave travel times were recorded for each sample (Table 1 in Appendix I). Acoustic emissions were monitored continuously during the uniaxial compression tests of gabbro and granite specimens. Two transducers were symmetrically mounted on end of the specimen and were placed 20 mm from the each end of sample. Sofranel SWC couplant 7 and elastic bond were used for fixing the transducers on specimens. Figure 5.2 schematically shows the AE set-up and loading system for carrying out the uniaxial tests. Details of the transducer attachment to the specimens in uniaxial and Brazilian tests are shown in figure 5.3. Figure 5.4 also shows a specimen after a test with mounted AE transducers and LVDT sensors.

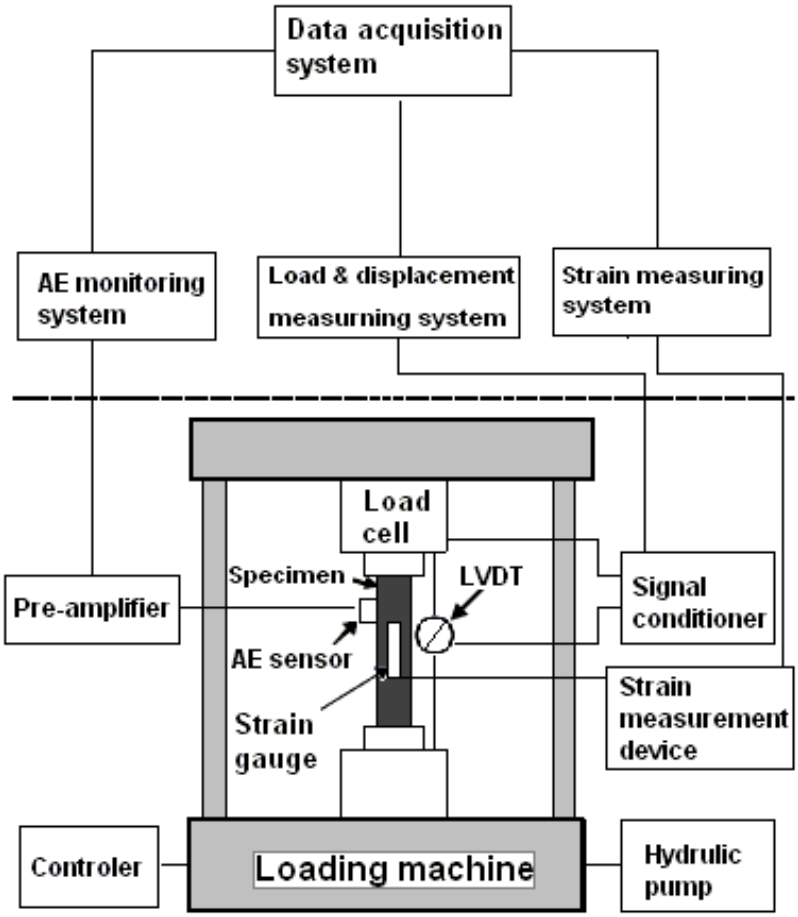

Figure 5.2: Schematic diagram of AE monitoring and loading systems

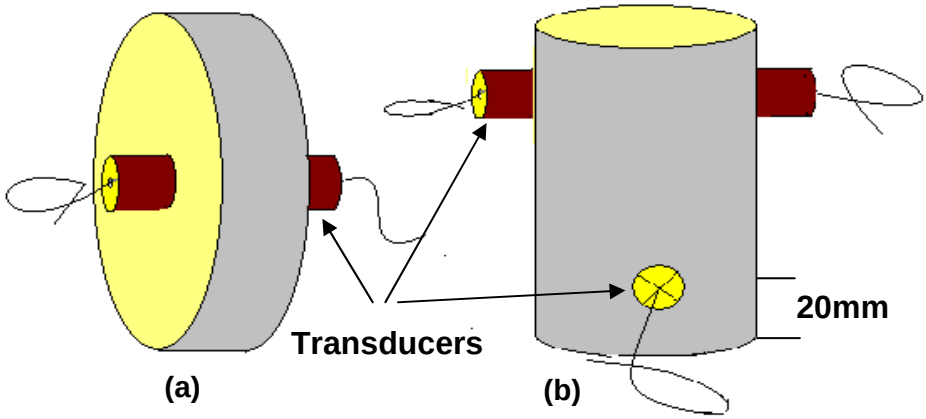

Figure 5.3: Diagram showing mounting of AE transducers on specimens for Brazilian (a) and uniaxial tests (b)

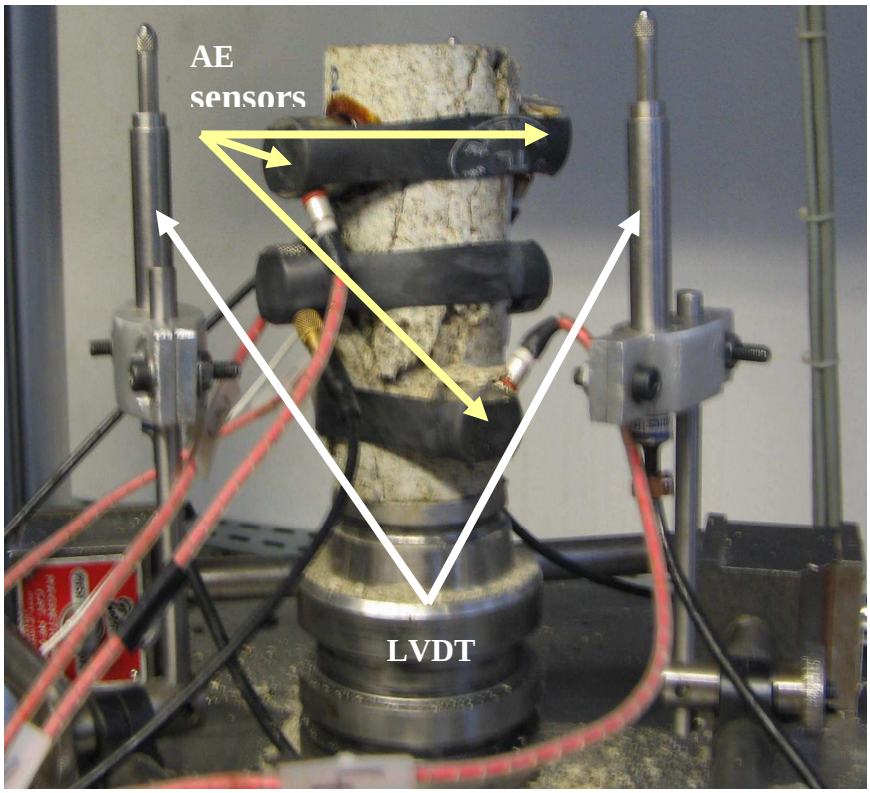

Figure 5.4: Specimen number Gr7 after a uniaxial compression test

5.3.2.1 AE Hit parameter

All AE parameters and AE definitions were previously presented in chapter 2. In this research work, we have used the AE hit number and AE energy parameter as the two most commonly considered in acoustic emission studies.

The recorded AE and stress-deformation data have yielded many useful time-histories and load-based plots of AE hits. We compared the AE parameters with conventional load-deformation data; for both rocks considered in this research, three visible AE hit rate steps could be delineated. The first step occurs at about 25 to 35 % and second at about 60 to 70 % of the failure stress for the Lavasan granite rock. The final step of AE hit occurs when the applied stress reaches almost 90–95 % of the failure stress in both rocks. The last step is more visible and sharper than the other two. These three steps could also be seen in the gabbro specimens with small differences. For all of gabbro specimens, the first step occurred below 20 percent (about 18 %) of the ultimate strength of rock.

For both rocks, the first two steps were lower than the last one. Therefore, the first step for some specimens were not quite visible; it seems that the noise rate for these types of records is high and does not allow the detection of damage related records. Both the granite and gabbro samples showed the same trends in occurrence rate of AE hits at stresses close to failure.

5.3.2.2 Cumulative AE energy

The graphs of the cumulative AE parameters (hit and energy) and stress versus deformations were drawn from recorded AE data. Like the results for the AE hit number, the energy rate of AE events was found to be quite low until the applied stress reached nearly 30 percent of ultimate failure stress in granite and 18 percent of ultimate strength for gabbro. It was then followed by a small increase to reach the second step at around 60 to 70 percent of the maximum strength of the rocks. Finally, near failure (90 to 95 % of ultimate strength), the third step occurred with extreme acoustic emissions. Unlike the AE hit, the AE energy steps were quite sharp for both rocks; however, the third step, similar to the AE hit rate, is sharper than the two first steps. Since both the gabbro and granite rocks are relatively isotropic and hard, there is not a big difference between the accumulated AE energy rates in these specimens.

We found that the AE energy parameter was the most effective way to follow the stress-induced rock failure procedure and to predict the ultimate strength of the rocks. The three steps identified are comparable to crack initiation (σ_{ci}), crack damage (σ_{cd}) thresholds and ultimate uniaxial strength in the stress-strain diagram presented by Martin in 1993 (Figure 5.1). It should be noted that since the crack closure (σ_{cc}) stage is not related to crack generation, it is not surprising that this stage is not detectable based on AE data.

Figures 5.5 to 5.8 show the accumulated AE hit numbers and energy for Lavasan granite and figures 5.9 to 5.11 present the same results for North African gabbro. Stress-deformation data of each specimen are also represented in the same graphs. In table 5.2 we have summarized all the results from AE monitoring on these two rocks types. In appendix I we present the AE hit and energy parameters for all of the uniaxial tests carried out to date.

Table 5.2: Different steps of AE energy and AE hit during uniaxial compression tests on Lavasan granite and North African gabbro and equivalent stresses

No of specimen	Geometry of specimens L×D (mm)	Max. uniaxial strength [MPa]	Equivalent stresses at AE steps 1 - 2 - 3	
			Stress [MPa]	Percent (%)
Lavasan granite				
Gr1	95×45	142	34 – 83 – 130	24 – 58 – 92
Gr3	101×45	121	25 – 72 – 110	21 – 60 – 91
Gr5	101×45	138	36 – 85 – 131	26 – 61 – 95
Gr6	99×45	147	38 – 85 – 138	26 – 58 – 94
Gr7	100×45	125	49 – 83 – 116	39 – 66 – 93
Gr10	101×45	123	30 – 82 – 117	24 – 67 – 95
Gr12	101×45	138	27 – 98 – 131	20 – 71 – 95
Gr15	100×45	135	38 – 66 – 128	28 – 49 – 95
Gr16	100×45	122	19 – 46 – 99?	16 – 38 – 81
Gr17	100×45	136	28 – 95 – 130?	21 – 70 – 96
North African gabbro				
Ga1*	142×70	160	36 – 118 – 150	23 – 74 – 94
Ga3	141×70	216	37 – 127 – 207	17 – 59 – 96
Ga4	141×70	238	44 – 135 – 217	18 – 57 – 91
Ga10	143×70	225	41 – 164 – 219	18 – 73 – 97

* Ga1 was previously damaged under ultra high triaxial loading.

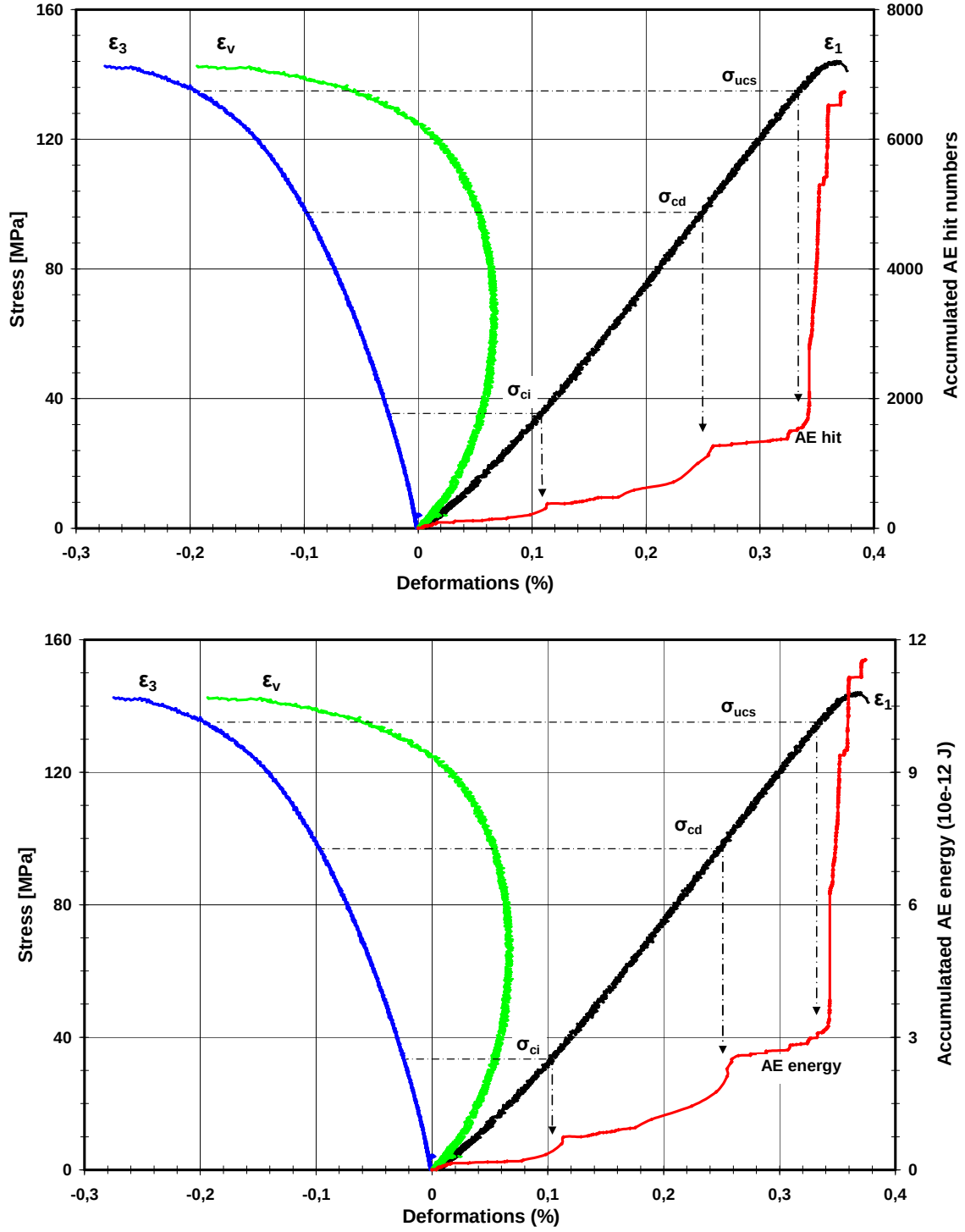

Figure 5.5: Accumulated AE hit (above) and energy (below) versus stress - deformation during a simple uniaxial compression test of Lavasan granite specimen Gr1. Axial (ε_1) and lateral (ε_3)deformations were measured by electrical resistance gauges; the volumetric deformation (ε_v) was calculated. σ_{ci} is crack initiation stress, σ_{cd} is damage crack threshold and σ_{ucs} is uniaxial compression strength.

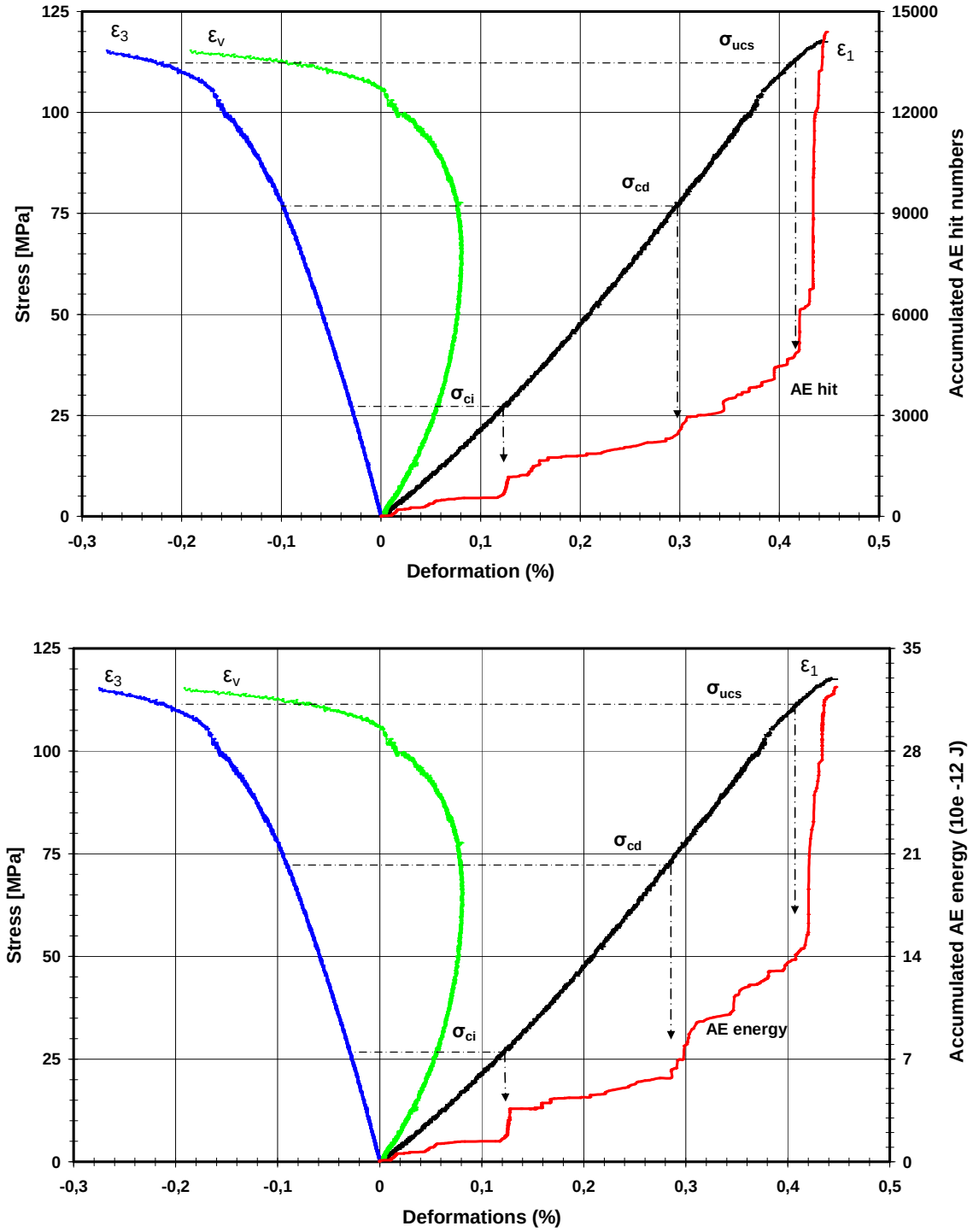

Figure 5.6: Accumulated AE hit (above) and energy (below) versus stress - deformation during a simple uniaxial compression test of Lavasan granite specimen Gr3. Axial (ε_1) and lateral (ε_3) deformations were measured by electrical resistance gauges; the volumetric deformation(ε_v) was calculated. Other symbols are given in figure 5.5

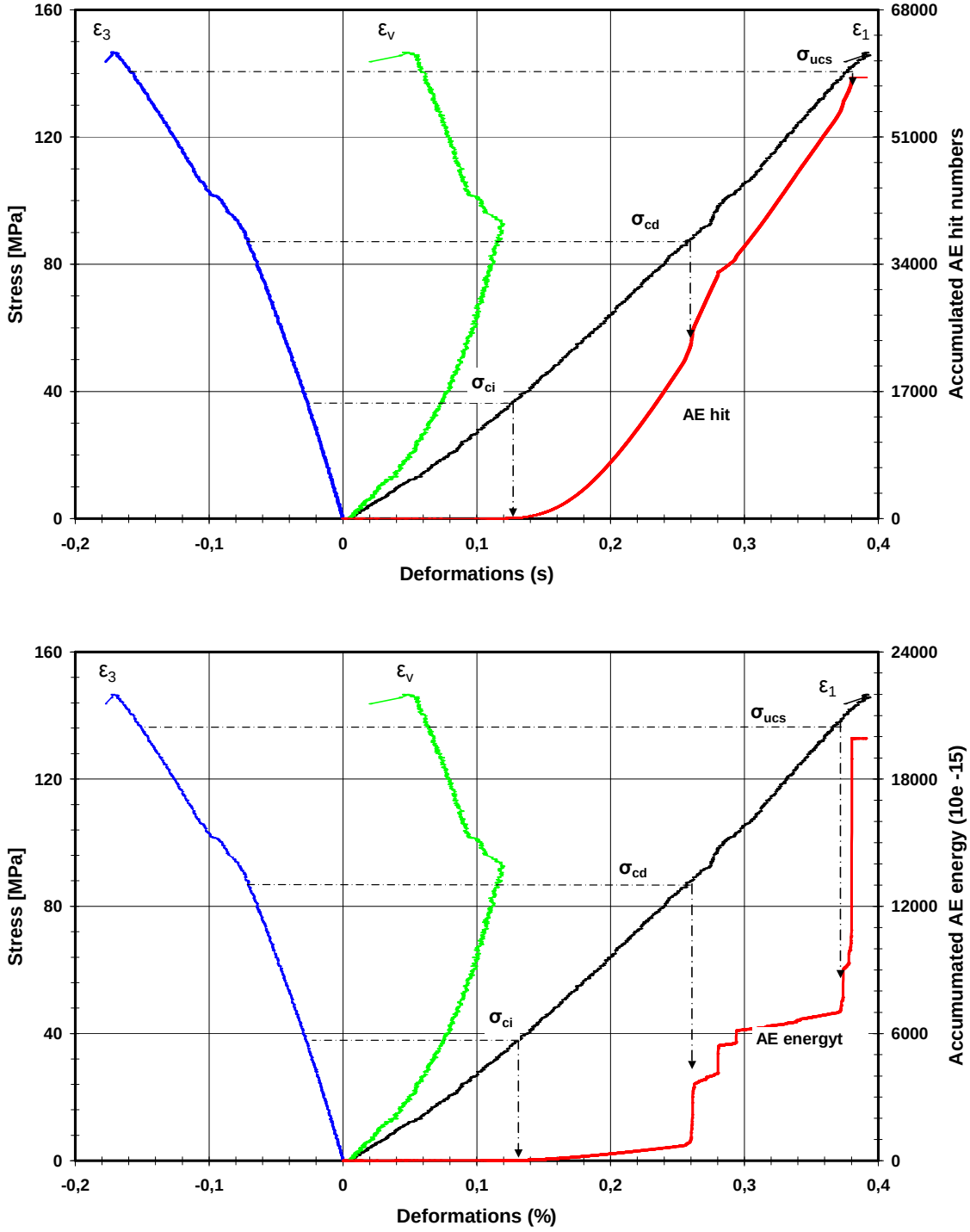

Figure 5.7: Accumulated AE hit (above) and energy (below) versus stress - deformation during a simple uniaxial compression test of Lavasan granite specimen Gr6. AE record is contaminated by noise; however the energy parameter visibly shows the steps. The perturbation in the deformation data is due to the detaching of a small slab of the specimen at about 50 % of ultimate strength.

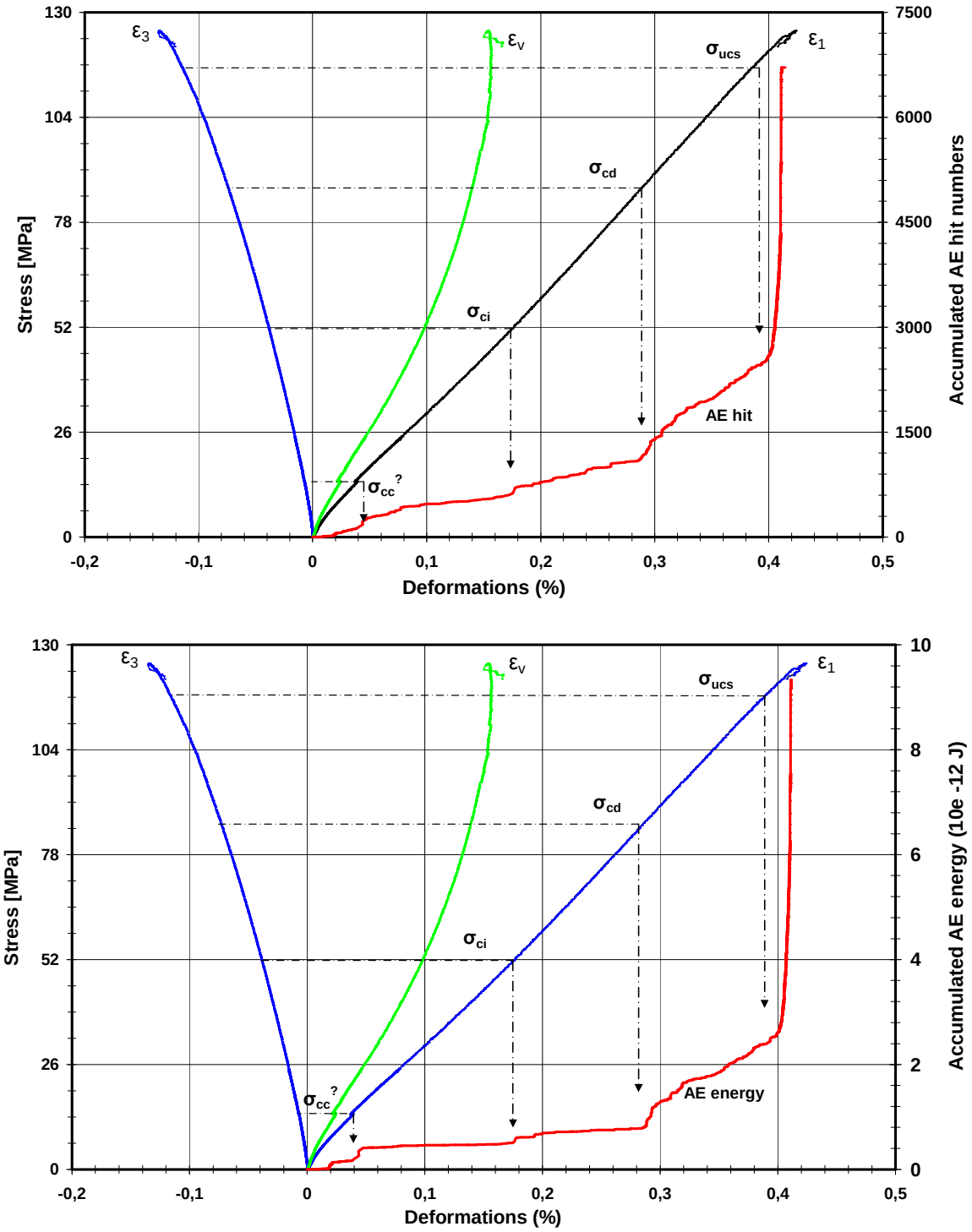

Figure 5.8: Accumulated AE hit (above) and energy (below) versus stress - deformation during a simple uniaxial compression test of Lavasan granite specimen Gr7. Small AE activity at the beginning of loading may be related to crack closure (σ_{cc}). A local small crack initiation and dislocation of specimenmight also be activating the AE at the start of loading.

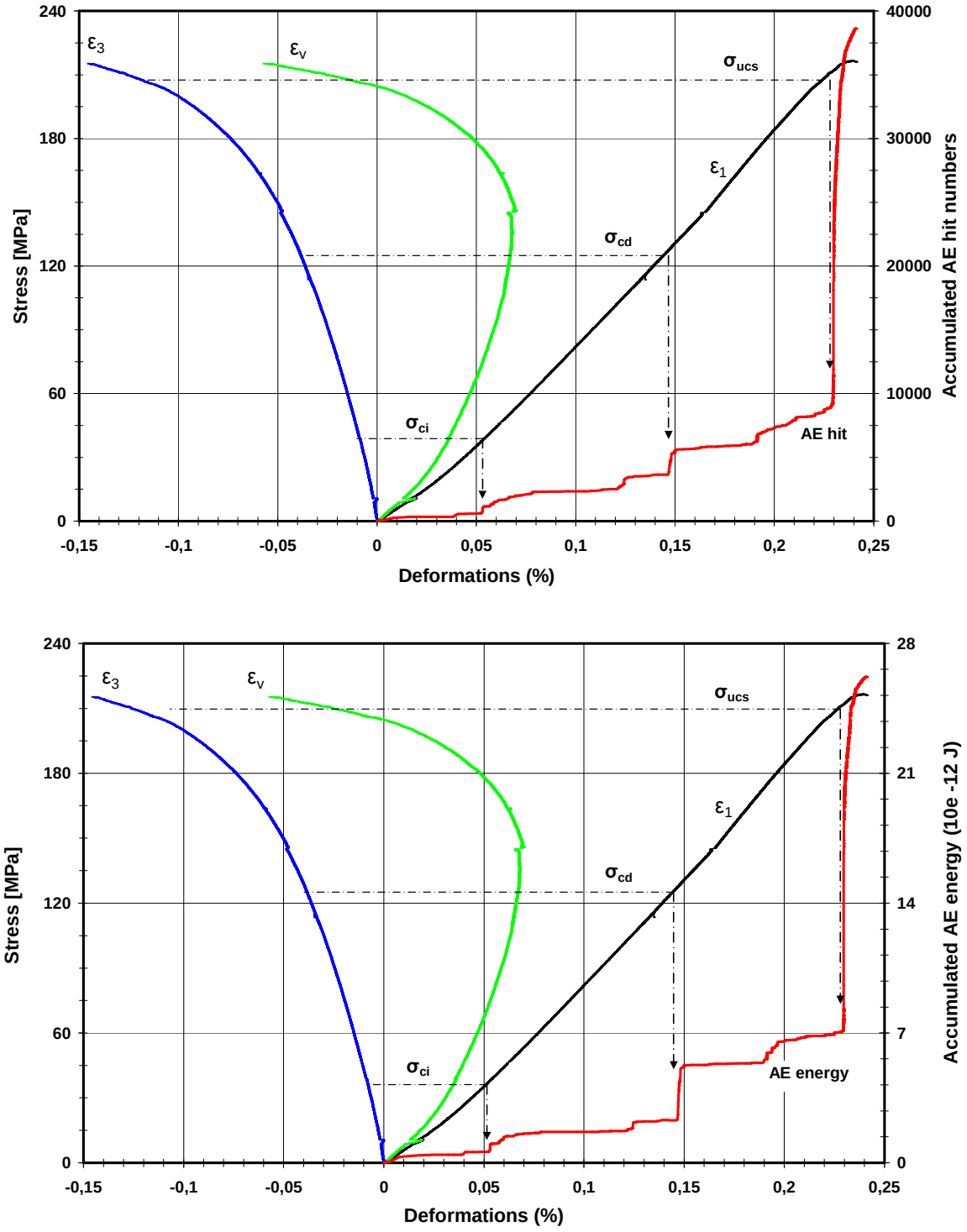

Figure 5.9: Accumulated AE hit (above) and energy (below) versus stress - deformation during a simple uniaxial compression test of North African gabbro specimen Ga3.

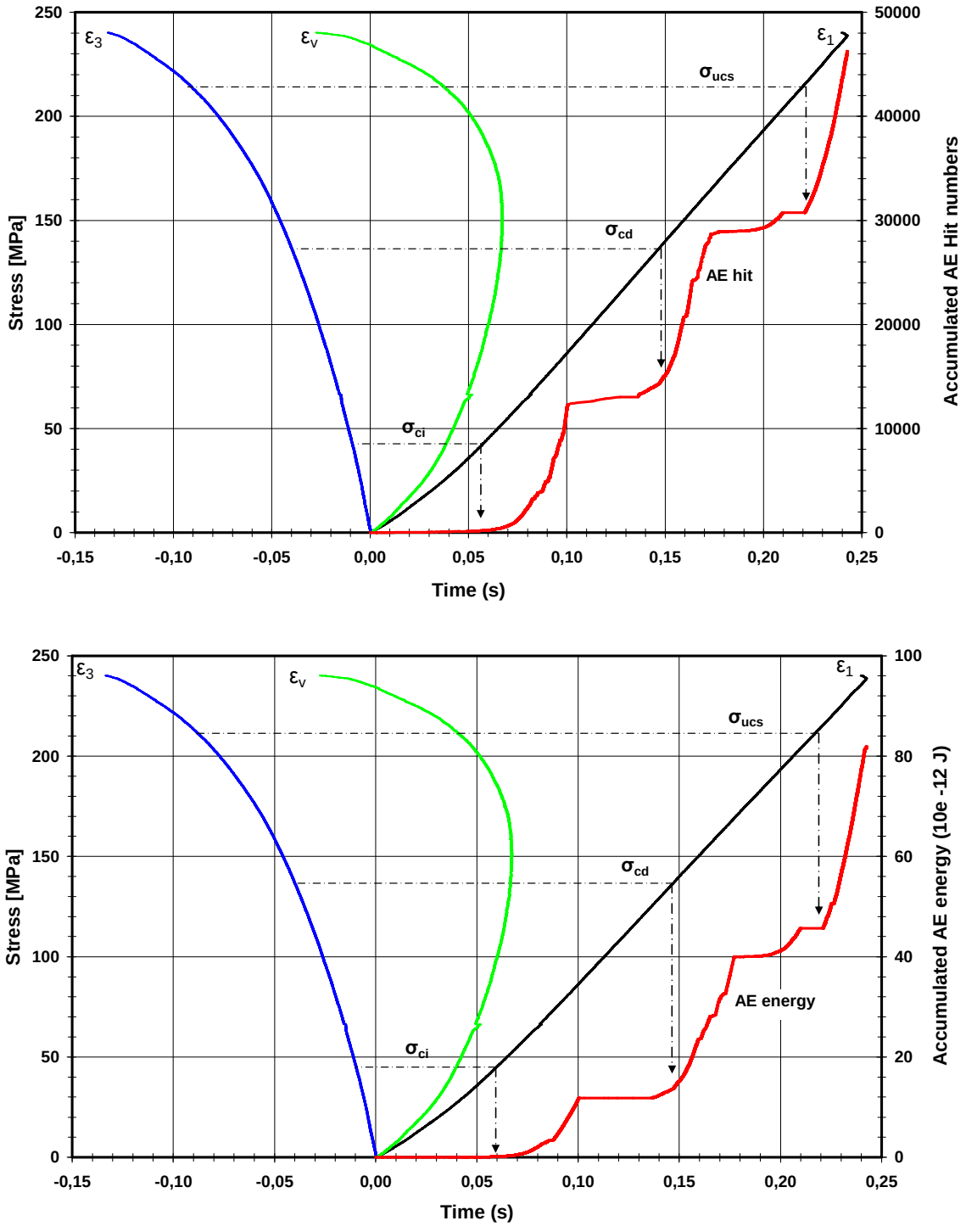

Figure 5.10: Accumulated AE hit (above) and energy (below) versus stress - deformation during a simple uniaxial compression test of North African gabbro specimen Ga4. The AE record is considerably contaminated by noise; however, the steps are clear.

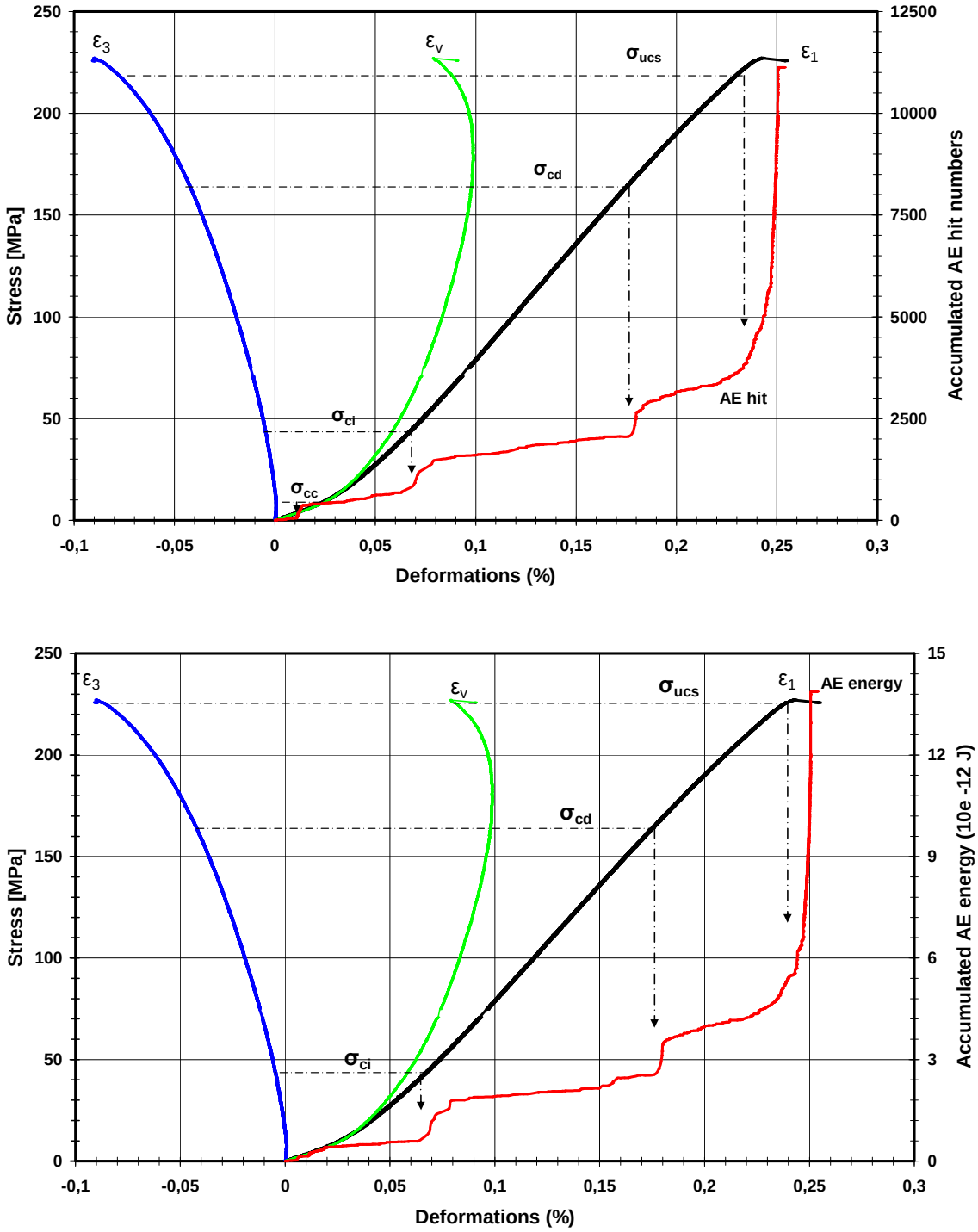

Figure 5.11: Accumulated AE hit (above) and energy (below) versus stress - deformation during a simple uniaxial compression test of North African gabbro specimen Ga10.

5.3.2.3 Comparison of AE steps with stress-deformation graphs

Considering the accumulated AE energy and the accumulated AE hit graphs of Lavasan granite and North African gabbro, three steps can be delineated for each test. These three steps are comparable to crack initiation (σ_{ci}), crack damage threshold (σ_{cd}) and uniaxial compression strength (ucs) in the stress-deformation diagram presented by Martin in 1993 (Figure 5.1). In spite of the definitive effects of these three stages, the crack closure (σ_{cc}) stage is not as clear based on AE parameters. We believe that, since this stage is not related to crack generation, it is not surprising that it is not detectable based on AE data.

The greatest difference in the AE records in the two rocks studied is the stress level at the start of the first step. While the first step for granite normally begins after 25 percent of the maximum strength of the specimen, for gabbro it is below 18 % (see table 5.2). This could be due to the lower porosity of gabbro compared to granite. This leaves gabbro with about 0.5 % porosity to reach the closure point sooner than granite, which has approximately 1 % porosity.

By comparing the AE parameter with the stress – deformation data, we found that using the AE record outlines each step of the failure process more definitively. Nevertheless, the limits of the failure procedure in the stress – deformation curves are not quite clear.

We have also noted that the AE energy parameter is the most effective way of following the stress-induced rock failure procedure and of predicting of the ultimate strength. In general, the steps based on the AE energy parameter are sharper than the steps delineated by the AE hit parameter.

5.3.3 AE monitoring during Brazilian tests

The AE investigation also involved the testing of a total of 11 gabbro disc-shaped specimens of two different diameter sizes (40 and 70 mm). The specimens were cored from the same block as the specimens for the uniaxial and triaxial tests. The diameters and the length-diameter ratios (L/D) of the specimens were based on ISRM (1978) and ASTM D3967–95a specifications. The results of Brazilian tests were previously presented in table 4.3 and in figure 4.17 in chapter 4.

The press described previously was used to load the specimens. The vertical displacement was measured by LVDT and internal displacement gauges. For all the tests, the velocity of loading was constant and it was maintained at about 10^{-3} mm/s. A spherical adapter was placed between the specimen and the bottom plate of the testing machine to make the effects of non-parallelism of specimen surfaces negligible (see figure 4.10).

For all of the Brazilian specimens, AE events were monitored using two transducers mounted directly to each side of the disc. The AE and deformation data were recorded continuously during loading until failure. Figure 5.12 schematically shows the location of transducers on the specimens and loading supplies. Figure 5.13 shows a gabbro specimen with AE sensors at the beginning of a Brazilian test.

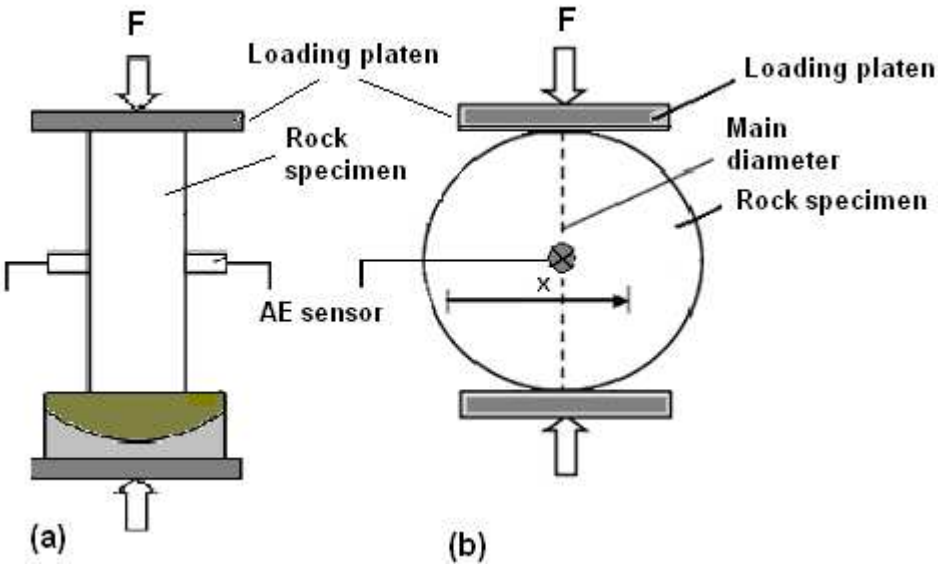

Figure5.12: Schematic views of loading system, Disc-shaped specimen and attached AE sensors (a) and details of the test assembly (b)

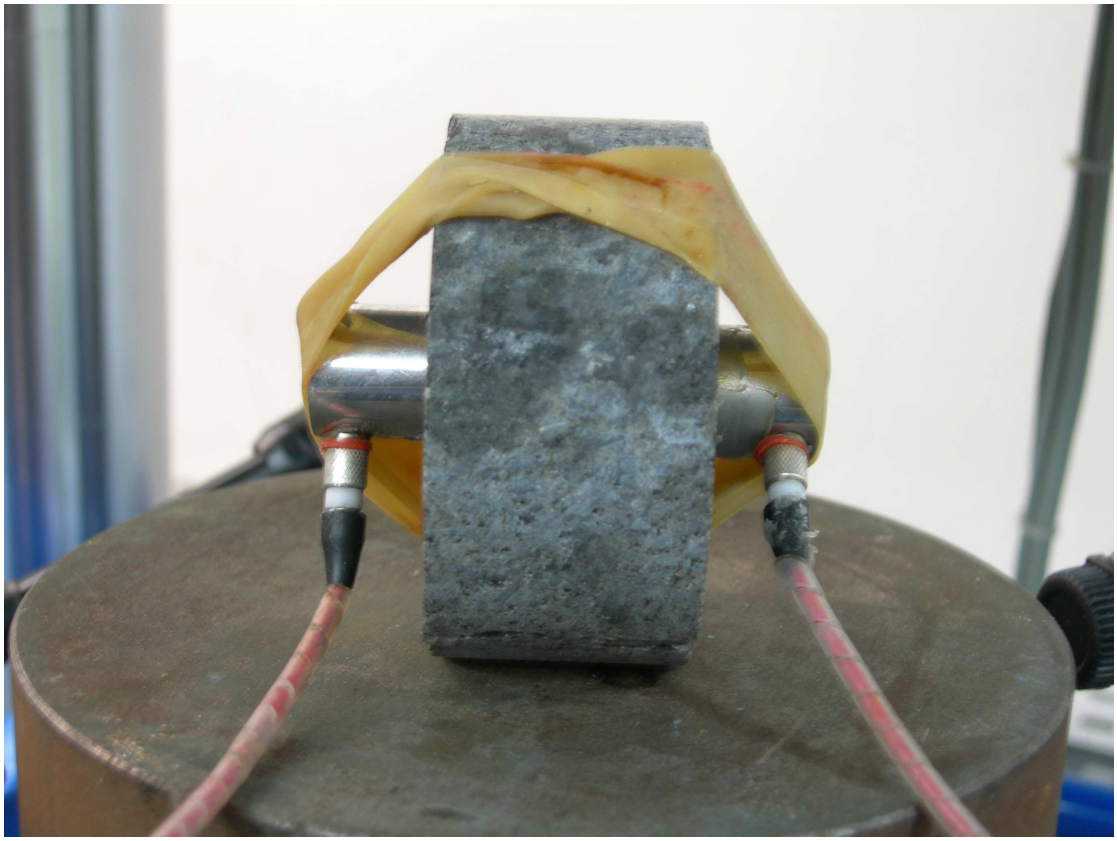

Figure 5.13: Gabbro disc-shaped specimen with AE sensors before Brazilian test

As noted in chapter 4, a review of the fracture pattern showed two visible wedges in the top and the bottom of the disc shaped specimens. The wedges were most visible in the specimens with a large diameter (70 mm).

Acoustic emission data were analyzed to develop a relationship between the AE activity and the micro crack nucleation and the accumulation of damage during indirect tensile tests. The AE event hit and AE event energy parameters were plotted versus time. Comparisons were also made between stress-time and stress versus deformation. Figures 5.14 to 5.17 show the accumulated AE hit and the accumulated AE event energy for some of the specimens. Other graphs of AE records are presented in appendix I. The graphs show different significant steps for all the 11 tests: AE records of specimens Gab1, Gab2, Gab3, Gab4, Gab7, Gab8, Gab9, Gab10 and Gab11 show three steps of AE hit and energy. However, for Gab5 and Gab6, only two steps are apparent. Results from the analysis of

event hits for each AE step and the correlated stresses are presented in Table 5.3. Based on the test results and considering the available studies on micro crack evolution in stress induced rocks, we can deduce that:

- The first step is related to nucleation of micro cracks in the middle part of the disc due to tensile micro crack propagation.
- The second step of the AE event rate increase corresponds to the development of the wedges at the top and the bottom of the disc.
- The last step is related to the ultimate tensile strength of specimen and failure.

Table 5.3: Different steps of AE energy and AE hit during Brazilian tests and the equivalent stress

No of specimen	Geometry L×D (mm)	Tensile strength [MPa]	Equivalent stresses of AE steps 1 - 2 - 3	
			Stress [MPa]	Percent (%)
Gab1	**35 × 70**	**10.3**	**2.4 – 6.5 – 9.9**	**23 – 63 - 96**
Gab2	**32 × 70**	**11.1**	**2.3 – 7.1 – 10.5**	**21 – 64 - 95**
Gab3	**31 × 70**	**11.6**	**1.8 – 6.2 – 10.8**	**16 – 53 - 93**
Gab4	**33 × 70**	**12.3**	**1.9 – 7.5 – 11.5**	**15 – 61 – 93**
Gab5	**34 × 70**	**11.6**	*** – 3.8 – 10.5**	*** – 33 – 91**
Gab6	**36 × 40**	**10.9**	*** – 5.8 – 10.4**	*** – 53 – 95**
Gab7	**22 × 40**	**11.7**	**1.7 – 7.2 – 11.3**	**15 – 61 – 96**
Gab8	**20 × 40**	**10.6**	**2.2 – 6.3 – 9.8**	**21 – 59 – 92**
Gab9	**21 × 40**	**10.2**	**1.7 – 6.6 – 9.4**	**17 – 65 – 92**
Gab10	**19 × 40**	**13.5**	**2.1 – * – 12.4**	**16 – * – 92**
Gab11	**22 × 40**	**12.2**	**1.8 – 6.1 – 11.5**	**15 – 50 – 94**

* The values were not identified due to noise and possible technical problems.

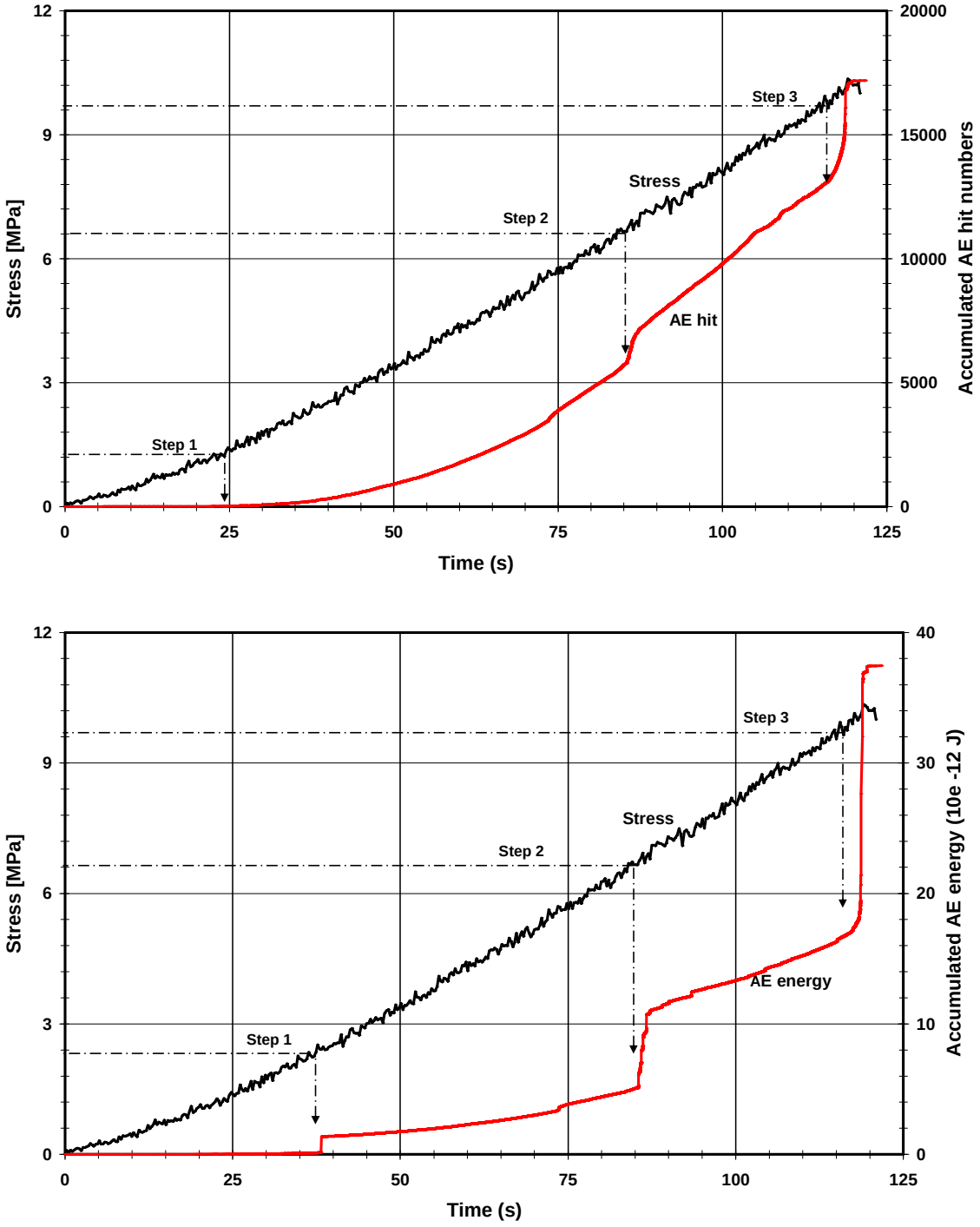

Figure 5.14: Accumulated AE hit (above), accumulated AE energy (below) and stress versus time during Brazilian test of gabbro specimen Gab1

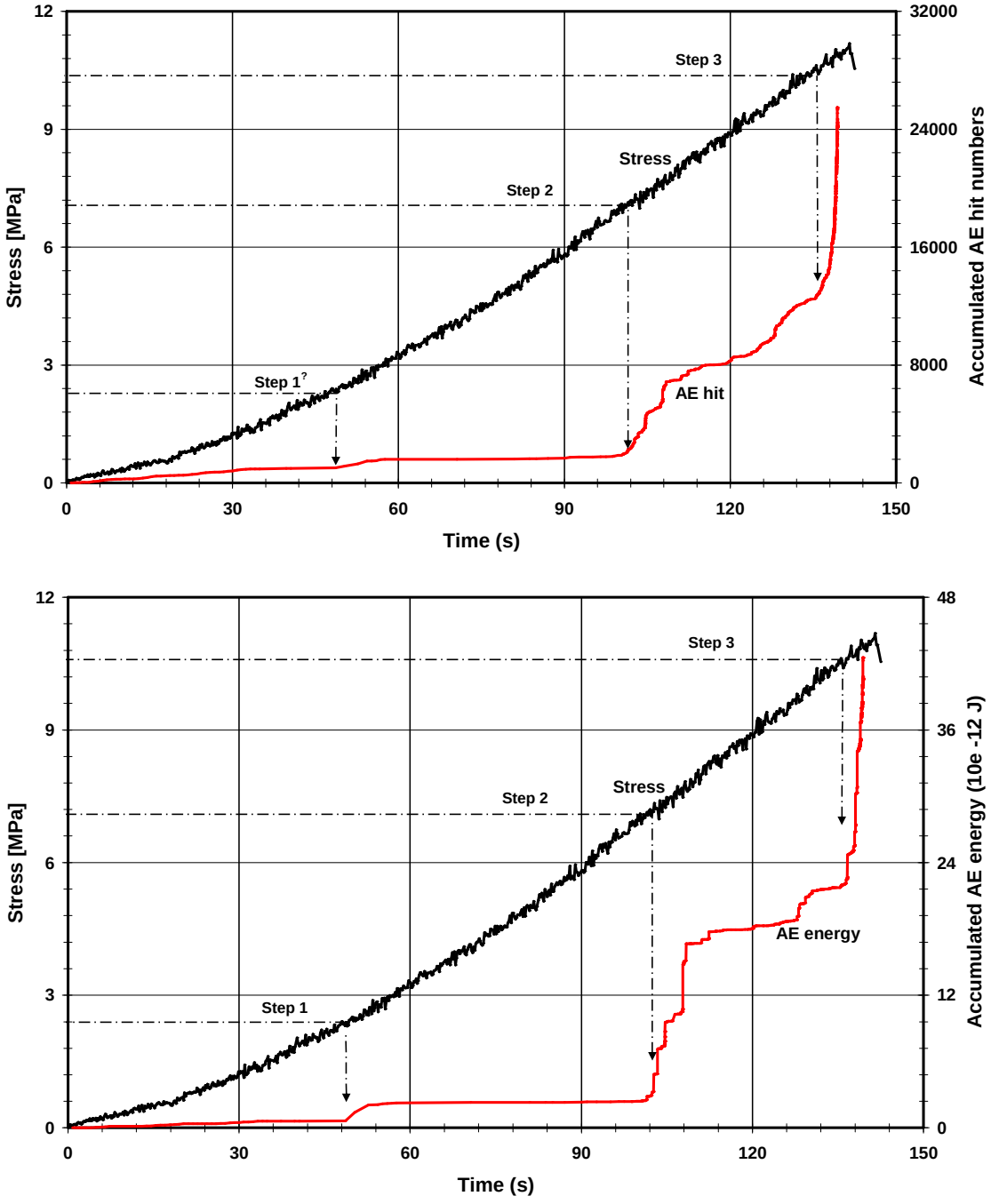

Figure 5.15: Accumulated AE hit (above), accumulated AE energy (below) and stress versus time during Brazilian test of gabbro specimen Gab2

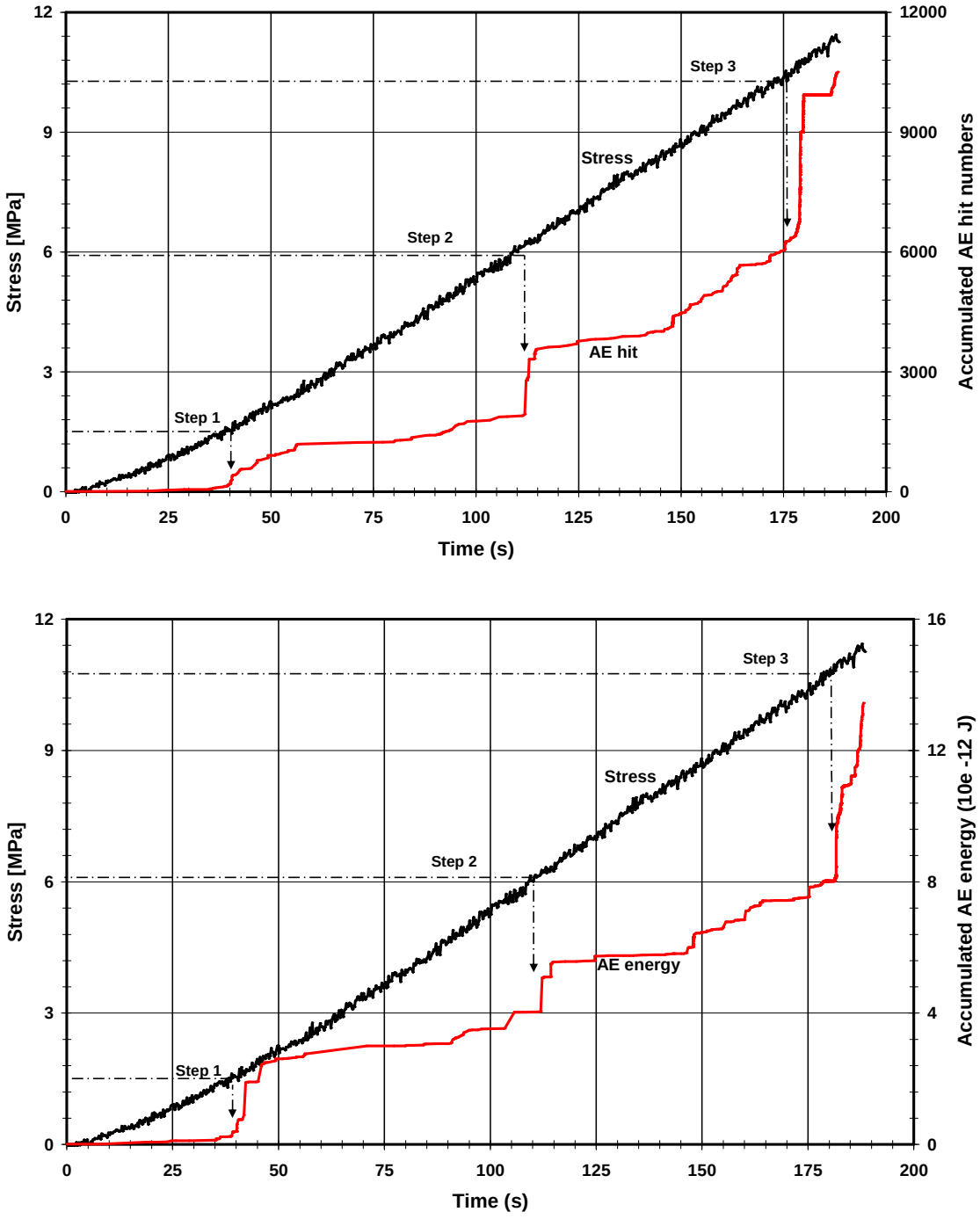

Figure 5.16: Accumulated AE hit (above), accumulated AE energy (below) and stress versus time during Brazilian test of gabbro specimen Gab3

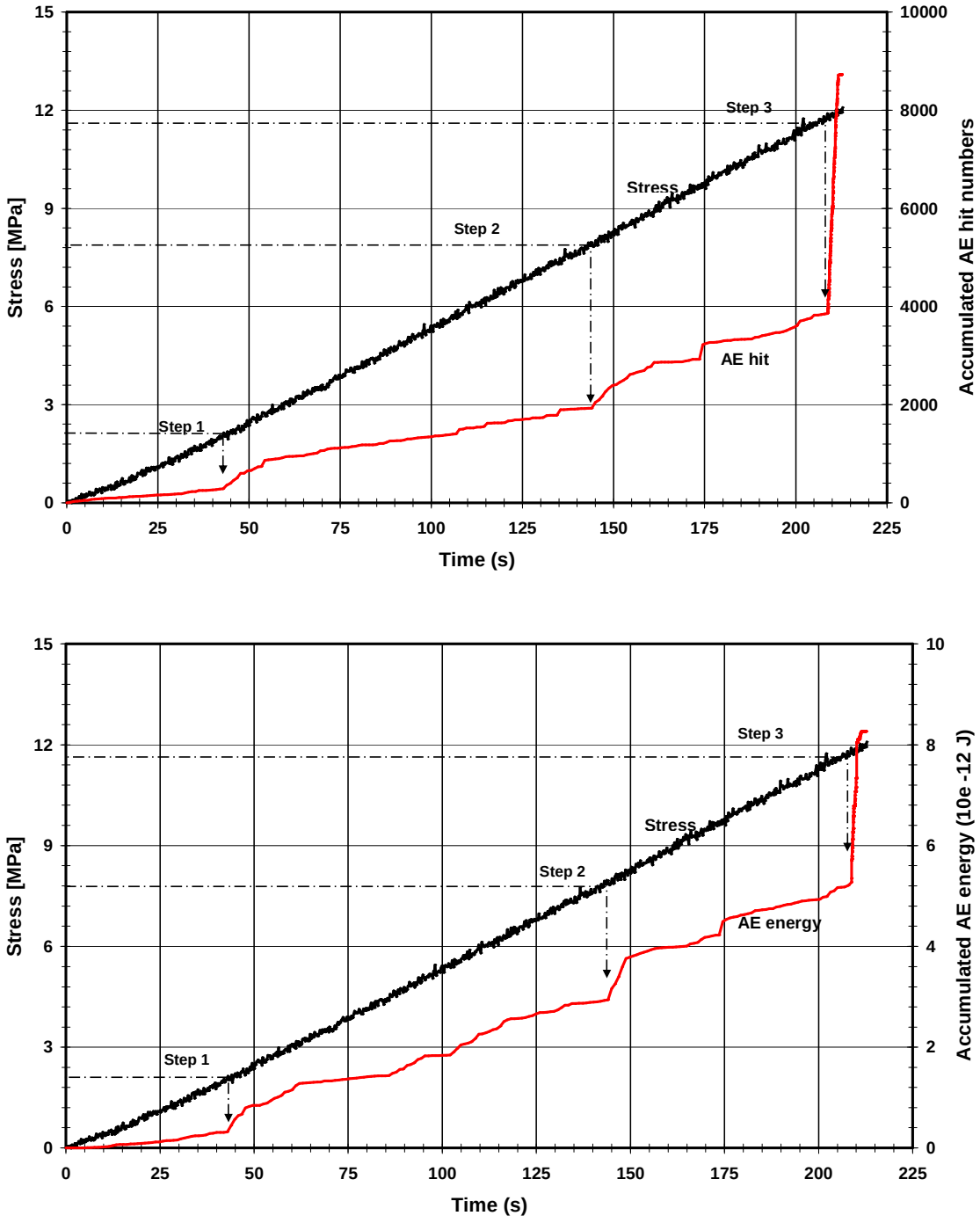

Figure 5.17: Accumulated AE hit (above), accumulated AE energy (below) and stress versus time during Brazilian test of gabbro specimen Gab4

5.3.4 Interpretation of the AE records from uniaxial compression tests and Brazilian tests

The main objective of this portion of the research was to investigate the damage procedure by monitoring AE events and comparing the AE results from uniaxial compression and Brazilian tests. In other words, the two main rock failure mechanisms, shear and tensile, were investigated by AE monitoring. For this purpose, a series of laboratory tests were carried out on isotropic brittle rock specimens. A direct comparison of the AE event data from both test methods showed that the AE activity in the Brazilian tests was considerably lower than in the uniaxial compression tests over the same time span. The high level of energy needed for shear failure in the cylindrical UC tests in comparison to the indirect tensile strength may be is the main cause of the difference. The better coupling of the transducers to the flat surface of the Brazilian specimen in contrast to the convex shape of the cylindrical specimen used in the UC tests is another reason for the observed differences. In the later case, the noise level increases due to movement of the transducers upon rock deformation of the UC specimens.

Plotting the accumulated AE hit number and the accumulated absolute AE energy versus deformation and time for each type of test shows three sharp steps in AE activity in the UC tests and also three steps in the Brazilian tests. The steps in UC tests are associated with the initiation of micro cracks, the onset of micro fracturing and damage nucleation, respectively. The three steps of AE events in the Brazilian tests could be related to the beginning of micro fracturing, wedge formation at the top and bottom of the disc and finally nucleation of a failure surface in the middle section of the disc.

We have found that absolute energy is a more effective way of predicting catastrophic failure of specimens than the conventional AE hit parameter for both test methods. Data processing shows that, despite the gradual increase of the accumulated AE hit quantity, the absolute energy parameter increases sharply in each phase of the failure process. A practical implication of this result is that an increased AE activity (hit per second) does not necessarily indicate that the test specimen has reached a critical state. The increase of the AE count could be related to other AE sources such as dislocations and noise which can be activated during loading (Keshavarz et al., 2008). Nevertheless, the sudden increase in absolute energy is most likely due to micro crack creation and damage propagation inside the specimens. Finally, we note that all the results presented here refer to two particular

brittle rocks and further research is necessary to examine whether the results described are applicable to other types of rocks.

5.4. Infrared measurement under cyclic loading

5.4.1 Stress induced infrared radiation

An object whose physical temperature is above absolute zero will produce infrared radiation (Luong, 1993). However, some experiments have verified that the infrared radiation (IR) of a rock samples can change during loading and rock can show IR abnormality before fracturing. Based on previous studies, Lixin (2006) has identified two different thermal radiations from loaded brittle rock as the thermoelastic effect and the frictional–thermal effect. The thermoelastic effect depends on energy exchange and its dissipations in loaded rock. For convenience Liu (2006) proposed the term IR for the average radiation temperature at beginning of loading and IRTI for thermal increase near the failure of loaded rock.

In a relatively independent closed system including a loading machine, rock sample and environmental air, the energy exchange (input and consumption) during rock deformation and rock failure is a complex process. Without consideration of the possible chemical reactions and related energy exchanges inside the loaded rock, the energy input to the loaded rock includes two parts: the mechanical work of the loading actuator and the heat input through positive thermal exchange from the loading platen and environmental air. The energy consumption by the loaded rock is much more complex in that it includes the energy accumulation in the rock and energy dissipation from the rock.

The Stefan–Boltzmann law, also known as Stefan's law, states that the total energy radiated per unit surface area of a black body in unit time (known variously as the black-body irradiance, energy flux density, radiant flux, or the emissive power), *J*, is directly proportional to the fourth power of the black body's thermodynamic temperature *T* (also called absolute temperature):

$$J=\sigma T^4 \tag{5.1}$$

The formula states that the infrared radiation strength (radiation flux density) of any material, at temperatures above absolute zero, is biquadratic to its surface physical

temperature. Hence, the rock surface infrared radiation is a comprehensive effect of rock deformation and the physical thermal state of the rock surface. The rock surface IR temperature could be an index reflecting the rock surface physical temperature and rock surface deformation field, which indicates the complex physical–mechanical process inside loaded rock.

In spite of thermal exchange and plastic deformation, the thermoelastic effect and the frictional–thermal effect (Lixin et al., 2006a) are two of the main physical mechanisms of IR radiation production from loaded brittle rock. In the stage of elastic deformation, the thermoelastic effect is the main cause of IR, while in the stage of plastic deformation or fracturing, the frictional–thermal effect plays a greater role. At the moment of rock fracturing or failure, the friction-heat effect becomes more significant. The friction-heat effect depends on two factors: frictional force (defined by normal stress and the frictional coefficient) and frictional speed. The larger the frictional force and the faster the frictional speed, the stronger the frictional heat effect.

Many studies have shown that the IR temperature at the failure of brittle rock increases a few degrees (Wu, 2002). The IR feature of rock at failure in other loading configurations was investigated by Lixin (2006). The relationship between the IR temperature increases and rock strength has also been investigated by Wu et al. (2000). Liu (2006) has shown different thermal radiation under different loading conditions and for different strengths. However, the correlation between IR and crack propagation on loaded rock masses has not been studied. It is still unclear how the IR changes with crack creation in a rock mass. Since the main source of AE is the crack propagation in loaded rock, it could be helpful to study IR and ITIR radiations in loaded brittle rocks. This could be done by attaching strain gauges to rock samples and measuring and comparing the results at different stages of loading and rock deformation. In chapter 3 reviews of previous IR studies and related terminology have been presented.

5.4.2 Infrared measurement of Lavasan granite

In this research, samples were taken from a granite intrusion mass near the Mosha Fault of Iran. This fault is situated north of Tehran, and it is the main and most active fault near Tehran. The collected samples are cut to a quadrangle shape with 100, 40 and 20 mm for height, width and thickness, respectively (figure 5.18). The diameter of the center part was reduced to allow stress to concentrate on a limited part of the tested sample and to

increase the effectiveness of measurements. The facilities of Laboratoire Mécanique du Solide (LMS) in Palaiseau were used to study the infrared radiation thermographically. This study was done cooperatively between the laboratory 3S-R and LMS. In this context, five granite specimens were loaded in different load conditions for evaluation of the IR characteristics of the rock.

The stress induced temperatures of the specimens were obtained with a fast multi-detector infrared camera (CEDIP Jade III MW), inspecting one surface of the flat sample (figure 5.19). The infrared camera has a very low noise, less than 20 mK, and a high spatial resolution of 320 pixel×240 pixel at a maximum frequency of 145 Hz. It is possible to increase this value to 418 Hz while working on a reduced format (1/4 of the mentioned image size). The spatial resolution (pixel size) depends on the adjustment of the focal distance.

The surface of each sample was polished smoothly to obtain blackbody properties compatible with the calibration law of the camera. Moreover, temperature results were always used relative to an ambient equilibrium temperature, which gave temperature variations less than 0.1°C.

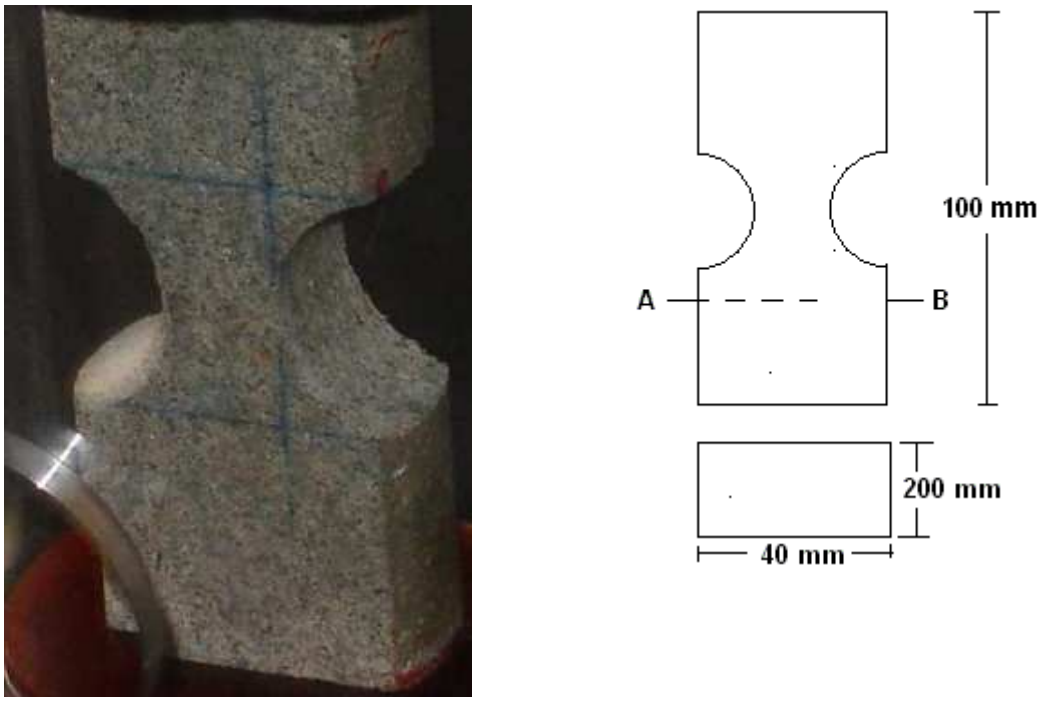

Figure 5.18: Shape and geometry of prepared specimen for infrared radiation test

The results of one of these tests are presented by different images at each stage of the test. The specimen was subjected to a given static simple compression (10, 15, 20, 25, 30kN; 22.5, 30, 45, 60, 75, 90MPa) superimposed by a cyclic loading (frequency = 30 Hz and 1800 cycles per stage) of constant amplitude (±5 kN or ±15MPa) to follow the evolution of the loops of hysteresis at various levels of loading. For each test, one thermal image was taken at the beginning (Fig. 5.20a.) and at the end of the test (Fig. 5.20b). The subtraction of these 2 thermal images gives the cumulative dissipation after 1800 cycles of loading (Figures 5.21). The details of the tests are shown in table 5.4, while figure 5.22 shows the final results of all tests. The related images for other tests are available in appendix II.

Table 5.4: Characteristics of IR measurements of Lavasan granite under cyclic loading

Static Force (kN)	Dynamic Force (kN)	Min. (kN)	Max. (kN)	ΔT (℃)	Name of Image*
1.2	±0.6	0.6	1.8	0	SYEA001 (reference)
2.5	±1.2	1.2	3.7	0	SYEB050
3.1	±1.9	1.2	5.0	0.16	SYEC050
3.7	±2.5	1.2	6.2	0.32	SYED050
5.0	±3.7	1.2	8.7	0.78	SYEE052
6.2	±5.0	1.2	11.2	1.11	SYEF052
7.4	±6.2	1.2	13.6	1.63	SYEG051
8.7	±7.4	1.2	16.1	2.32	SYEH052
9.9	±8.7	1.2	18.6	2.91	SYEI051
11.1	±9.9	1.2	21	3.50	SYEJ052
12.4	±11.2	1.2	23.6	4.07	SYEK050
13.6	±12.4	1.2	26.0	5.19	SYEL050

*The images are presented in appendix II.

Figure 5.19: The facilities for Infrared radiation measurement and the loading supply equipments in LMS, Palaiseau.

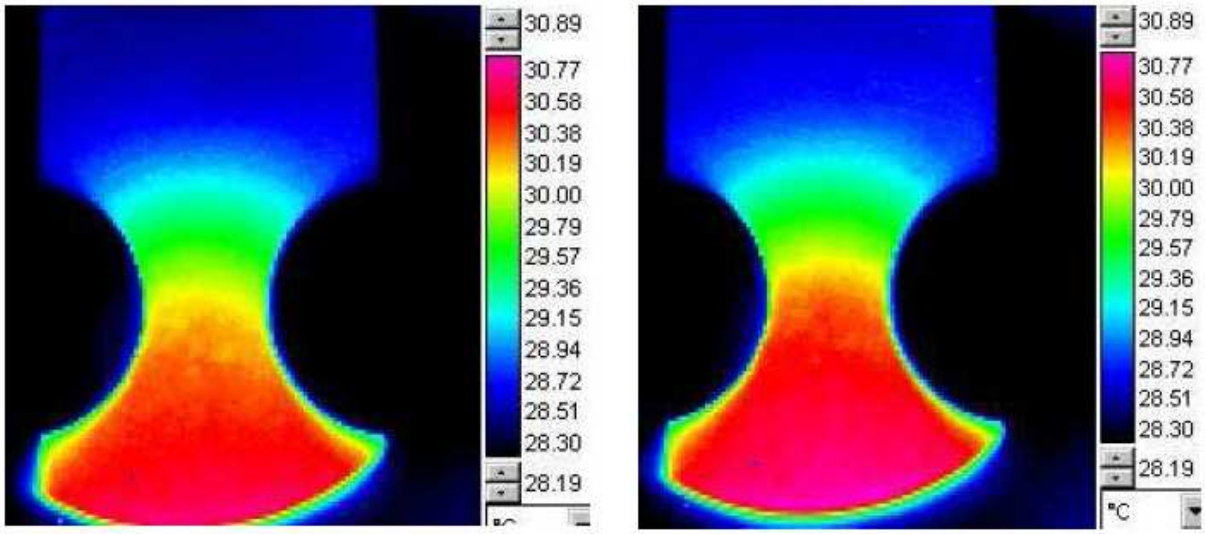

Figure 5.20: Thermal image at the beginning (left) of the cyclic stage of loading and at the end of loading (right).

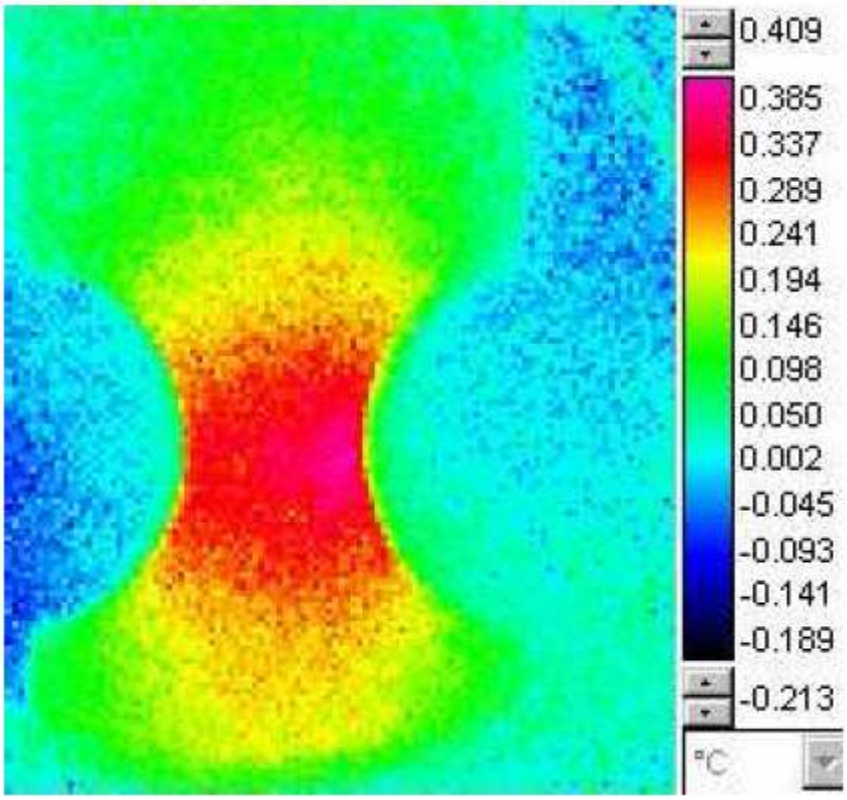

Figure 5.21: Cumulative dissipation of 1800 cycles with 22.5 MPa of static compression.

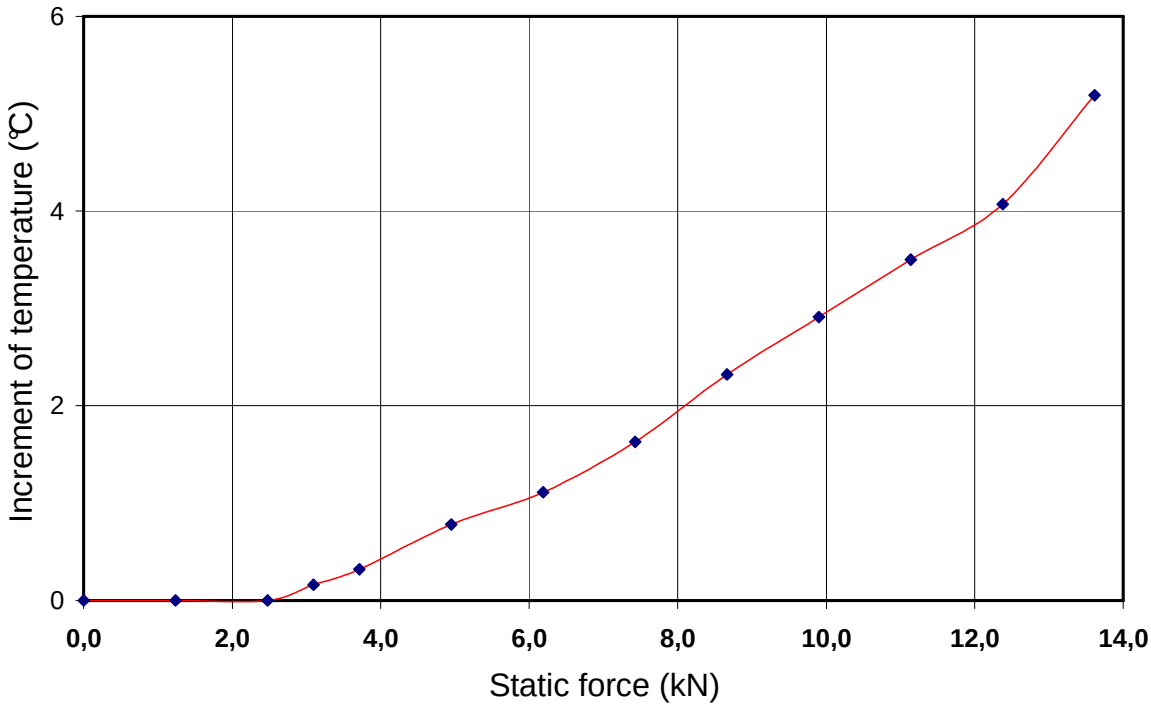

Figure 5.22: The result of IR temperature measurement during uniaxial cyclic loading of Lavasan granite

The experimental results show that infrared radiation (8 - 14 μm) temperature increases with loading. In fact the mechanical energy accumulates inside and can potentially be transformed into other types of energy such as acoustic emission energy and heat energy, caused respectively by the formation of micro fractures and by friction of crack surfaces and grains. The increment of IR temperature was started when the cyclic loading reached 2.5 kN. By increasing the loading, the IR temperature increased gradually. At 26 kN force (85 % σ_{max}), the maximum temperature of infrared radiation was achieved.

5.5 Discussion and conclusion

The main objective of this chapter was to investigate the feasibility of using acoustic emissions and infrared radiation to monitor crack propagation and rock failure prediction in the laboratory. In this chapter the main results of laboratory tests on two typical crustal rocks, granite and gabbro, were presented. A systematic laboratory study involving uniaxial compression and tensile loading of homogeneous granite and gabbro rocks was carried out. An advanced acoustic emission system (AE) was used to continuously monitor the AE events during loading. Infrared thermography was also measured using the facilities at LMS. From the experiment results, the following conclusions can be drawn:

1. The most suitable setup for AE monitoring is 40 dB for pre and 45 dB for post-amplifiers and the selection of a frequency range to be passed through a frequency filter between 200 to 500 kHz. Peak Definition Time = 50 μs; Hit Definition Time = 200 μs; Hit Lockout Time = 300 μs are the other suitable settings for the test system.

2. By plotting cumulative AE hit and cumulative AE energy versus time, we have found that the AE energy parameter is a more effective way than the conventional AE hit to detect different stages of the rock failure process.

3. Based on AE monitoring in uniaxial compression tests, three steps of AE dramatic activities are distinguishable. The first step occurs about 25% and the second step at about 60% of failure stress. Finally, the amount of acoustic emission activities in the third step dramatically increases when the stress level is close to the peak strength (90 to 95 %). These three steps also take place during Brazilian tests.

Acoustic emission activity patterns were correlated with stress-deformation behaviour. The steps are comparable to crack initiation, crack damage thresholds and uniaxial strength in the stress-deformation diagram that was presented by Bieniawski (1967). By comparing

the AE method with the stress – deformation data, we found that the AE record outlines the limits of each failure course more definitively.

4. We realized that noise level plays a key role in the quality of AE data. Therefore, signal discrimination and noise reduction are extremely important for successful AE applications. Besides the conventional noise reduction methods, we realized that good sensor coupling can also be useful to decrease noise level. For example, the noise level recorded during Brazilian tests with good coupling between sensors on the flat surface of the specimens is considerably less than in the uniaxial tests where the coupling between the curved surfaces of the cylindrical specimens and the sensors is not complete.

5. The preliminary tests indicate the possibility of using IR to study failure evolution; however, it not possible to use this method together with AE monitoring for prediction of failure in the laboratory. Increasing the stress levels leads to a rise in the infrared temperature in granite specimens. In laboratory studies, cyclic loading is necessary to produce measurable IR temperatures. Conversely, cyclic loading generates enormous noise and does not allow the detection of suitable AE records. Measuring IR with AE monitoring could be used for long-term evaluation in field investigations; for example, using the methods simultaneously to monitor the stability of underground excavations or fault rupture is recommended and, as a result, could be used for earthquake prediction.

Chapter 6

AE monitoring, physical measurements and mechanical tests on thermally and mechanically damaged gabbro

6.1 Introduction

The investigation of microcrack propagation and consecutive damage is one of the most important aspects of rock mechanics and rock engineering studies. In this chapter we focus on laboratory examination of damage in gabbro rock induced by stress and thermal heating.

The previous chapter described the monitoring and processing of acoustic emission records and then investigated the effectiveness of hit and energy parameters to study microcrack propagation and rock failure. Since the initiation and propagation of cracks are known to be the main source of AE events, monitoring AE of pre-damaged specimens could give a good insight into understanding the relationship between damage and AE events. In this chapter we investigate thermally and mechanically damaged gabbro by AE monitoring and by measuring the physical and mechanical changes that occur due to this damage. The probable damage mechanisms will be discussed based on an interpretation of the test results.

A short literature review of thermal and stress pre-damaged studies will be presented followed by an explanation of the laboratory procedures for each type of test. The effects of thermal and stress damage on the physical and mechanical properties of specimens were studied by measuring the elastic wave velocity and by carrying out uniaxial tests. Thin sections were also prepared from all of the damaged specimens in order to assess the

damage at the microscopic scale. The last part of this chapter is devoted to an explanation of the mechanisms of damage through thermal effects and mechanical loading of the rock.

A comparison of the thermal and stress damage using mechanical and AE test measurements is the other objective of this research. We will also study the main causes of degradation of the mechanical parameters by microscopic investigation.

6.2. Review of previous studies

Most of the physical properties of crustal rocks are influenced by cracks whose origin arises from various geological processes, the two main ones being: thermal processes and tectonic loading (David et al., 1999). The first processes related to variations in temperature, while the second is associated with stress changes in the rock mass. Stress damage has been widely investigated over the last few decades and in recent years special attention has been paid to thermal damage in relation to the extraction of geothermal energy, with rock characterization for potential nuclear waste disposal as well as for the design refractors. For all of these issues, the question is basically the same: how do changes in temperature influence the physical properties of materials? David et al., (1999) reported the results of recent laboratory studies which show clearly how thermal cracking modifies the elastic moduli (Heard and Page, 1982; Nasseri et al., 2007; Chaki et al., 2007), permeability (Menendez et al., 1999), acoustic velocities and attenuation (Bauer and Johnson, 1979) and mechanical strength (Homand et Troalen, 1984; Homand et Houpert, 1989) in crystalline granite and oollitic limestone. Jansen et al. (1993) investigated the development of thermal cracks by continuously monitoring acoustic emissions (AE) generated during thermal cycles in a granite and showed that these microcracks open at temperatures above 800°C, and that microcracks can coalesce to form a macroscopic fracture. They concluded that this type of material alteration could have dramatic consequences on the permeability evolution of a nuclear waste disposal repository. Homand and Houpert (1989) found that Scanning Electronic Microscope (SEM) analysis coupled with stereological analysis was a useful tool to characterize thermally-induced cracks in granites. Based on laboratory investigations on thermally treated granitic rock, Chaki at al., (2007) showed that thermal damage had a strong influence on porosity, permeability and ultrasonic wave velocity.

Laboratory studies have also shown how the physical properties change during stress application. Variations in permeability (Zoback and Byerlee, 1975), acoustic velocity

(Hadley, 1976) and attenuation (Oda et al., 1990) in granites have been reported. One of the major contributions of these studies was to show that microcracking and dilatancy significantly affect the rock properties when the stress level is larger than approximately half the ultimate strength of the rock. This is in agreement with the basic knowledge in rock mechanics (Vutukuri, 1978).

In spite of these broad investigations on the mechanical behaviour of thermally and stress damaged rocks, there is limited research on the mechanisms of damage evolution, especially in thermally treated specimens. This might be due to a lack of interdisciplinary research between rock petrology and rock mechanics. In the literature, to our knowledge, there are limited explanations as to the effects of the rock type and its mineralogy on microcrack propagation and damage mechanisms. It appears, at the moment, that there is a real lack of information concerning the mechanisms of damage from a mineralogical point of view.

Our goal in this work is to investigate how thermal cracking is generated in crystalline rocks and how this cracking influences some important physical and mechanical properties of gabbro. What role does the mineralogy of the rock play during progressive thermal damage?

The damage effects of ultra high stress on gabbro were also studied in this research. AE monitoring, mechanical tests, elastic wave velocity measurements and microscopic investigations were used to evaluate the two types of damage. For this purpose, two sets of gabbro samples were prepared, one for thermal treatment, in which thermal cracks were induced in an electric furnace, and a second one in which cracks were generated under increasing stress conditions by ultra high triaxial stresses. In order to avoid possible problems related to specimen variability, all the specimens were cored from a single block of gabbro rock in the same direction.

6.3 Mechanical test on stress damaged specimen

In order to be able to compare thermal damage with conventional stress damage, one test was conducted on a gabbro specimen taken from the same gabbro block that the other specimens were cored previously. Giga press was used to apply ultra high triaxial stress to damage the rock. The characteristics of this machine were given in chapter 4. Two electrical resistance gauges were mounted on to the specimen to measure the axial and the

lateral deformations during triaxial loading. A Linear Variable Differential Transformer (LVDT) was used to measure the axial deformation. Details of the procedure of specimen preparation for the Giga press are described in chapter 4. After preparation and placement inside the confining cell, the specimen was loaded up to maximum capacity of machine. For this purpose, the confining pressure was first boosted up to 650 MPa at a constant loading rate (100 MPa/minute). Then axial loading was applied over 15 minutes at a constant rate up to 2350 MPa. The same rate was used for the unloading cycle. The stress vs deformation graphs of the test were presented previously in chapter 4.

Following the ultra high triaxial damage of sample Ga1(650), the elastic wave velocity of the damaged specimen was measured. A uniaxial test was also performed on this specimen with AE monitoring. As with the thermally treated tests, a small slab of the specimen was removed after the triaxial test to prepare thin sections for subsequent microscopic study. The cut end of the specimens were again polished and measured to ensure the smoothness and parallelism. Finally, electrical strain gauges were mounted for measuring the deformations under uniaxial compression tests. in order to compare the mechanical damage with the thermal damage, the results of uniaxial tests and AE monitoring as well as elastic wave velocity measurements of specimen Ga1(650), will be presented in the following sections.

6.4 Thermal damage procedures and measurements

6.4.1 Sample preparation

In this work, North African gabbro was selected because it is an isotropic and fresh hard rock. However, a few Lavasan granite specimens were also examined during thermal damage studies to check and compare the results. The physical and mechanical properties of the selected rocks have already been studied and the results presented in previous chapters. A series of gabbro and granite specimens in two different sizes were prepared for thermal damaging in laboratory tests. One group of specimens had a height of 140 mm and diameter of 70 mm while the others were 90 mm in height and 40 mm in diameter. All the selected specimens were cored from a single block of rock (either granite or gabbro). The specimens were prepared based on the existing standards to have smooth and exactly parallel planes to ensure that load is evenly distributed over all the loaded surfaces of the

sample. The smoothness and the parallelism (with an end parallelism of 0.01 mm) of each sample were tested using a V-block and displacement dial gauge (see chapter 4 for details).

6.4.2 Thermal treatment

For thermal treating tests, we chose 10 homogeneous gabbro specimens with almost the same mechanical and physical properties. Before treatment the samples, the elastic wave velocities (Vp and Vs) are measured at room conditions using the contact transmission technique, presented in chapter 4. The specimens were then heated in a programmable electrical furnace at atmospheric pressure at a rate of 100°C/hour until the nominal temperature was reached, using the facilities of group LTPCM (Laboratoire de Thermodynamique et Physicochimie Métallurgiques) at Grenoble University. Figure 6.1 shows a photo of the furnace with a specimen in it. The slow rate of heating was used to ensure that cracking events resulted only from the temperature effect and were not due to thermal gradients across the specimens. This slow rate of heating also avoids thermal shock and any resultant unwanted micro-fracturing. The elastic wave velocity of the specimens was then measured. Each specimen was heated to 150, 300, 450, 500, 600, 700, 800 and 1000°C, and maintained for 1 hour at the maximum temperature before cooling at same rate (100°C/hour). The scheme of heating the specimens is shown in figure 6.2. After cooling, the elastic wave velocities of the specimens were measured once again at ambient conditions.

Before conducting uniaxial compression tests, a 10 mm disc-shaped slab was cut from one end of the specimens in order to prepare thin sections for later microscopic inspection. The cut end of samples were again polished and measured in order to ensure the smoothness and the parallelism of the specimens. Electrical strain gauges were then mounted onto the samples to measure axial and radial deformations during uniaxial compression tests. Figures 6.2 and 6.3 show the stress-time and stress-strain graphs respectively.

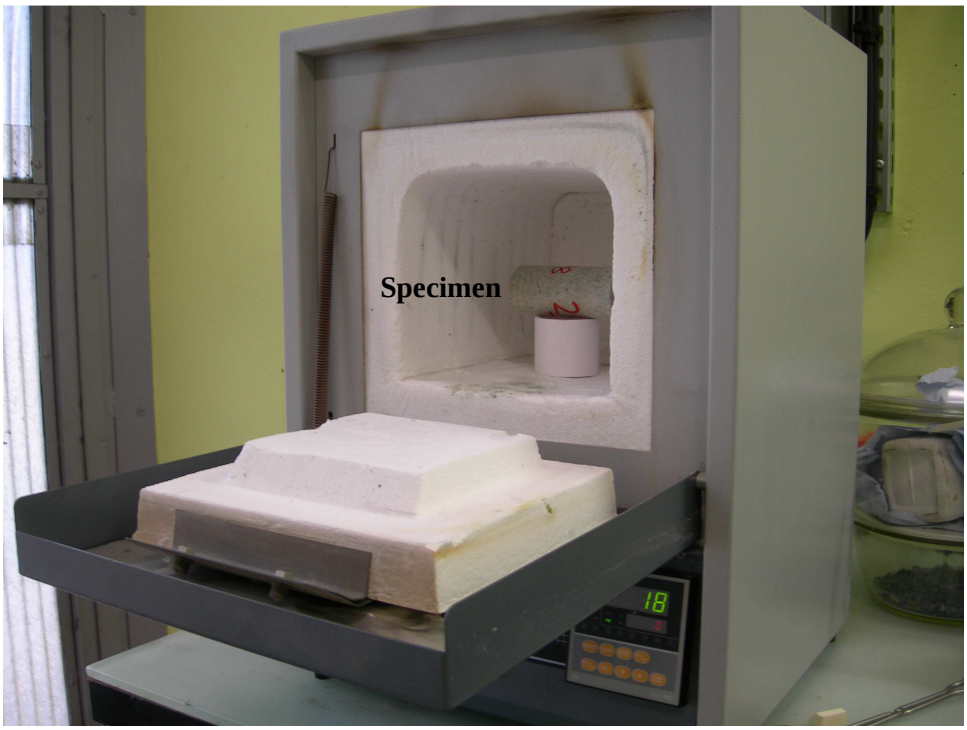

Figure 6.1: Programmable electrical furnace of LTPCM that was used to thermally treat gabbro specimens

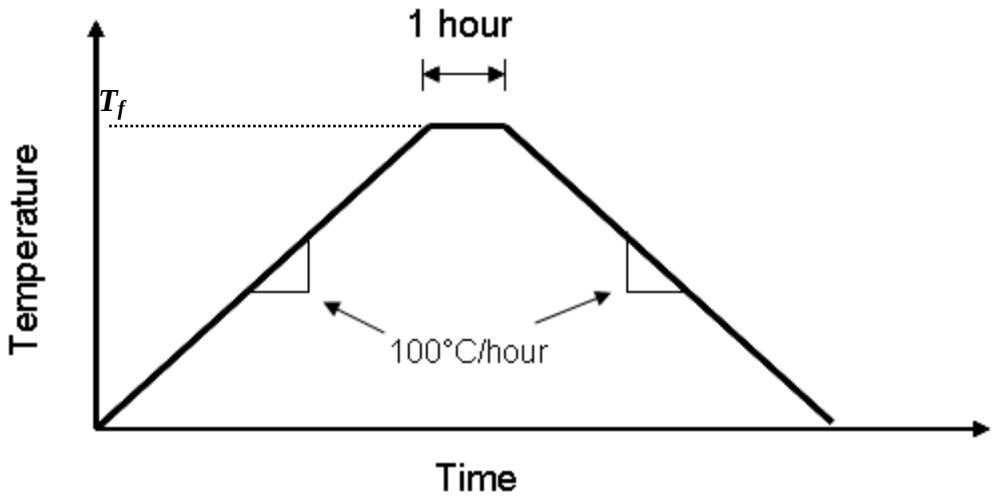

Figure 6.2: Diagram of thermal treatment of gabbro specimens. T_f is the final temperature that specimens reached in furnace.

6.4.3 Mechanical parameters

The uniaxial behavior of rock under compression depends mainly on microcracks induced by thermal loading (Lion et al., 2005). In order to estimate the thermal and the stress effects on the mechanical parameters of gabbro specimens, uniaxial compression tests were performed. The most noticeable modifications were generally a decrease of Young's modulus and the rock's compressive strength (Takarli et al., 2008; Nasseri et al, 2007). A decrease of Young's modulus is always observed for carbonated rocks (Ferrero et al., 2001 and Lion et al., 2005) whereas strength evolution is less definite as certain authors find either an increase (Mahmutoglu, 1998). The main purpose of this study was to evaluate how pre-heating rock specimens affect their mechanical properties. The possible changes to the elastic properties (Young's modulus and Poisson's ratio) and the strength characteristics were investigated by uniaxial compression tests.

After thermal treatment in an electric furnace under with planned temperature conditions, the specimens were uniaxially loaded to failure. The experimental setup and procedure for sample preparation for the uniaxial tests were presented in chapter four. The stress- deformation graphs were drawn using data recorded in the acquisition system of the Schenck press. The Young's modulus E and Poisson's ratio υ are calculated in the linear domain by:

$$E = \frac{\Delta\sigma_1}{\Delta\varepsilon_1} \tag{6.1}$$

and

$$\upsilon = -\frac{\varepsilon_3}{\varepsilon_1} \tag{6.2}$$

where $\Delta\sigma_1$ is the difference of stresses in the linear part of the stress-deformation graph, and $\Delta\varepsilon_1$ is the difference of the corresponding deformations. Furthermore, ε_1 and ε_3 are, respectively, the axial and lateral strains. Figures 6.3 and 6.4 show the stress vs deformations and stress vs volumetric deformation graphs for thermally and mechanically damaged as well as intact specimens. The stress–time graph of these tests is presented in figure 6.5. The comparative results are presented in table 6.1 and in figures 6.6 and 6.7.

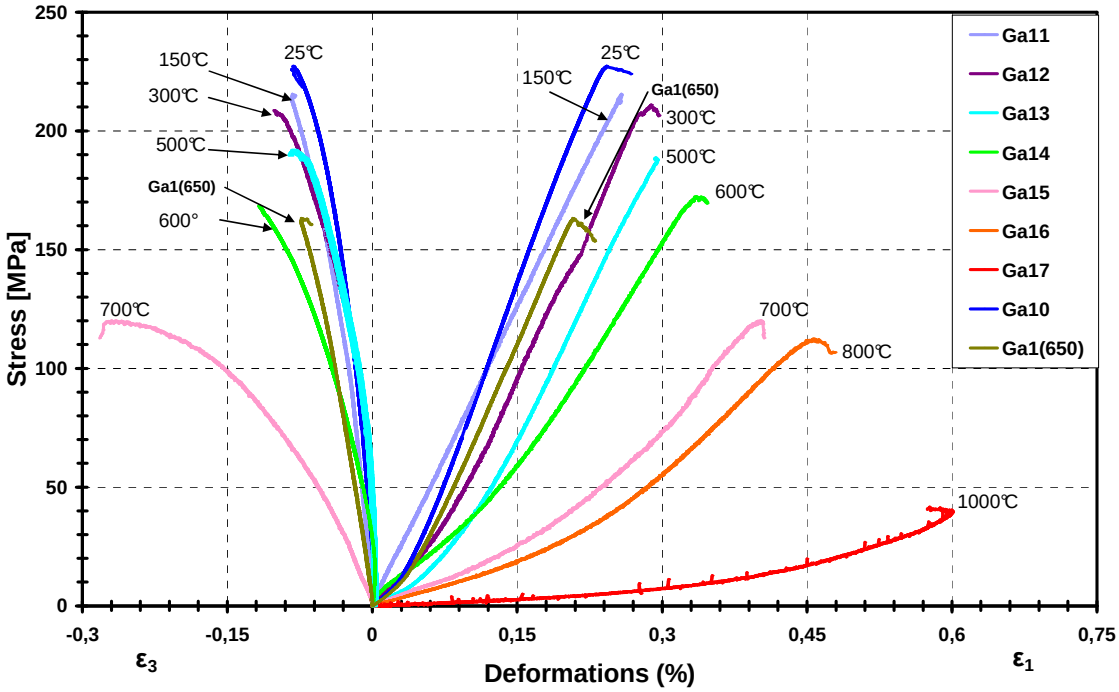

Figure 6.3: Comparison of stress-deformation records of thermally treated, mechanically damaged and intact gabbro specimens during simple uniaxial compression tests

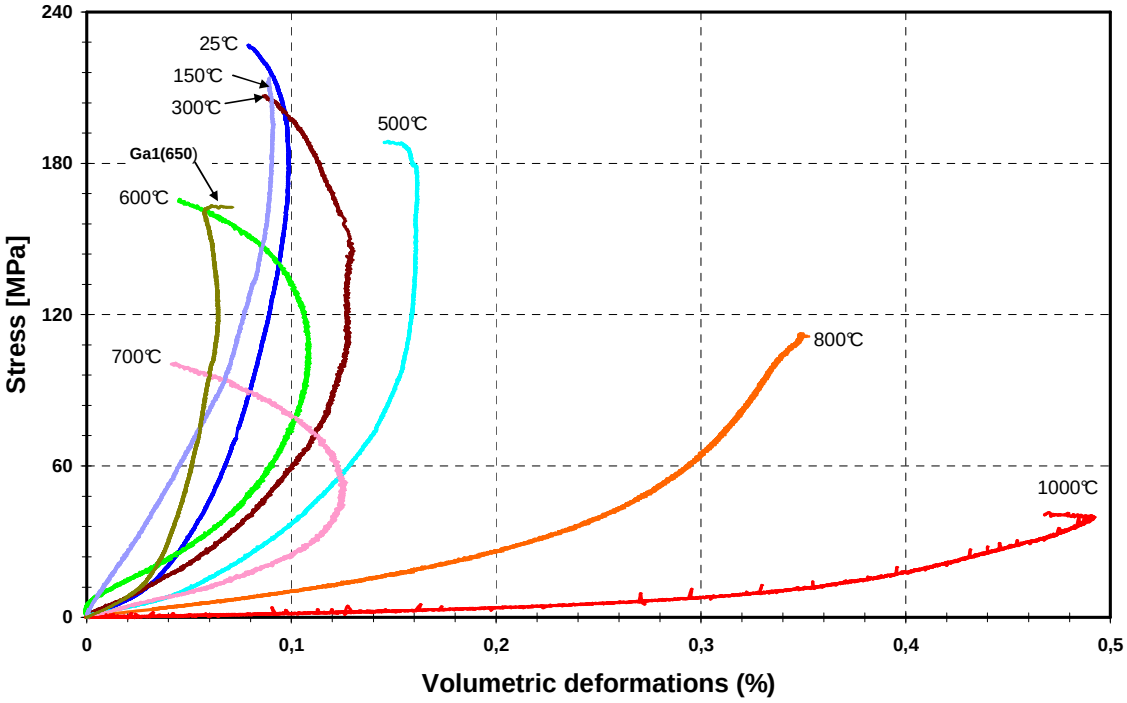

Figure 6.4: Comparison of stress–volumetric deformation of thermally treated, mechanically damaged and intact gabbro specimens during simple uniaxial compression tests

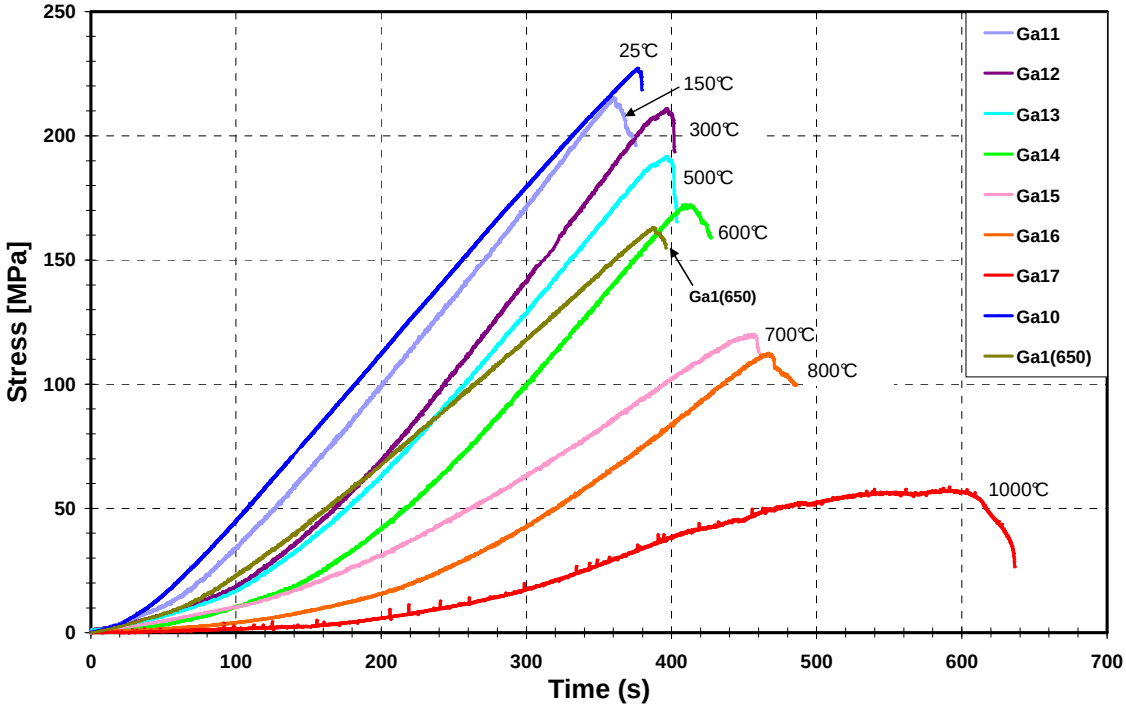

Figure 6.5: Comparison of stress-time curves of thermally treated, mechanically damaged and intact gabbro specimens during simple uniaxial compression tests

Table 6.1: The changes in mechanical parameters of thermally treated gabbro and a comparison of the results for intact and mechanically damaged gabbro

No. Specimens	Temperature (℃)	Uniaxial Strength [MPa]	Elasticity Modulus [GPa]	Poisson's ratio
Ga10	25	225	85	0,18
Ga1 (650)	25	160	72	0.25
Ga11	150	216	84	0,22
Ga12	300	211	66	0,19
Ga13	500	191	53	0,15
Ga14	600	172	45	0,33
Ga15	700	118	22	0,52
Ga16	800	112	18	0.03?
Ga17	1000	42	2.6	0.04?

Intact specimen	Mechanically damaged	Thermally damaged

? **Values are not reliable, for details see section 6.4.3 and figures 6.9 and 6.10.**

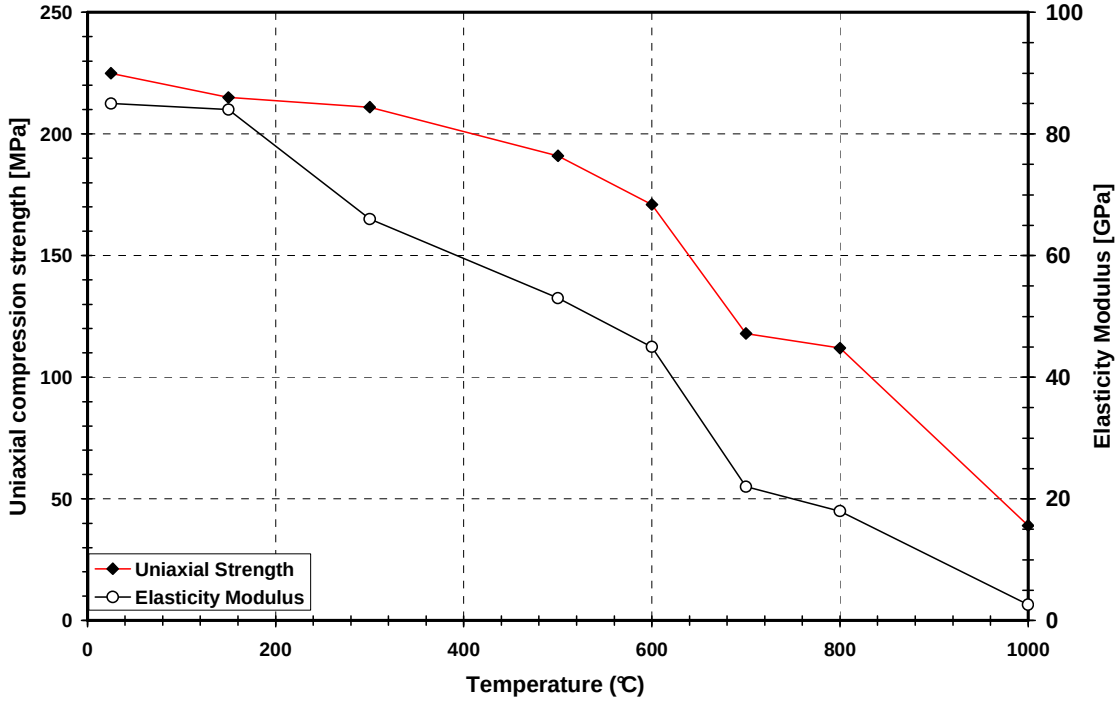

Figure 6.6: Changes in maximum uniaxial compression strength (ucs) and elasticity modulus of thermally treated gabbro specimens

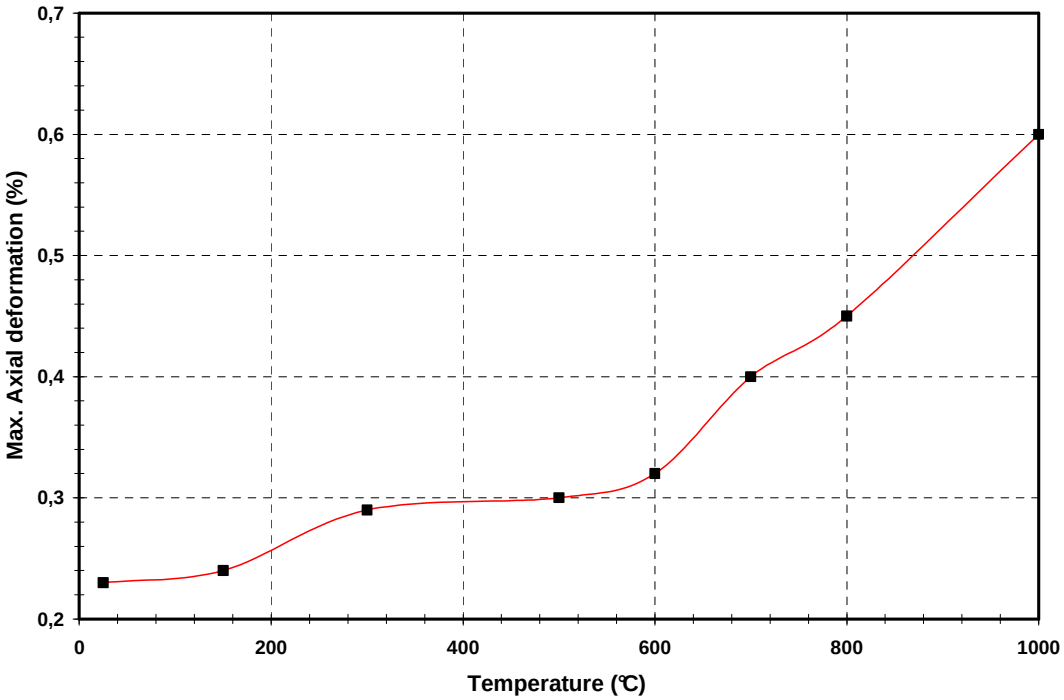

Figure 6.7: Maximum axial deformation of thermally treated gabbro based on electrical resistance gauge measurements

Young's modulus and the maximum uniaxial compression strength of specimens decrease continuously when the loading temperature increases, much like the elastic wave velocity. A relatively sharp decrease is observed in the maximum uniaxial strength above 600°C. However, the slope of the Young's modulus does not show a significant variation at this point. On the other hand, a drastic decrease was seen in the Young's modulus after 150°C. The axial strain changes were recorded by LVDT and electrical resistance gauges and show a good agreement with the strength and elastic wave velocity changes (figure 6.7). In fact, the axial deformation rate increases constantly up to 700°C at a low rate and then increases sharply with further temperature increases.

The evolution of Poisson's ratio is more complicated: Poisson's ratio variations are plotted in figure 6.8. Poisson's ratio decreases gradually until the temperature reaches 500°C and then increases sharply at 600°C and continues to 700°C. At higher temperatures the Poisson's ratio cannot be computed due to abnormalities in lateral deformations. Therefore the results of lateral deformations of specimens that were heated to over 700°C are not reasonable and we have not considered them in this work. Figures 6.9 and 6.10 show the stress vs deformation graphs of specimens Ga16 and Ga17 that were heated to 800°C and 1000°C, respectively. As the graphs show, the lateral strains of the specimens exhibit a strange behavior during uniaxial loading and require further investigation. Preparation of the specimens in different directions and measuring the lateral deformations using several gauges is recommended for any such future research at temperatures above 700°C.

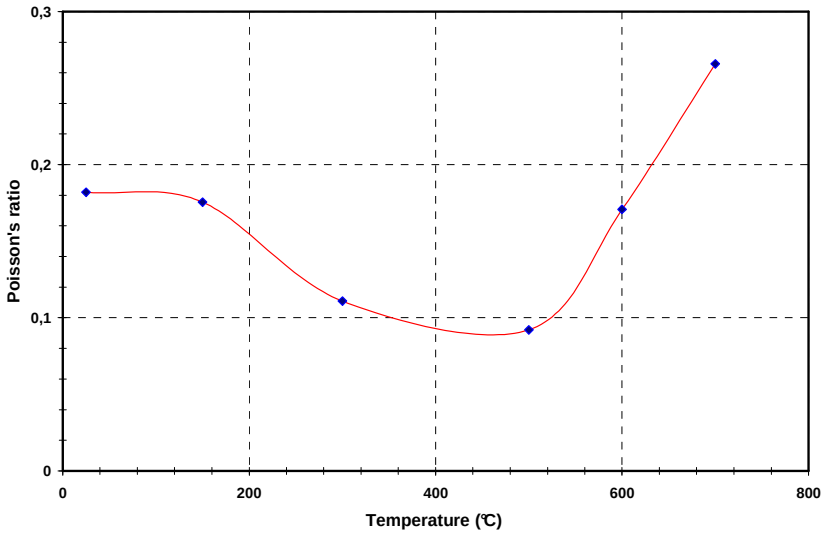

Figure 6.8: Poisson's ratio changes versus temperature of gabbro specimens

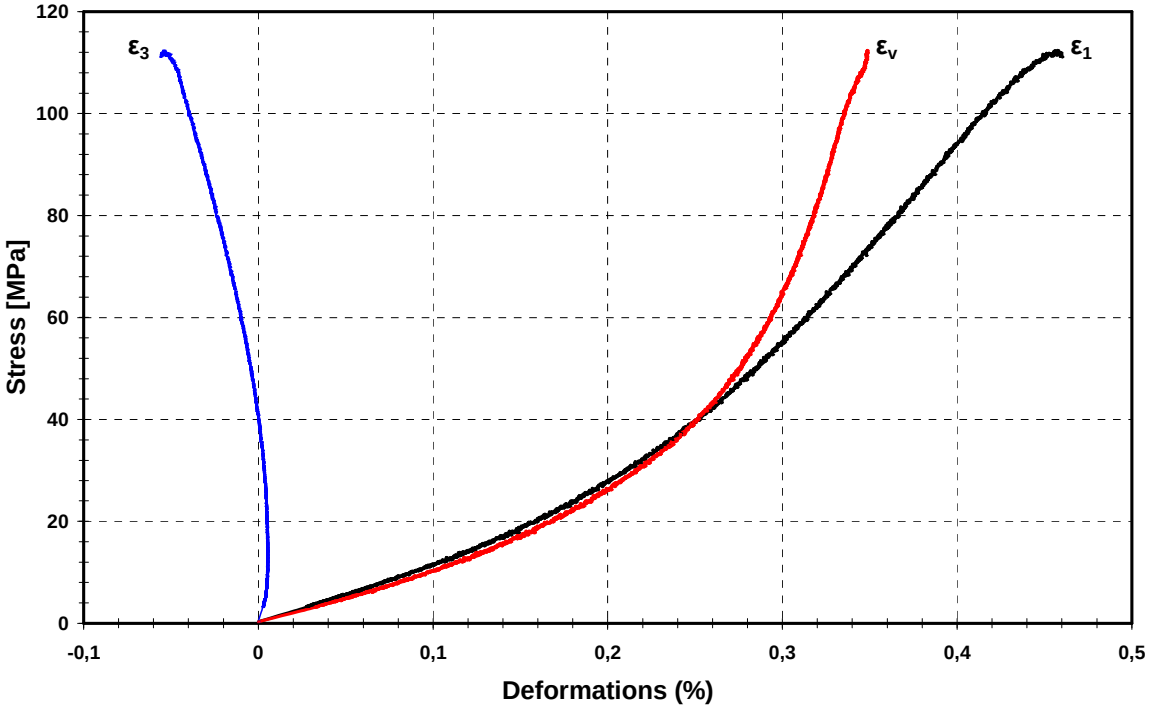

Figure 6.9: Stress- deformation graphs of gabbro specimen Ga16 heated to 800℃. Notice the strange evolution of lateral deformation before 48 MPa stress.

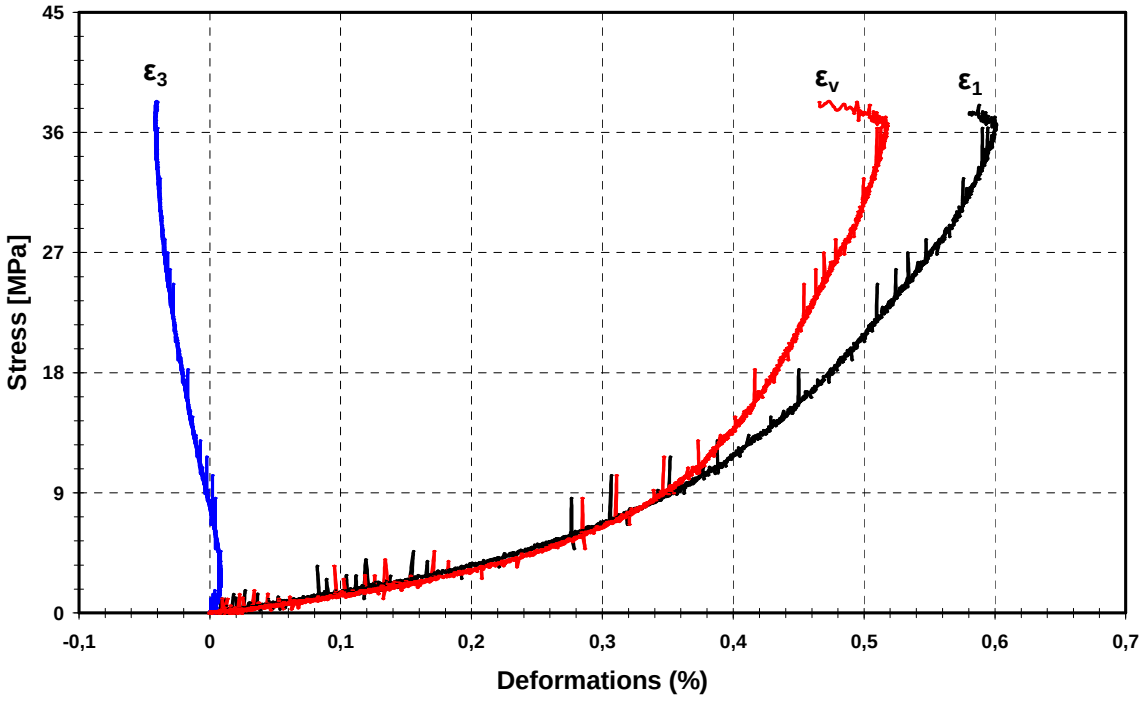

Figure 6.10: Stress- deformation graphs of gabbro specimen Ga17 heated to 1000℃. Like specimen Ga16, before 9MPa stress, the lateral deformation gauge records contraction rather than expansion.

6.4.4 Elastic wave velocity

After cooling, the longitudinal (Vp) and the shear wave (Vs) velocities of specimens were measured. The velocities of elastic waves for thermally damaged samples were also measured before conducting uniaxial compression tests. The procedures of elastic wave velocity measurement were presented in chapter 4. The results of these measurements are shown in table 6.2. Figures 6.11 and 6.12 show the elastic wave changes after thermal treatment and the normalized values, respectively.

Table 6.2: Elastic wave velocity changes during thermal treatment of gabbro specimens.

No. of Specimens	Temperature (℃)	Before (intact)		After (thermally treated)		Normalized values	
		Vs (m/s)	Vp (m/s)	Vs (m/s)	Vp (m/s)	(Vs)	(Vp)
Ga17	1000	3906	6593	1050	1360	0,27	0,21
Ga16	800	3926	6608	1621	2400	0,41	0,36
Ga15	700	3915	6607	2105	2800	0,54	0,42
Ga14	600	3927	6623	3245	4300	0,83	0,65
Ga13	500	3969	6300	3500	4600	0,88	0,73
Ga12	300	4005	6450	3600	5300	0,90	0,82
Ga11	150	3962	6393	3790	6025	0,96	0,94
Ga10	25	4150	6666	4150	6666	1	1

A review of the results shows that thermal treatment decreases the two elastic waves velocities. An increase of temperature decreases the elastic wave velocity at a slow rate up to 600°C and more significantly for higher temperatures. This is mainly due to the progressive propagation of microcracks in intercrystalline and intracrystalline components. A sharp decrease takes place between 600°C and 700°C. Plotting of the normalized values shows that the decrease of the Vp is more than that of the shear wave velocity for all of the temperatures. However, a large difference shows up between temperatures of 300°C and 700°C. Therefore, we can conclude that for gabbro the Vp is generally more affected by thermal loading than the Vs.

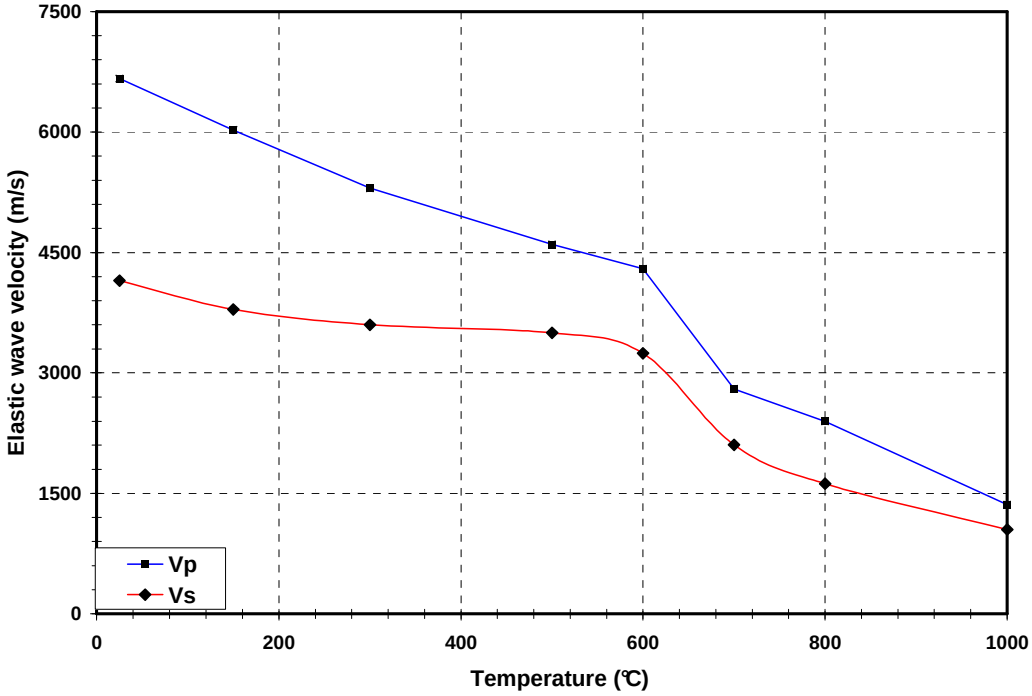

Figure 6.11: Elastic wave velocity changes during thermal treatment of gabbro specimens

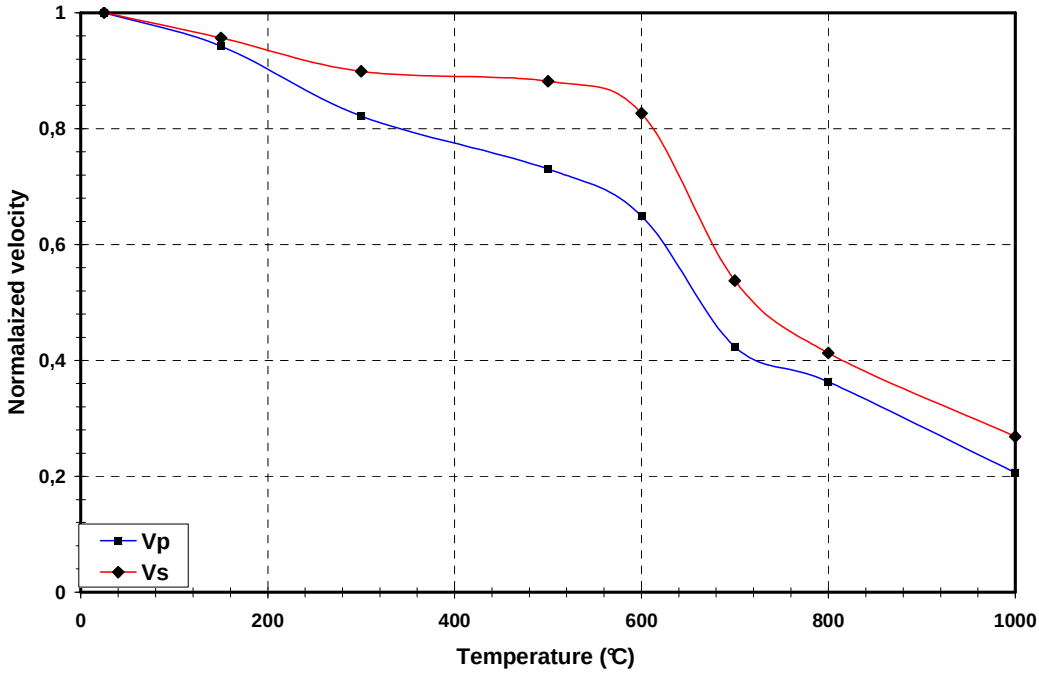

Figure 6.12: Normalized velocities of thermally treated gabbro specimens

From the mechanical and physical parameter changes of thermally treated gabbro, three different zones can be distinguished (figure 6.13):

Zone I: Degradation of the mechanical and physical parameters at a low rate between ambient temperatures up to 600°C. In this zone microcrack damage increases with an increase in the heating temperature at a low and constant rate.

Zone II: This zone begins at 600°C showing a sharp decrease in uniaxial strength and elastic wave velocities. However, this drastic reduction point is not noticeable in the elasticity modulus.

Zone III: For all the specimens treated at temperatures higher than 700°C, a progressive decrease in the measured parameters was observed. After 700°C, degradation in measured parameters continued at a constant rate and, around 1000°C, the specimen entirely softened due to microcracks and different phase transformations. This issue will be discussed in the following sections.

According to the stress-strain graphs, the behavior of samples thermally treated below 600°C are comparable to that of the unheated samples. Nevertheless, for the samples that were treated at temperatures above 700°C, strange lateral deformations were observed.

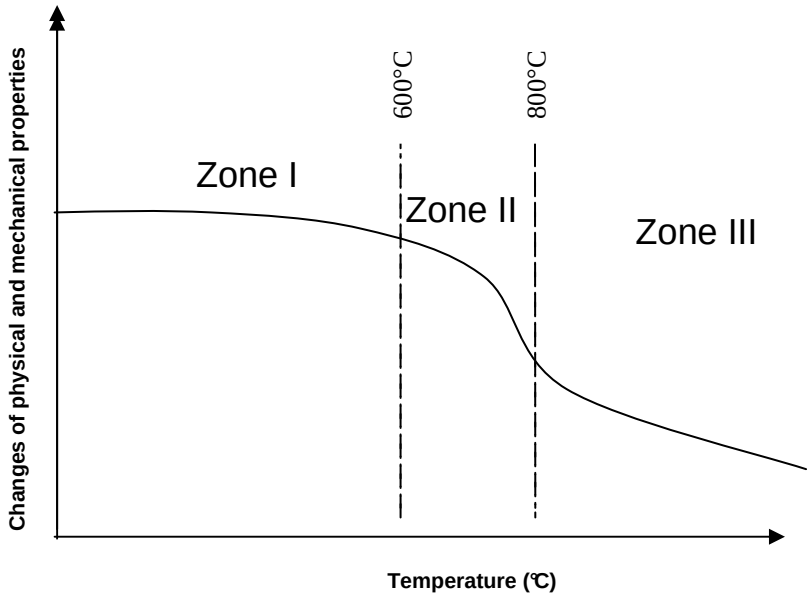

6.13: Zones of changes in physical and mechanical parameters during thermal treatment

6.4.5 AE monitoring

The acoustic emissions were monitored during uniaxial compression tests. The purpose of this study is to investigate AE activity during simple uniaxial loading of pre-damaged gabbro rock and to compare it with the AE behaviour during uniaxial loading of intact specimens. Comparing the AE records of thermally and mechanically pre-damaged specimens are the other objective of this research. Acquisition of AEs was performed as described in Section 5.3.2. The recording system and parameters were the same and the loading rate for all the specimens was constant at about 10^{-4} mm/s.

The Schenck press was used to supply the mechanical loading while electrical resistance gauges and LVDT were used to measure axial and lateral deformations. For AE monitoring four sensors were attached directly onto the surface of the sample and Sofranel SWC couplant 7 was used as an ultrasonic couplant. This gives good coupling onto the sample's surface and allows direct ray paths to be used during AE measurements. The AE events were recorded continuously up to specimen failure.

The previously described MISTRA 2001 system, manufactured by the Physical Acoustic Corporation (PAC), was used for the AE measurements. Considering background noise, the post-amplifier trigger level was set to 45 dB. Time parameters for AE waveforms include Peak Definition Time (PDT), Hit Definition Time (HDT) and Hit Locking Time (HLT). In order to obtain proper data, these parameters were set to 50, 200 and 300μs respectively. Based on sensor characteristics and preliminary tests, the bandpass filter was set to between 200 to 500 kHz. Other parameters of the system were like those of the tests presented in chapter 5.

Ten tests were performed on thermally damaged gabbro specimens. The preferred size for thermal damage tests was 80 mm height and 40 mm diameter. However, a few tests were carried out on specimens of gabbro with a height of 140mm and a 70mm diameter. One uniaxial compression test with AE monitoring was also performed on a stress pre-damaged gabbro specimen. The AE records during uniaxial loading of 8 thermally treated gabbro specimens and the mechanically damaged specimen (Ga1(650)) are given in figure 6.14, which shows the accumulated AE event number versus time, and figure 6.15, which shows the AE energy versus deformation.

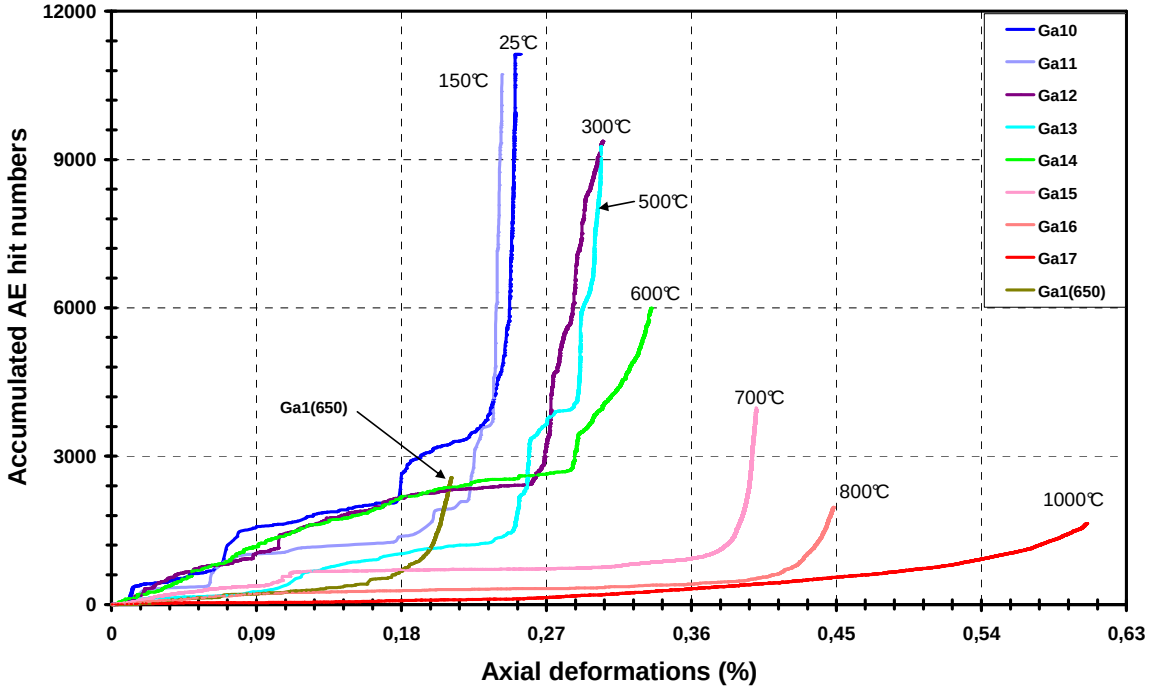

Figure 6.14: Accumulated AE hit records of intact, mechanically damaged and thermally treated gabbro specimens during simple uniaxial compression tests

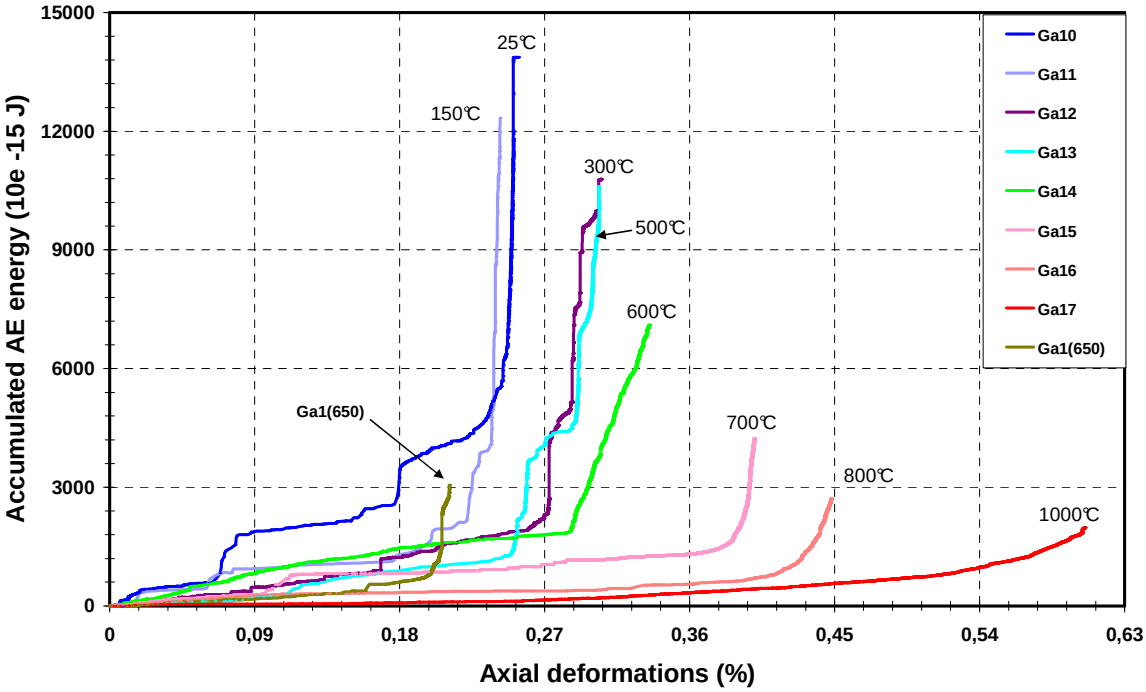

Figure 6.15: Accumulated AE energy parameter of intact, mechanically damaged and thermally treated gabbro specimens during simple uniaxial compression tests

The plots of the AE parameters indicate that the behaviour of the AE events from thermally treated and mechanically damaged specimens are markedly different from those seen in the intact rock. The acoustic emission hit numbers in thermally treated rocks are considerably less than those in intact samples. The number of AE hits drastically decreases as temperature increases. The final shapes of the AE accumulated hit number and AE energy versus time graphs are notably different for the pre-treated specimens compared to those of the intact rock, as are the steps of the AE events. The graphs of the specimens that were treated to more than 600°C are gentler and the steps are not visible based on the accumulated number and energy parameters of AE events. For these types of specimens, the AE events are silent up to 90 percent of the ultimate stress level and then they start to increase gradually to failure. Plotting of the AE accumulated energy versus time shows almost the same results.

A dramatic decrease of AE hit and energy parameters was seen for the mechanically damaged specimen; even though the uniaxial strength and elastic wave velocity of this specimen was reduced to a maximum of 25 percent, the number of AE events decreased to 70 percent in comparison to intact specimens. The characteristics of AE records are presented on table 6.3. Figure 6.16 shows the numbers of AE hits and the values of the AE energy vs temperature in the specimens that were thermally treated.

As noted in the previous chapter, by plotting the AE events of intact rocks, there were two sharp steps in the number and energy of events before the final step (at 95% of ultimate strength). The first step occurred when the stress level reached values of about 20 % and the second one when the stress level reached 50-60 % of the ultimate strength of the rocks. These two steps can be viewed as the crack initiation (σ_{ci}) and the crack damage (σ_{cd}) thresholds in the stress-deformation diagram presented by Martin in 1993 (Figure 5.1). In contrast to the sharp steps of AE events for intact rocks, the steps of the thermally treated specimens were gentler, especially for specimens that were heated above 600°C. For the specimen that was pre-damaged by ultra high triaxially loading, there were no visible.

The graphs of AE energy and AE hit number vs deformation and stress for all of the thermally treated specimens are given in appendix III.

Table 6.3: Characteristics of AE events of intact and thermally treated gabbro specimens during uniaxial compression tests

No. Specimens	Temperature (℃)	TTT(s)*	Numbers of AE Hits	Ac. AE Energy (10^{-15} J)
Ga10	25	379	11126	13870
Ga1(650)	25	405	2570	3051
Ga11	150	368	10723	12328
Ga12	300	367	9377	10787
Ga13	500	386	9271	10605
Ga14	600	407	5992	7097
Ga15	700	425	3977	4233
Ga16	800	448	1964	2713
Ga17	1000	466	1640	1982

* Total time of test

Intact specimen	Mechanically damaged	Thermally damaged

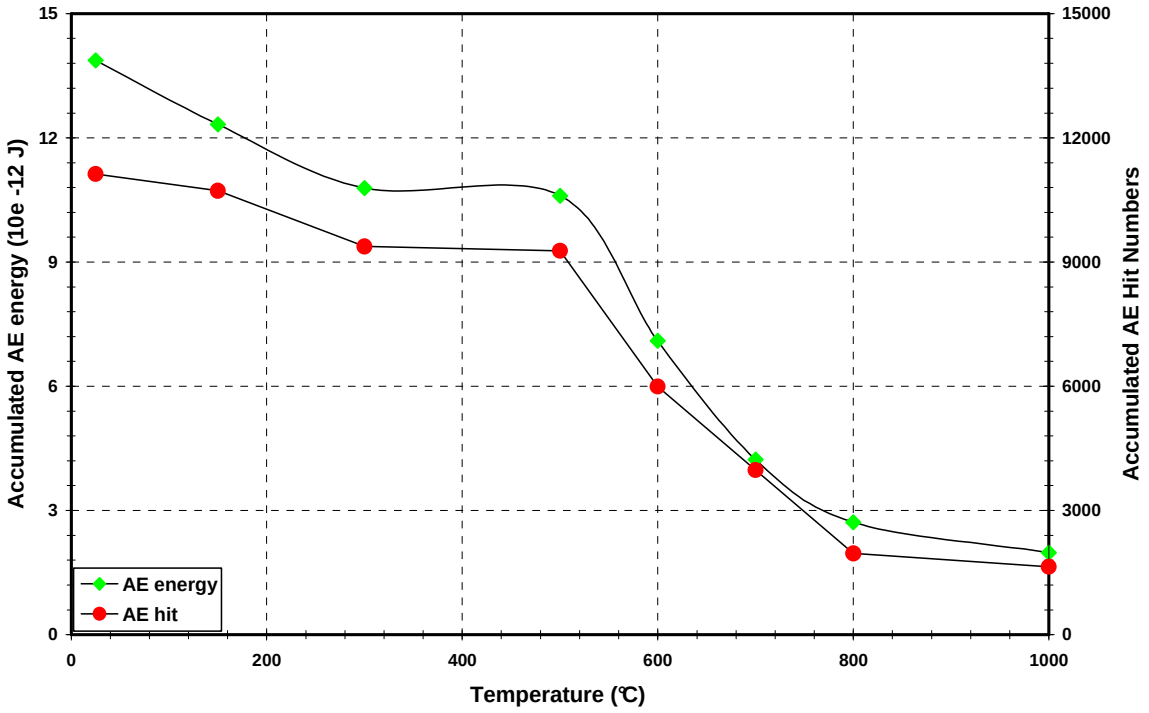

Figure 6.16: The variations of AE hit number and AE energy parameters for thermally treated gabbro specimens under uniaxial compression

6.4.6 Microscopic studies

The effect of temperature on rock properties has been widely studied at the laboratory scale (Heard and Page, 1982; Homand and Troalen, 1984; Homand and Houpert, 1989; Jansen et al., 1993; David et al., 1999; Ferrero and Marini, 2001; William et al., 2005; Chaki et al., 2008). The experiments have addressed two main components: the effect of temperature on the macroscopic properties (figure 6.17) and, secondly, microscopic studies on grain-scale effects. Our macroscopic tests were associated with a petrographic study that was performed using light microscope investigations in order to identify the rock structure and the microcracking mechanism. These investigations provide additional insight into the conventional laboratory tests. The light microscopy study of thin sections allowed us to enlarge microscopic images from thermally treated and stress damaged specimens.

After damaging the specimens, a small slab was cut and mounted in epoxy where the surface of the rock is normal to the cross-sectional surface. The chips were polished to making the specimens transparent. The polishing process allows the polarized and normal lights to pass through the polished rock slice.

Figure 6.17: A general view of thermally treated specimens after uniaxial testing. Notice the obvious colour change and failure pattern from the intact rock to the specimen thermally treated to 1000℃.

We examined the texture and the mineralogy of damaged samples to determine how the microcracks formed and how they degrade the mechanical parameters of the rock. The progressive thermal and stress damage can be seen at the mineralogical scale. During microscopic observations, different types of damage are recognized in thermally treated specimens. We found that four factors play a role in creating progressive thermal changes:

- Crystal boundary separation due to different expansion coefficients of minerals (figure 6.18),
- Separation of existing texture in minerals, for example, twinning, macles, intergrowths and so on (figures 6.18 and 6.19).
- Phase transformations of crystals and oxidation of Fe-, Mg- and Ti-enriched minerals, like pyroxenes, ilmenite and dioxide titanium (figure 6.18),
- Blow up of the small liquid intrusions due to an increase in the temperature (figure 6.19),

A thin section was prepared from a high stress damaged specimen in order to determine the effects of ultra high stresses on brittle gabbro. Generally, it is accepted that changes in the stress in a rock mass is the main cause of mechanical damage in rock. In this study the rock sample was loaded triaxially up to 2.35GPa axial stress and then physical and mechanical parameters were measured. In spite of the ultra high confining and deviatoric stresses, the damage in the rock was not substantial, according to the measured parameters. It seems, that the small deformations that occur due to a low porosity of rock and high strength of grains, play a key role in propagating the microcracks inside the specimen. Limited mechanical micro-fracturing is the basic cause of degradation of the mechanical parameters during high levels of triaxial loading. The different aspects and evidences of thermal effects and mechanical fracturing are shown in figures 6.18 to 6.20.

It should be emphasized that this study was performed on only one type of igneous rock; other rocks have different properties, such as crystallographic, texture and grain orientation, character of grain boundaries, porosity, grain size, and composition, all of which will affect their mechanical behaviour against thermal and stress effects. Extrapolation of the results from one type of rock to another will require more extensive research.

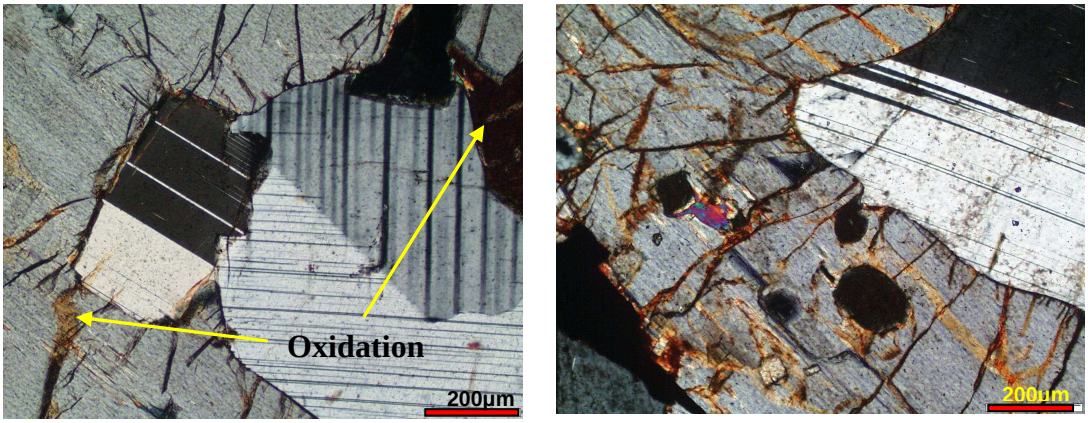

Figure 6.18: Evidence of oxidation in microcracks at 500℃ (left) and its vast distribution in Pyroxene minerals at a temperature of 800℃ (right)

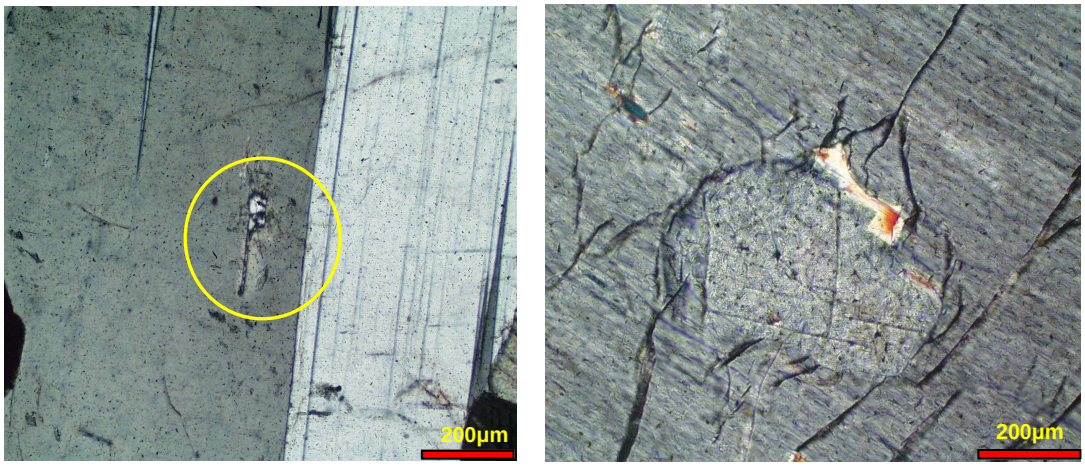

Figure 6.19: Evidence of a liquid inclusion blow up in plagioclase (left). On the right, the effect of thermal expansion differences between pyroxene and plagioclase at 300℃

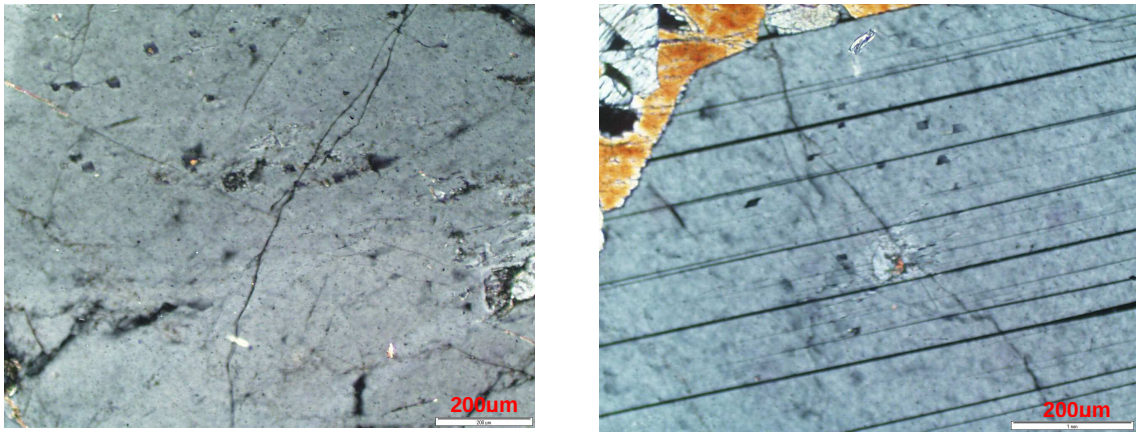

6.20: Photos taken from a gabbro specimen that was subjected to ultra high stresses (650 MPa confining and 2350 MPa axial stresses). Notice the sharp edge of the micro cracks and their orientation that is almost perpendicular to the original macles in plagioclase crystal (right).

6.5 Discussion

We studied two common types of damage in gabbro, the first due to temperature and the second stress. Four different techniques were used to assess damage in rock in this research, namely, AE monitoring, elastic wave velocity changes, uniaxial compression tests and microscopic investigation. Ten gabbro specimens were heat treated from 150°C to 1000°C in a furnace at rates of 100°C/hour and 50°C/hour. In addition, one gabbro specimen was damaged by ultra high triaxial loading (0.65GPa confining stress and 2.35GPa axial stress).

In general, thermal treatment degrades the mechanical and physical parameters of rock due to microcrack propagation, which becomes more pronounced. The maximum strength, elastic modulus, and elastic wave velocities decreased during thermal loading; however, the rate of degradation of the parameters and the drastic changes in the graphs need explanation. The probable mechanisms and the causes of these two types of damages are discussed at below.

6.5.1 Volumetric thermal expansion

The thermal expansion coefficient α_v, defined by $\alpha_v = (1/v)(\partial v/\partial T)_p$ is used to express the volume change of a substance due to a temperature change. When the rock is heated, micro stresses develop because of the difference in the thermal expansion coefficients of the minerals and also within each mineral, because the expansion varies along the crystallographic axes. It has been suggested that thermal loading of rocks generates localized fracturing, or microcracking, via two different mechanisms (Chaki et al, 2008). Firstly, mismatched thermal expansion of adjacent crystalline grains in a homogeneous temperature field may result in stresses large enough for microcrack formation. These types of micro-fractures are termed thermal cycling cracks. Secondly, cracking can also result when thermal stresses due to an inhomogeneous temperature field exceed the local strength of the rock (thermal gradient cracks). A sufficient density of these microcracks can potentially coalesce into macroscopic fracture patterns.

Gabbro is a polycrystalline rock, containing minerals with different thermal expansion coefficients. This rock contains two types of pyroxene and calcium enriched plagioclases. Demelza (1997) indicated that there is a wide range of data for α_v values of Mg–rich orthopyroxens from 20.8×10^{-6} K^{-1} to 36×10^{-6} K^{-1}. The values of 32.2 and 27.5 $\times10^{-6}$ K^{-1} were calculated by Helmez (1997) for ortho- and clino-pyroxene crystals, respectively.

Plagioclases are the matrix minerals of the gabbro examined in this study. The value of α_v for plagioclases lies between 9 and 15×10^{-6} K^{-1} (Fei, 1995). Thus, there is a significant difference between α_v values of the matrix and the pyroxenes (the α_v of pyroxenes are almost twice those for plagioclases). For ilmenite (FeTiO3), another minor mineral in this particular gabbro, the α_v value is calculated at around 10×10^{-6} K^{-1}. Considering the significant difference in volumetric thermal expansion coefficients of crystals, we conclude that this factor plays a major role in the degradation of the mechanical parameters of thermally treated gabbro rock especially at low temperatures (less than 600°C).

Mineralogical structure and grain size are other parameters that could affect thermal expansion. The phenomenon of intergrowth of crystals into each other intensifies the role of the thermal expansion coefficient. Since North African gabbro is an equigranular rock (all crystals are of approximately the same size), we believe that mineral size is not a dominant effect.

6.5.2 Oxidation and phase transformation

Chemical reactions, such as oxidation, and phase transformation are other phenomena that take place during thermal treatment of crystallized rocks. Oxidation of iron and magnesium-enriched compounds is a known chemical reaction at ambient pressure that also takes place in thermally treated rocks. Phase transformation is a phenomenon observed in thermally treated rocks; for instance, Chaki et al. (2008) mentioned obvious changes in the physical characteristics of thermally treated granite due to a phase transition in quartz, which occurs at 573°C and room pressure. Since North African gabbro lacks quartz, the oxidation of Fe-, Mg- and Ti-containing crystals plays a key role in altering the mechanical and physical parameters. According to microscopic observations, oxidation is a phase transition in this type of rock. Decomposition of calcium hydroxide, which takes place at about 450°C (Chen and Dollimore, 1995), is another aspect of phase transition in plagioclase.

Results of microscopic studies show oxidation in gabbro specimens treated at high temperature; this oxidation of minerals at ambient pressure begins at 500°C. The oxidation starts as a thin coat around the Fe-pyroxenes. With increasing temperature, oxidation develops on other crystals and finally, at around 800°C, there is oxidation of the inclusions containing Fe and Mg. The brown dotted points seen on the plagioclases in figure 6.18 are oxidized compounds.

6.5.3 The blow up of fluid inclusions

Based on microscopic investigations, the blow up of fluid inclusions is recognized as another cause for the observed decrease in the mechanical and physical parameters of thermally treated gabbro (figure 6.19). Fluid inclusions are small quantities of fluid, usually 5 – 30 μm along the longest axis, (liquid and/or vapor) trapped in mostly small cavities within minerals (Van den Kerkhof et al., 1991).

Fluid inclusions occur in many rock-forming minerals from most terrestrial environments. Theoretically, almost all minerals can be studied for fluid inclusions. Quartz is the ideal example of fluid inclusions in igneous as well as in metamorphic rocks particularly as quartz is ubiquitous in nearly all metamorphic rocks and contains the most inclusions. It is also stable at all metamorphic conditions within the crust. Figure 6.21 schematically shows the inclusion formation based on pressure and temperature conditions.

The basic reason for fluid inclusion studies is to identify the physico-chemical parameters, most notably of pressure and temperature (P – T), as well as fluid chemistry during trapping. However, in this research we considered the role of blow up in the degradation of the investigated parameters. Study of thin sections of gabbro showed that the blow up of fluid inclusions plays a minor role in the evolution of mechanical parameters of thermally treated rock. In fact, their small number and small size in comparison with the sizes of the crystals could be significant.

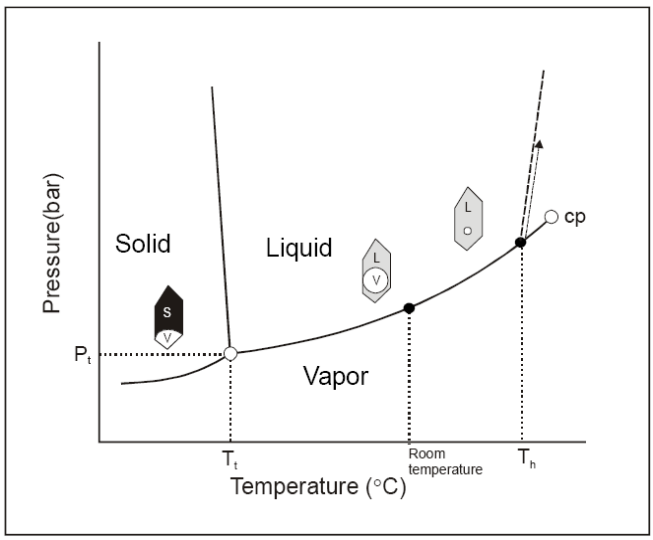

Figure 6.21: The P–T evolution of an aqueous fluid inclusion trapped at some pressure and temperature, then subsequently cooled down along a path of constant density

S = Solid, L=Liquid, V=Vapour, Th= homogenization temperature, Pt–Tt=Pressure and temperature at the Triple point of water; cp = critical point (Klemd, 1989).

6.6 Specimen size and heating rate effects

As previously noted for thermal tests we used cylindrical specimens 40 mm in diameter and 90 mm in height. The slow rate of heating (100 °C/hour) ensured that the observed changes were a result of only the temperature effects and not thermal gradients across the sample or thermal shock. However, a few tests were conducted on a larger sample of gabbro to check whether size affected the results. For this purpose, new samples were fabricated to 70 mm diameter and 140 mm height. The number of specimens and characteristics of test are summarized in table 6.4.

Table 6.4: Characteristics of uniaxial test on gabbro rock to study the effects of size and heating rate

No of specimen	Geometry L×D (mm)	Heating rate	Max. temperature (°C)
Ga12a	40×90	100°/hour	300
Ga12b	40×90	50°C/hour	300
Ga14a	40×90	100°C/hour	600
Ga14b	40×90	50°C/hour	600
Ga14c	70×140	100°/hour	600

The test results are shown in figure 6.22. Larger specimens show a more complex behaviour after heat treatment in the same manner. While both the uniaxial strength and elasticity modulus of the large specimens were higher than for the small samples, the elastic wave velocity showed lower values. Meanwhile, with a decrease of 45%, the P-wave velocity was more affected in the larger specimens after thermal treatment at temperatures higher than 600 °C. The decrease of S-wave velocity for the larger size (35%) is about twice that for the small specimens (18%).

A few tests were carried out using a lower rate of thermal heating. For this purpose two specimens with 40 mm diameter and 90 mm height were treated to 300°C and 600°C at a rate of 50°C/hour. The results are presented in figures 6.23 and 6.24.

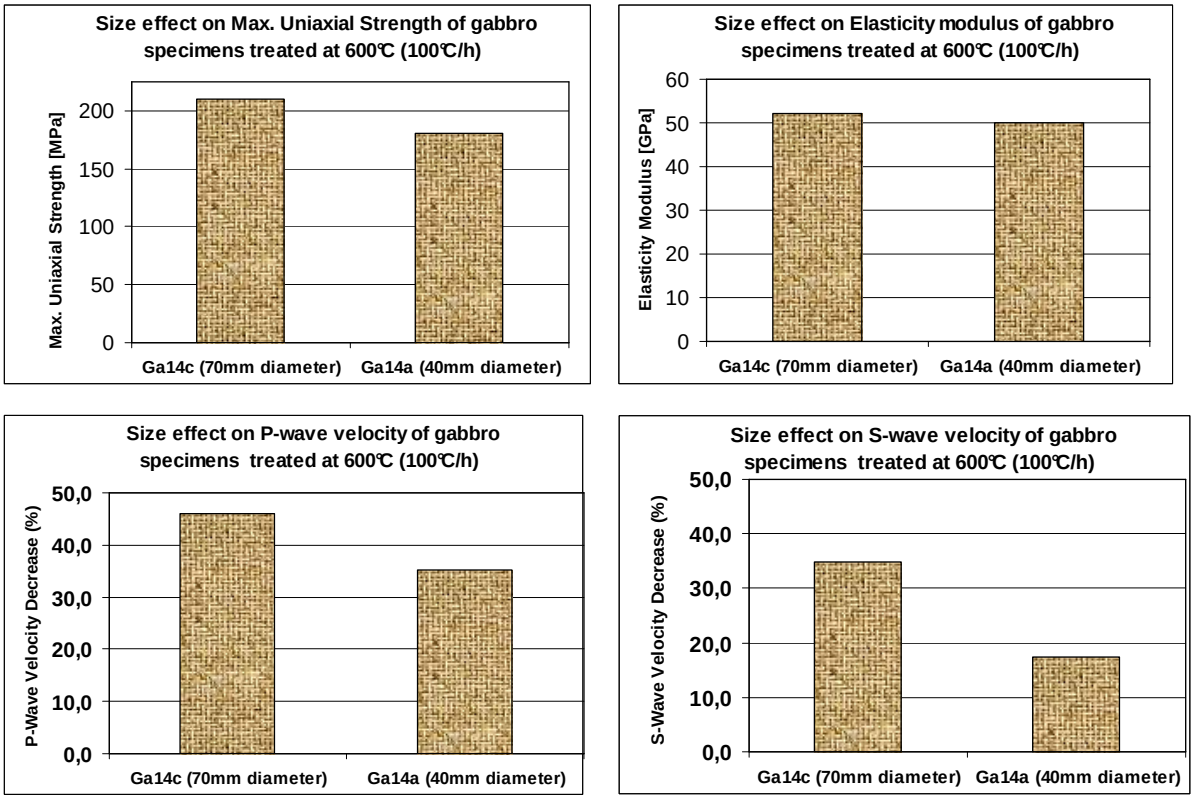

Figure 6.22: Sample size effect on maximum uniaxial compression strength, elasticity modulus, S-Wave and P-Wave velocities of gabbro rock. The specimens were heat treated up to 600℃ at a rate of 100℃/hour.

The mechanical parameters (σ_{max}. and E) were more affected at the slower rate of thermal heating up to both 300 and 600°C. In other words, the samples submitted to a low rate of thermal loading were more damaged. Regarding elastic wave velocity, there was a noticeable change. Shear wave and longitudinal wave velocity decreased at the same rate at 600°C for both sample sizes. However, there was a significant difference between the samples heated at rates of 50°C/hour and 100°C/hour up to 300°C. In summary:

- The heating rate affects the results at low temperatures more than at high temperatures,
- Decreasing the heating rate for both temperatures (300 and 600°C), induces more damage based on uniaxial and elasticity modulus measurements of gabbro specimens,
- P-wave velocity was more affected than S-wave at both rates of heating (50°C and 100°C/hour),
- Low rate heating affects the P-wave more than S-wave at 300°C; however, during heating to 600°C, the P and S wave values decrease in the same manner,
- It seems that 600°C is the critical temperature that separates the physical and mechanical degradation modes.

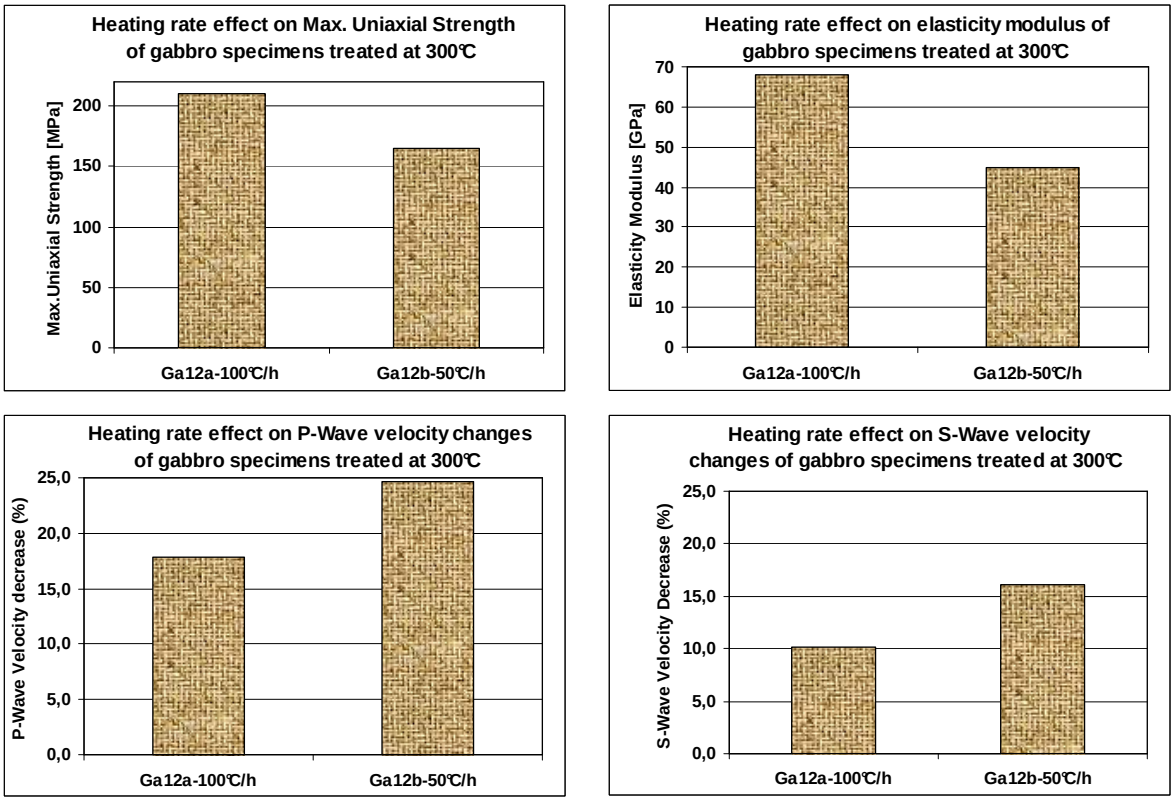

Figure 6.23: Heating rate effect on uniaxial strength, elasticity modulus, S-Wave and P-wave velocities of gabbro rock. The specimens were heat treated up to 300℃.

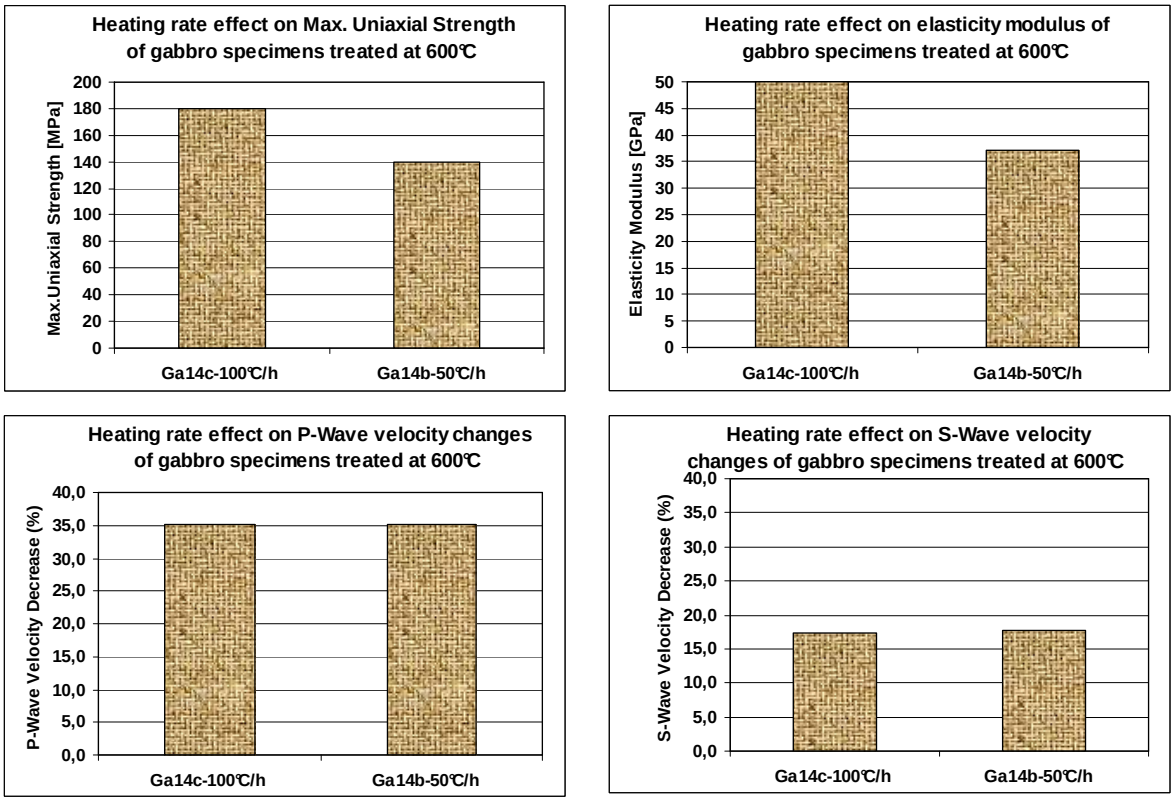

Figure 6.24: Heating rate effect on uniaxial strength, elasticity modulus, S-Wave and P-wave velocities of gabbro rock. The specimens were heat treated up to 600℃.

6.7 Comparison of the two types of damage

A brief comparison of the two types of damage is presented. We succeeded in preparing a set of gabbro specimens in which irreversible thermal or mechanical cracking was induced. Acoustic emission, elastic wave velocity and uniaxial tests as well as microscopic investigations were performed to measure each type of damage. From these investigations, it was observed that thermal treatment and stress damage have a strong influence on the mechanical and physical parameters of the tested rock. However, the degree and quantity of damage based on these parameters were significantly different. A comparison and summary of these observations is given below:

- The main difference between the mechanically damaged (MD) and thermally damaged (TD) samples is in the alterations in the elastic wave velocity. Based on elastic wave velocity measurements, the velocity of highly stress damaged specimens (σ_1=2300 and σ_3=650 MPa) were comparable with 150°C thermally damaged specimens. Nevertheless the maximum uniaxial strength and elasticity modulus of this specimen was comparable with thermally damaged specimens at 600°C. In other words, the elastic wave velocity is a more sensitive parameter of thermal treatment than uniaxial strength.
- The AE hit number also shows large differences between mechanically damaged and thermally damaged specimens. The number of AE hits decreased when thermal treatments were increased. A drastic decrease in the AE hit number and energy parameters could be seen in the specimens treated to over 600°C; however, the number of AE events in the MD specimen was less than in the TD specimen treated to 700°C. This leads us to conclude that mechanical damage has a greater effect on the AE parameters than thermal treatment.
- Thermal and mechanical damage not only affect the number of AE events, they also cause a big difference in the reaction steps that we have identified in this research: The first two reaction steps did not take place, based on accumulated AE hit and energy, during uniaxial tests on the mechanically damaged specimen Ga1(650), and the final step is also gentler than in the intact specimens. However, for thermally treated rock, the steps disappear after 700°C. Therefore we can conclude that mechanical damage affects the AE sources.

- Another difference between the two types of damage investigated is in the existence of cracks relative to crystal grains of the rock. Cracks in MD specimen were mostly propagated inside the plagioclases, whereas in the TD specimens the cracks were visible around the crystals or developed within existing micro structures. Figure 6.25 shows the differences between the mechanical and thermal damage at the microscopic scale.

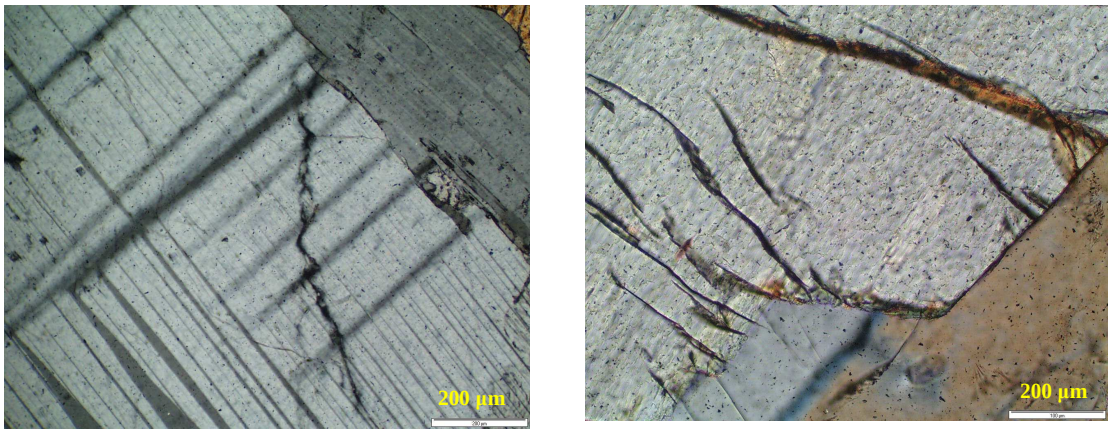

Figure 6.25: Photomicrographs of mechanically damaged (a) and thermally treated (b) gabbro specimens. Note the extensive grain-boundary damage and separation at some boundaries. The rock has been heat treated to 500℃ and slight oxidation has appeared in existing cracks.

6.8 Concluding remarks

The effect of thermally and stress induced microcracks on the mechanical and physical parameters of gabbro rock was studied. Uniaxial compression tests, elastic wave velocity measurement, thin section investigations and acoustic emission monitoring were carried out. The conclusions of the experimental studies are as follows:

1. Thermal treatment of gabbro affects the deformation and strength under uniaxial compressive stress conditions. The gabbro specimens thermally treated above 150°C showed significant reductions in the measured parameters. The strength of specimen heat treated up to 600°C is 20% less than in intact rock. A drastic decrease in uniaxial strength was observed in the specimens treated to temperatures higher than 600°C. However, the elasticity modulus decreases at a constant rate with respect to an increase in temperature. The changes in the elastic wave velocities were comparable to the strength reduction rates.

2. Comparing the acoustic emissions data for intact and thermally treated samples showed a considerable difference in the number and steps of acceleration of AE events. It

appears that microcrack evolution due to thermal damage plays a key role in decreasing the AE hit number during uniaxial tests on heated specimens. The AE records of intact and thermally treated specimens below 600°C are comparable. On the other hand, there is a significant difference between the records of specimens heated to over 600°C and the unheated gabbro.

3. Investigation of the sample size and heating rate effects on the above parameters clearly show a significant difference; the heating rate plays a more definitive role in low temperature treatment than at higher temperatures. Decreasing of heat rate to reach both of the final temperatures (300°C and 600°C), caused more damage in the uniaxial strength and elasticity modulus of gabbro specimens. P-wave velocity was more affected than S-wave velocity during heat treatment at a rate of 50°C and 100°C/hour Low rate heating to a temperature of 300°C caused a difference between the P and S wave values; however at 600°C, the P and S wave values decreased by the same percentages.

4. The decrease in the AE hit number is a more competent means of showing the differences in thermally treated and stress induced gabbro specimens. Plotting the accumulated AE energy and hit versus time, reveals that the form of the thermally damaged specimen graphs are gentler than the AE records for the stress damaged specimen. The main difference between the MD and TD samples is in the elastic wave velocities; based on the elastic wave velocity changes, the highly stress-damaged specimen (σ_1 = 2350 and σ_3 = 650 MPa) was comparable to the 150°C thermally-damaged specimen. On the other hand, the maximum uniaxial strength and elasticity modulus of the ultra high stress damaged rock is comparable to the specimen that was thermally damaged at 600°C.

5. Finally based on all the parameters that were investigated, we concluded that the temperature of 600°C is a critical temperature that causes physical and mechanical degradation in this type of gabbro. However, it should be emphasized that this study was conducted on only one type of intrusion rock; others have different properties, such as crystallographic, texture and grain orientation, character of grain boundaries, porosity, grain size, and this composition will affect their mechanical behaviour when subjected to thermal and stress effects. Extrapolation of the results from one type of rock to another will require more extensive research.

Chapter 7

Conclusions and Perspectives

7.1 Conclusions

Laboratory experiments were carried out to study the damage evolution and behavior of granite and gabbro rock specimens under compression. The Lavasan granite samples were chosen adjacent to the Mosha Fault, which located north of Tehran and the gabbro was selected from a few construction rocks that came from North of Africa (Algeria). Simple uniaxial compression, triaxial and Brazilian test have been performed on selected rocks. For all these tests, acoustic emissions were recorded continuously during loading. Axial and lateral displacements were also measured using electrical strain gauges and LVDTs. This work performed in the framework of failure prediction in stress induced rock specimens by monitoring physical precursors. Since Infrared Thermography is one of the newly developed methods in this field, a few infrared measurements were carried out on Lavasan granite under cyclic loading, using the facilities of LMS in Paris. The main results of these laboratory investigations can be sorted in four main categories:

1. General characteristics, physical and mechanical parameters of selected rocks:

- From a petrology point of view, Lavasan granite is a medium size intrusion rock with alkali rich plagioclase, quartz and mica minerals. Some of Fe- and Mg-rich minerals are slightly altered to secondary minerals such as amphibole, which give a pale green colouration to the rock mass. North African gabbro is a well crystallized two pyroxene (ortho- and clino-pyroxenes) gabbro with Ca^{2+} rich plagioclases.

- According to uniaxial tests, the strength of gabbro is more than twice as high as that of the granite. The average uniaxial compression strengths for granite and gabbro are about 130 MPa and 225 MPa, respectively. The average elasticity modulus for granite is 30GPa and the average Poisson's ratio is about 0.27. For gabbro, the elasticity modulus is about 90 GPa with a 0.21 Poisson's ratio. Brazilian tests were performed on two different sizes of gabbro specimens and the unconfined tensile strength for gabbro rock was obtained about 12 MPa. Based on these tests, we concluded that the size of the specimen does not play a major role in the tensile strength. The primary (Vp) and the secondary (Vs) elastic wave velocities are, respectively, 4050 and 2537 m/s for granite rock and 6560 and 4080 m/s for gabbro rock.
- Two triaxial tests were also performed under ultra high stresses using a Giga press. RocLab software was used to calculate the Hoek-Brown criteria and to plot Mohr-Coulomb and stress path envelopes. The maximum axial stress of gabbro rock is about 1480 MPa under 200 MPa of confining pressure. The cohesive strength of gabbro in this condition is 68 MPa and the angle of internal friction is about 43 degrees.

2. Acoustic emission monitoring during uniaxial and Brazilian tests:

- The most important contribution of AE to civil engineering is that it can provide early warnings of severe, sudden failures. Acoustic emissions can detect the accumulation of micro damage inside components, especially under service conditions. Acoustic emission tests were carried out on loaded rock samples. The most suitable setup for AE monitoring is 45 dB for pre- and 40 dB for post-amplifiers and the selecting of a frequency range for passage through a frequency filter of between 200 to 500 kHz. Peak Definition Time = 50 µs; Hit Definition Time = 200 µs; Hit Lockout Time = 300 µs are the other suitable settings for the test system.
- By plotting cumulative AE hit and cumulative AE energy versus time, we found that the AE energy parameter is a more effective way than the conventional AE hit number to detect different stages in the rock failure process. Based on AE

monitoring during uniaxial tests, three distinct steps of AE activities were identified for granite and gabbro specimens. The first step for granite occurred before 30% of failure stress and the second occurred at about 60% of ultimate stress. The last step took place around 90 to 95% of the ultimate rock strength. For gabbro rock the last two steps occurred at the same level of stress (i.e., at 60 and 90% of ultimate strength). However, the first step occurred before 20% of the ultimate stress of the rock. For both rocks, the amount of acoustic emission activity in the third step increased dramatically when the stress level was close to the peak strength. These steps are comparable to crack initiation (σ_{ci}), crack damage (σ_{cd}) thresholds and uniaxial compression strength (ucs) in the stress-strain diagram presented by Martin in 1993.

- Acoustic emission patterns in rock correlate closely with the stress-strain behaviour. It appears that the homogeneity and isotropy of rocks plays a major role in this regard. Both the North African gabbro, with 0.35% porosity, and Lavasan granite (1.0% porosity) are homogeneous and isotropic, therefore the same AE activities were observed for both of them.
- A direct comparison of the AE event data from uniaxial compression and Brazilian tests showed that the AE activity in the Brazilian tests was relatively lower than in the uniaxial compression tests over the same time span. The higher energy requirement to shear failure in the cylindrical UC tests compared to the indirect tensile strength is the main explanation for this difference. The better coupling of transducers to the flat shape of Brazilian test specimens in contrast to convex shape of uniaxial compression test specimens is another reason for the observed differences. In the latter case, the noise level increases due to movement of the transducers upon the rock deformation. By plotting the accumulated AE hit and energy versus time for each type of test, we have shown that three sharp steps in AE activity occur during both the uniaxial compression and Brazilian tests. Considering the stress level in Brazilian tests, we found that the three steps occurred at about 20, 60 and 95% of the maximum tensile strength of rock. The three steps in the AE events in the Brazilian tests could be related to the beginning

of micro fracturing, wedge formation at the top and bottom of the disc and finally nucleation of a failure surface in middle section of the disc.

- Review of the fracture pattern showed two visible wedges at the top and bottom of the disc-shaped specimens. The wedges were more visible in the specimens with larger diameters (70 mm). It seems that the larger contact surface area plays a main role in this phenomenon. On the other hand, when the contact area between the specimen and the loading plate is too small, the contact area is almost a line. Therefore the fracture shape occurs as planar in the mid section of the disc. With the larger surface contact area, however, a pseudo uniaxial loading system is created at the top and bottom of the specimen and the disc fails by the formation of two wedges at the sides of the disc.

3. Feasibility of using acoustic emission and infrared measurement simultaneously to predict failure in stress induced hard rock:

The preliminary tests showed the possibility of using IR to study failure evolution; however, it is not possible to use this method in conjunction with AE monitoring for prediction of failure in the laboratory. Increasing the stress leads to a rise in infrared temperature in granite specimens. In laboratory studies, cyclic loading is necessary to produce the measurable IR temperature. Conversely, cyclic loading generates enormous noise and does not allow the detection of suitable AE records. Measuring IR with AE monitoring could be used for long-term evaluation in field investigations, for example, using the methods simultaneously to monitor the stability of underground excavations or fault rupture is recommended. In addition, it could also be used for earthquake prediction.

4. Laboratory tests on thermally and mechanically damaged rock using AE monitoring:

- The effect of thermally and stress induced microcracks on the mechanical and physical parameters of gabbro rock was studied. The gabbros specimens that had been thermally treated to more than 150°C showed significant reductions in the measured parameters. The strength of gabbro thermally treated up to 600°C was 20% less than in the unheated gabbro specimens. A drastic decrease in the uniaxial strength occurred in the specimens that were treated to temperatures above 600°C

(see figure 6.6). However, the elasticity modulus decreased at a relatively constant rate with respect to an increase in the temperature. The changes in elastic wave velocities were comparable to the strength reduction rates.

- A comparison of acoustic emission data for intact and thermally treated samples showed a considerable difference in the number and in the steps of acceleration of AE events. It appears that microcrack evolution due to thermal damage plays a key role in decreasing the number of AE hits during uniaxial tests in heated specimens. The AE records of intact and thermally treated specimens below 600°C are comparable. On the other hand, there is a significant difference between the records of specimens heated to above 600°C and unheated gabbro specimens.
- Investigation on the sample size and heating rate effects on the above mentioned parameters showed a significant difference in the results. The heating rate plays a more effective role at low treating temperatures than at high temperatures. Decreasing the rate of heating for both of the final temperatures (300°C and 600°C), causes more damage in the uniaxial strength and elasticity modulus of gabbro specimens. P-wave velocity was more affected than S-wave during both heating rates of 50°C and 100°C/hour. Low rate heating to a temperature of 300°C caused a difference between P and S wave values; however at 600°C P and S wave values decreased by the same amounts.
- The reduction of the AE hits number is a more comparable parameter when considering thermally treated and stress induced gabbro specimens. Plotting the accumulated AE energy and hit vs time showed that, at less than 600°C, the form of the thermally damaged specimen's graphs was more similar to intact rock than to mechanically damaged rock. However, the shape of the graph for thermally damaged specimens heated to more than 600°C, were the same as the mechanically damaged ones. Other difference between the MD and TD samples is seen in the elastic wave velocities. Based on elastic wave velocity changes, the ultra high stress-damaged specimens (σ_1 = 2350 and σ_3 = 650MPa) is comparable to a 150°C thermally-damaged specimen. Nevertheless, the maximum uniaxial strength and elasticity modulus of the ultra high stress-damaged rock is comparable with a specimen that was thermally damaged at 600°C.

- Based on all the parameters that were investigated, it was found that 600°C is a critical temperature that causes physical and mechanical degradation in this type of gabbro. However, it should be emphasized that this study was conducted on only one type of intrusion rock. Others have differing properties such as crystallographic, texture and grain orientation, character of grain boundaries, porosity, grain size and composition, all of which will affect the mechanical behaviour against thermal and stress effects. Extrapolation of the results from one type of rock to another will require more extensive research.

7.2 Recommendations for future researches

In this thesis the AE procedure was applied to three case studies. However, it proved to be extremely effective in the monitoring and prediction of failure in hard rocks. Our laboratory investigations showed the capability of AE monitoring to failure mechanisms and to failure evolution investigations. We propose to apply this method to monitor rock slopes and underground excavations. Although some research has been done previously using AE hit activities, AE event energy has not been studied for these purposes.

We have shown that three steps of AE activities occur during uniaxial compression tests and in Brazilian tests. The relationship of microcrack initiation and nucleation with AE activities requires further investigation. X-ray investigation and tomography on specimens after each step (before ultimate failure) are recommended in this regard.

There were some interesting results from thermal damage studies on gabbro rock. All results presented in this thesis refer to one particular brittle rock and further research is necessary to examine whether these results are applicable to other types of rock. Preparing a model with consideration of thermal expansion differences between crystals, and comparing the results with these findings, is also proposed.

.

Bibliography

Andrew A. T., Hayakawa M. and Molchanov O. A., 2002, Thermal IR satellite data application for earthquake research in Japan and China, Journal of Geodynamics 33, 519 - 534.

ASTM 2001, Standard test method for splitting tensile strength of intact rock core specimens, Designation D 3967 - 95a.

Aydin A. and Basu A. 2006, The use of Brazilian Test as a Quantitative Measure of Rock Weathering, Technical Note, Rock Mechanics and Rock Engineering, 39 (1), 77 - 85.

Ayling M. R., Meredith P. G. and Murrell A. F., 1995, Microcracking during triaxial deformation of porous rocks monitored by changes in rock physical properties, I. Elastic-Wave propagation measurements on dry rocks, Tectonophysics, 245, 205 - 221.

Baud P., Klein E. and Wong T., 2004, Compaction localization in porous sandstones: spatial evolution of damage and acoustic emission activity, Journal of Structural Geology 26, 603 - 624.

Bieniawski, Z. T., 1967, Mechanism of brittle rock fracture. Part II. Experimental studies, Int. J. Rock Mech. Min. Sci. & Geomech. Abstracts, 4(4), 407 - 423.

Bauer S. J. and Johnson B., 1979, Effects of slow uniform heating on the physical properties of Westerly and Charcoal granites. Proc. US Symposium Rock Mech., Austin, TX.

Brown, E. T. 1970, Strength of models of rock with intermittent joints. J. Soil Mech. Foundn Div., ASCE 96, SM6, 1935 - 1949.

Byerlee, J. D. and Lockner, D.A. 1977, Acoustic emission during fluid injection in rock. In: Proc. 1st Conf. on Acoustic Emission/Microseismic Activity in Geological Structures and Materials (ed. H.R. Hardy and F.W. Leighton), 87 - 98.

Cai M. and Kaiser P. K., 2005, Assessment of excavation damaged zone using a micromechanics model, Tunnelling and Underground Space Technology, 20, 301 - 310.

Chaki S., Takarli M. and Agbodjan, W. P., 2008, Influence of thermal damage on physical properties of a granite rock: Porosity, permeability and ultrasonic wave evolutions, Construction and Building Materials, 22, 1456 - 1461.

Chen H., Parnell J. and Gong Z., 2006, Large-scale seismic thermal anomaly linked to hot fluid expulsion from a deep aquifer, Journal of Geochemical Exploration, 89, 53 -56.

Chen D. and Dollimore, D., 1995, Kinetic analysis of the calcium hydroxide formed in the hydration of pure C3S and with the addition of Ca (NO3)2, Journal of Thermal Analysis and Calorimetry, 44 (5), 1001-1011.

David C., Menéndez B. and Darot M., 1999, Influence of stress-induced and thermal cracking on physical properties and microstructure of La Peyratte granite, Int. J. Rock Mech. Min. Sci., 36(4), 433 - 448.

Dunegan H. L., 1998, Modal Analysis of Acoustic Emission Signals, Journal of Acoustic Emission, 15, 1- 4.

Demelza H. J., 1997, Thermal expansion of MgSiO3 and FeSiO3 ortho-and clinopyroxenes, American Mineralogist, 82(7, 8), 689 - 696.

Eberhardt E., Stead D., Stimpson B. and Read R. S., 1998, Identifying crack initiation and propagation thresholds in brittle rock, Can. Geotech. J., 35, 222 - 233.

Eberhardt E., Stead D. and Stimpson B., 1999, Quantifying progressive pre-peak brittle fracture damage in rock during uniaxial compression, Int. J. Rock Mech. Min. Sci., 36, 361-380.

Fabre G. and Pellet F., 2006, Creep and time dependent damage in argillaceous rocks, Int. J. Rock Mech. Min. Sci., 43(6), 950 - 960.

Falls S. D. and Young R. P., 1998, Acoustic emission and ultrasonic-velocity methods used to characterise the excavation disturbance associated with deep tunnels in hard rock, Tectonophysics, 289, 1 - 15.

Fei. Y., 1995, Mineral Physics and Crystallography, A Handbook of Physical Constants Carnegie Institution of Washington, Geophysical Laboratory, Washington, DC.

Fernanda C. S., Carvalho J. and Labuz, F., 2002, Moment tensors of acoustic emissions in shear faulting under plane-strain compression, Tectonophysics, 356, 199 - 211.

Ferrero A. M. and Marini P., 2001, Experimental studies on the mechanical behaviour of two thermal cracked marbles, Rock Mechanics and Rock Engineering, 34(1), 57 - 66.

Finkenthal D. 1996, Introduction to the electromagnetic spectrum, General atomic, http://www.fusioned.gat.com/images/pdf/EMcurriculum.pdf.

Friedemann T. F., 2002, Charge generation and propagation in igneous rocks, Journal of Geodynamics 33, 543 - 570.

Friedemann T. F., 2003, Study on the electrical conductivity structure of testable continental crust, Journal of Geodynamics 35, 353 - 388.

Frocht, M. M., 1948, Photoelasticity, Vol. II. John Wiley, New York.

Gabet T., 2006, Comportement triaxial du béton sous fortes contraintes : Influence du trajet de chargement, PhD. thesis, Université Joseph Fourier.

Bibliography

Gabet T., Malécot Y. and Daudeville L., 2008, Triaxial behaviour of concrete under high stresses: Influence of the loading path on compaction and limit states, Cement and Concrete Research 38, 403 - 412.

Gatelier N., Pellet F. and Loret, B., 2002, Mechanical damage of an anisotropic porous rock in cyclic triaxial tests, Int. J. Rock Mech. Min. Sci., 39(3), 335-354.

Gatelier N., 2001, Etude expérimentale et théorique de l'endommagement des roches anisotropes, PhD. thesis, Université Joseph Fourier.

Geological survey of Iran (GSI), 2008, Rodehen quadrangle geological map, scales 1:100000.

Hadley K., 1976, Comparison of calculated and observed crack densities and seismic velocities in Westerly granite, Journal of Geophysical Research, 81, 3484 - 3494.

Hall S. A., Sanctis F. and Viggiani G., 2006, Monitoring fracture propagation in a soft rock (Neapolitan Tuff) using acoustic emissions and digital images, Pure and Applied Geophysics, 163, 2171 - 2204.

Hardy H. R., 1985, Theory and Application of Acoustic Emission/ Microseismic Techniques, Transtech Publications, Clausthal, Germany.

Hardy H. R. and Shen H. W., 1992, Recent Kaiser Effect studies in rock, Progress in Acoustic Emission VI, the Japanese Society for NDI, 149 - 157.

Hardy H. R., 1994, Geotechnical field applications of AE/MS techniques at the Pennsylvania State University: a historical review, NDT & E International, 27(4), 179 - 232.

Hardy H. R., 2003, Acoustic emission/Microseismic activity, Volume 1: Principles, Techniques and geotechnical applications, A.A. Balkema.

Heard H. C, and Page L., 1982, Elastic moduli, thermal expansion and inferred permeability of two granites to 508°C and 55 MPa, Journal of Geophysical Research, 87, 9340 - 9348.

Hoek E, Brown E. T., 1997, Practical estimates of rock mass strength. Int. J. Rock Mech. Min Sci., 34(8), 1165 - 1186.

Hoek E. and Brown E. T., 1980a, Empirical strength criterion for rock masses. J. Geotech. Engng. Div., ASCE 106 (GT9), 1013-1035.

Hoek E. and Brown E. T., 1980b, Underground Excavations in Rock, Institute of Mining and Metallurgy, London.

Hoek E., 1968. Brittle failure of rock. In Rock Mechanics in Engineering Practice. (eds K.G. Stagg and O. C. Zienkiewicz), 99-124. London, Wiley.

Bibliography

Homand E. F. and Houpert R., 1989, Thermally induced microcracking in granites, characterization and analysis, Int. J. Rock Mech. Min. Sci. Geomech. Abstr., 26(2), 125 - 34.

Homand E. F. and Troalen J. P., 1984, Behaviour of granites and limestone subjected to slow and homogeneous temperature changes, Eng. Geol., 20 20(3), 219-233.

Huang M., Jiang L., Liaw P. K., Brooks C. R., Seeley R., and Klarstrom D. L., 1998, Using Acoustic Emission in Fatigue and Fracture Materials Research, Non-destructive Evaluation: Overview, JOM-e, 50(11).

Hudson J. N., 1993, Comprehensive rock engineering, principals, practice and projects, volume 3, Rock testing and site characterization, Pergamon press, 67 - 85.

International Society on Rock Mechanics, 1978, Suggested methods for determining tensile strength of rock materials, Int. J. Rock Mech. Min. Sci. Geomech. Abstr., 15, 99 - 103.

International Society on Rock Mechanics, 1972, suggested method for determining the uniaxial compressive strength on rock materials and the point load strength Index. ISRM Commission on standardization of laboratory and field tests documents no. 1.

Jackson J., Priestley K., Allen M. and Berberian M., 2002, Active tectonics of the South Caspian Basin, Geophysical Journal International, 148, 214 - 245.

Jansen D. P., Hutchins A.D. and Young R.P., 1993, Ultrasonic imaging and acoustic emission monitoring of thermally induced microcracks in Lac du Bonnet granite, Journal of Geophysical Research, 98, 22231 - 22243.

Keshavarz M., Pellet F. L., Amini Hosseini K., and Rousseau C., 2008, Comparing the results of acoustic emission monitoring in Brazilian and uniaxial compression tests, Proc. 5th Asian Rock Mechanics Symposium, Tehran, Iran, 357-363.

Keshavarz M., Pellet F. L., and Amini Hosseini, 2009, Comparing the effectiveness of AE energy and AE hit parameters to predict of rock failure, Sinorock International Symposium on Rock Mechanics: Rock Characterisation, Modelling and Engineering Design Methods, Hong Kong, China.

Khair A. W. 1984. Acoustic emission pattern: an indicator of mode of failure in geologic materials as affected by their natural imperfections. Proc. 3rd Conference on Acoustic Emission/Microseismic Activity in Geologic Structures and Materials, 1981, University Park, Pa. Ed. by H. R. Hardy and F. W. Leighton. Trans Tech Publications, Clausthal, Germany, 45 - 66.

Klemd R., 1989, P-T evolution and fluid inclusion characteristics of retrograded eclogites, Münchberg Gneiss Complex, Germany, Earth and Environmental Science, Volume 102.

Bibliography

Knopoff L., Aki K., Allen C., Rice J.R. and Sykes L., 1996, Earthquake Prediction: The Scientific Challenge, National Academy of Sciences (NAS).

Lavrov A., Vervoort A., Wevers M. and Napier J.A.L., 2002, Experimental and numerical study of the Kaiser effect in cyclic Brazilian tests with disk rotation, Int. J. Rock Mech. Min. Sci., 39, 287 - 302.

Lavrov A., 2001, Kaisser effect observation in brittle rock cyclically loaded with different loading rates, Mechanics of Materials, 33, 669 - 677.

Lei X. L., Nishizawa O., Kusunose K., Cho A., Satoh T. and Nishizawa O., 2000a, Compressive failure of mudstone samples containing quartz veins using rapid AE monitoring: the role of asperities, Tectonophysics, 328, 329 - 340.

Lei X. L., Kusunose K., Rao M., Nishizawa O. and Satoh T., 2000b, Quasi-static fault growth and cracking in homogeneous brittle rock under triaxial compression using acoustic emission monitoring, Journal of Geophysical Research 105 (B3), 127- 139.

Lei X. L., Kusunose K., Nishizawa O., Cho A. and Satoh T., 2000c, On the spatio-temporal distribution of acoustic emissions in two granitic rocks under triaxial compression: the role of pre-existing cracks, Geophysical Research Letters, 27 (13).

Lei X. L., Kusunose K., Nishizawa O., Satoh T. and Nishizawa O., 2003, The hierarchical rupture process of a fault: an experimental study, Physics of the Earth and Planetary Interiors 137, 213 - 228.

Lei X. L., Masuda K., Nishizawa O., Jouniaux L., Liub L., Ma W., Satoh T. and Kusunose K., 2004, Detailed analysis of acoustic emission activity during catastrophic fracture of faults in rock, Journal of Structural Geology 26, 247 - 258.

Lion M., Skoczylas F and Ledesert B., 2005, Effects of heating on the hydraulic and poroelastic properties of Bourgogne limestone, Int. J. Rock Mech. Min. Sci., 42(4), 508-520.

Liu S., Wu L., and Wu Y., 2006, , Infrared radiation of rock at failure, Technical note, Int. J. Rock Mech. Min. Sci., 43(6), 972 - 979.

Lixin W., Shanjun L., Yuhua W. and Chuanyin W., 2006a, Precursors for rock fracturing and failure—Part I: IRR image abnormalities, Int. J. Rock Mech. Min. Sci., 43, 473 - 482.

Lixin W., Shanjun L., Yuhua W. and Chuanyin W., 2006b, Precursors for rock fracturing and failure—Part II: IRR T–Curve abnormalities, Int. J. Rock Mech. Min. Sci., 43, 483 - 493.

Lockner D. A., Byerlee J. D., Kuksenko V., Ponomarev A. and Sidorin A., 1991, Quasi-static fault growth and shear fracture energy in granite, Nature, 350, 39–42.

Bibliography

Luong M. P., 1993, Infrared thermographic observations of rock failure: Comprehensive Rock Engineering Principles, Practice and Projects, vol. 4, chapter 26, Oxford: Pergamon, 715 - 730.

Luong M .P. and Dang Van K., 2005, Introducing infrared thermography in dynamic testing on reinforced concrete structures, Proc. 18th International Conference on Structural Mechanics in Reactor Technology (SMiRT 18), Beijing, China, 7-12.

Luong M. P., 1987, Infrared observation of failure processes in plain concrete, Durability of Building Materials and Component 4 DBMC, November 1987, Singapore, Pergamon, 2, 870-878.

MacKenzie W. S., Donaldson C. H. and Guilford C., 1982, Atlas of igneous rocks and their textures, Longman.

Mahmutoglu Y., 1998. Mechanical behaviour of cyclically heated fine grained rock, Rock Mech. Rock Eng., 31(3), 169-179.

Martin C. D., 1993, The strength of massive Lac du Bonnet granite around underground openings. Ph.D. thesis, University of Manitoba, Winnipeg, Canada.

Meglis I. L., Chows T. M. and Young R. P., 1995, Progressive micro-crack development in tests on Lac du Bonnet Granite – I. Acoustic emission source location and velocity measurements, Int. J. Rock Mech. Min. Sci. Geomech. Abstr., 32 (8) 741-750.

Menendez B., David C. and Darot, M., 1999, A study of the crack network in thermally and mechanically cracked granite samples using confocal scanning laser microscopy, Phys. Chem. Earth., 24(7), 627-32.

Nasseri M. H. B., Schubnel A. and Young R. P., 2007, Coupled evolutions of fracture toughness and elastic wave velocities at high crack density in thermally treated Westerly granite, Int. J. Rock Mech. Min. Sci., 44 (4) 601 - 616.

Ohnaka M. and Mogi K., 1982, Frequency characteristics of acoustic emissions in rocks under uniaxial compression and its relation to the fracturing process to failure. Journal of Geophysical Research, 87(B5), 3873 - 3884.

Olivieri A., Mannheimer A. and Ripper-Neto A. P. , 2000, On the Use of Acoustic Signals for Detection and Location of Partial Discharges in Power Transformers Conference Record of the 2000 IEEE International Symposium on Electrical Insulation, Anaheim, CA USA.

Orengo Y., 2003, Vitesse de propagation des ondes P, LGIT – Université Grenoble I.

Ouzounov D. and Freund F., 2004, Mid – Infrared emission prior to strong earthquakes analyzed by remote sensing data, Advanced Space Research 33, 268 - 273.

Bibliography

Pellet F., Keshavarz M., Jafari M. K. and Amini Hosseini K., 2007, Variation of acoustic emission and shear wave velocity of Lavasan granite under uniaxial compression test, Proc. 5th International Conference on Seismology and Earthquake Engineering (SEE5), Tehran-Iran.

Pellet F., and Fabre G., 2007. Damage evaluation with P-wave velocity measurements during uniaxial compression tests on argillaceous rocks, Int. J. Geomech., ASCE, 7(6), 431 - 436.

Physical acoustic corporation (PAC), 2002, AEwin Users Manuel, Princeton Jct., New Jersey, USA.

Prikry R., Lokajek T., Li C. and Rudajev V., 2003, Acoustic emission characteristics and failure of uniaxially stressed granitic rocks: the effect of rock fabric, Rock Mechanics and Rock Engineering. 36(4), 255 - 270.

Ramirez G. Engelhardt M. and Fowler T. J., 2006, On the endurance limit of fiberglass pipes using acoustic emission, Journal of pressure vessel technology, 128(3), 454 - 461.

Rocco C., Guinea G. V., Planas J. and Elices M., 1999, Mechanisms of rupture in splitting tests. ACI Mater. J. 96, 52 - 60.

Sala Ph., 1982, Etude expérimentale de la fissuration et de la rupture des roches par émission acoustique, PhD. thesis, Université scientifique et médicale, Grenoble.

Shi W., Wu Y. and Wu L., 2007, Quantitative analysis of the projectile impact on rock using infrared thermography, International Journal of Impact Engineering, 34(5), 990 -1002.

Shiotani T., Ohtsu M. and Ikeda K., 2001, Detection and evaluation of AE waves due to rock deformation, Construction and Building Materials 15, 235 - 246.

Scholz, C.H., 1968, Experimental study of the microfracturing process in brittle rock, J. Geophys. Res., 73 (4), 1447 - 1454,

Spies T. and Einsenblatter J., 2001, Acoustic emission investigation of microcrack generation at geological boundaries, Engineering Geology 61, 181-188.

Stanchits, S. Vinciguerra S. and Dresen G., 2006, Ultrasonic Velocities, Acoustic Emission Characteristics and Crack Damage of Basalt and Granite, Pure and Applied Geophysics, 163, 974 - 993.

Stanchits S.A., Lockner D. and Ponomarev A. V., 2003, Anisotropic Changes in P-Wave Velocity and Attenuation during Deformation and Fluid Infiltration of Granite, Changes in velocity and attenuation in granite, Bull. Seismological Society of America, 93(4), 1803 - 1822.

Surkov V.V., Pokhotelov O.A., Parrot M. and Hayakawa M., 2006, Study on the origin of stable IR anomalies detected by satellites above seismo-active regions, Physics and Chemistry of the Earth, 31, 164 - 171

Tang C.A., Liu H., Lee P.K.K., Tsui Y. and Tham L.G., 2000, Numerical studies of the influence of microstructure on rock failure in uniaxial compression Part I: effect of heterogeneity, Int. J. Rock Mech. Min. Sci., 37, 555 - 569.

Thiercelin M, 1980, Application de l'émission acoustique à l'étude de la fissuration et de la rupture des roches, PhD. thesis, Université scientifique et médicale, Grenoble.

Tinkey B. V., Fowler T. J. and Klingner R. E., 2000, Non-destructive Testing of Pre-stressed Bridge Girders with Distributed Damage, Research Report 1857-2, Texas Department of Transportation.

Trovato C., Stanchits S., Vinciguerra S. and Dresen G., 2006, Crack density and seismic velocities in Etna basalt, Geophysical Research Abstracts 8, 07163.

Utagawa M, Seto M, Katsuyama K. 1997, Determination of in situ stress using DRA and AE techniques. Proc. International Symposium on Rock Stress, Kumamoto, Japan, Balkema, 187 - 192.

Van den Kerkhof, A. M., Touret, J. L. R., Maijer, C. and Jansen, J. B. H., 1991, Retrograde methane-dominated fluid inclusions from high-temperature granulites of Rogaland, southwestern Norway. Geochim. Cosmochim. Acta, 55, 2533 - 2544.

Villaescusa E., Jianping L. and Masahiro S. 2002, Stress measurements from oriented core in Australia, Proc. 5th International Workshop on the Application of Geophysics in Rock Engineering, Toronto, Canada.

Vutukuri VS, Lama RD, Saluja SS. 1978, In: Handbook on mechanical properties of rocks, Series on Rock and Soil Mechanics, vol. 1. Clausthal, Germany: Trans Tech Publications.

William K., Rhee I. and Xi Y., 2005, Thermal Degradation of Heterogeneous Concrete Materials, Journal of Materials in Civil Engineering, 17(3) 276 – 285.

Winter J. D., 2001, An introduction to igneous and metamorphic petrology, Prentice Hall, 473 - 474.

Wu L. and Wang J. Z., 1998, Infrared radiation features of coal and rocks under loading, Int. J. Rock Mech. Min. Sci., 35(7), 969 - 976.

Wu L., Cui C., Geng N. and Wang J.Z., 2000, Remote sensing rock mechanics (RSRM) and associated experimental studies, Int. J. Rock Mech. Min. Sci., 37, 879 - 888.

Wu L., Liu S., Wu Y. and Wu H., 2002, Technical Note, Changes in infrared radiation with rock deformation, Int. J. Rock Mech. Min. Sci., 39, 825 - 830.

Bibliography

Wu L., Wu Y., Liu S. and Li Y., 2004, Infrared radiation of rock impacted at low velocity, Technical Note, Int. J. Rock Mech. Min. Sci., 41, 321 - 327.

Wu L., Liu S., Wu Y. and Wang C., 2006, Precursors for rock fracturing and failure—Part I: IRR image abnormalities, Int. J. Rock Mech. Min. Sci., 43, 473 - 482.

Young R. P., Collins D. S., Reyes-Montes J.M. and Baker C., 2004, Quantification and interpretation of seismicity, Int. J. Rock Mech. Min. Sci., 41, 1317 - 1327.

Young R. P. and Collins D.S., 2001, Seismic studies of rock fracture at the underground research laboratory, Canada, Int. J. Rock Mech. Min. Sci. 38, 787 - 799.

Zang A., Wagner C., Stanchits S., Dresen G., Andresen R and Haidekker M. A., 1998, Source analysis of acoustic emissions in Aue granite cores under symmetric and asymmetric compressive loads, Geophysical Journal International, 135, 1113 - 1130.

Zoback M. D. and Byerlee J. D., 1975, The effect of microcrack dilatancy on the permeability of Westerly granite, Journal of Geophysical Research., 80, 752 - 755.

Zuji Q. and Xudeng X., 1990, Satellite TIR anomaly-earthquake precursor, Science Report of China, 35, 1324 -1327.

Appendix I

Elastic wave velocity and AE monitoring results during uniaxial and Brazilian tests

Table 1: Vp and Vs measurements results of 45 Lavasan granite specimens

Sample No.	Length(mm)	Vp(m/s)	Vs(m/s)	Remarks
Gr1	95.1	4105	2527	
Gr2	100.7	4500	2827	
Gr3	85.4	3820	2441	
Gr4	101.3	4121	2643	
Gr5	100.6			No signal
Gr6	95	4282	2782	
Gr7	96	3695	2276	
Gr8	101.3	4400	2600	
Gr9	100.5	4370	2805	
Gr10	101.1	4252	2606	
Gr11	99.8	3770		Poor signal
Gr12	100.5	4152	2595	
Gr13	100.3		2338	No signal
Gr14	100.8			No signal
Gr15	100.4	4278	2747	
Gr16	100.1	3764	2447	Poor Signal
Gr17	99.7	4274	2750	
Gr18	99.7	3830	2546	
Gr19	99.7	4033	2620	
Gr20	100	4084	2743	
Gr21	99.9			No signal
Gr22	99.6	4060	2604	
Gr23	100.4	4048	2481	
Gr24	101.1	4027	2504	
Gr25	99.6	3776	2423	
Gr26	99.6	4053	2515	
Gr27	99.6	4183	2578	
Gr28	99.9	4139	2532	
Gr29	99.6	4419	2720	
Gr30	99.1	4356	2594	
Gr31	100.4	4397	2676	
Gr32	99.5	4202	2615	
Gr33	100.7	3646	2353	Poor Signal
Gr34	99.4	3878	2475	
Gr35	99.9	3990	2409	
Gr36	100.9		2706	No signal
Gr37	100.1			No signal
Gr38	100.7	3737	2321	
Gr39	99.6	4011	2927	
Gr40	99.5	4127	2519	
Gr41	99.2	3913	2493	
Gr42	99.5	3725	2591	Poor Signal
Gr43	100		2504	No signal
Gr44	100	4119	2506	Existing a crack
Gr45	100.9	4005	2519	
Mean/Standard deviation		4051/ ±239	2537/ ±170	

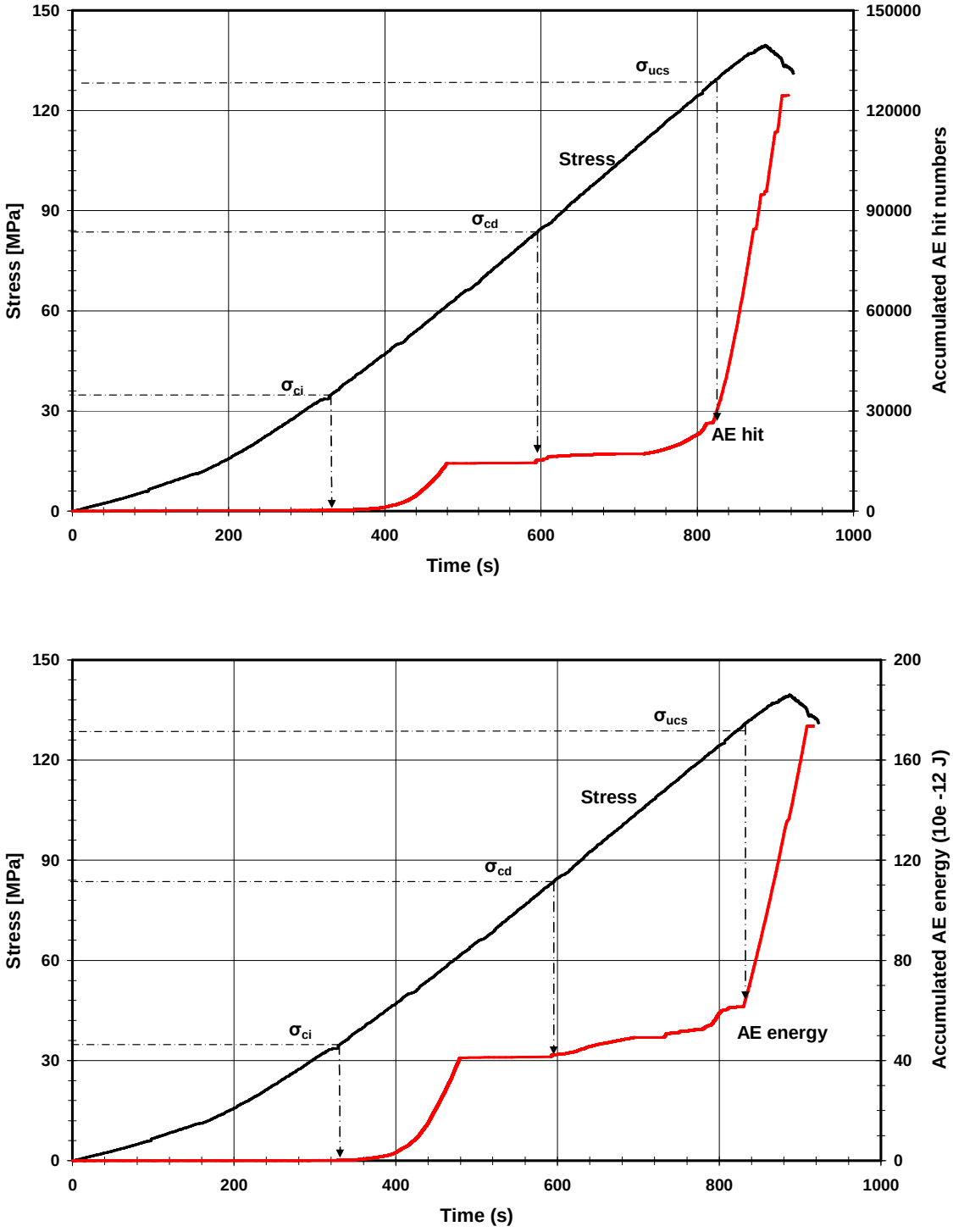

Figure 1: Accumulated AE hit (above) and energy (below) versus stress - time during uniaxial simple compression test of Lavasan granite specimen Gr5. The symbols are presented in chapter 4, previously. σ_c=138 MPa, E=27 GPa,

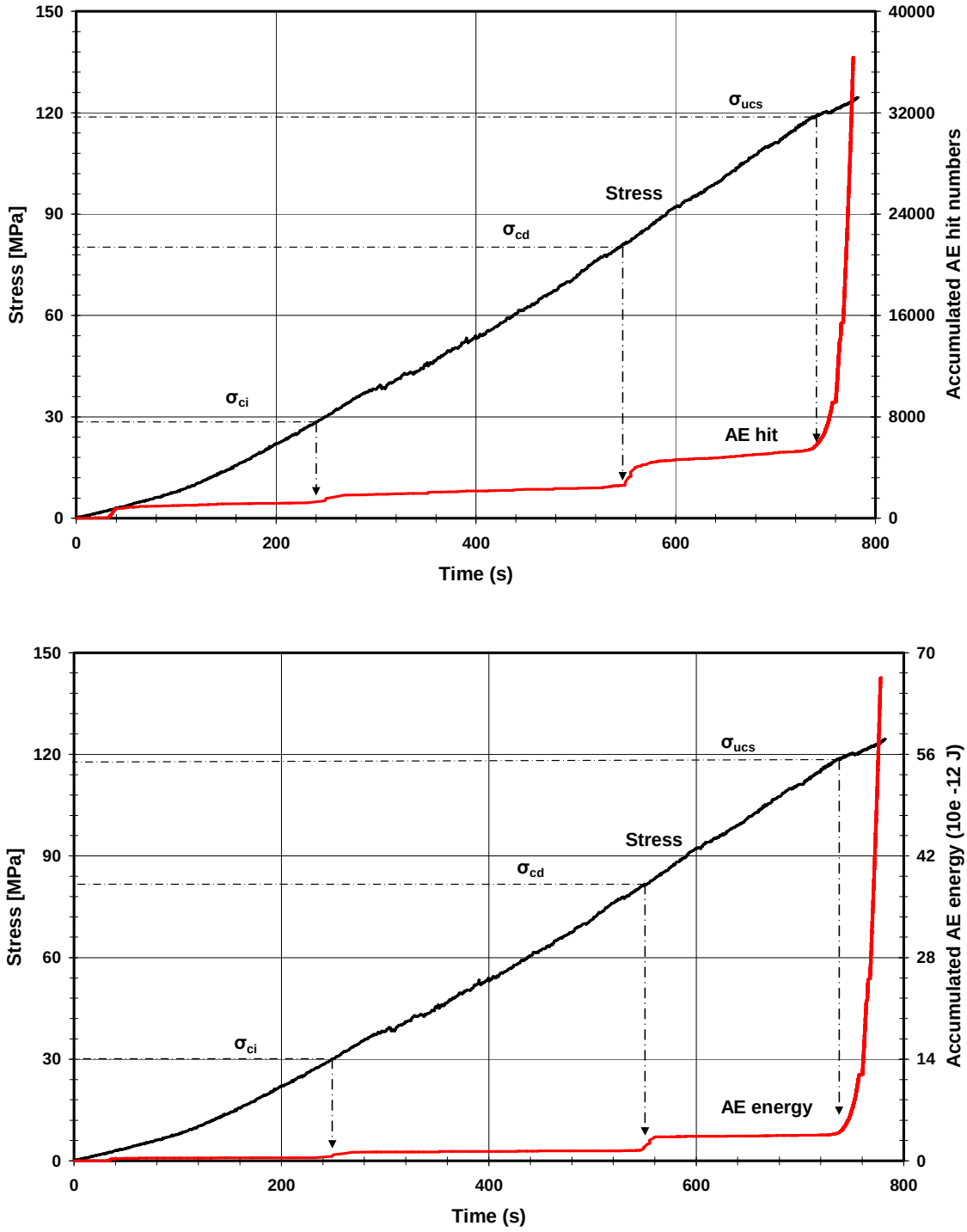

Figure 2: Accumulated AE hit (above) and energy (below) versus stress - time during uniaxial simple compression test of Lavasan granite specimen Gr10. σ_c=123 MPa. E=31GPa.

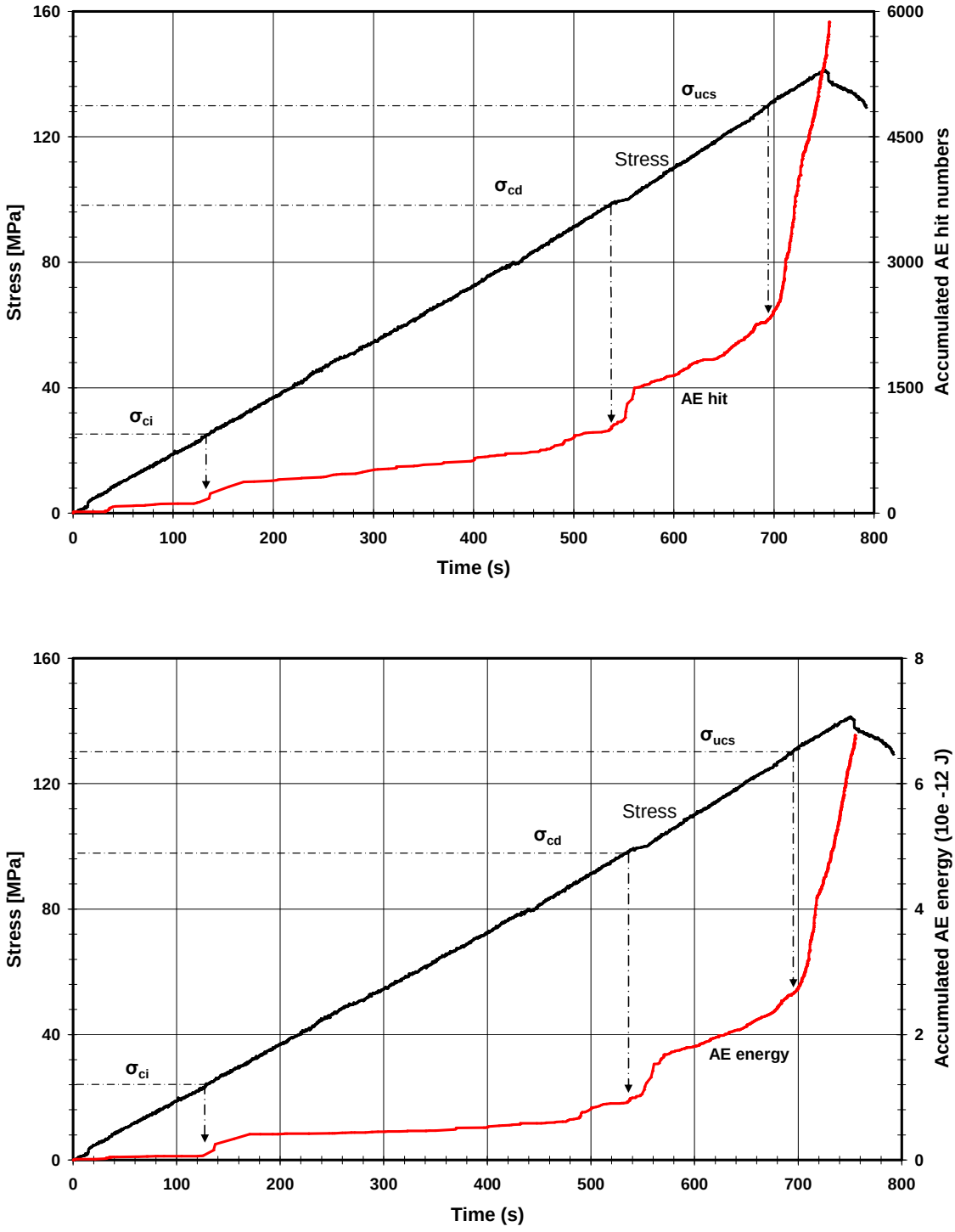

Figure 3: Accumulated AE hit (above) and energy (below) versus stress - time during uniaxial simple compression test of Lavasan granite specimen Gr12. σ_c=138 MPa The axial deformation has been recorded by LVDT.

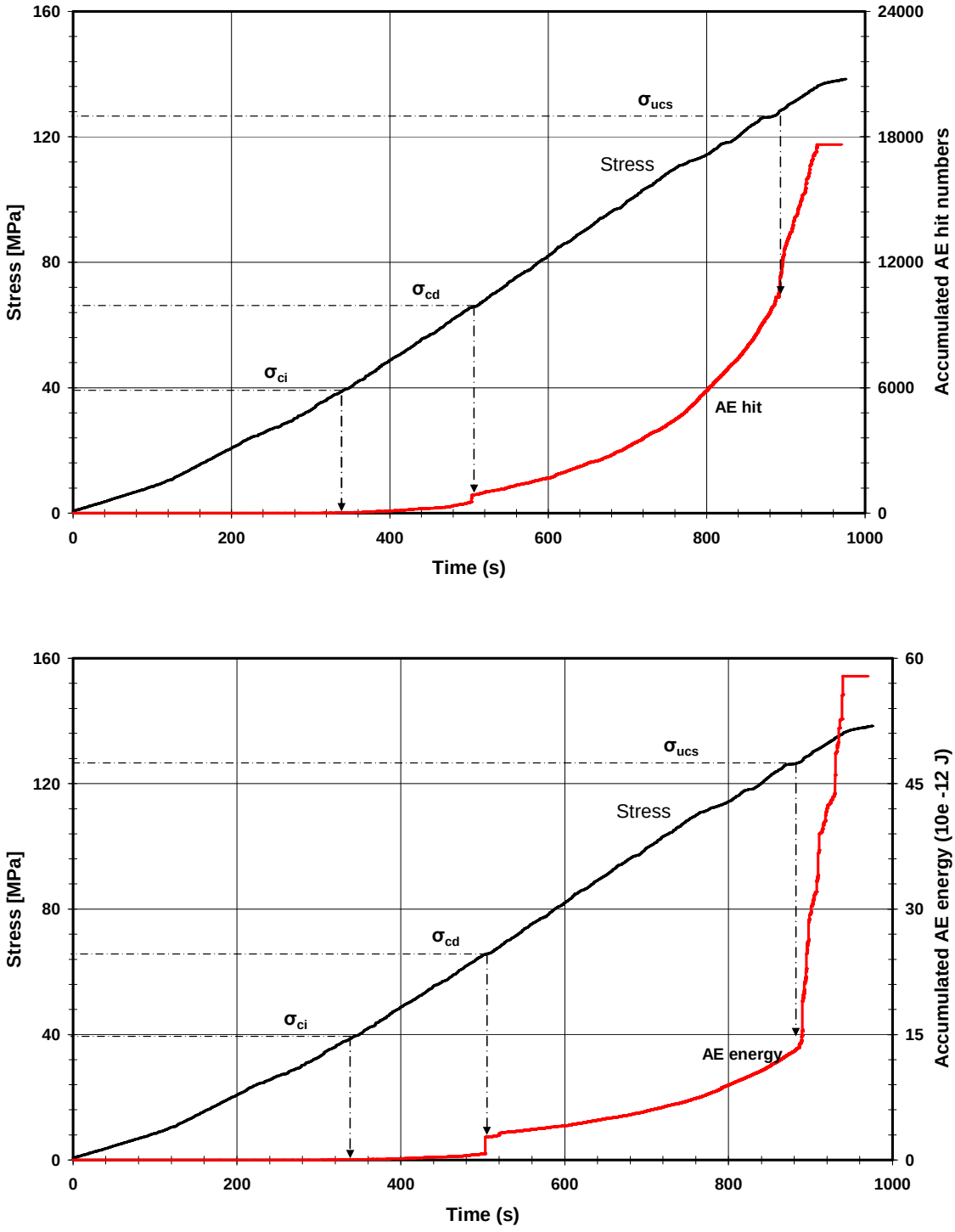

Figure 4: Accumulated AE hit (above) and energy (below) versus stress - time during uniaxial simple compression test of Lavasan granite specimen Gr15. σ_c=135 MPa The axial deformation has been recorded by LVDT.

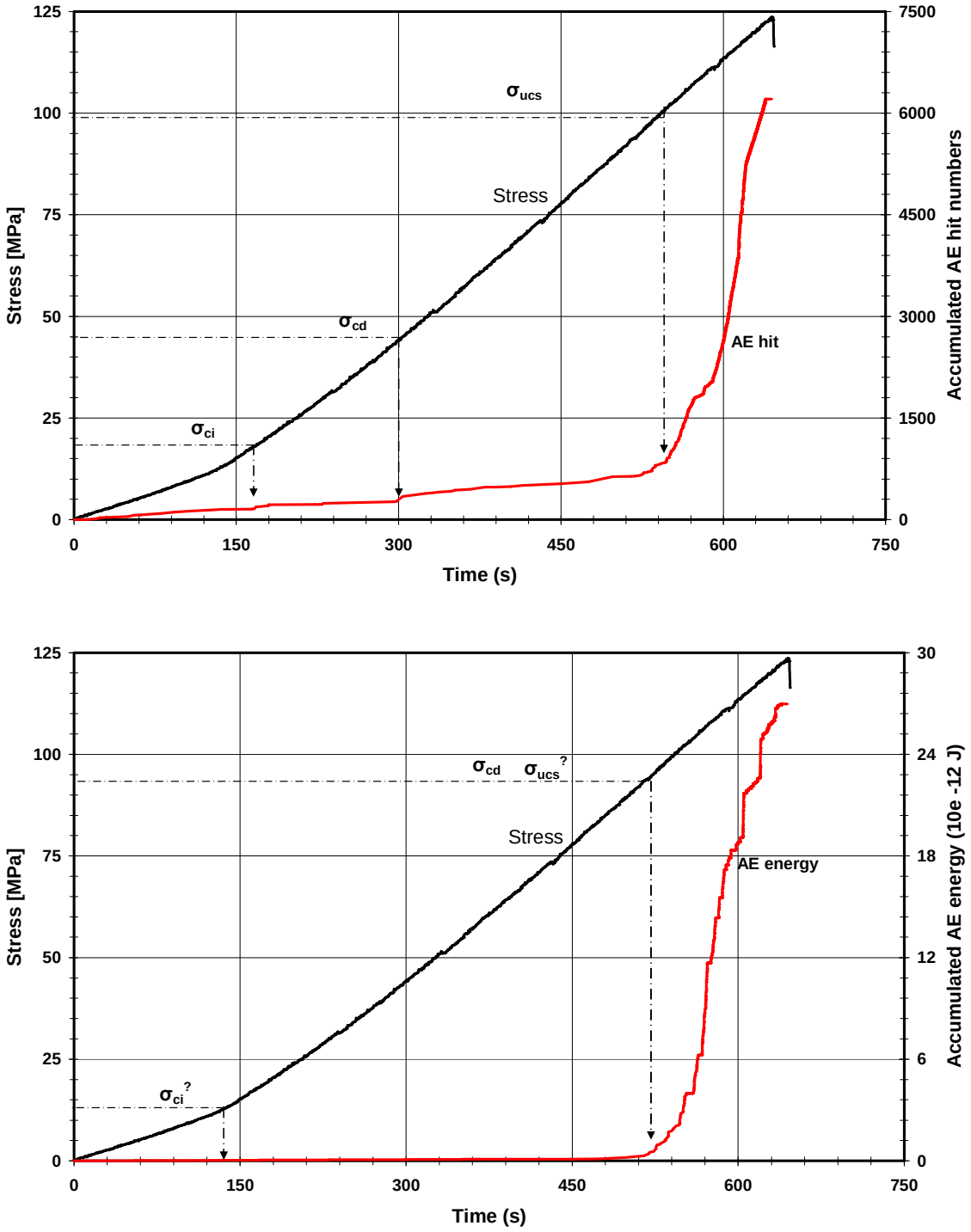

Figure 5: Accumulated AE hit (above) and energy (below) versus stress - time during uniaxial simple compression test of Lavasan granite specimen Gr16. σ_c=122 MPa. The axial deformation has been recorded by LVDT.

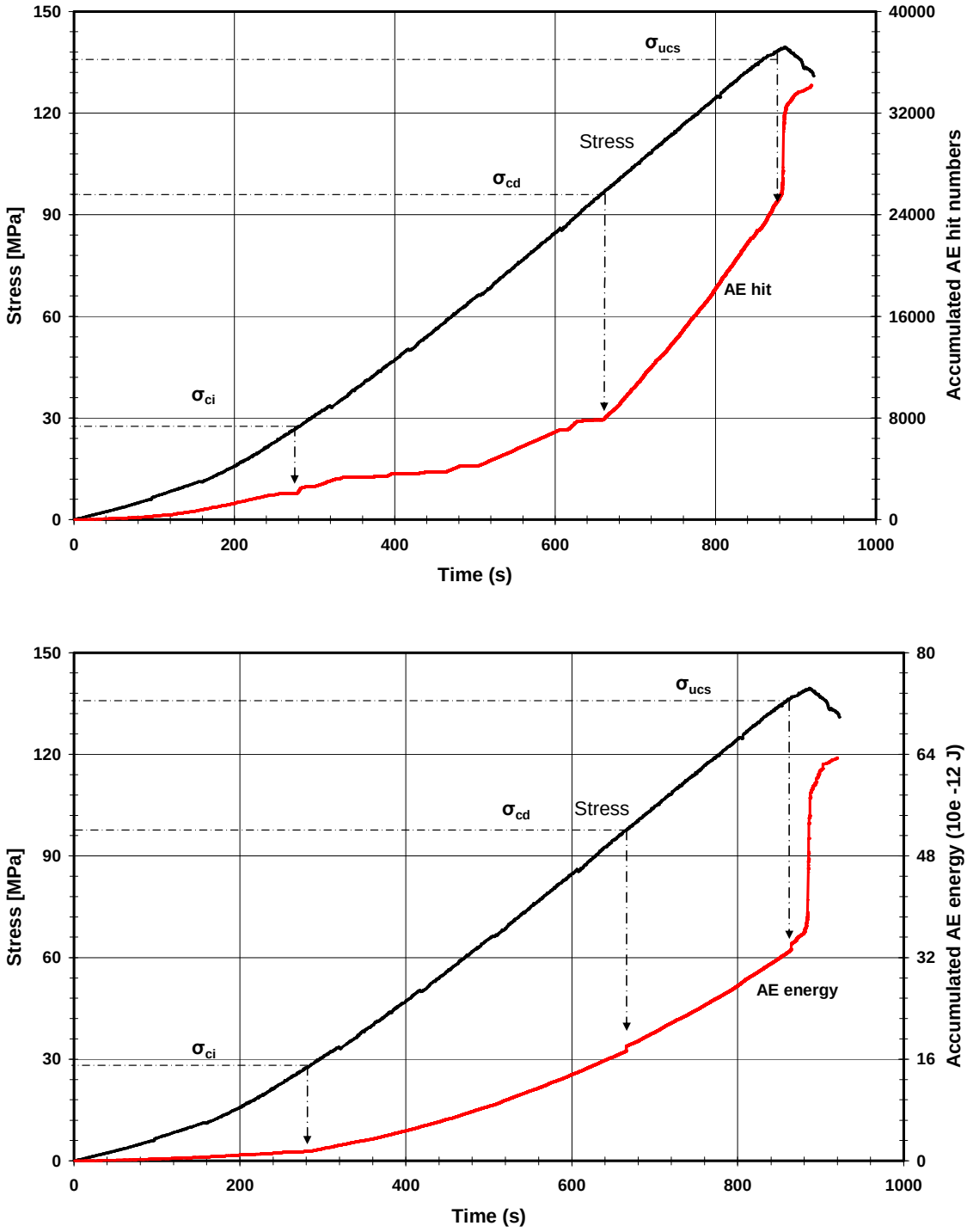

Figure 6: Accumulated AE hit (above) and energy (below) versus stress - time during uniaxial simple compression test of Lavasan granite specimen Gr17. σ_c=136 MPa. The axial deformation has been recorded by LVDT.

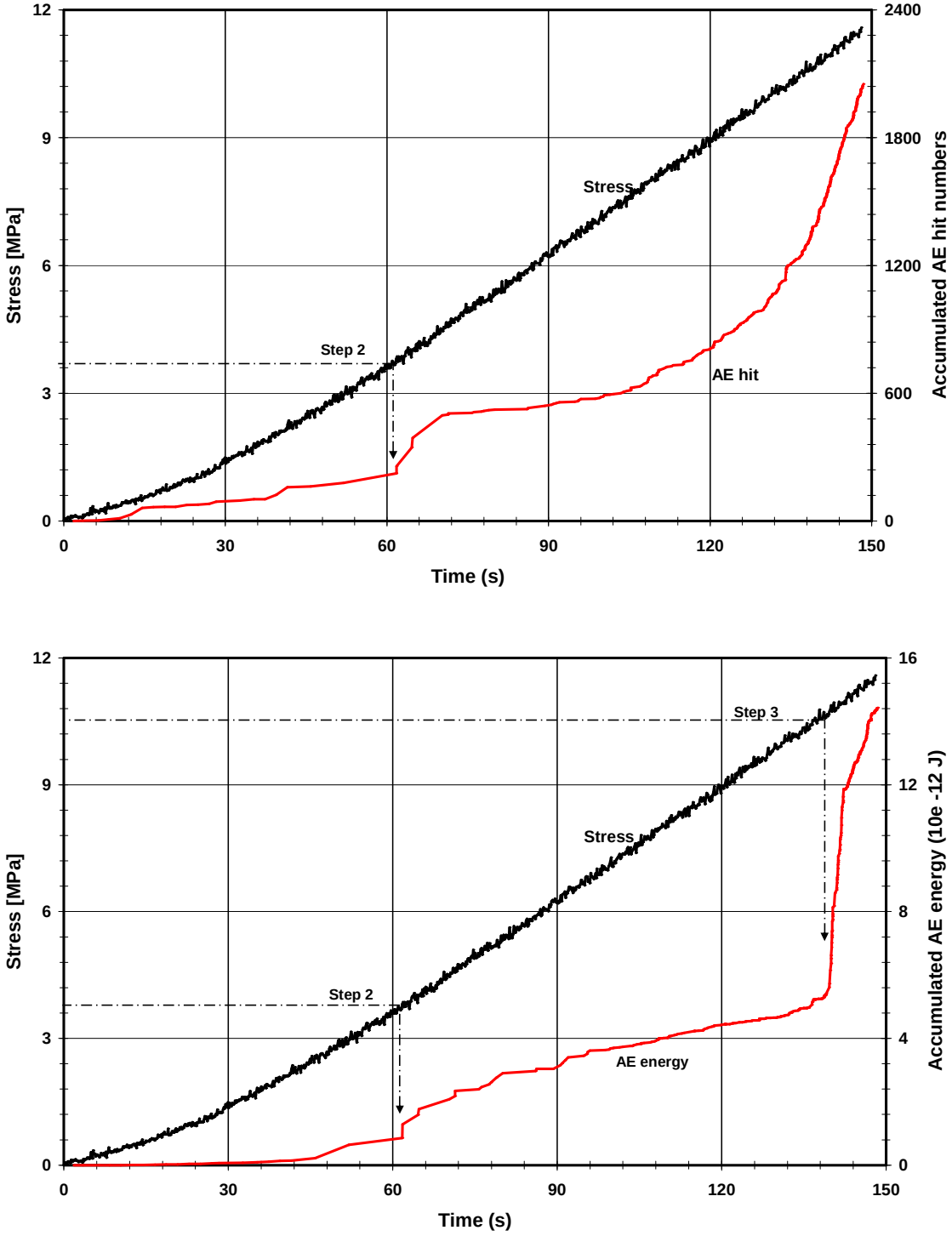

Figure 7: Accumulated AE hit (above) and energy (below) versus stress - time during Brazilian test on gabbro specimen Gab5. Tensile strength =11.6 MPa. Deformation has been measured by LVDT.

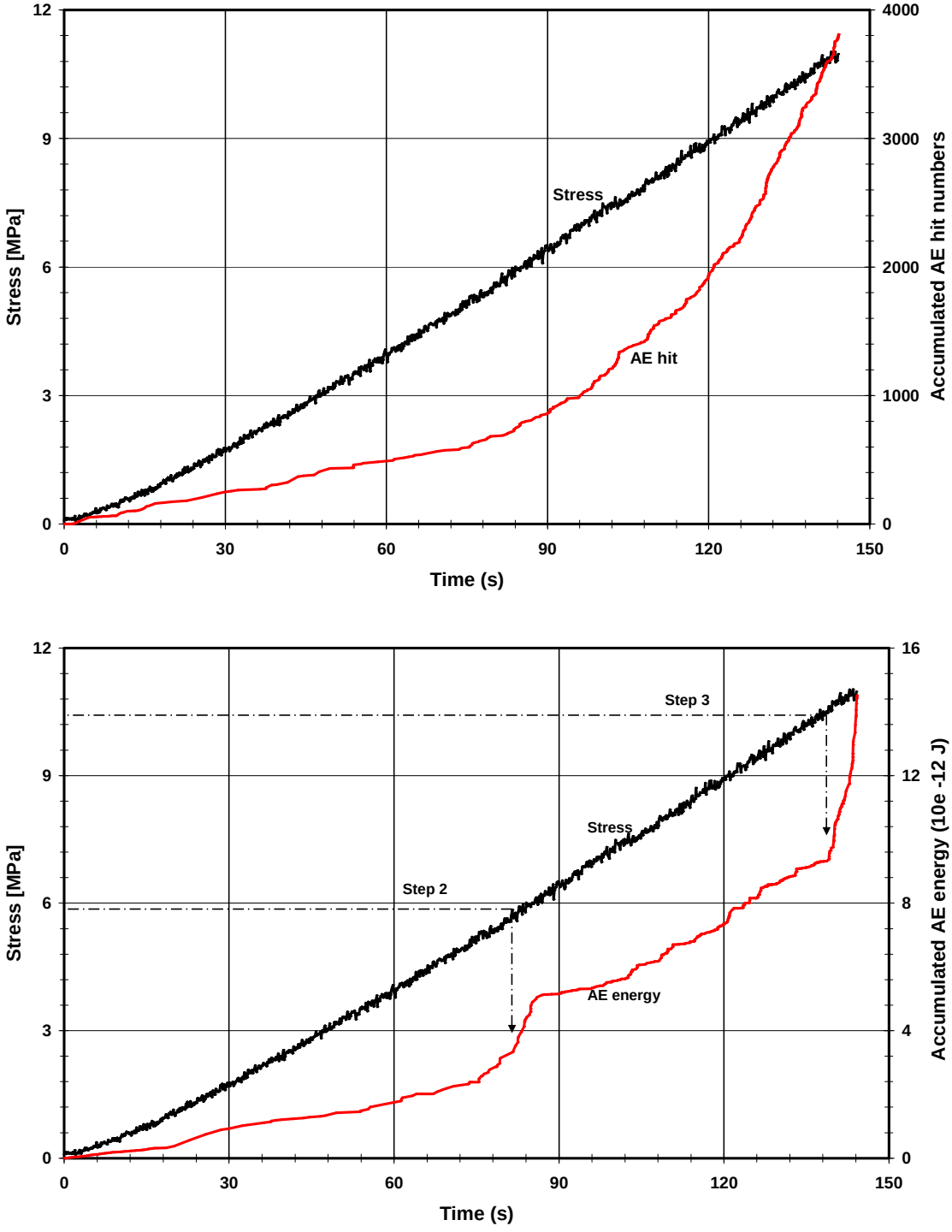

Figure 8: Accumulated AE hit (above) and energy (below) versus stress - time during Brazilian test on gabbro specimen Gab6. Tensile strength =10.9 MPa. Deformation has been measured by LVDT.

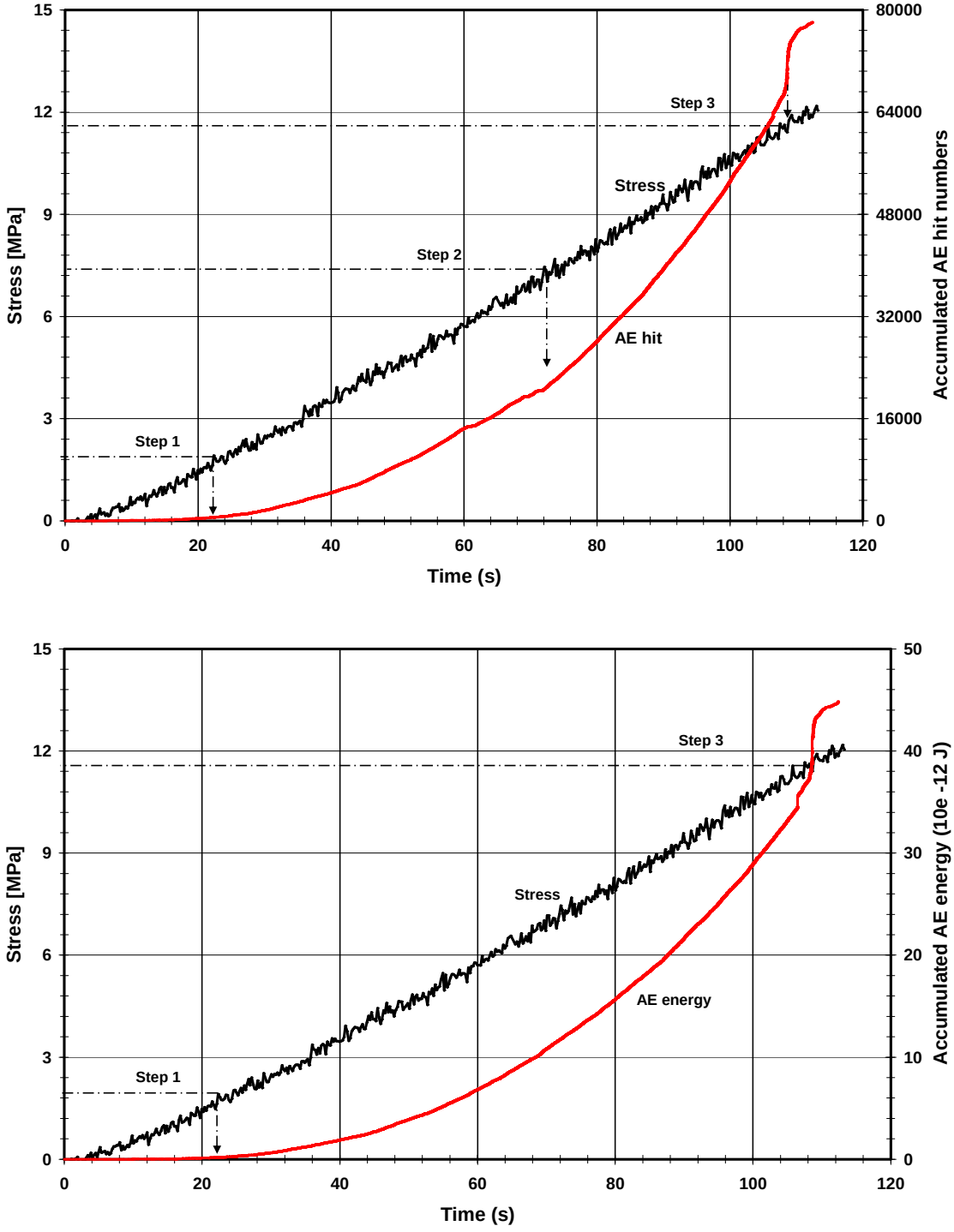

Figure 9: Accumulated AE hit (above) and energy (below) versus stress - time during Brazilian test on gabbro specimen Gab7. Tensile strength =11.7 MPa. Deformation has been measured by LVDT.

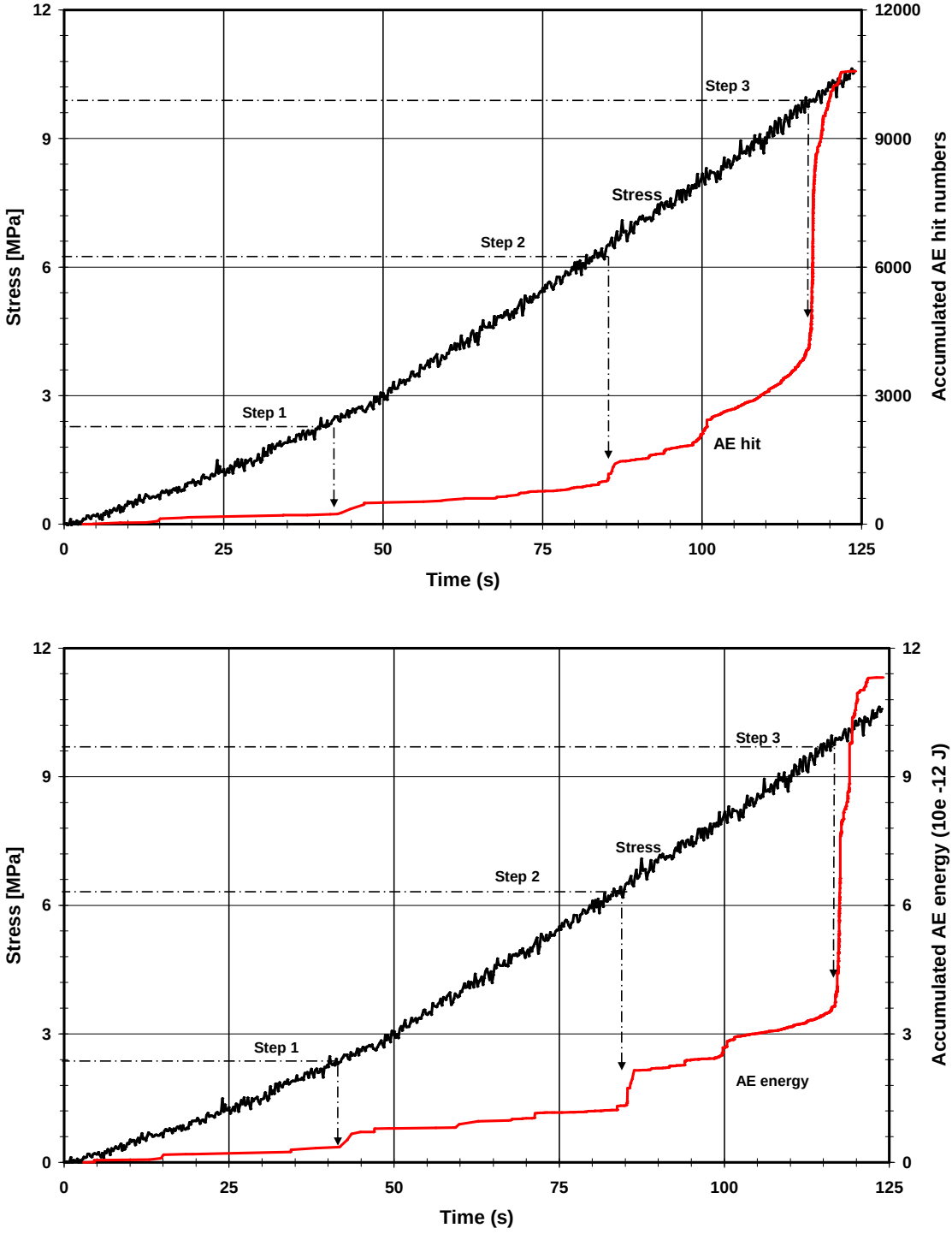

Figure 10: Accumulated AE hit (above) and energy (below) versus stress - time during Brazilian test on gabbro specimen Gab8. Tensile strength =10.6 MPa. Deformation has been measured by LVDT.

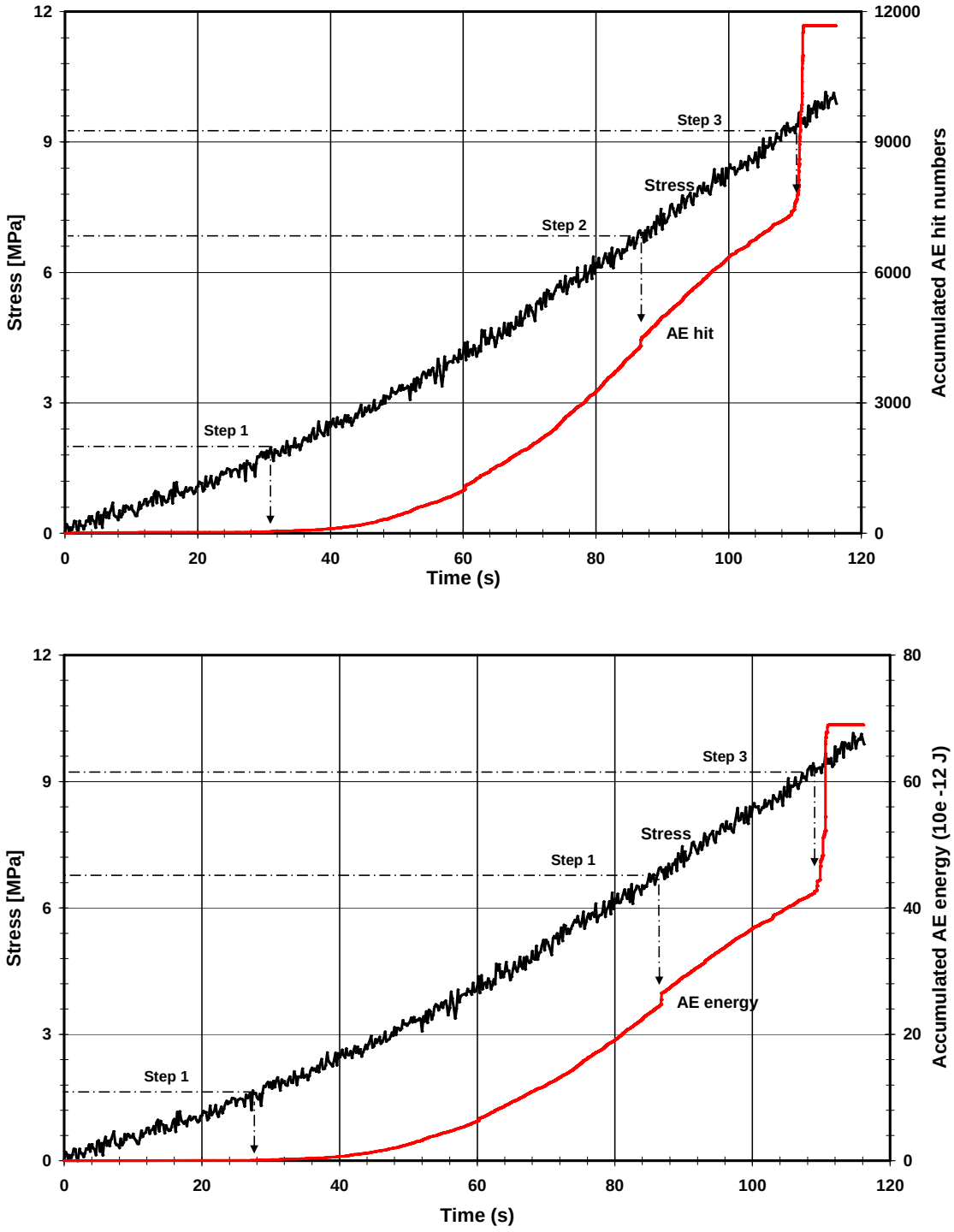

Figure 11: Accumulated AE hit (above) and energy (below) versus stress - time during Brazilian test on gabbro specimen Gab9. Tensile strength =10.2 MPa. Deformation has been measured by LVDT.

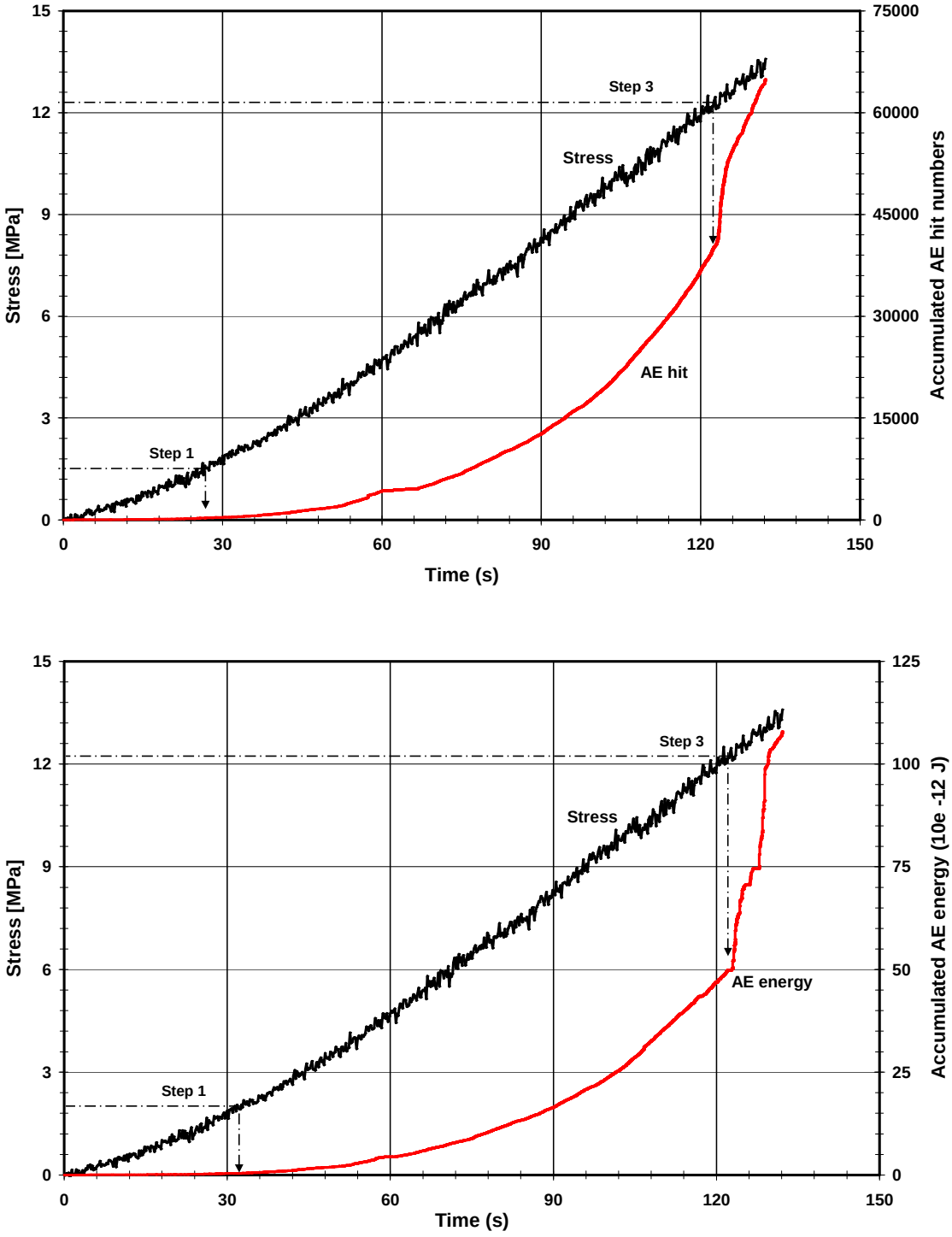

Figure 12: Accumulated AE hit (above) and energy (below) versus stress - time during Brazilian test on gabbro specimen Gab10. Tensile strength =13.5 MPa. Deformation has been measured by LVDT.

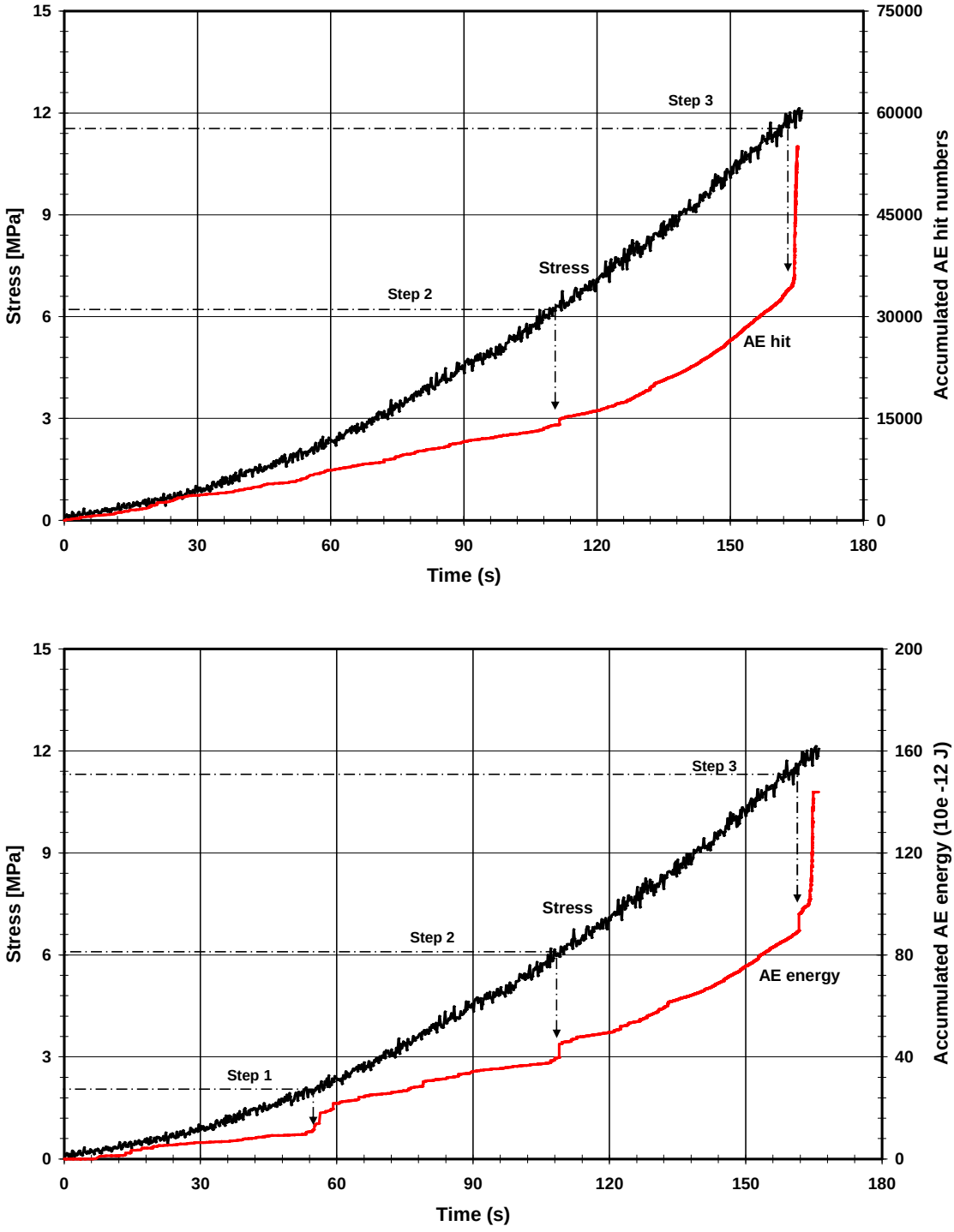

Figure 13: Accumulated AE hit (above) and energy (below) versus stress - time during Brazilian test on gabbro specimen Gab11. Tensile strength =12.2 MPa. Deformation has been measured by LVDT.

Appendix II

Infrared measurement results of Lavasan granite

Table 2: Details of infrared measurements from Lavasan granite under uniaxial cyclic tests

Force (kN)	Static Force (kN)	Dynamic Force (kN)	Min. (kN)	Max. (kN)	ΔT (℃)	Name of Image*
1.2	1.2	±0.6	0.6	1.8	0	SYEA001 (reference)
2.5	2.5	±1.2	1.2	3.7	0	SYEB050
3.1	3.1	±1.9	1.2	5.0	0.16	SYEC050
3.7	3.7	±2.5	1.2	6.2	0.32	SYED050
5.0	5.0	±3.7	1.2	8.7	0.78	SYEE052
6.2	6.2	±5.0	1.2	11.2	1.11	SYEF052
7.4	7.4	±6.2	1.2	13.6	1.63	SYEG051
8.7	8.7	±7.4	1.2	16.1	2.32	SYEH052
9.9	9.9	±8.7	1.2	18.6	2.91	SYEI051
11.1	11.1	±9.9	1.2	21	3.50	SYEJ052
12.4	12.4	±11.2	1.2	23.6	4.07	SYEK050
13.6	13.6	±12.4	1.2	26.0	5.19	SYEL050

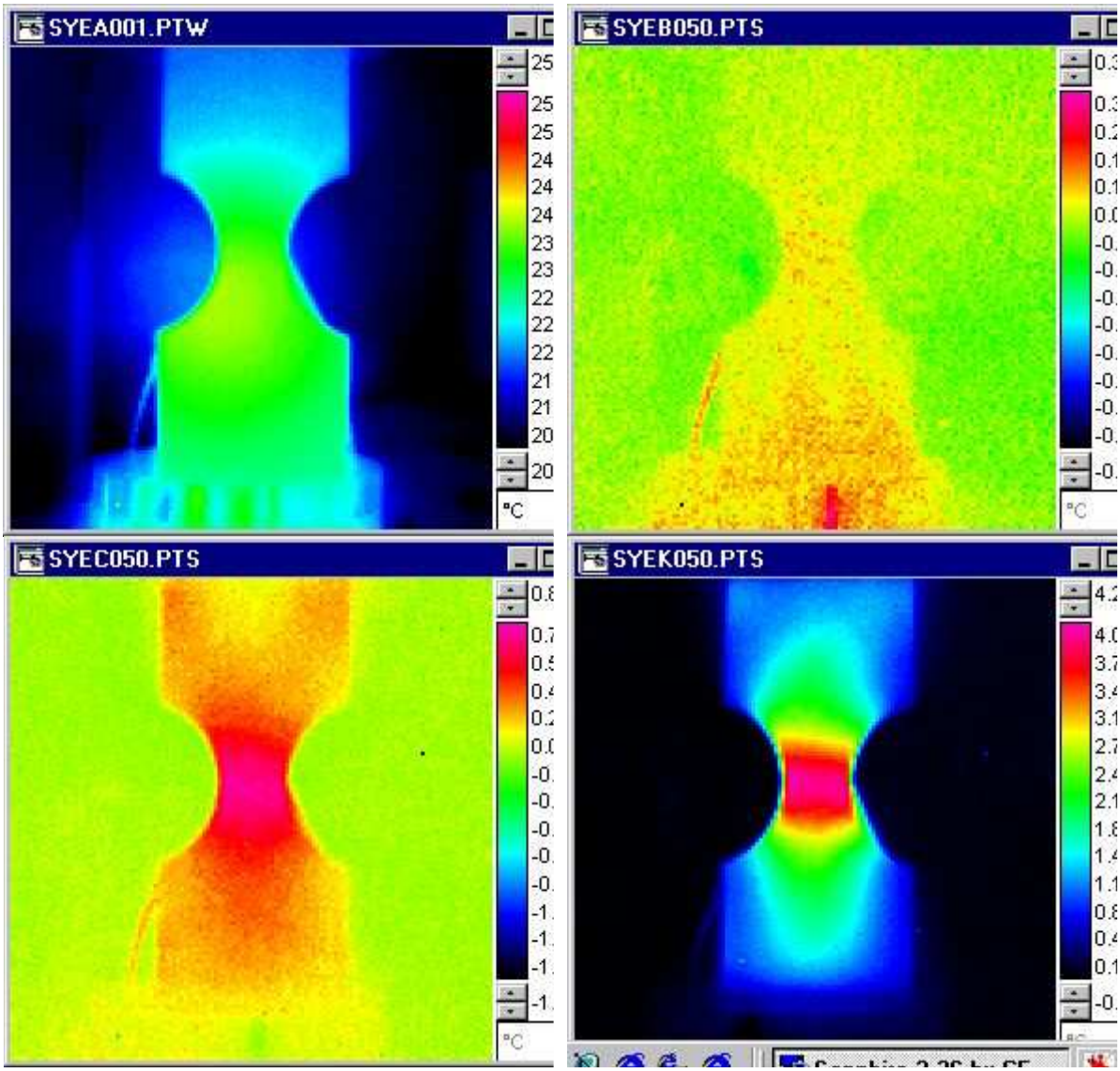

Figure 14: Infrared measurements of Lavasan granite under cyclic loading. Specimen SYEA001 is a reference picture and has been taken at beginning of test. Picture SYEK050 is taken at the maximum loading (Fmax. = 23.6 kN). Note to the focus of heat at middle part of the specimens.

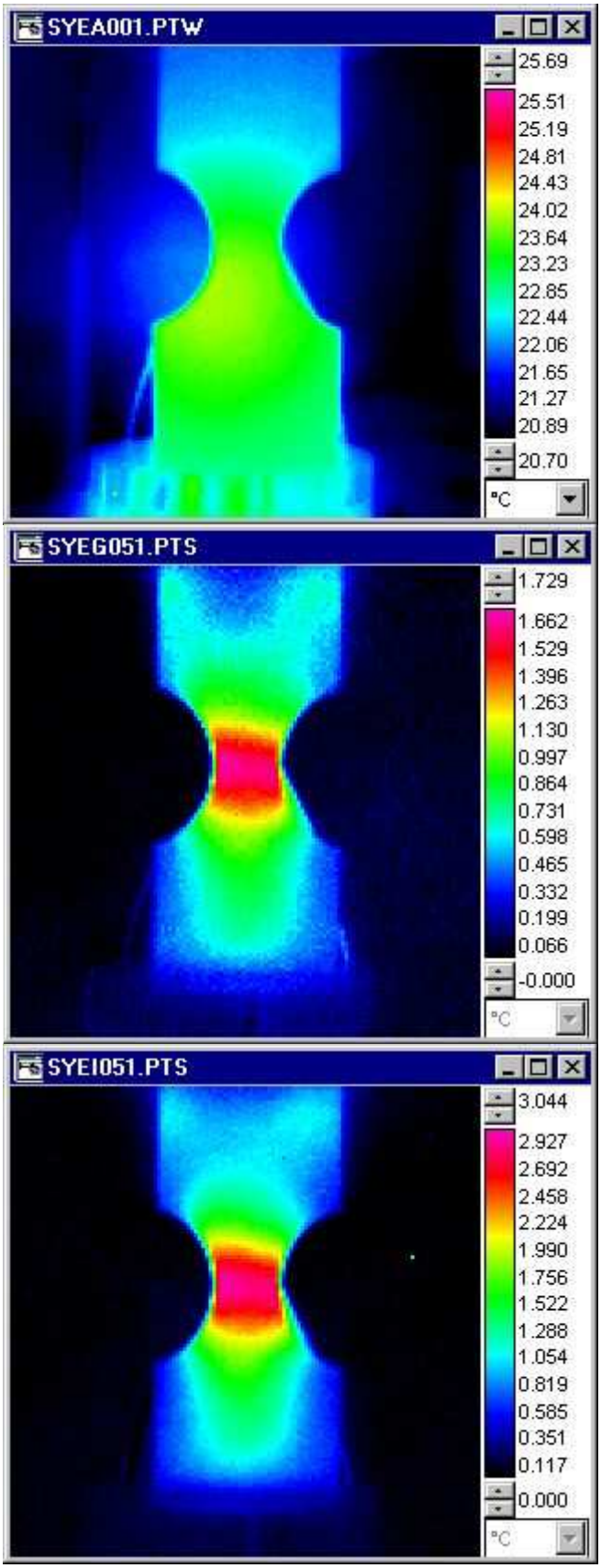

Figure 15: Infrared measurements of Lavasan granite under cyclic loading. Specimen SYEA001 is a reference picture. Picture SYEI051 is taken at the maximum loading (Fmax. = 18.6 kN).

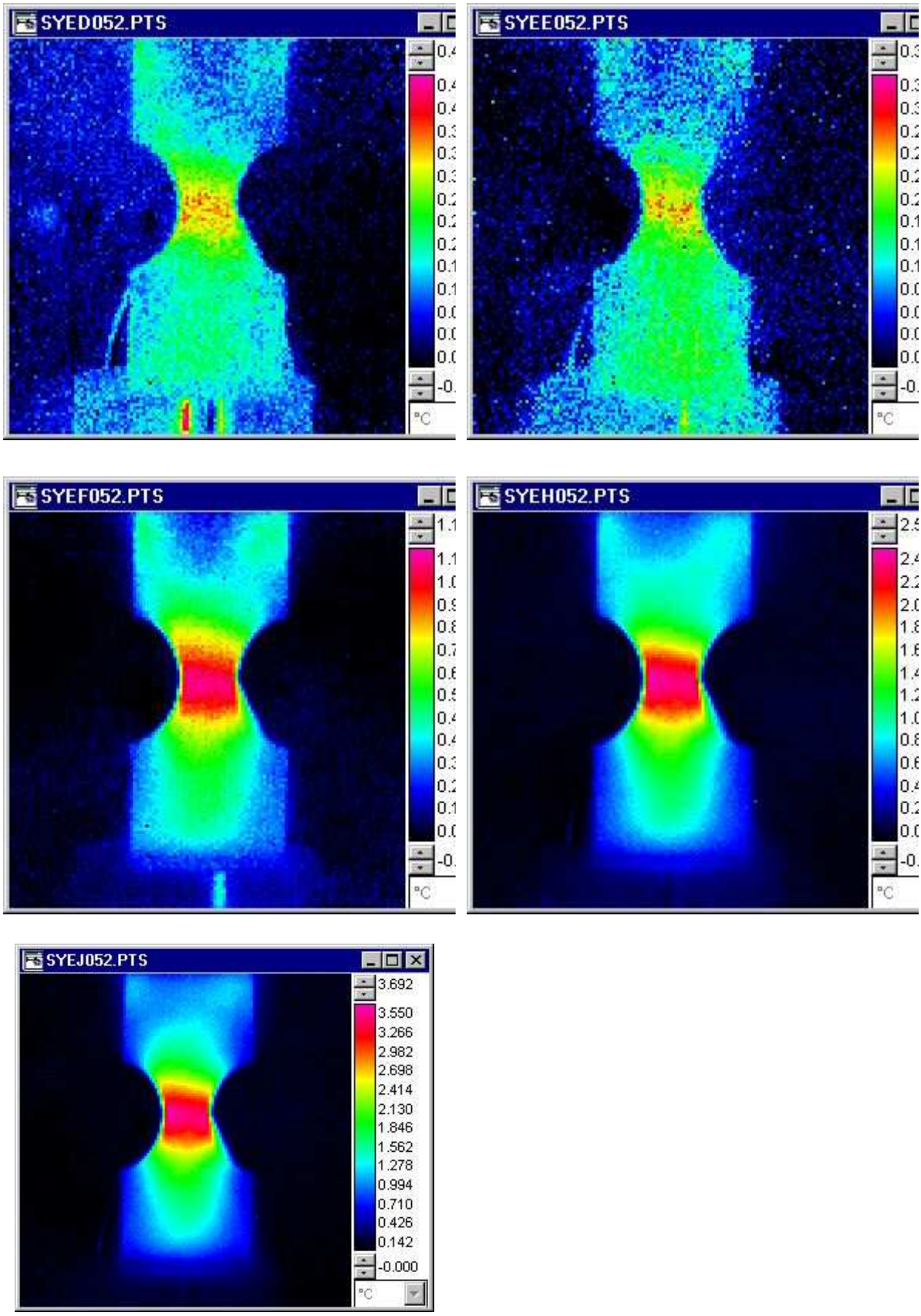

Figure 16: Infrared measurements of Lavasan granite under cyclic loading. Specimen SYED052 is taken at minimum of loading (F = 6.2 kN) and picture SYEL052 is taken at the maximum of loading (F = 26 kN).

Appendix III

AE monitoring of thermally treated gabbro specimens and stress-deformation data

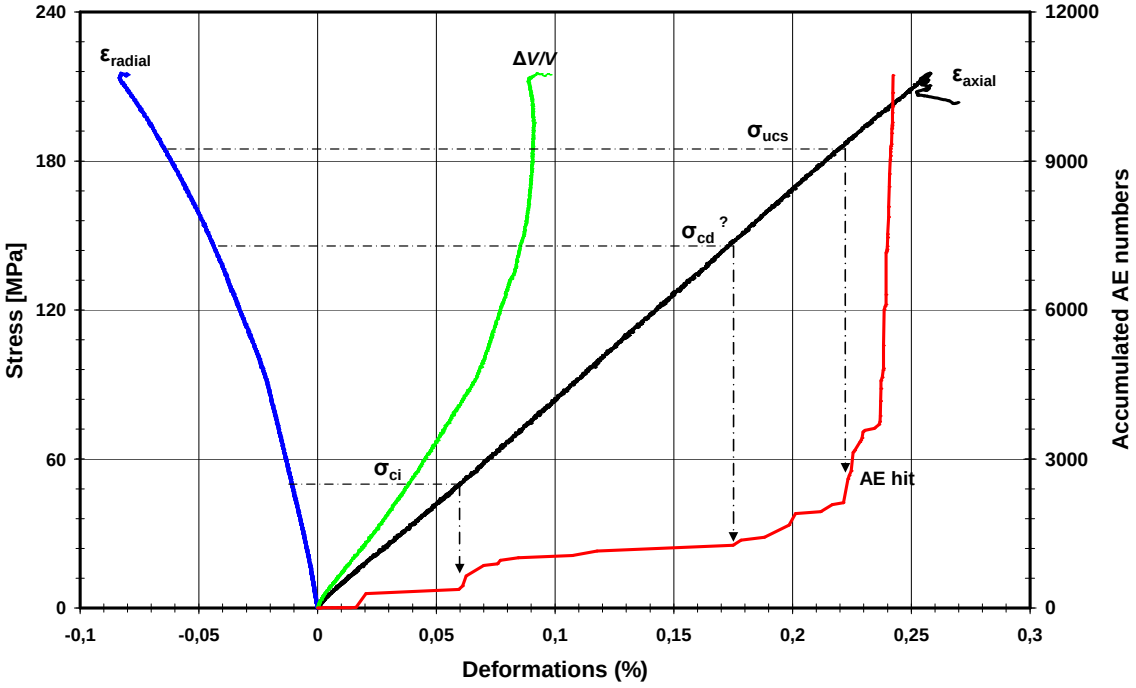

Figure 17: Accumulated AE hit records versus deformation and stress of 150℃ thermally treated gabbro specimen Ga11 during simple uniaxial compression tests.

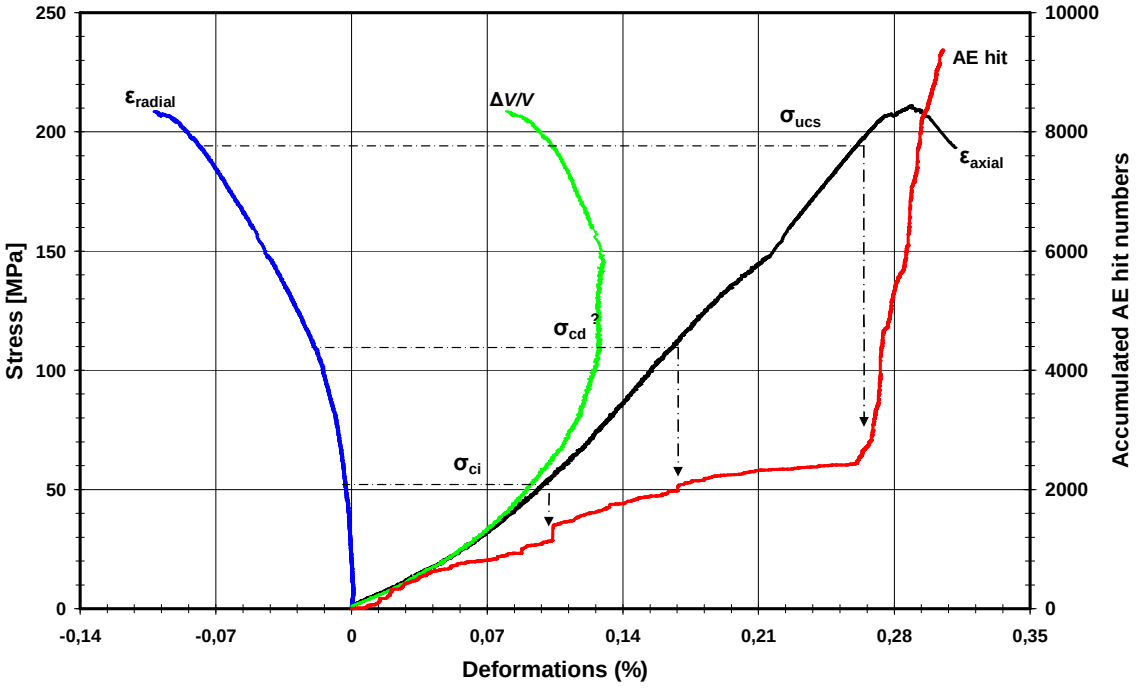

Figure 18: Accumulated AE hit records versus deformation and stress of 300℃ thermally treated gabbro specimen Ga12 during simple uniaxial compression tests.

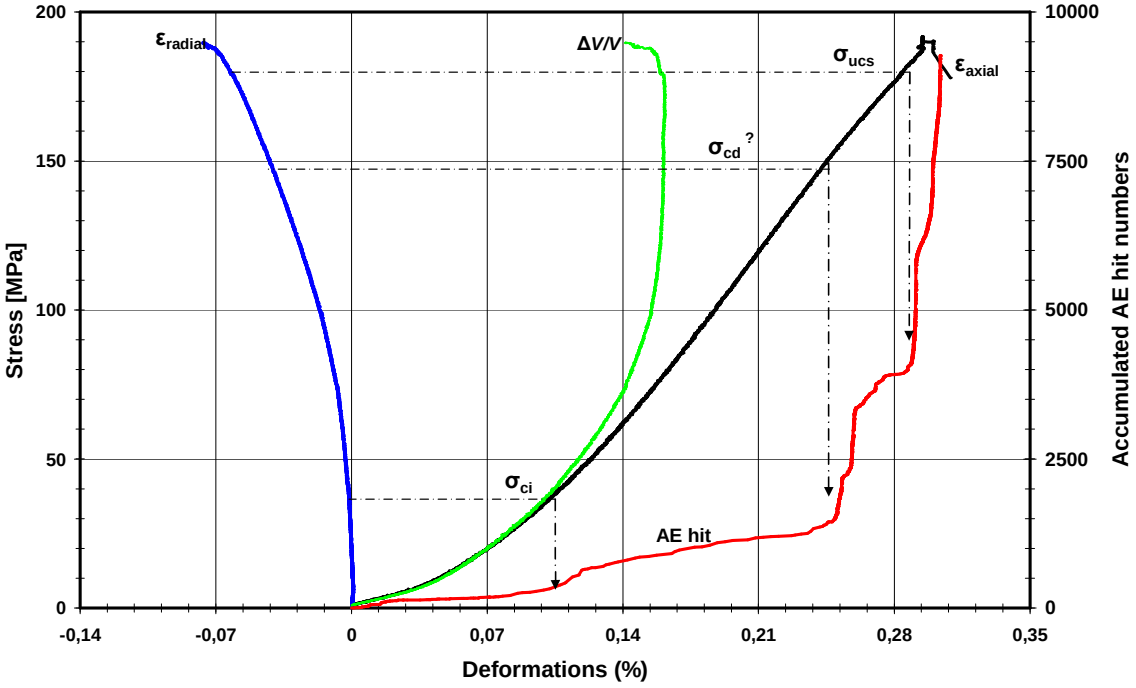

Figure 19: Accumulated AE hit records versus deformation and stress of 500℃ thermally treated gabbro specimen Ga13 during simple uniaxial compression tests.

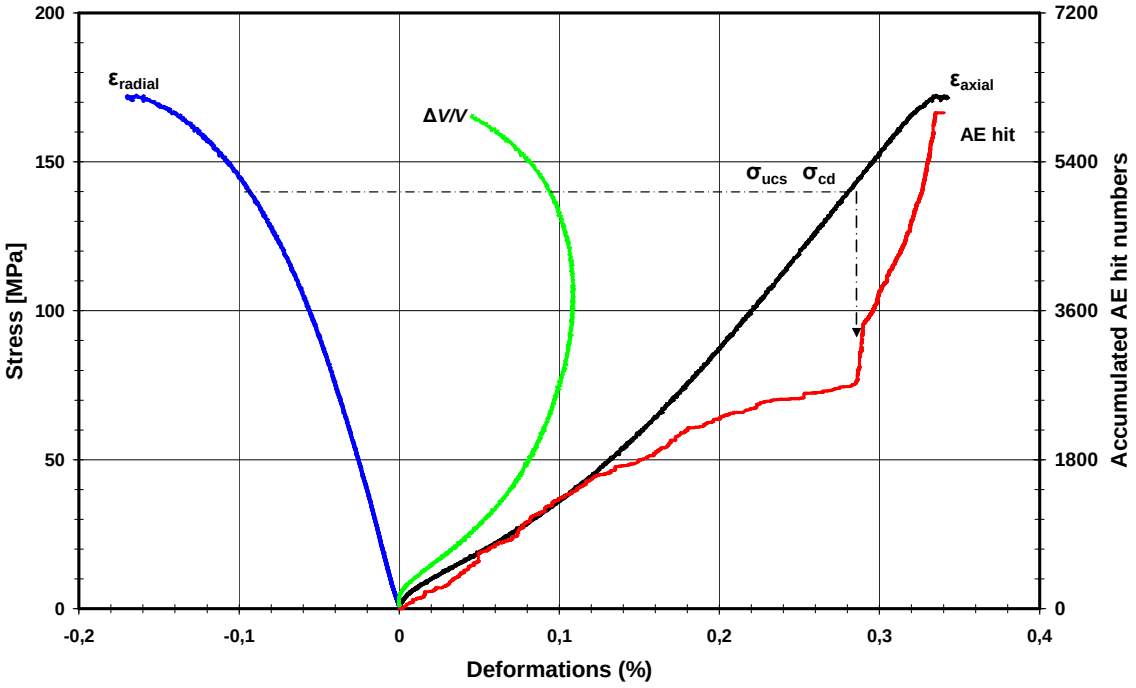

Figure 20: Accumulated AE hit records versus deformation and stress of 600℃ thermally treated gabbro specimen Ga14 during simple uniaxial compression tests.

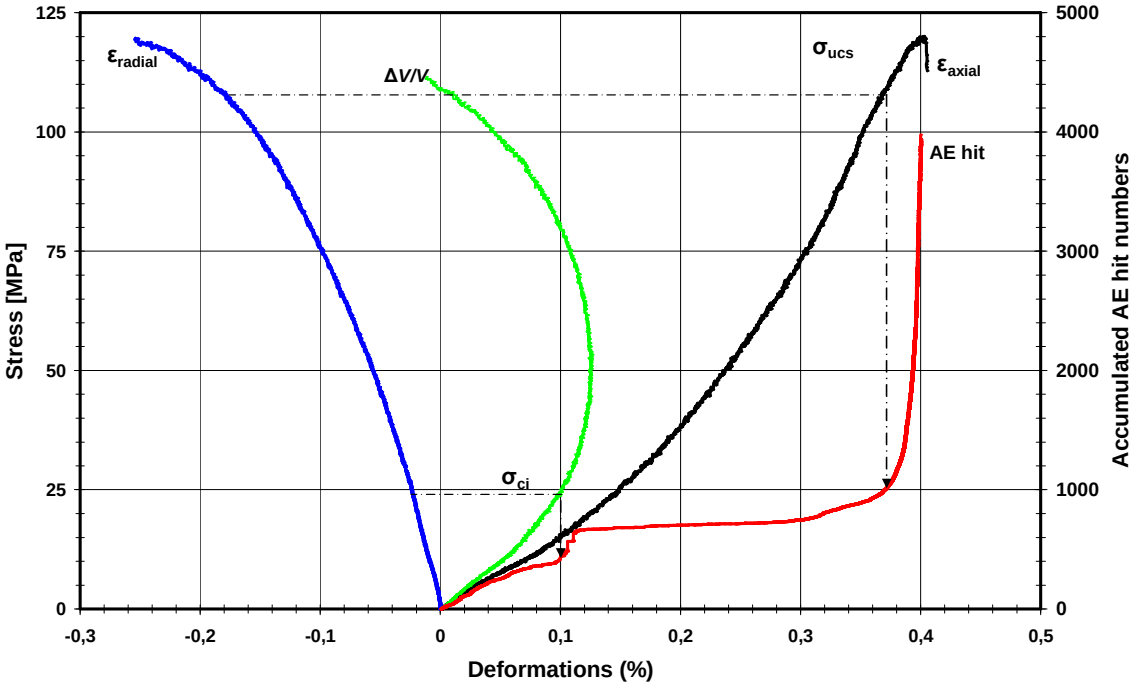

Figure 21: Accumulated AE hit records versus deformation and stress of 700℃ thermally treated gabbro specimen Ga15 during simple uniaxial compression tests.

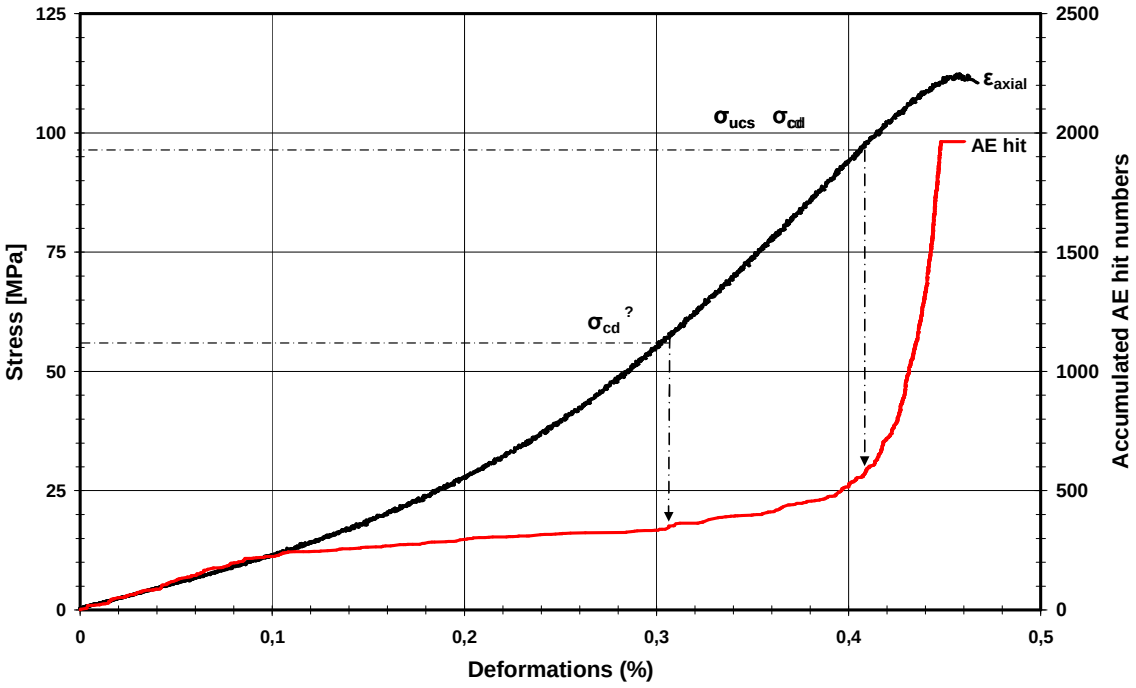

Figure 22: Accumulated AE hit records versus deformation and stress of 800℃ thermally treated gabbro specimen Ga16 during simple uniaxial compression tests.

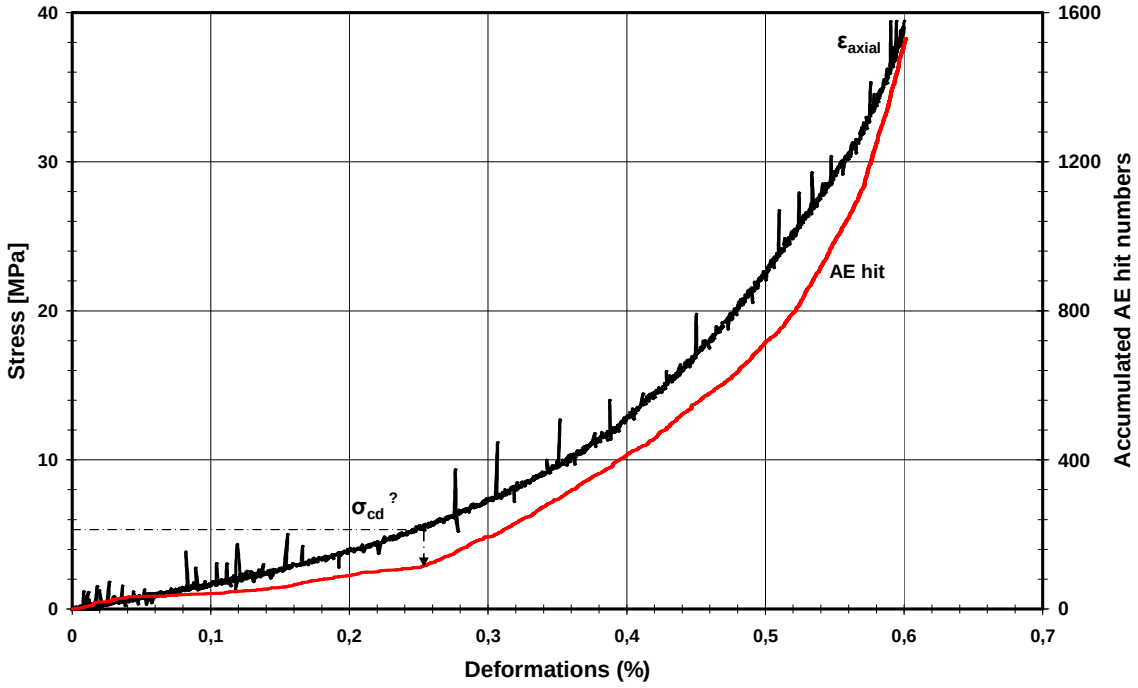

Figure 23: Accumulated AE hit records versus deformation and stress of 1000℃ thermally treated gabbro specimen Ga17 during simple uniaxial compression tests.